ISNM
Vol. 149

Multiscale Modeling in Epitaxial Growth

Edited by
Axel Voigt

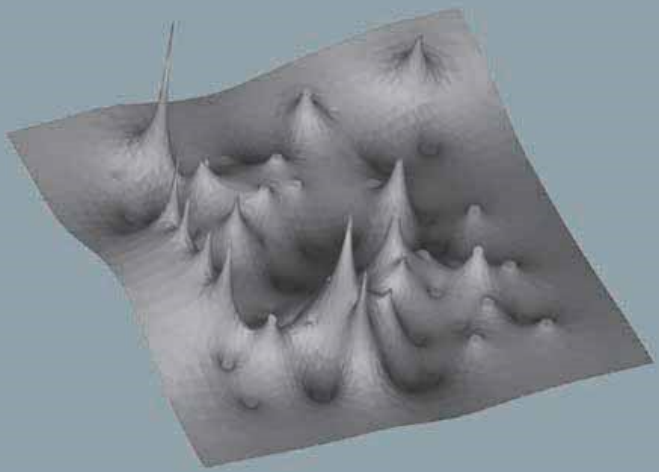

Birkhäuser

ISNM
International Series of Numerical Mathematics
Vol. 149

Multiscale Modeling in Epitaxial Growth

Edited by
Axel Voigt

Birkhäuser Verlag
Basel · Boston · Berlin

Editor:

Axel Voigt
research center caesar
Crystal Growth Group
Ludwig-Erhard-Allee 2
D-53175 Bonn
Germany

2000 Mathematics Subject Classification 35R35, 80A22, 82B80

A CIP catalogue record for this book is available from the Library of Congress, Washington D.C., USA

Bibliographic information published by Die Deutsche Bibliothek
Die Deutsche Bibliothek lists this publication in the Deutsche Nationalbibliografie; detailed bibliographic data is available in the Internet at http://dnb.ddb.de.

ISBN 3-7643-7208-7 Birkhäuser Verlag, Basel – Boston – Berlin

The cover picture shows the adatom density on a submonolayer, the finite element solution of the Burton-Cabrera-Frank equation.

Part of Springer Science+Business Media
Printed on acid-free paper produced of chlorine-free pulp. TCF ∞
Printed in Germany
ISBN-10: 3-7643-7208-7
ISBN-13: 978-3-7643-7208-8
9 8 7 6 5 4 3 2 1 www.birkhauser.ch

Multiscale Modeling in Epitaxial Growth

Mini-Workshop at Mathematisches
Forschungsinstitut Oberwolfach
January 18–24, 2004

ISNM 149
ISBN 3-7643-7208-7

Edited by

A. Voigt

Editors:

Axel Voigt
Crystal Growth group
research center caesar
Ludwig-Erhard-Allee 2
D-53175 Bonn
Germany

Contents

Preface

Thin film growth by molecular beam epitaxy (MBE) is a modern technology of growing single crystals that inherit atomic structures from substrates. It is technologically relevant, experimentally well explored and a very active area of theoretical research. Modeling of epitaxial growth is a challenging multi-scale problem. Given the fact that the macroscopic evolution of the growing film is directly related to movements of adatoms on surfaces and their various bonding configurations, it is appealing to use atomic scale simulations for a theoretical description of epitaxial growth. However in order to reach the length and time scales of interest for various applications continuum models have to be used. Today a hierarchy of models has been investigated to describe epitaxial growth: From fully atomistic models, via semi-discrete step flow models to continuum models for the height of the growing film. The main challenge in modeling epitaxial growth is to bridge the gap between these different models and to describe growth process on a continuous scale by incorporating atomistic effects. With the advent of powerful numerical techniques for the solution of such models combined with a deep understanding of the physical and chemical phenomena during the growth process this goal might be achieved in the near future.

The goal of the book is to summarize recent developments in modeling epitaxial growth, with emphasis on multi-scale approaches and numerical methods. The book provides a compact overview and can serve as an introduction for applied mathematicians, theoretical physicists and computational materials scientists into this highly active interdisciplinary field of research.

The book results from a workshop held at the *Mathematisches Forschungsinstitut Oberwolfach* on *Multiscale Modeling in Epitaxial Growth* from January 18th to 24th 2004. This volume contains 14 refereed original papers which are subdivided into three parts corresponding to the three classes of models. Each part starts with an introductory review article.

Part 1: *Atomistic models.* The methods discussed range from first-principle methods, which determine energy pathways and barriers to diffusion and other kinetic processes; classical Molecular-Dynamics method, which are applied to study the diffusion on a crystalline surface; kinetic Monte Carlo methods, which are combined with Molecular-Dynamics to study the influence of strain on the morphology of the film and quasi-continuum Monte Carlo methods which coarse grain the atomistic picture and draw a connection to step flow models.

Part 2: *Step flow models.* At sufficiently low temperatures the surface of a crystal consists of atomic steps. These steps provide a basis for the description of the surface morphology on an intermediate mesoscopic scale, between atomistic and continuum scales. The steps are assumed to be continuous curves of zero thickness which serve as free boundaries for the adatom density on the terraces. Sharp interface and phase field methods for this class of free boundary problems are discussed. Simulations show the influence of various anisotropies on the shape of single islands, investigate instabilities in step dynamics and study homoepitaxial Ostwald ripening.

Part 3: *Continuum models.* The surface of the film is described through a partial differential equation for the evolution of the interface between film and vapor. The discrete nature of the steps is coarse grained and a smooth surface is assumed on a macroscopic scale. The derivation of such models makes use of inherent symmetries in the physical process, i.e., mass conservation and crystal symmetry, and results in nonlinear diffusion equations for the height of the growing film. Besides this heuristic derivation a computational approach to derive a continuum model from step flow models is discussed. Furthermore a more thermodynamical approach for the evolution of a surface, which is based on an anisotropic surface energy is considered and numerically solved by a level set method.

I hope that this book will contribute to the exciting ongoing discussion in the field of epitaxial growth and will encourage young researchers to join this area. I express my gratitude to the authors, to the publisher and last but not least to the *Mathematisches Forschungsinstitut Oberwolfach*.

Bonn, July 20th 2004 Axel Voigt

Part 1

Atomistic Models

International Series of Numerical Mathematics, Vol. 149, 3–18

Lattice Gas Models and Kinetic Monte Carlo Simulations of Epitaxial Growth

Michael Biehl

Abstract. A brief introduction is given to Kinetic Monte Carlo (KMC) simulations of epitaxial crystal growth. Molecular Beam Epitaxy (MBE) serves as the prototype example for growth far from equilibrium. However, many of the aspects discussed here would carry over to other techniques as well. A variety of approaches to the modeling and simulation of epitaxial growth have been applied. They range from the detailed quantum mechanics treatment of microscopic processes to the coarse grained description in terms of stochastic differential equations or other continuum approaches. Here, the focus is on discrete representations such as lattice gas and Solid-On-Solid (SOS) models. The basic ideas of the corresponding Kinetic Monte Carlo methods are presented. Strengths and weaknesses become apparent in the discussion of several levels of simplification that are possible in this context.

Mathematics Subject Classification (2000). Primary 82B24; Secondary 82B80.

Keywords. Crystal growth; Lattice gas; Kinetic Monte Carlo; vicinal surfaces.

1. Introduction

An impressing variety of methods is applied in the theory, modeling, and simulation of epitaxial growth. They range from the faithful quantum mechanics treatment of the microscopic dynamics to the description in terms of coarse grained continuum models. An overview of the field can be obtained from, e.g., [1, 2, 3, 4] and this volume.

The purpose of this contribution is to provide a brief introduction to one of the most widely used approaches: the Kinetic Monte Carlo (KMC) simulation of lattice gas models. It is not intended to give a detailed exhaustive review or historical summary of the many aspects of this line of research. The aim is to introduce and illustrate some of the basic concepts of the method and to provide a starting point for the interested reader. The selection of examples from the literature also reflects this purpose and the list of references is far from being

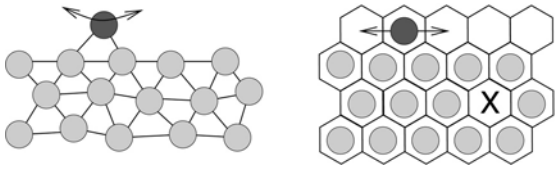

FIGURE 1.
Cartoon of hopping diffusion on a flat surface (cross section).
Left: Particles can assume continuous positions in space, straight lines correspond to nearest neighbor bonds. In an MD simulation, thermal fluctuations of the entire system may result in a jump of the adatom (dark) to a neighboring pair of surface atoms.
Right: Simplifying lattice gas representation of the same situation. Atoms can only occupy pre-defined lattice sites as represented by the hexagonal cells, here. In a KMC simulation, the adatom jumps to the left or right neighbor cell with a given rate. The cross marks a vacancy in the bulk which would be, like overhangs, *forbidden* in Solid-On-Solid models.

complete in any sense. It is the result of a very personal and often random choice of examples. Numerous important contributions to the advancement of the KMC technique and its applications cannot be mentioned here and the interested reader is directed to, e.g., [1, 2, 3, 4, 5] for further references.

Among the different realizations of epitaxial growth, Molecular Beam Epitaxy (MBE) is a particularly clear-cut one [1, 2, 3, 4]. In this technique, one or several adsorbate materials are heated in an oven which is contained in an ultra-high-vacuum chamber. The evaporating particles form an atomic or molecular beam which is directed onto a substrate crystal. Arriving particles are incorporated and contribute to the growing film upon the substrate. The term homoepitaxy is used if the deposited adsorbate and the substrate material are identical, whereas in heteroepitaxy they differ. Apart from the selected materials, the most important experimental control parameters in MBE growth are the substrate temperature and the flux of incoming particles.

MBE has become a well-established technique for the production of high-quality crystals, as it allows for a very precise control of the growth conditions. It is, for instance, possible to add monoatomic layers of a compound semiconductor to the growing film by alternating deposition of the elements in Atomic Layer Epitaxy (ALE).

Molecular Beam Epitaxy is applied, for example, in the growth of layered semiconductor heterostructures for electronic devices or in the development of thin magnetic films for novel storage media. MBE plays also a significant role as a tool in the design of nano-structures, such as Quantum Wires or Dots [6]. The

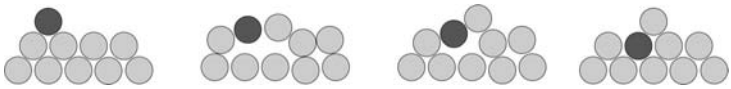

FIGURE 2. Illustration of an exchange diffusion process (cross section). A concerted move of several particle leads to the exchange of the adatom (dark) with a surface atom. Note that, if all atoms represent the same chemical element, the final states of hopping and exchange diffusion in this illustration would be identical whereas the transition states differ significantly.

range of materials used in MBE includes conventional semiconductors, elementary metals, metal-oxides, and organic molecules.

Growth in an MBE environment is clearly far from equilibrium, as the system is constantly driven by the deposition flux and an extremely low pressure is maintained in the vacuum chamber. This is different from, say, growth from the vapor which can be much closer to thermal equilibrium. This feature makes MBE highly attractive from a theoretical point of view. It provides a workshop in which to put forward analytical approaches and develop tools for the simulation of more general non-equilibrium systems.

In the following section, relevant atomistic processes and some approaches to the theory and modeling of MBE growth are discussed. Many aspects would directly carry over to the physics and modeling of similar growth techniques. In Section 3, the basic features of lattice gas models and the corresponding Monte Carlo kinetics are presented and a short conclusion is given in Section 4.

2. Atomic scale processes in MBE growth

In MBE, physical processes in a very wide range of time and length scales are relevant. Accordingly, a set of quite different methods of modeling is required when aiming at a more or less complete realistic picture of the growth process.

Ultimately, all macroscopic features of the growing surface emerge from the interactions of atoms and their microscopic kinetics. Therefore, a faithful quantum mechanical description on the atomistic level is clearly desirable. The so-called *Density Functional Theory* (DFT) is particularly suitable in this context [7]. This method is based on the, in principle exact, description of many electron systems in terms of the electron density only. Despite the clear advantage over an explicit treatment of the many particle Schrödinger equation, the computational cost of the method is significant. It is therefore often applied to relatively small systems of a few atoms or molecules, or to unit cells of periodic structures.[1]

[1]The use of relatively vague terms like *relatively small systems* relates to the fact that their meaning steadily changes with the rapid evolution of available computer power.

As just one example for the latter, by means of DFT calculations it is possible to evaluate and compare the specific ground state energies of different reconstructions of a particular material surface. The calculation yields also the precise structure of the reconstruction, i.e., the location of the atoms. Clearly such information is valuable in the development of models describing the surface or its evolution in a non-equilibrium situation. For examples in the context of compound semiconductor surfaces see [8, 9] and references therein.

The analysis of dynamical properties such as diffusion processes is obviously more involved than the investigation of ground state properties only [10]. Impressing progress has been achieved in recent years in the combination of the DFT approach with other methods such as Kinetic Monte Carlo simulations. Reference [10] gives an introduction to this promising line of research.

Often, the results of DFT calculations depend crucially on the quality of the actual approximations made, which can lead to significant discrepancies in the literature. As an example, a discussion and comparison of energy barriers obtained for diffusion on various fcc(111) metal surfaces is given in [4].

One of the most important tools for describing the temporal evolution of many particle systems is Molecular Dynamics (MD), see for instance [11] and the contribution by K. Albe to this volume [12]. In its simplest version it amounts to the numerical integration of Newton's equations of motion based on classical interactions of the particles. Methods have been devised that allow for imposing a constant temperature or other physical conditions on the system [11].

Frequently, the interactions are given in terms of classical pair or many particle potentials. These can range from simple model interactions to highly sophisticated material specific potentials. The latter can be obtained from first principles, e.g., by means of DFT calculations, or result from fitting suitable parameterizations to experimentally observed material properties. It is also possible to incorporate the quantum mechanics of the system directly into the MD scheme, as for instance in the celebrated DFT-based Car-Parrinello method [13].

Efficient implementations and modern computers allow for the simulation of relatively large systems. However, a serious restriction of all MD techniques remains: the physical real time intervals that can be addressed are usually quite small, see the discussion in [12] (this volume). Even with sophisticated acceleration techniques, such as proposed in [14], it seems currently infeasible to reach MBE relevant time scales of seconds or minutes. MD aims at a faithful representation of the microscopic dynamics in continuous time. The relevant time scale of atomic vibrations in a solid is, for instance, $10^{-12}s$. Hence, an MD procedure should advance time by even smaller steps in the numerical integration.

Consider, as an example, a single adatom on top of a flat surface as sketched in Figure 1. Thermal fluctuations may result in a *jump* of the adatom to a neighboring pair of surface atoms. However, such an event will occur quite rarely. A large portion of an MD computation will be used to simulate the collective vibration of the crystal which does not change the system significantly over relatively long

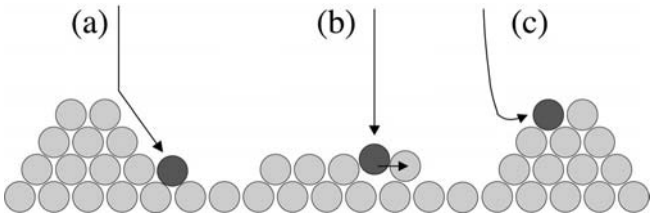

FIGURE 3. Some kinetic effects that may play a role in the incorporation of deposited adatoms.

(a) *Downhill funneling*: the deposited particle slides down a slope until a local minimum of the surface height is reached.
(b) *Knockout process*: the momentum of the arriving particle suffices to push out a surface adatom at a terrace edge.
(c) *Steering effect*: attractive forces can influence the trajectory of the arriving particle significantly.

Obviously, (a) and (c) are unlikely to occur both under the same conditions.

periods of time. It is precisely this difficulty which motivates the basic idea of KMC simulations, see Section 3.

As the discussion in Section 3 will show, perhaps the most attractive advantage of Molecular Dynamics over standard KMC techniques is that no *a priori* assumptions about the possible microscopic processes have to be made. As an example, it is not necessary to know in advance whether adatom diffusion occurs by *hopping* or by concerted *exchange processes* involving many particles, see Figure 2 for an illustration. A similar problem is that of island mobility: in several materials it has been observed that, after mobile adatoms meet and coalesce, they may perform diffusion as a more or less rigid cluster on the surface. Such cluster diffusion can influence the growth kinetics significantly [12]. In principle, an MD simulation which is based on a faithful representation of atomic interactions will produce all relevant single particle or concerted moves *automatically* [12, 14]. In contrast, one usually has to pre-define a catalogue of possible events in KMC simulations, see Section 3.

Molecular Dynamics should also be the natural technique for simulating processes which cannot be described as thermally activated. This concerns in particular the *transient mobility* of freshly deposited adatoms on the surface. A more detailed discussion of such processes can be found in [4], which also provides references to related experimental studies of specific materials.

A deposited particle may arrive with a certain momentum at the surface. Not only was the particle part of a directed beam, it may also pick up additional kinetic energy when it is attracted by the surface. The term *downhill funneling* describes one possible consequence: an adatom that arrives at an inclined portion of the

surface may slide down the slope until it reaches a local minimum in surface height, see Figure 3 (a) for an illustration of the process. It is clearly to be distinguished from thermally activated diffusion which occurs only after the particle has been incorporated into the crystal surface.

Another possible effect is sketched in Figure 3 (b): the arriving particle may *knock out* an atom at a terrace edge. This process will smoothen a surface and would favor layer-by-layer growth, effectively.

The interaction of the deposited atom with the surface may have a significant impact on the particle's trajectory and may lead to a deviation of the adatom position from the deposition site, cf. Figure 3 (c). Such *steering effects* have been observed explicitly in, e.g., metal epitaxy, see also [4] for references.

The capture of arriving adatoms in weakly bound intermediate states may play an important role as well. For several compound semiconductors it is assumed that one of the elements may reside in a highly mobile state close to the surface before a regular lattice position is reached. Examples in the literature discuss the role of mobile As in GaAs epitaxy [8] or Te in ALE growth of CdTe [9].

Frequently, the deposition process is complicated by the fact that molecules or small clusters of atoms, e.g., dimers, arrive at the surface. Their dissociation may be a highly complex process which is not governed by thermal activation. Again, MD should be the method of choice for the simulation and understanding of the deposition kinetics. In lattice gas models and KMC simulations such processes can be implemented in a highly simplifying effective fashion, at best.

In spite of its practical restrictions, Molecular Dynamics has been and continues to be extremely useful in the context of epitaxial growth, see [12] for specific examples. Simplifying faster techniques like Kinetic Monte Carlo simulations rely in general on the *a priori* knowledge of the catalogue of relevant microscopic processes. In particular when aiming at material specific investigations, MD can provide valuable detailed insights in this context.

3. Kinetic Monte Carlo simulations and lattice gas models

3.1. Thermally activated processes

The Kinetic Monte Carlo method extends the range of accessible time scales by implementing appropriate *short cuts* in the treatment of thermally activated processes. Only those configurations are explicitly taken into account, in which the system resides for significant time intervals. A stochastic process is defined which takes the system from one such state to a neighboring one in configuration space. Obviously, the physical properties must be taken care of when specifying the transition rates.

In order to illustrate the basic idea of the KMC approach, we return to the above example of hopping diffusion, cf. Figure 1. A simplifying interpretation of such a situation is illustrated in Figure 4: if we assume the rest of the crystal is *frozen*, the adatom moves in a potential energy surface (PES) that results from its

interactions with the other atoms. In reality, the underlying crystal rearranges and reacts to any movement of the adatom. However, as long as this does not lead to topological changes, the *frozen crystal picture* is essentially valid and appropriate for the following considerations, see also [16] (this volume). The local minima in the PES, cf. Figure 4, correspond to the relevant configurations in the KMC approach and are termed the *binding states*. As discussed above, thermal fluctuations will occasionally provoke a jump from one such minimum to a neighboring one. One implicitly assumes that the time required for the actual transition can be neglected in comparison with the time spent in the binding states. Under further simplifying assumptions, only some of which will be discussed below, the typical waiting time for a transition is given by an Arrhenius law of the form

$$\tau = \tau_o \exp\left[\frac{(E_t - E_b)}{k_B T}\right] \qquad \text{or} \qquad r = \nu_o \exp\left[-\frac{(E_t - E_b)}{k_B T}\right] \tag{3.1}$$

for the corresponding rate, respectively, where k_B is Boltzmann's constant. The rate r decreases exponentially with the height $(E_t - E_b)$ of the energy barrier that has to be overcome in the process, cf. Figure 4. E_b is the energy of the so-called *binding state*, whereas E_t corresponds to the *transition state*. The barrier is compared with the typical thermal energy $k_B T$ in the system, i.e., the higher the temperature T the more frequent becomes the event. The prefactor ν_o is termed the *attempt frequency*. In the Arrhenius law it is assumed to be independent of the temperature.

Figure 4 displays the PES as for a single particle in the vicinity of a terrace edge. In the center of the upper or lower terrace, the potential is oscillatory with equivalent minima at the regular lattice sites and identical barriers. Near the edge, however, the shape of the PES shows some distinct features: a very deep minimum is found right at the step due to the good coordination, i.e., the interaction with many neighbors. Consequently, a particle that has attached to the upper terrace will detach with a relatively low rate only. A second pronounced feature is the additional, so-called Ehrlich-Schwoebel barrier E_S [1, 2, 3, 4] for hops from the upper to the lower terrace (or vice versa). Here, the transition state is very weakly bound and hence *interlayer diffusion* is hindered effectively. This can result in the formation of pronounced mounds in the course of growth, see [2, 3, 4] for discussions of the effect.

In Transition State Theory, the Arrhenius law is motivated by arguing that the occupation of binding and transition states should correspond to an effective thermal equilibrium situation. Following this line of thought one obtains directly the form of Eq. (3.1). This and other approaches to the evaluation of transition rates are discussed briefly in [4, 10, 14] and in greater detail in e.g., [17, 18].

In principle it is also possible to determine the attempt frequency by taking into account the (vibrational) entropies, i.e., the free energies of binding and transition state, see [4, 10, 17, 18] and references therein. However such an evaluation can be quite involved and has to go beyond the frozen crystal approximation. Consequently, good estimates of attempt frequencies are hardly available in the

literature. Very often it is therefore simply assumed that the attempt frequency is the same for all possible diffusion processes in the system. A popular choice is $\nu_o = 10^{12}/s$, corresponding to the typical frequency of atomic vibrations. Usually, there is no obvious justification for this crude simplification. In fact, several authors have argued that it is simply incorrect in particular cases, see [4] for example references.

From a practical point of view, the simple picture of a single attempt frequency has several striking advantages: with only one ν_o in the system this quantity can be taken to define the unit of time and does not have to be taken care of explicitly. More importantly, Arrhenius rates with identical attempt frequency are guaranteed to satisfy the condition of detailed balance [4, 5]: for two neighboring binding states b_1 and b_2 with energies E_1, E_2 one obtains directly

$$\frac{r(b_1 \to b_2)}{r(b_2 \to b_1)} = \frac{e^{-E_2/(k_B T)}}{e^{-E_1/(k_B T)}} \tag{3.2}$$

as ν_o and the dependence on E_t cancel in the ratio. The detailed balance condition is by no means a necessary requirement for meaningful simulations, especially not in situations far from equilibrium. However, it conveniently guarantees that the system – in absence of deposition and desorption – would approach the correct thermal equilibrium eventually, i.e., a Boltzmann distribution of binding states [5]. If it is violated one might have to worry, for instance, about unphysical cycles of diffusion events in which the system could pick up (free) energy constantly [20].

Note that deposition and desorption in MBE models necessarily violate detailed balance. Deposition is not an activated process anyway and the discussion of detailed balance is meaningless, the same is true for the kinetic processes illustrated in Figure 3. In desorption a particle has to overcome a barrier which is simply identical with its binding energy at the surface. Hence, desorption can be implemented with the corresponding Arrhenius rate. However, the process is irreversible: in an ideal MBE environment a perfect vacuum is maintained in the chamber and desorbed particles will be removed immediately. The situation differs significantly from a surface that may exchange particles with a surrounding vapor or melt.

The validity of the Arrhenius law for thermally activated processes, Eq. (3.1), hinges on several assumptions, which will not be discussed in detail, here. A more thorough discussion of these conditions and further references can be found in [4, 14, 17, 18], for instance. One important requirement is, loosely speaking, that the minima in the energy surface have to be deep enough to guarantee that

(a) the system remains in the binding state for a significant time interval – Arrhenius rates describe only *infrequent events* correctly.
(b) once the transition state is reached, the system is caught in the neighboring minimum, indeed.

The importance of these conditions can be demonstrated by a counter-example: if an adatom moves in a PES with very shallow minima, thermal fluctuations might very well provoke double or multiple jumps directly to more distant binding states.

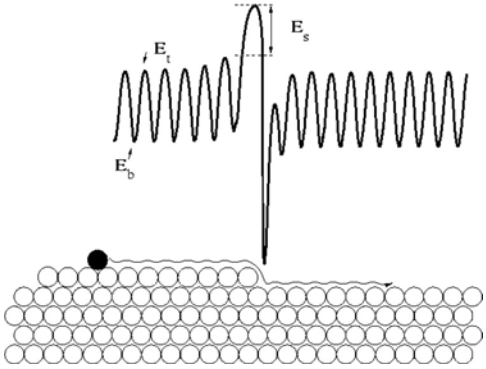

FIGURE 4. Sketch of the potential energy surface (PES) for single adatom hopping diffusion on a terraced surface, courtesy of Florian Much [15]. In this particular example, pairwise interactions according to a Lennard-Jones potential were assumed, see [15] for details. E_b is the energy of a binding state, whereas E_t corresponds to the transition state of hopping diffusion. The Ehrlich-Schwoebel barrier E_S hinders inter-layer hops at the terrace edge.

According to [19] the rate for double jumps can still be written in a form similar to Eq. (3.1) but with an explicit temperature dependence of the prefactor: $\nu_o \propto \sqrt{T}$.

Most KMC simulations in the literature are indeed based on the above simple Arrhenius picture. In fact, further simplifications are frequently applied, some of which will be discussed in the following section.

3.2. Lattice gas and Solid-On-Solid models

In principle it is well possible to implement the above basic ideas of KMC in off-lattice models with continuous particle positions, see [16] for an example in this volume. It requires the evaluation of the relevant barriers from the PES *on the fly*. The vast majority of KMC studies, however, applies important additional simplifications.

If the material is expected to crystallize in a regular lattice without dislocations or other defects, one might as well pre-define the set of potential lattice sites. In such lattice gas models, a particular site is either occupied or empty and particles can only be placed precisely at one of the sites as illustrated in Figure 1. Diffusion processes are then represented by hops between lattice sites.

The popular class of Solid-On-Solid (SOS) models fulfills further conditions. Assuming that vacancies in the bulk or *overhangs* do not occur in the system, one ends up with a crystal that is uniquely described by the height of the surface above the substrate. A simple cubic model crystal, for instance, is then fully specified by an integer array of variables above a substrate square lattice, see Figure 5 for an illustration.

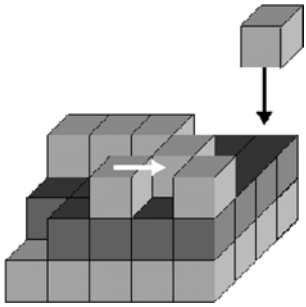

FIGURE 5. Illustration of a simple cubic Solid-On-Solid lattice gas model. For clarity alternating layers are colored differently. As overhangs and bulk vacancies are excluded, the surface is fully characterized by an integer array of height variables above a square lattice substrate. As example processes, the deposition of a new particle (black arrow) and the diffusion hop of an adatom attaching to neighboring particles (white arrow) are shown.

The layout of the actual lattice structure, the design of a catalogue of relevant events, and the assignment of rates can be more or less closely related to the physical reality. The necessary or adequate level of sophistication clearly depends on the problem under investigation. The following paragraphs highlight only a few of the many choices one has to make in the design and simulation of lattice gas models.

The lattice

In principle, all relevant lattice structures can be implemented in a Solid-On-Solid fashion. When aiming at material specific simulations, the correct topology should be represented in the model as it determines, for instance, neighborhood relations and the potential diffusion events. The practical implementation of several lattice types is discussed, for instance, in [5]. To name just one specific example: the (001) surface of a compound zinc-blende structure is represented as an SOS model in reference [9]; the system can be treated as the superposition of four simple cubic sublattices.

One aspect that deserves particular attention is the geometry of the substrate and the use of appropriate periodic boundary conditions in order to reduce boundary effects in the simulation of finite systems. Imposing an inadequate geometry, e.g., using a square shape substrate in the SOS representation of an fcc(111) surface, may result in subtle difficulties. For example, the shape of large islands that align with the lattice axes might conflict with the substrate geometry. In order to avoid such artefacts, the design of the substrate should reflect the lattice symmetries, see [5] for recipes in particular cases.

Monoatomic simple cubic models are employed frequently in the literature. Whereas they obviously cannot describe any real material faithfully, they serve as

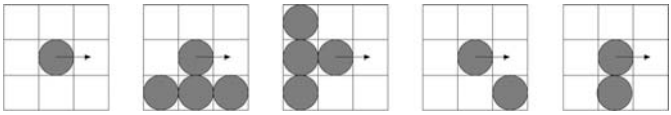

FIGURE 6. Diffusion hops of an adatom on a crystal surface with cubic symmetry, illustration after [24]. In each picture, the adatom in the center is assumed to hop to the right, and four different configurations of the neighborhood (3×3 sites) are shown. In principle there are $2^7 = 128$ possible configurations, due to symmetry only 72 situations are distinct. From left to right, the illustrations correspond to diffusion on a flat surface, movement along a terrace (step edge diffusion), detachment from an edge, and one possibility for the formation of a pair and its dissociation.

prototype systems for the investigation of many basic and qualitative features of epitaxial growth. Several properties of growth processes are believed to be *universal*, i.e., they should not depend on the lattice type and other details of the model, see e.g., [21] and references therein. In the investigation of, for example, scaling laws in kinetic roughening one resorts to the simplest models available [2, 3].

Deposition and transient mobility

An ideal beam of particles in MBE growth deposits, on average, the same amount of adsorbate material per unit time and area everywhere on the substrate. Fluctuations on the atomistic level are usually represented in SOS models by choosing one of the substrate lattice sites with equal probability for each deposition event. Almost always it is assumed in MBE models that single atoms arrive at the crystal, despite the fact that the beam often contains molecules or small clusters of a few atoms which dissociate at the surface.

Effects of transient mobility upon deposition, like the above discussed *downhill funneling* or *knockout* at terrace edges, can be represented very conveniently in SOS models. A simplifying realization of funneling, for instance, amounts to the deterministic search for the lowest surface height in a neighborhood of the deposition site. Clearly, such implementations cannot take into account the microscopic details faithfully, it is only possible to capture the most essential features.

Adatom mobility

In the conceptually simplest models, only the most recently deposited particle is considered mobile at a given time. It may, for instance, move to an available empty site of lower height in a neighborhood of the deposition site and then become immobile. Thereafter, the simulation proceeds with the deposition of another single adatom. Often, only the immediate incorporation of the particle upon arrival at the surface is modeled, whereas activated diffusion over longer distances is completely neglected. Clearly, this is computationally very cheap and allows for the simulation of large systems and very thick films of, say, 10^6 layers or more. Consequently,

such *limited mobility models* are employed, for example, in the investigation of basic phenomena like kinetic roughening of self-affine surfaces, see e.g., [2]. Their applicability in material specific modeling is, however, rather limited in general.

In contrast, *full diffusion models* consider all atoms mobile at the same physical time, in principle. In the simulation, deposition is only one possible event among all other processes and has to be implemented with the corresponding rate. As many adatoms move simultaneously the system displays a much broader spectrum of possible events.

In the standard SOS approach only atoms right at the surface are considered mobile. Bulk particles are surrounded by occupied lattice sites and vacancies are excluded. Unless concerted moves or exchange processes are implemented explicitly, the entire bulk remains fixed. In the example of the simple cubic lattice this could mean that only particles with less then six nearest neighbors are considered mobile at all.

In fact, in many cases the adatom mobility is further restricted due to simplifying assumptions in the model design, see the discussion in the next session. Some of these are made for practical reasons mainly, others reflect peculiarities of the non-equilibrium growth conditions.

The catalogue of events and rates

The key step in designing a KMC lattice gas model is the setting up of the catalogue of possible events. Closely related and equally important is the assignment of rates to the considered processes.

As an illustrative example we consider the diffusion of a single adatom within one layer of a monoatomic crystal surface with cubic symmetry, cf. Figure 6. Already simplifying, let us assume that only hops to nearest neighbor sites occur and that their rates depend only on the configuration of a very small neighborhood of, say 3×3 sites. Only four examples are shown in the illustration, Figure 6, in total there are 72 essentially different neighborhood configurations. For each of those a different rate has to be specified in the model, in principle.

For several material systems, such detailed catalogues of rates have indeed been worked out. For the particular example of diffusion of a single adatom on an fcc(001) metal surface, see for instance [22, 23, 24]. Note, however, that the evaluation of rates by first principles or approximate methods requires a careful analysis of the physical process. For instance, the rate of hopping and potential exchange processes must be compared for each of the configurational changes and the task of finding the correct transition path can be very demanding, see e.g., [25].

The faithful representation of all relevant events in a KMC simulation can be quite involved. In our example, inter-layer hops at terrace edges and the like have not even been included yet. The potential extension to island mobility and other concerted processes would make the catalogue of events even more complex. For practical reasons or because the required detailed information about the rates is simply not available, one frequently resorts to simplifying schemes. The aim

is to capture the essential features of a material system or to study qualitative properties of the growth process.

In some cases it is possible to find efficient parameterizations of the relevant barriers in terms of a small number of independent quantities. *Bond counting schemes* have been particularly successful in this context [4, 5, 23, 26]. The idea is to consider only very few distinct barriers, but to take into account the energies of the involved binding states explicitly. In particularly simple schemes only the energy of the initial state determines the rate, whereas, in general, initial and final configuration are considered. In our example we could assume that the quantity E_o plays the role of the characteristic barrier for all nearest neighbor hops within the layer and assign a rate of the form

$$r = \nu_o \exp[-E/(k_B T)] \qquad \text{with} \qquad E = \max\{E_o, E_o + (E_f - E_i)\}. \tag{3.3}$$

Here, E_i and E_f are the energies of the initial and final state, respectively. In the simplest cases, their determination amounts to counting nearest or next nearest neighbor bonds adding up the associated binding energies. The rate (3.3) is of the Arrhenius form, where the diffusion barrier is directly given by E_o if the number of bonds decreases or remains the same in the process. In the opposite case the energy gain adds to the barrier. Note that the rates in Eq. (3.3) satisfy the detailed balance condition by construction. Apart from the extra barrier, which cancels out in (3.2), the prescription is equivalent with Metropolis like rates in equilibrium MC simulations [5].

If only one characteristic E_o is present in the system, the factor $e^{-E_o/(k_B T)}$ appears in all rates and might be taken to re-define the time scale. However, several such barriers may apply to different types of events, e.g., to planar diffusion or hops along the border of an existing terrace (step edge diffusion). The above discussed Ehrlich-Schwoebel effect, for instance, would be represented by a distinct barrier for inter-layer diffusion.

Often, several processes are excluded explicitly from the simulation. For large enough flux, for instance, the time required for adding an entire monolayer may be much smaller than the typical waiting time for a desorption event. In such a case, desorption may be disregarded or considered *forbidden*, whereas in a vacuum chamber without incoming flux it is clearly relevant and the crystal sublimates, see [9] for the discussion of an example.

One can also expect that the detachment of an atom from a terrace edge or from a small island will occur with a very small rate if typical binding energies are large. Hence, one might consider all detachment processes *forbidden* in an extreme case, which reduces the number of possible events considerably. Note that the implementation of irreversible attachment immediately violates detailed balance as only one of the rates in Eq. (3.2) is non-zero. Again, the justification of the simplification hinges on a comparison of the relevant time scales which are mainly determined by the incoming flux and the substrate temperature.

The risk of missing relevant microscopic processes is one of the main dangers in KMC simulations, especially in the context of material specific investigations.

Complicated and – at first sight – counter-intuitive concerted moves may be very well relevant in a specific system. This can lead to an oversimplified catalogue of events. In addition, wrong rates can be assigned to the implemented events whenever alternative pathways to the same final state have been ignored.

On the other hand, the potential to explicitly *allow* or *forbid* certain processes is one of the major strengths of the KMC approach. It allows to investigate the relevance of particular microscopic processes and their influence on the macroscopic properties of the growing crystal systematically. As just one example for this strategy, the role of step edge diffusion on the morphology and scaling behavior of surfaces can be studied by *switching* the process *on* and *off* in simulations, see e.g., [27] and references therein.

Implementation of the Monte Carlo Kinetics

The standard textbook realization of the stochastic Monte Carlo kinetics in computer simulations amounts to (a) suggesting one of the possible events with equal probability, and (b) evaluate or look up its rate r_i and accept or reject it with a corresponding probability.

This conceptually simple strategy is easy to implement and has been widely used in both equilibrium and off-equilibrium simulations [5]. In terms of efficiency its major drawback is that quite frequently a suggested event is rejected and potentially expensive computations have been performed without changing the system at all.

In contrast, *rejection-free* or *event-based* methods do perform one of the possible n events at each step of the procedure. Given a certain configuration of the system, the next process, say event number i, has to be selected with the correct probability $r_i \,/\sum_{i=1}^{n} r_i$. Next, the associated waiting time t_i is evaluated and the physical time in the model is advanced accordingly. For infrequent events as considered here, elementary considerations show that the time t_i is exponentially distributed with mean value $1/\sum_{k=1}^{n} r_k$ [4, 5].

The simplest realization of the correct selection requires only one random number $z \in [0, 1]$: the event i which satisfies the condition

$$\sum_{k=1}^{i-1} r_k \leq z \sum_{k=1}^{n} r_k \leq \sum_{k=1}^{i} r_k \tag{3.4}$$

is chosen and performed. The costly linear search can be replaced by more sophisticated tree-like representations of the catalogue of events [5]. In simulations with a limited number of distinct processes it is efficient to group the events according to their rate. However, the basic idea of rejection free simulations remains the same.

The price paid for the gain in efficiency is that, at any given time, all possible processes must be known and stored. Their number and nature as well as their rates can change with every event that occurs in the system. Depending on the structure of the model this can require sophisticated bookkeeping and costly frequent re-evaluations of all rates.

4. Conclusion

Kinetic Monte Carlo simulations of lattice gas systems constitute one of the most widely used tools in the modeling of epitaxial growth. The success of the approach is due to the fact that it is extremely flexible and versatile.

Conceptually very simple models can be used in the investigation of basic, perhaps universal properties. It is quite straightforward to set up, for instance, a simple cubic model with only a few distinct rates. Such a system can be implemented very efficiently and already allows for the study of various essential phenomena.

On the other hand, lattice gas models offer the potential for material specific simulations, as well. The success of such attempts depends on the availability of detailed information about the microscopic processes. To a certain extent, this knowledge can arise from comparison with experiments. In turn, simulations allow for testing hypotheses about the microscopic causes of macroscopic surface properties.

First principle calculations or approximate theoretical treatments are clearly most desirable as a basis of material specific models. A particularly promising route seems to be the incorporation of such methods into the on-going simulation.

A complete description of epitaxial growth requires the consideration of processes on many different time and length scales. Lattice gas models and Kinetic Monte Carlo simulations in general, will certainly play an essential role in the further development of the multi-scale approach.

Acknowledgment

The author would like to thank the organizers and all participants of the MFO Mini-Workshop on *Multiscale Modeling in Epitaxial Growth* for the most stimulating atmosphere and many useful discussions.

References

[1] I.V. Markov, *Crystal Growth for Beginners: Fundamentals of Nucleation, Crystal Growth and Epitaxy.* World Scientific (1995).

[2] A.-L. Barabàsi and H.E. Stanley, *Fractal Concepts in Surface Growth.* Cambridge University Press (1995).

[3] A. Pimpinelli and J. Villain, *Physics of crystal growth.* Cambridge University Press (1998).

[4] T. Michely and J. Krug, *Islands, mounds and atoms. Patterns and Processes in Crystal Growth far from equilibrium.* Springer (2004).

[5] M.E.J. Newman and G.T. Barkema, *Monte Carlo Methods in Statistical Physics,* Oxford University Press (1999).

[6] B.A. Joyce, P. Kelires, A. Naumovets, and D.D. Vvedensky (eds.), *Quantum Dots: Fundamentals, Applications, and Frontiers.* Kluwer, to be published.

[7] R.M. Dreizler, E.K.U. Gross, *Density Functional Theory.* Springer (1990).

[8] M. Itoh, G.R. Bell, A.R. Avery, T.S. Jones, B.A. Joyce, and D.D. Vvedensky, *Island nucleation and growth on reconstructed GaAs(001) surfaces.* Phys. Rev. Lett. **81** (1998) 633.

[9] T. Volkmann, M. Ahr, and M. Biehl, *Kinetic model of II–VI(001) semiconductor surfaces: Growth rates in atomic layer epitaxy.* Phys. Rev. **B 69** (2004) 165303.

[10] P. Kratzer and M. Scheffler, *Surface knowledge: toward a predictive theory of materials.* Computing in Science & Engineering **3** (2001) 16.

[11] D.C. Rapaport, *The Art of Molecular Dynamics Simulation.* Cambridge University Press (1995).

[12] K. Albe, this volume.

[13] M. Parrinello, *From silicon to RNA: The coming age of ab initio molecular dynamics.* Solid State Comm. **102** (1997) 107.

[14] A.F. Voter, F. Montalenti, and T.C. Germann, *Extending the time scale in atomistic simulations of materials.* Annu. Rev. Mater. Res. **32** (2002) 321.

[15] F. Much, *Modeling and simulation of strained heteroepitaxial growth.* Dissertation Universität Würzburg (2003).

[16] M. Biehl, F. Much, C. Vey, *Off-lattice Kinetic Monte Carlo simulations of heteroepitaxial growth.* This volume.

[17] F. Jensen, *Introduction to Computational Chemistry,* Wiley (1999).

[18] P. Hänggi, P. Talkner, M. Borkovec, *Reaction-rate theory: fifty years after Kramers.* Rev. Mod. Phys. **62** (1990) 251–341.

[19] J. Jacobsen, K.W. Jacobsen, and J.P. Sethna, *Rate theory for correlated processes: Double-jumps in adatom diffusion.* Phys. Rev. Lett. **79** (1997) 2843.

[20] The author would like to thank J. Krug for drawing his attention to this point.

[21] M. Ahr, M. Biehl, M. Kinne, and W. Kinzel, *The influence of the crystal lattice on coarsening in unstable epitaxial growth.* Surface Science **465** (2000) 339.

[22] M. Breeman, G.T. Barkema, and D.O. Boerma, *Annealing of Cu-adatom configurations on Cu(100).* Surf. Sci. **303** (1994) 25.

[23] H. Mehl, O. Biham, I. Furman, and M. Karimi, *Models for adatom diffusion on fcc (001) metal surfaces.* Phys. Rev. **B 60** (1999) 2106.

[24] I. Furman and O. Biham, *Epitaxial growth of Cu on Cu(001): Experiments and simulations.* Phys. Rev. **B 62** (2000) R10649.

[25] G.T. Barkema and N. Mousseau, *Event-based relaxation of continuous disordered systems.* Phys. Rev. Lett. **77** (1996) 4358.

[26] M. Schroeder, P. Smilauer, and D.E. Wolf, *Bond counting in a simulation model of epitaxial growth.* Phys. Rev. **B 55** (1997) 10814.

[27] S. Schinzer, M. Kinne, M. Biehl, and W. Kinzel, *The role of step edge diffusion in epitaxial crystal growth.* Surface Science **439** (1999) 191.

Michael Biehl
University Groningen
Institute for Mathematics and Computing Science
P.O. Box 800, NL-9700 AV Groningen, The Netherlands
e-mail: `biehl@cs.rug.nl`

International Series of Numerical Mathematics, Vol. 149, 19–28

Cluster Diffusion and Island Formation on fcc(111) Metal Surfaces Studied by Atomic Scale Computer Simulations

Karsten Albe and Michael Müller

Abstract. The role of cluster diffusion on Pt and Ir surfaces is discussed in the context of island nucleation on metals. By using molecular dynamics simulations based on a newly developed bond-order potential, the diffusion of Pt_2 on a Pt(111) surface is studied. We observe that dimer diffusion proceeds via concerted motion on an hcp-bridge position towards the neighboring fcc-site. The importance of cluster diffusion is then investigated for the case of Ir island nucleation on Ir(111). We study the role of varying deposition rates on the island formation using an extended kinetic lattice Monte Carlo method that takes into account cluster diffusion and includes stacking fault positions. Our results reveal the strong influence of the deposition rate on island densities and shapes.

Mathematics Subject Classification (2000). Primary 82B24; Secondary 82B80.

Keywords. Kinetic Monte Carlo; Molecular Dynamics; Cluster Diffusion; Island Shapes.

1. Introduction

The rapid development of epitaxial growth techniques has prompted the desire to develop modelling methods that are capable of helping in the interpretation of experimental data and do potentially aid in the selection of optimum growth conditions. Epitaxial phenomena involve processes on very different time and length scales. Therefore modelling of thin film formation in general is a challenging multiscale problem. Given the fact that the macroscopic evolution of growing films is directly related to movements of adatoms on surfaces and their various bonding configurations, it is appealing to use atomic scale simulation methods for modelling thin film growth.

In recent years, a set of complimentary methods has matured that are very useful for understanding processes on the atomic scale and will be briefly described here:

First-principles methods are typically based on density-functional theory (DFT) and provide solutions for the time-independent Schrödinger equation. They deliver detailed information on the energetics of given atomic configurations and have been widely used for determining energy pathways and barriers to diffusion and other kinetic processes. Because of their computational demands, however, they only allow to treat small supercells of a few hundred atoms in maximum. For this reason, first-principles approaches are useful in connection with static energy minimisation schemes, but not for dynamic calculations.

Real-space trajectories can be obtained by the classical Molecular Dynamics method (MD), where Newton's equations of motion are solved numerically for a set of interacting atoms. This method contains the complete thermodynamic information, provided that appropriate boundary conditions are chosen. The key ingredient of MD simulations are the forces acting on each atom in the system, which are usually derived from analytical interatomic potentials. Therefore the outcome of such simulations sensitively depends on the particular potential, which might or might not be appropriate for the kinetic processes studied. In principle, it is possible to use more reliable forces obtained from first-principles, but the additional computational overhead, allows to calculate only a few lattice vibrations. Independent of the origin of the interatomic forces, numerical integration schemes are only accurate, if time step lengths of a few femtoseconds are used. Therefore some 10^9 integration steps are needed to get into the range of microseconds, which is still far far below the times needed for studying thin film growth. Consequently, MD-simulations are most useful for simulations of detail processes occurring during epitaxial growth, but not for modelling the complete film formation.

In order to study thin film growth under realistic deposition conditions, kinetic Monte Carlo (KMC) simulations are a very powerful approach. The basic idea of the KMC method is to include only processes deemed to be important in the simulation, while the explicit treatment of lattice vibrations is avoided. By assigning specific jump rates, to every single hop, atomic jumps are treated as probabilistic. If the jump rate are not known from experiments first-principle calculations and MD-simulations can be used to obtain the necessary parameters.

The early stage of thin film growth involves the arrival and accommodation of atoms on the surface, their diffusion and the nucleation of two-dimensional adatom islands. While in this stage the number density of adatom islands is determined by adatom mobilities and binding energies, island shapes are mostly determined by atomic processes at the edges and the diffusion field of the adatoms.

Understanding the diffusion mechanisms of adatoms or small clusters on clean, infinite surfaces seems to be conceptually simple, but is a largely unresolved problem, since direct measurements of individual atoms or clusters are only possible for a few elements (notably Ir, Pt, Re, Pd) [9, 11] in a narrow range of

temperatures. Moreover, no direct insights on the diffusion mechanisms can be achieved from experiments because of the limited time resolution.

The (111) surfaces of Pt and Ir are of particular interest because of their chemical inertness and therefore have been thoroughly investigated in the past. While significant effort has been spent on investigating diffusion mechanisms of single atoms, questions remain concerning the role played by dimers in the kinetics of growth and in particular shape evolution of islands as function of temperature and deposition rate.

In this paper, we present both, MD and KMC simulations on cluster diffusion. Firstly, the mechanism of Pt_2 diffusion on Pt(111) surfaces is studied by means of molecular dynamics simulations, which are performed using an analytical potential derived from DFT-data and experimental input. Secondly, we present simulations based on an extended lattice Monte Carlo scheme that includes stacking fault positions and allows for cooperative cluster motions. By feeding this scheme with data taken from theory and experiments, we finally study the influence of varying deposition rates on the island formation on Ir(111).

2. Molecular-dynamics studies of dimer diffusion on Pt(111)

For Pt-dimer diffusion an activation energy of $E_D = 0.37$eV has been experimentally determined by Kyuno et al. [10]. Precisely the same number was calculated by Boisvert and Lewis using a density functional theory method [4]. For the calculation, they assumed that the diffusion path for dimers consists of a sequence of concerted two-atom jumps with local reorientations. Although their result is in full agreement to the experiment, a detailed inspection of the diffusion mechanism by MD simulations would provide further support for this result. This is in practice not a simple task, since a model potential is necessary that describes not only the bulk properties, but also the dimer and surface configurations. Pair-like embedded-atom potentials are for principle reasons unable to describe metals which tend to be elastically isotropic, such as platinum, because no angular dependent terms are involved. Baskes has therefore proposed a modified embedded-atom (MEAM) potential, which includes angular dependent electron densities and was parametrised for Pt [2]. Although this potential delivers a very good description of surface energies, the dimer properties are not well described.

An alternative potential was derived by Albe et al., which is based on an angular dependent analytical bond-order approach (see Ref. [1] for details). It reproduces elastic properties, surfaces, point defects of the fcc-bulk phase as well as the dimer properties with good accuracy and is therefore an appropriate choice for studying dimer motion on surfaces. The potential is based on the idea that individual bond-lengths (r_B) and the bond energies (E_B) for structures with different local atomic coordination can be related by the Pauling criterion

$$E_b = -D_o \exp\left(-\beta\sqrt{2S}(r_b - r_o)\right),$$

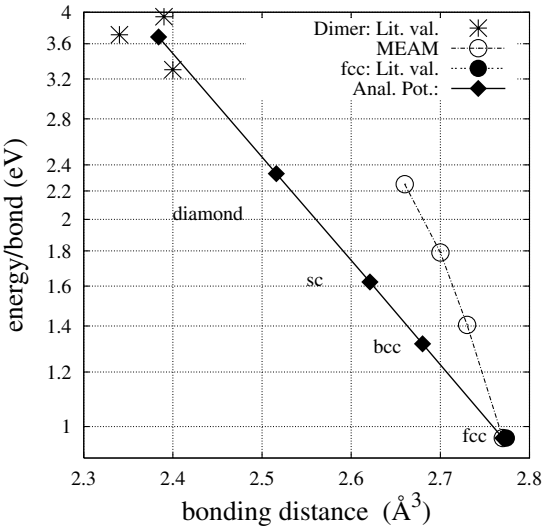

FIGURE 1. Fit of the Pauling energy-bond relation to the Pt-dataset. Shown are the literature values of the dimer and fcc structure. The analytical Pt bond-order potential is represented by the solid line. Open circles are the equilibrium energies and distances for the corresponding structures as calculated with the MEAM potential of Baskes[2]. Black squares indicate the corresponding minimum configurations of different other solid structures (diamond,sc,bcc and fcc) as calculated with the analytical potential.

where D_o and r_o are the binding energy and equilibrium distance of a dimer, while β and S serve as adjustable parameters. Fig. 1 shows the minimum energies and bond lengths for structures with varying coordinations in comparison to the MEAM approach. One obvious feature of the bond-order potential for Pt in comparison to the MEAM approach is the good description of the dimer properties, which agree very well with results based on quantum chemical calculations.

Using this model potential, molecular dynamics simulations were carried out at 600 K for a Pt_2 molecule that was randomly dropped on a (111) fcc Pt surface and than followed in time. A sequence of six consecutive snapshots taken in time intervals of 1 fs is shown in Fig. 2. Different gray levels indicate different [111]-planes. Initially, the dimer is positioned on a regular fcc site. Diffusion then proceeds via concerted motion on an hcp-bridge position towards the neighboring fcc-site. The observed diffusion path is the one predicted by Boisvert and Lewis based on total energy calculations [4]. From the observed jump frequencies we conclude that this process is even active at lower temperature, where it can contribute to mass transport and should not be neglected.

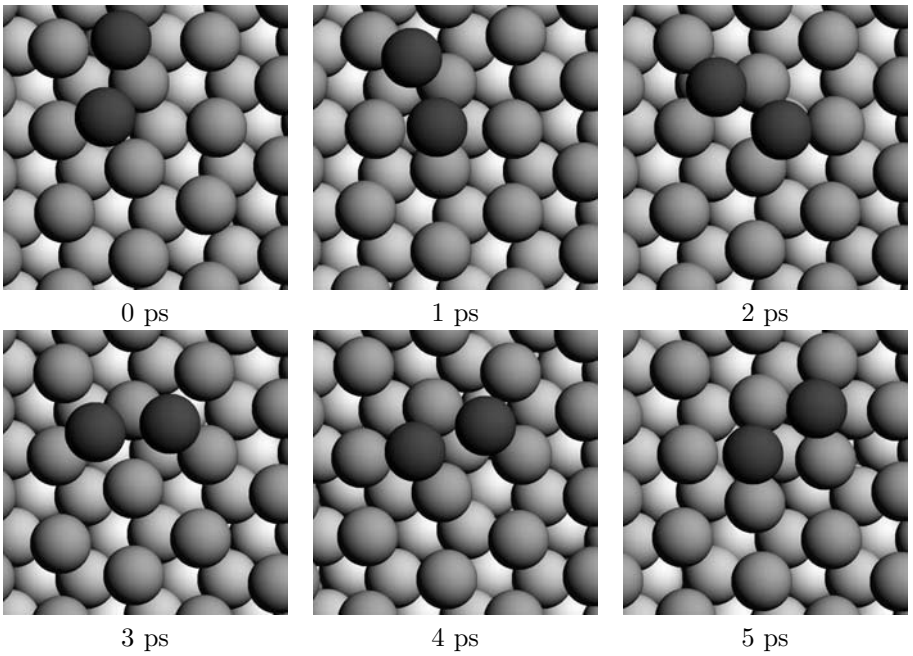

FIGURE 2. Cooperative motion of a Pt-dimer on fcc(111) Pt at 600 K. The sequence of snapshots shows an individual jump between regular lattice positions. Different lattice layers are shown in different grey levels.

The importance of such cluster motion for the formation of stacking-fault islands is discussed in the next section for the example of Ir deposition on the Ir(111) surface.

3. KMLC simulations of stacking-fault nucleation on Ir(111)

An important defect during epitaxial growth of fcc(111) metal surfaces is the formation of stacking-faults due to nucleation of adatom islands in hcp binding sites. For the case of island nucleation on Ir(111) it has been recently shown that the diffusion behavior of small clusters determines the temperature dependence of the stacking-fault island density [6].

In order to implement the formation of stacking-fault islands in a lattice Monte Carlo model, we have developed an improved KLMC code that includes stacking fault positions and cluster diffusion by concerted motion. Details of this code are given elsewhere [6, 12] and will only briefly be described here:

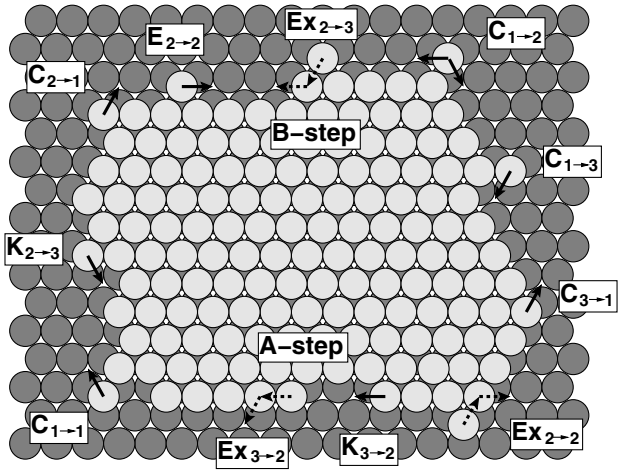

FIGURE 3. Illustration of the diffusion processes at island edges implemented in our KLMC model. The notation is adopted from Ref. [3]: The letters denote **c**orner, **e**dge, **k**ink and **ex**change, the subscripts give the in-layer coordination numbers before and after the process. All processes can take place at A- and B-steps of regular as well as stacking-fault islands.

Adatoms must be allowed to occupy regular fcc as well as hcp sites. This is achieved by using a refined fcc lattice with additional sites at all possible stacking-fault positions. On this lattice, terrace diffusion of adatoms is described by jumps of an atom from a fcc binding site to one of the three neighboring hcp binding sites and vice versa. The detailed diffusion mechanisms of adatom clusters can be very complex, as seen before in case of the small Pt_2 molecule and are even more complicated for larger clusters [15]. Therefore only translational motion by concerted jumps from fcc to hcp binding sites and vice versa is considered. In doing so, no distinction is made between compact clusters or chains of atoms. Diffusion of clusters larger than pentamers, which are the largest mobile species at 400 K, is neglected.

In contrast to terrace diffusion, diffusion of atoms bound to island edges is implemented by single atom jumps between fcc sites for regular and hcp sites for stacking-fault islands. A large number of different diffusion processes at island edges can be distinguished, as shown in Fig. 3. The influence on the kinetically controlled island shape has been thoroughly investigated by KLMC simulations [8, 13, 3, 7, 5] in the past. High diffusivity at island edges leads to the formation of compact islands surrounded by close-packed steps. On a fcc(111) surface {100}-microfaceted A-steps and {111}-microfaceted B-steps can be distinguished, which mostly differ in their step free energy. Therefore the potential energy landscape for diffusion along the island edges is anisotropic [14]. In most cases, this results in preferential growth of A-steps and islands with a triangular envelope, bounded

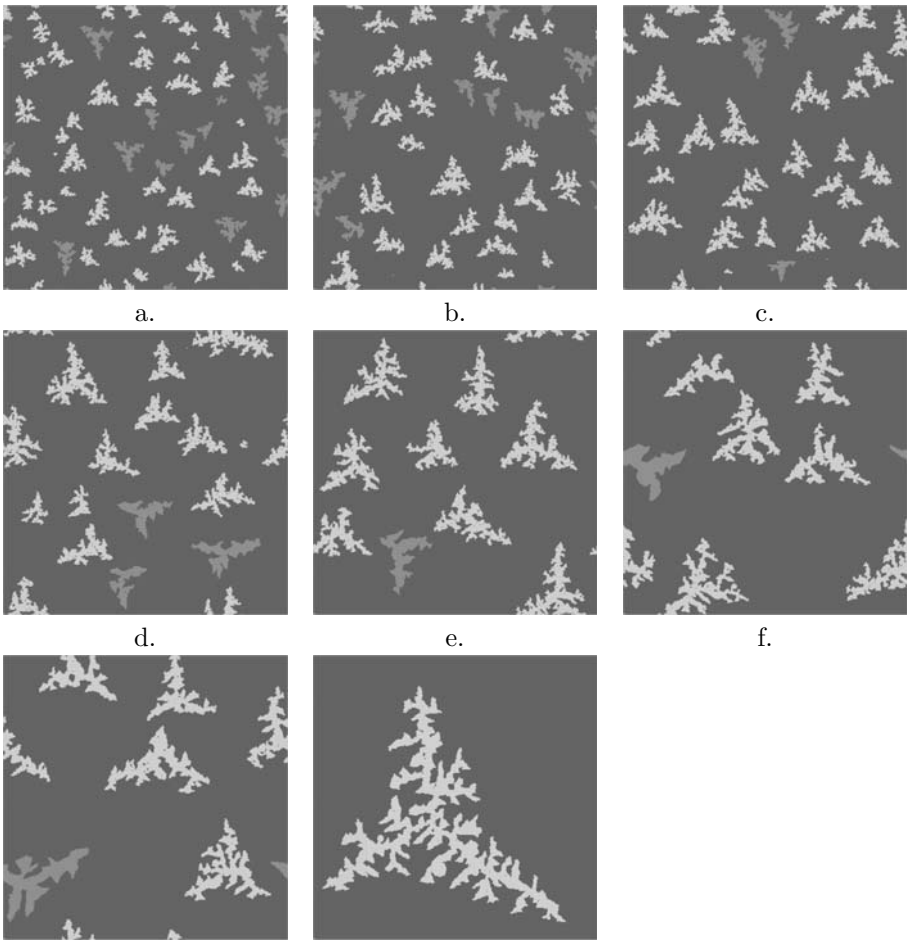

FIGURE 4. Deposition 0.13 monolayers iridium on a fcc(111) iridium surface (800 x 800 $Å^2$) at 375 K. The corresponding deposition rates are a.) 0.5 ML/s, b.) 0.1 ML/s, c.) 0.05 ML/s, d.) 0.01 ML/s, e.) 0.005 ML/s, f.) 0.001 ML/s, g.) 0.0005 ML/s, h.) 0.0001 ML/s. Light grey atoms belong to fcc islands, dark grey atoms show stacking-fault islands.

predominantly by the slower growing B-steps [11]. If the diffusivity at island edges is reduced, ramified fractal islands are formed.

In a preceding study, we investigated the influence of the target temperature on island densities and shapes in comparison to experiments [12]. Here we report on KLMC simulations of the deposition of 0.13 monolayers (ML) iridium on (111)

iridium at 375 K at varying deposition rates. The entire event database was taken from experiments and is identical to that reported in Ref. [12]. A specific feature of iridium is the fact that hcp sites are more favorable for adatoms and dimers. For trimers the binding energy on both positions is equal, while larger cluster prefer to occupy regular lattice sites. At the given temperature all clusters are mobile and can undergo concerted jumps. Therefore the probability of stacking fault nucleation is in principle determined by the stacking fault probability of the largest mobile cluster, which can be estimated from the Boltzmann-factor of the binding energy difference between fcc and hcp positions.

Fig. 4 shows the results for different deposition rates. At the lowest deposition rate one island is formed on regular lattice site showing a typical dendritic shape with a triangular envelope. With growing deposition rate more nucleation events can occur and smaller islands are formed. Regular islands appear to be more ramified than those nucleated on stacking fault positions, which is in agreement to experimental results [6]. Since atoms on hcp positions are more weakly bound as compared to fcc positions, activation energies are smaller for identical saddle point energies. Therefore edges of stacking fault islands can smooth out more easily. A quantitative measure for the island shape is the in-layer coordination number which corresponds to the average coordination per atom and increases with decreasing fractality. Fig. 5 shows the in-layer coordination for all fcc-islands as a function of deposition rate. It clearly can be seen that with increasing deposition rate the coordination is decreasing. Although at the same time the island density is increasing and therefore more edges will be formed, the individual islands at the high deposition rate are more fractal than the branches of the large islands formed at lower deposition rates.

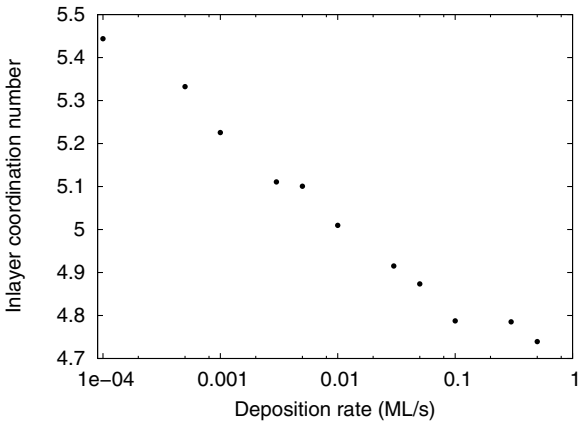

FIGURE 5. In-layer coordination numbers for different deposition rates as obtained from KLMC simulations. Only regular islands on fcc-sites are considered.

4. Conclusion

Cluster diffusion on metal surfaces can be very important for island nucleation and thin film formation. In this study, we have shown that a combination of total energy calculations, molecular dynamics and Monte Carlo methods is most powerful in gaining insights on structure formation processes on the atomic scale. First-principles methods are most valuable for calculating activation barriers. At the same time, results based on total energy approaches can be used for parametrising analytical potentials as briefly described for the case of platinum. Using such potentials molecular-dynamics simulations can be performed that allow to investigate diffusion mechanisms even for complicated geometries. Taking the example of Pt_2 diffusion on a Pt(111) surface we can confirm that cooperative atomic motion is an important transport mechanism on metal surfaces. The role of cluster diffusion for structure formation processes is shown by our studies of island formation on Ir(111), where diffusion of clusters up to pentamers is decisive for stacking fault nucleation. Using an extended kinetic Monte Carlo scheme, the strong influence of the deposition rate on cluster density and structure is revealed.

Acknowledgment

The authors are most grateful to Prof. Thomas Michely and Dr. Carsten Busse at RWTH Aachen for many inspiring discussions. K.A. would like to thank the organizers of the MFO Mini-Workshop "Multiscale Modelling in Epitaxial Growth" for arranging this constructive and stimulating meeting.

References

[1] K. Albe, K. Nord Lund, and R.S. Aver back, *Modelling the metal-semiconductor interaction: Analytical bond-order potential for platinum-carbon*, Phys. Rev. B **65** (2002), 195124.

[2] M.I. Baskes, *Modified embedded-atom potentials for cubic materials and impurities*, Phys. Rev. B **46** (1992), 2727.

[3] A. Bogicevic, J. Strömquist, and B.I. Lundqvist, *Low-symmetry diffusion barriers in homoepitaxial growth of Al(111)*, Phys. Rev. Lett. **81** (1998), 637.

[4] Ghyslain Boisvert and Laurent J. Lewis, *Diffusion of Pt dimers on pt(111)*, Phys. Rev. B **59** (1999), no. 5.

[5] H. Brune, H. Röder, K. Bromann, K. Kern, J. Jacobsen, P. Stoltze, K. Jacobsen, and J. Nørskov, *Anisotropic corner diffusion as origin for dendritic growth on hexagonal substrates*, Surf. Sci. **349** (1996), L115.

[6] C. Busse, C. Polop, M. Müller, K. Albe, U. Linke, and T. Michely, *Stacking-fault nucleation on Ir(111)*, Phys. Rev. Lett. **91** (2003), 056103.

[7] J. Jacobsen, K.W. Jacobsen, and J.K. Nørskov, *Island shapes in homoepitaxial growth of Pt(111)*, Surf. Sci. **359** (1996), 37.

[8] H. Jónsson, *Theoretical studies of atomic-scale processes relevant to crystal growth*, Ann. Rev. Phys. Chem. **51** (2000), 623.

[9] G.L. Kellogg, *Field-ion microscope studies of single-atom surface-diffusion and cluster nucleation on metal-surfaces*, Surf. Sci. Rep. **21** (1994), 1.

[10] K. Kyuno, A. Gölzhäuser, and G. Ehrlich, *Growth and the diffusion of platinum atoms and dimers on Pt(111)* Surf. Sci. **397** (1998), 191.

[11] T. Michely and J. Krug, *Islands, Mounds and Atoms*, Springer-Verlag, Berlin, 2003.

[12] M. Müller, K. Albe, C. Busse, A. Thoma, and Th. Michely, *unpublished*.

[13] S. Ovesson, A. Bogicevic, and B. Lundqvist, *Origin of compact triangular islands in metal-on-metal growth*, Phys. Rev. Lett. **83** (1999), 2608.

[14] M.J. Rost, T. Michely, and G. Comsa, *Comment on "Self-diffusion and dynamic behavior of atoms at step edges on iridium surfaces"*, Phys. Rev. B **57** (1998), 1992.

[15] S.C. Wang and G. Ehrlich, *Structure, stability, and surface diffusion of clusters: Ir_x on Ir(111)*, Surf. Sci. **239** (1990), 301.

Karsten Albe and Michael Müller
Institut für Materialwissenschaft
Petersenstr. 23
D-64287 Darmstadt
Germany
e-mail: albe@hrzpub.tu-darmstadt.de
e-mail: mueller@mm.tu-darmstadt.de

International Series of Numerical Mathematics, Vol. 149, 29–39

A Multiscale Study of the Epitaxial CVD of Si from Chlorosilanes

Carlo Cavallotti, Davide Moscatelli and Alessandro Veneroni

Abstract. The deposition of epitaxial thin solid films of Si from chlorosilanes was investigated using a multiscale approach. Gas phase and surface kinetic schemes were developed using kinetic constants that, when not found in the literature, were calculated using density functional and transition state theory. Temperature fields, velocity profiles and mass transport rates inside the deposition reactor were calculated solving mass, momentum and energy conservation equations in two dimensions. Finally, the morphology evolution of the film was investigated with three-dimensional Kinetic Monte Carlo. Diffusion parameters of adsorbed Cl atoms were calculated with density functional theory representing the surface as clusters. The results of the simulations show that the surface chemistry might be more complicated than expected. The calculated presence of a significant concentration of islands and rough terrace steps is in fact likely to influence the HCl desorption kinetics, which appears now to be not consistent with experimental data.

Mathematics Subject Classification (2000). Primary 82B24; Secondary 82B80.

Keywords. Chemical vapor deposition; quantum chemistry; kinetic Monte Carlo.

1. Introduction

Chemical Vapor Deposition (CVD) is a process by which thin solid films of inorganic and, more rarely, organic materials are deposited on a substrate positioned on a heated susceptor [1]. The process consists in feeding a carrier gas in which other chemical species, usually called precursors to the growth, are diluted to a reaction chamber that contains the substrate. The growth of the thin solid film is obtained through the dissociation of the precursors over the susceptor, which can be obtained activating the gases either raising the temperature of the reactor, or through electron and ion bombardment, or passing the gases over a heated filament. The CVD process has a great importance in the electronic industry since

it is at the basis of the production of microelectronic and optoelectronic devices, such as ultra large scale integrated circuits (ULSI) or solid state lasers [1, 2, 3].

The availability of a global model of the growth system, which might be able to relate the operating conditions of the deposition process, such as temperature, pressure, inlet flow rate of the carrier and precursor gases, as well as the reactor geometry, to the final quality of the deposited thin solid film, would help greatly in improving the performances of a CVD reactor. The quality of the deposited layer is defined in terms of uniformity of the thickness, controlled morphology, level of defects and dopant concentration. However, in order to be able to correctly describe through a single model all the chemical and physical phenomena occurring in the reaction chamber, a multiscale approach is required. This is made necessary by the fact that there is a direct relation between key features of the material that need to be controlled and a corresponding characteristic length scale. Thus, film growth rate and local composition are usually determined by the geometry, fluid dynamics and thermal field inside the growth reactor, which are defined at a length scale comprised between 10^{-3} and 1 meters, which we will refer to in the following as the reactor scale. Suitable models to describe these processes are continuum models based on the solution of partial differential equations, such as mass, energy and conservation equations, usually by means of finite elements, finite volumes or finite differences methods [4].

The morphology of the film is defined by processes that take place at a length scale that goes from 10^{-7} to 10^{-9} meters, which is usually called mesoscale. This is the scale that should be addressed to investigate whether the deposited material will have an epitaxial or polycrystalline structure, or to determine which are the mechanisms of development of defects. Models apt to describe processes occurring on this scale are usually atomistic models, Kinetic Monte Carlo, Molecular dynamics (e.g., [5], contributions in this volume) or thermodynamically consistent continuum models (e.g., [6], contributions in this volume).

Finally, all the models above introduced require parameters that can either be obtained experimentally or by simulation performed at the atomic scale, which is usually comprised between 10^{-9} and 10^{-10} meters and explicitly considers electrons. Atomic models are usually based on the solution of the Schrödinger equation and can be used to predict surface properties such as kinetic constants of surface reactions, electronic properties, diffusion rates of adsorbed adatoms and surface reconstructions [7].

The multiscale approach for thin solid film growth consists in the development of a complex model that is made of different sub-models, each designed to describe a particular length scale, that are linked together consistently through appropriate boundary conditions. The aim of multiscale models for CVD systems is to provide a thorough description of the growth process, from reactor to atomic scale, that can be either compared directly with experimental data in order to gain new insight into the process itself, or used to design new processes. It is here worth mentioning however that in order to be able to design new processes for the production of materials with better properties it is fundamental that the model is first checked

and validated carefully against experimental data, otherwise it would be easy to make wrong predictions [8].

In this paper we present the multiscale model we have developed to study the epitaxial deposition of Si from chlorosilane precursors. In particular we used quantum chemistry to calculate energetic and kinetic parameters that could not be found in the literature, FEM simulations to investigate the reactor fluid dynamics and determine the adsorption fluxes and kinetic Monte Carlo to investigate the morphology evolution of the film.

2. Methodology

The approach we followed in order to investigate the Si CVD from chlorosilanes consists of several parts. First a detailed kinetic scheme, comprehensive of gas phase and surface reactions was developed and was then embedded in a reactor fluid dynamic model that was used to calculate the overall growth rate and adsorption fluxes on the surface. Then the adsorption fluxes were fed to the kinetic Monte Carlo model, which was used to investigate the surface morphology evolution during the film growth.

2.1. Quantum Chemistry calculations

Quantum chemistry was used to investigate the desorption kinetics of HCl from the Si surface and the diffusion parameters for adsorbed Cl. All calculations were performed using density functional theory representing the surface through clusters of various dimensions. In particular to calculate the desorption of HCl clusters containing 9 and 16 Si atoms were used, while for the investigation of the diffusion rate of adsorbed Cl larger clusters, containing up to 55 Si atoms, were necessary. All calculations were performed using the Becke 3 parameters and the Lee Yang Parr functionals to determine exchange and correlation energies [9, 10]. As a general rule, compound basis sets were used for the calculations. The $6-31g(d,p)$ basis set was adopted for atoms belonging to the upper layer or directly involved in the investigated reaction, while for the Si and H atoms of the lower layers the $6-31g$ and STO-3G basis sets were used, respectively. Clusters geometries were fully optimized without imposing any constraint. Frequency calculations were performed only for the clusters of smaller dimensions and the stability of the calculated structures was confirmed by the absence of negative vibrational frequencies [11]. Transition state structures were characterized by a single imaginary vibrational frequency [11].

2.2. 3D Kinetic Monte Carlo model

We chose to investigate the morphology evolution of the thin solid films with 3-dimensional kinetic Monte Carlo, that has the advantage over other mesoscale models to require as inputs kinetic constants or diffusion parameters that can be directly calculated by means of quantum chemistry. Our implementation of KMC follows the theory outlined by Weinberg [12], with direct tracking of real time

and a rejection free choice of the random transition. Our implementation of three-dimensional kinetic Monte Carlo for a Si(100) surface is described in detail in [13], from which it differs only for the introduction of the Cl adsorption and diffusion moves. The model explicitly accounts for the 2×1 surface reconstruction and for the possible formation of Si dimers, but not for their diffusion. The starting conditions of the KMC simulation are the surface structure at time 0, the surface temperature and the fluxes of gas phase species towards the surface. The FCC structure of the Si solid is represented through a Solid on Solid lattice model, which neglects the presence of defects in the film. The output of a KMC simulation consists in the detailed surface morphology of the film after the deposition of a certain amount of layers. It is thus possible to determine the growth regime of the film, be it three-dimensional terrace step flow or two-dimensional, as well as to visualize how the surface looks like during the growth process.

2.3. Reactor scale: computational fluid dynamics

The CVD fluid dynamic model used in the simulations has been described in detail previously [14] and will thus be only briefly summarized here. It consists of mass, energy and momentum balance equations, which are solved using the finite element method within a two-dimensional axisymmetric mesh. The effect of radiative heat transfer is explicitly considered. A fixed temperature is imposed on the graphite susceptor and the temperatures of all the surfaces of the reactor are calculated solving the energy balance equation.

3. Results and discussion

3.1. Gas Phase and surface chemistry

The kinetic mechanism used in the simulations is essentially similar to the one we described in [14], from which it differs only for the HCl desorption chemistry, which we investigated through quantum chemistry and discuss here in detail. The contemporary presence of hydrogen and chlorine on the silicon surface and the consequent HCl desorption are key issues in the quantitative understanding of silicon epitaxy. The adsorption of H and Cl on the surface is the consequence of the dissociative adsorption of H_2, HCl, $SiCl_2$, and $SiHCl_3$, which are the most abundant species in the gas phase during the Si deposition from chlorosilanes. The removal of Cl from the Si surface occurs through the desorption of HCl, since the direct desorption as Cl_2 is prohibited by thermodynamic limitations that favor the desorption of $SiCl_2$. In order to compute the HCl desorption rate, three different surface species that can be considered precursors to the desorption reaction were considered and are sketched in Fig. 1.

On a Si(100) surface H and Cl can occupy neighboring positions either as being part of the same surface dimer (Fig. 1 (A)), or as being adsorbed on the same Si atom (Fig. 1 (B)), or, being adsorbed on two different neighboring Si adatoms (Fig. 1 (C)). This last species can be viewed in two ways: a species where the Si-Si

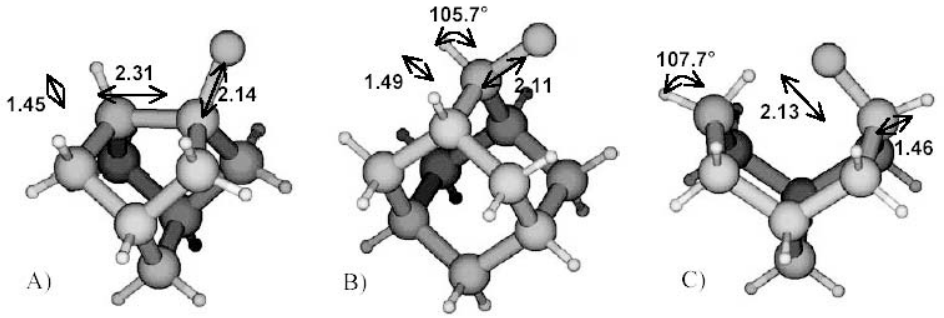

FIGURE 1. Surface species containing HCl that were considered as precursor to the desorption reaction: (A) H-SiSi-Cl, (B) H-Si-Cl and (C) H-Si-H + Cl-Si-H. Distances are reported in Å.

reconstruction has been destroyed and a species where H and Cl are bonded to different dimers along the same row. In the latter case the two H atoms sketched in Fig. 1 (C) at the edge of the cluster are to be intended as a continuation of the row. The three different HCl desorption reactions can therefore be defined as:

$$\text{H-SiSi-Cl} \longrightarrow \text{HCl} + \text{Si} = \text{Si} \tag{R1}$$

$$\text{H-Si-Cl} \longrightarrow \text{HCl} + \text{Si} \tag{R2}$$

$$\text{H-Si-H} + \text{Cl-Si-H} \longrightarrow \text{HCl} + \text{H-SiSi-H} \tag{R3}$$

to which correspond the adsorption reactions:

$$\text{HCl} + \text{Si=Si} \longrightarrow \text{H-SiSi-Cl} \tag{R4}$$

$$\text{HCl} + \text{H-SiSi-H} \longrightarrow \text{H-Si-H} + \text{Cl-Si-H} \tag{R5}$$

Transition states structures and energies for adsorption and desorption reactions were calculated and are reported in Fig. 2.

Kinetic constants were calculated using conventional transition state theory. The contribution of the rotational partition function was neglected for both reactant and transition state, while the surface mobility of adsorbed species was considered calculating the translational partition function for an adsorbed species, which could be either H or Cl, free to diffuse in two dimensions. In particular reaction R1 was considered to be a bimolecular rather than a unimolecular process. This assumption is justified by the fact that the underlying 2×1 surface reconstruction provides a 2-dimensional space that can be randomly occupied by adatoms such as H and Cl. The calculated kinetic constants are reported in Table 1. As a test of the reliability of the calculations, kinetic constants were determined using the $Si_{15}H_{16}$ cluster too.

The data reported in Table 1 suggest that the kinetic pathways that are more likely to lead to the desorption of HCl are essentially two: the direct desorption from H-SiSi-Cl and the mediated desorption through H-Si-Cl. A comparison of

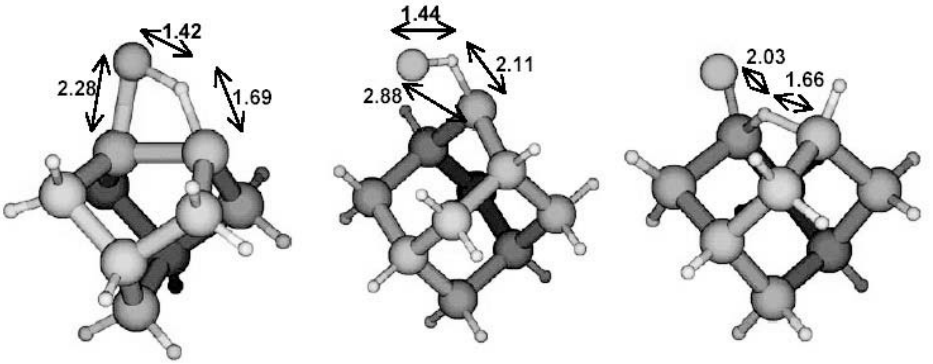

FIGURE 2. Transition state structures calculated for reactions R1–R3. Distances are reported in Å.

	Si_9H_{12}			$Si_{15}H_{16}$		
reaction	$\log_{10} k$	α	E_a	$\log_{10} k$	α	E_a
H-SiSi-Cl ⟶ HCl + Si = Si	23.2	0	71.0	23.2	0	69.1
H-Si-Cl ⟶ HCl + Si	13.7	0	63.3	-	-	-
H-Si-H + Cl-Si-H ⟶ HCl + H-SiSi-H	21.6	0	60.5	-	-	-
HCl + Si=Si ⟶ H-SiSi-Cl	11.4	0.5	0.8	11.4	0.5	0
HCl + H-SiSi-H ⟶ H-Si-H + Cl-Si-H	11.4	0.5	40.8	-	-	-

TABLE 1. Kinetic constants for the HCl desorption and adsorption reactions calculated with transitions state theory and expressed as $k = AT^{\alpha} \exp(-E_a/RT)$. Unimolecular and bimolecular desorption kinetic constants expressed as s^{-1} and $cm^2 s^{-1} mol^{-1}$. Adsorption kinetic constants in $cm^3 mol^{-1} s^{-1}$ and activation energies in kcal/mol.

the results of the quantum chemistry calculations with temperature programmed desorption experimental data is possible considering that in TPD the initial surface coverage is usually smaller than 1 and that the 2×1 surface reconstruction is consistent with a precursor state for desorption that should be the H-SiSi-Cl surface species. The reaction that is more likely to take place in these conditions is therefore reaction R1. This seems to be confirmed by the fact that Mendicino and Seebauer measured through TPD an activation energy for the desorption of HCl from a Si(100) surface of 71.4 kcal/mol [15]. This value is similar to the 72 kcal/mol measured by Coon et al. for the desorption of HCl from a Si(111) surface [16]. Because of the high temperatures and H_2 gas phase concentrations at which the growth process is usually conduced, the H concentration on the surface was assumed to be at the steady state. Thus, being H adsorbed and desorbed with kinetic constants k_{ads} and k_{des} through bimolecular surface reactions, its surface

mole fraction is defined by the Langmuir isotherm and can be expressed as a function of the H_2 gas phase concentration as:

$$x_{H^*} = \frac{1}{1 + \sqrt{\frac{k_{des}}{k_{ads} H_2}}}$$

Thus, in the following Monte Carlo and reactor simulations, the dependence of the desorption rate of adsorbed Cl from the H surface concentration is incorporated directly in the kinetic constant multiplying it by the mean hydrogen surface mole fraction reported above.

3.2. Reactor simulations of Si(100) deposition from $SiHCl_3$

The model reactor we used to study the epitaxial deposition of Si is a standard vertical axisymmetric reactor with the substrate positioned perpendicularly with respect to the direction of the inlet gas. The calculated gas phase temperature profile, streamlines and concentration of $SiHCl_3$, that is, together with $SiCl_2$, the main precursor to the film growth, are sketched in Figure 3.

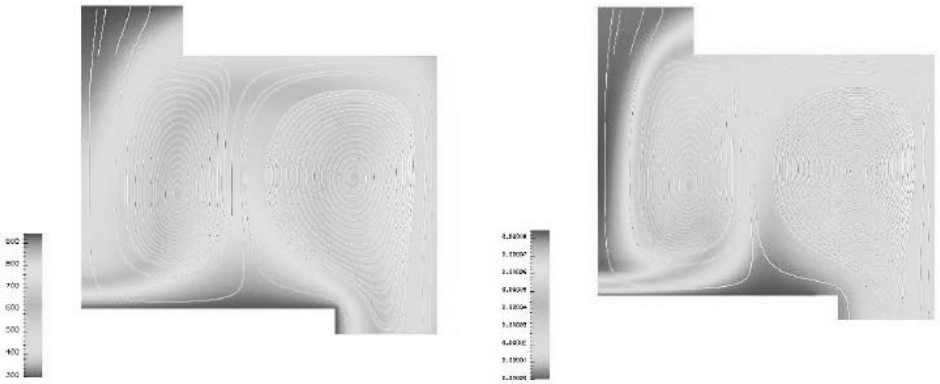

FIGURE 3. Calculated local temperature, streamlines and gas phase concentration of $SiHCl_3$ for a substrate temperature of 1200 K.

$SiHCl_3$ is partially decomposed upon the entrance in the reactor into $SiCl_2$ and HCl, which concentrations are sketched in Figure 4, because of the high temperature. $SiCl_2$, after being produced in the gas phase, is successively rapidly consumed at the surface, where it reacts with adsorbed hydrogen to give HCl and Si, which is incorporated in the film.

The calculated Si growth rate at 1200 K is about 0.2 mm/h and is strongly dependent on the desorption rate of HCl from the surface. This growth rate value is smaller than the experimental data by about a factor of 10. This can be ascribed either to a significant error in the quantum chemistry calculations or to the fact that during the growth process different surface reactions are active than those

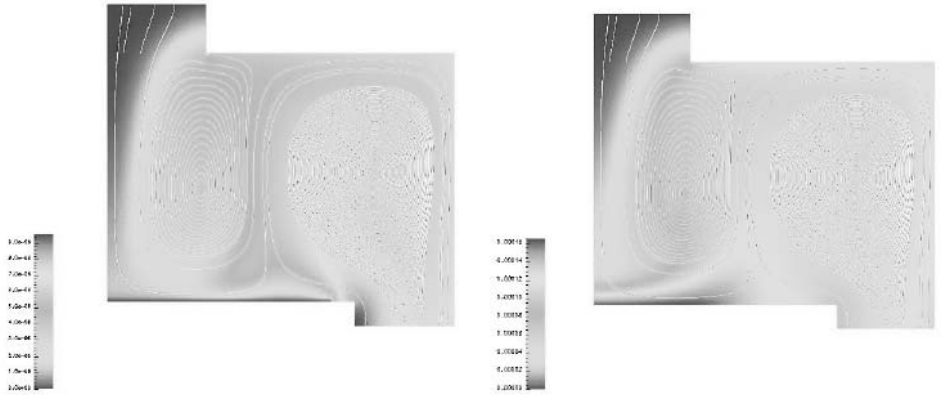

FIGURE 4. Calculated gas phase concentrations of $SiCl_2$(left) and HCl(right) for a substrate temperature of 1200 K.

expected. The contemporary presence of Cl and H on the surface significantly complicates the surface morphology evolution as described in the following section.

3.3. Morphology evolution during Si deposition

The KMC model here implemented was developed to describe the morphological evolution of the Si(100) surface during chemical vapor deposition. The KMC simulation requires as input the adsorption fluxes of $SiCl_2$ and $SiHCl_3$ from the gas phase, which are determined through the solution of the reactor scale model. As explained in Section 3.1, the hydrogen surface dynamics is not explicitly considered, since in the high temperature conditions at which the growth of Si is performed it is likely that its concentration on the surface is at the equilibrium. This is confirmed by the reactor scale simulations. On the other side chlorine is present on the surface in a significant concentration. Chlorine diffusion parameters were calculated through quantum chemistry using clusters of 55 Si atoms on which a single Cl atom is adsorbed. Cl can diffuse in two directions: perpendicular or parallel to the underlying dimer rows. Activation energies for the 2 processes were calculated at the B3LYP/6-31g(d,p) level. The transition state structures so located are reported in Figure 5, the corresponding activation energies for the diffusion of Cl along and perpendicularly the dimer rows were 29 and 29.5 kcal/mol, which shows that the Cl diffusion process is essentially isotropic.

Simulations were performed at two substrate temperatures to investigate the effect that this parameter has on the morphology evolution. The surface structures, after the deposition of two monolayers, are compared in Figure 6.

The simulations show that, because of the large concentration of Cl on the surface, the terrace step is significantly deformed and some island can nucleate on the terrace surface.

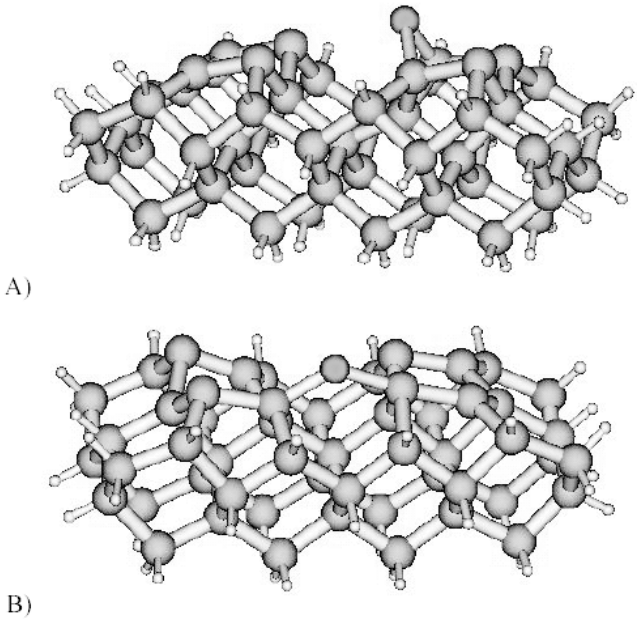

FIGURE 5. Calculated transition state structures for the diffusion of adsorbed Cl atoms along (A) and perpendicularly (B) to the dimer rows on a Si(100) 2×1 surface.

4. Summary and Conclusions

We investigated the morphological and chemical evolution of Si during its chemical vapor deposition from chlorosilanes using a multiscale modeling strategy. The model is organized so that kinetic and energetic parameters not available from the literature are estimated by means of quantum chemistry calculations and used as input for the reactor scale and mesoscale models. The local gas phase composition, velocity and temperature fields are computed solving mass, momentum, and energy conservation equations in the growth reactor. The gas phase fluxes so computed are fed to the 3D Kinetic Monte Carlo model, which is used to study the morphology of the film during the growth. The main result of this study is that it gives an atomistic description of the morphology of the Si surface during the growth that would otherwise be difficult to obtain experimentally, mainly because of high temperature of the surface and for the contemporary presence of a highly reactive gas phase. From the results of our calculations it appears that the presence of a significant concentration of Cl atoms on the surface can easily trigger the formation of islands on the surface, which then coalesce in the rapidly advancing terrace. This growth mechanism might provide an explanation for the formation of point defects in these materials, being the coalescence of two advancing fronts

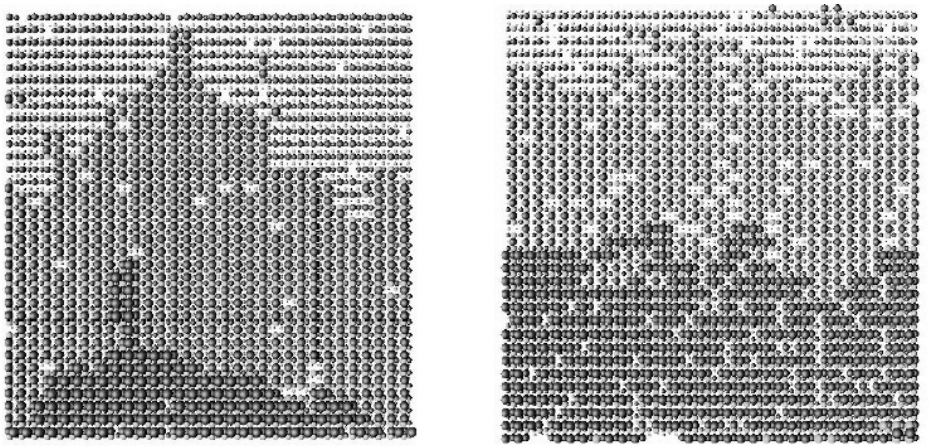

FIGURE 6. Top view of the calculated surface structure at: (A) 1100 K and (B) 1200 K. Si atoms belonging to even and odd Si layers are represented in green and blue, respectively. Cl atoms are sketched in red.

a kinetic instability that might lead to lattice imperfections. Finally and more generally, it can be concluded that multiscale modeling appears as a useful tool to investigate and optimize the thin film deposition process. The main limitation to this approach seems to be the availability of reliable parameters for surface reaction and diffusion processes. Quantum chemical calculations seem to be the way to determine these parameters, when experimental data are unavailable.

References

[1] M.L. Hitchmann, K.F. Jensen, *Chemical Vapor Deposition – Principles and Applications.* Academic Press (1993).

[2] M. Masi, V. Bertani, C. Cavallotti, S. Carra, *Towards a multiscale approach to the growth of silicon films by chemical vapor deposition.* Mat. Chem. Phys. **66** (2000), 229–235.

[3] C. Cavallotti, M. Masi, D. Crippa, L. Rode, M. Masi (Ed.), *Silicon Epitaxy.* Academic Press (2001).

[4] C. Hirsch, *Numerical Computation of Internal and External Flow, Vol. 1.* John Wisley & Sons (1988).

[5] C.C. Battaile, D.J. Srolovitz, *Kinetic Monte Carlo simulation of chemical vapor deposition.* Ann. Rev. Mat. Res. **32** (2002), 297–319.

[6] T. Uehara, R.F. Sekerka, *Phase field simulations of faceted growth for strong anisotropy of kinetic coefficient.* J. Crystal Growth **254** (2003), 251–261.

[7] H. Simka, B.G. Willis, I. Lengyel, K.F. Jensen, *Computational chemistry predictions of reaction processes in organometallic vapor phase epitaxy.* Prog. Cryst. Growth Charact. **35** (1997), 117–147.

[8] K.F. Jensen, S.T. Rodgers, R. Venkataramani, *Multiscale modeling of thin film growth.* Current Opinion in Solid State & Materials Science **6** (1998), 562–569.

[9] A.D. Becke, *Density-functional thermochemistry: 3. The role of exact exchange.* J. Chem. Phys. **98** (1993), 5848–5652.

[10] C. Lee, W. Yang, R.G. Parr, *Development of the Colle-Salvetti correlation-energy formula into functional of the electron-density.* Phys. Rev. B **37** (1988), 785–789

[11] C. Peng, P.Y. Ayala, H.B. Schlegel, M.J. Frisch, *Using redundant internal coordinates to optimize equilibrium geometries and transition states.* J. Comp. Chem. **17** (1996) 49–56.

[12] K.A. Fichthorn, W.H. Weinberg, *Theoretical foundations of dynamic Monte Carlo simulations.* J. Chem. Phys. **95** (1991) 1090–1096.

[13] G. Valente, C. Cavallotti, M. Masi, S. Carra, *Reduced order model for the CVD of epitaxial silicon from silane and chlorosilanes.* J. Crystal Growth **230** (2001) 247–257.

[14] C. Cavallotti, V. Gupta, C. Sieber, K.F. Jensen, *Dissolution reaction of Cu-I(hfac)L compounds relevant to the chemical vapor deposition of copper.* Phys. Chem. Chem. Phys. **5** (2003) 2818–2817.

[15] M.A. Mendicino, E.G. Seebauer, *Adsorption of $TiCl_4$, SiH-4, and Hcl on Si(100) – Application to TiSi-2 chemical vapor deposition and Si etching.* J. Electrochem Soc. **140** (1993) 1786–1793.

[16] P. Gupta, P.A. Coon, B.G. Koehler, S.M. George, *Adsorption and desorption-kinetics for $Sicl_4$ on Si(111)*7×7. J. Chem. Phys. **93** (1990) 2827–2835.

Carlo Cavallotti, Davide Moscatelli and Alessandro Veneroni
Dept. Chimica, Materiali e Ingegneria Chimica
Politecnico di Milano
Via Mancinelli 7
I-20131 Milano
Italy
e-mail: carlo.cavallotti@polimi.it
e-mail: davide.moscatelli@polimi.it
e-mail: alessandro.veneroni@polimi.it

International Series of Numerical Mathematics, Vol. 149, 41–57

Off-lattice Kinetic Monte Carlo Simulations of Strained Heteroepitaxial Growth

Michael Biehl, Florian Much and Christian Vey

Abstract. An off-lattice, continuous space Kinetic Monte Carlo (KMC) algorithm is discussed and applied in the investigation of strained heteroepitaxial crystal growth. As a starting point, we study a simplifying (1+1)-dimensional situation with inter-atomic interactions given by simple pair-potentials. The model exhibits the appearance of strain-induced misfit dislocations at a characteristic film thickness. In our KMC simulations we observe a power law dependence of this critical thickness on the lattice misfit, which is in agreement with experimental results for semiconductor compounds. We furthermore investigate the emergence of strain induced multilayer islands or *Dots* upon an adsorbate wetting layer in the so-called Stranski-Krastanow (SK) growth mode. At a characteristic kinetic film thickness, a transition from monolayer to multilayer island growth occurs. We discuss the microscopic causes of the SK-transition and its dependence on the model parameters, i.e., lattice misfit, growth rate, and substrate temperature.

Mathematics Subject Classification (2000). Primary 82C22; Secondary 62F30.

Keywords. Heteroepitaxy; Off-lattice Kinetic Monte Carlo.

1. Introduction

Atomistic models of crystal growth in Molecular Beam Epitaxy and similar techniques continue to attract considerable interest, see for example [1, 2, 3, 4] for overviews, a very brief introduction is given in [5], this volume. Many interesting aspects of epitaxial growth can be discussed for the case of homoepitaxy where only one material is present. This includes the deposition of, for instance, a metal or a semiconductor compound on a matching substrate crystal.

The term heteroepitaxial crystal growth refers to situations, where the deposited adsorbate material differs from the substrate. The mismatch can be quite fundamental, as for instance in the growth of organic films upon metal substrates. Perhaps the most frequent and, certainly, the conceptually simplest situation is

that where adsorbate and substrate would crystallize in the same type of lattice, but with slightly different lattice spacings.

The latter case is of particular relevance in the fabrication of semiconductor heterostructures for potential technical applications, such as modern optoelectronic or storage devices. Prominent examples are the deposition of Ge on Si, InAs on GaAs, or CdTe on ZnSe. Frequently, the aim is to produce a smooth adsorbate film of a well defined thickness on a given substrate. However, the misfit induced strain can perturb the lattice structure and result in, e.g., dislocations which reduce the quality of the film drastically.

On the other hand, mechanisms of strain relaxation can also be useful in epitaxial growth. The most prominent example is perhaps the self-organized formation of multilayered islands in the so-called Stranski-Krastanov growth mode [1]. The ideal process would yield dislocation-free three-dimensional objects of well defined size and shape which furthermore display spatial ordering. These so-called Quantum Dots can capture single or few electrons and may play the role of *artificial atoms* in a novel type of solid-state-lasers, for example. For a recent overview of the many interesting experimental and theoretical aspects of Quantum Dot physics, see [6].

Besides the obvious technological relevance of heteroepitaxial growth, it is also highly interesting from a theoretical point of view. The self-assembly of Dots might be considered a prototype example of self-organized ordering processes. Heteroepitaxy remains furthermore a challenge in the design of growth models and the development of novel simulation techniques.

The natural tool for mismatched heteroepitaxy appears to be Molecular Dynamics (MD) [7] or quantum mechanical variations thereof, e.g., [8]. This very attractive but computationally demanding approach is discussed in a specific application in [9] (K. Albe, this volume), see [10] for an example application in the context of dislocation formation. Whereas modern computers allow for the simulation of very large systems, the most serious limitation of the MD technique remains: The physical time intervals that can be targeted are generally quite small, e.g., on the order of microseconds. MBE relevant time scales of seconds or even minutes do not seem feasible currently, even when applying highly sophisticated acceleration techniques as in [11].

In simplifying lattice gas models, the particles can only be placed exactly at pre-defined sites. Nevertheless, it is possible to incorporate certain misfit effects into such models. In fact, some of the earliest KMC simulations were performed in the context of strained heteroepitaxial crystal growth [12]. So-called *ball and spring* models consider additional harmonic interactions, i.e., *springs*, between adsorbate or substrate atoms at neighboring lattice sites, see [12] and [13, 14] for more recent examples. In other approaches, continuum elasticity theory is applied to evaluate the contribution and influence of strain for a given configuration of the lattice [15] (and references therein).

However, traditional lattice based models cannot cope with the emergence of defects or dislocations in a straightforward fashion. In the following we will discuss

an off-lattice model and the corresponding Kinetic Monte Carlo (KMC) technique, which allows for continuous particle positions and in which strain results directly from the atomic interactions. Schindler and Wolf have essentially formulated the model and simulation method in [17, 18], and some of the results presented here have been published previously in [19, 20, 21]. For a detailed description of the concept and its applications see also [22].

The method incorporates the essential features of hetero-epitaxy in a natural way, and, at the same time, enables us to perform simulations over reasonable physical time scales. In contrast to earlier realizations or similar concepts, see, e.g., [17, 18, 23, 24], we are also able to simulate the growth of rather thick films over a wide range of misfits.

In Section 2 we will define the model and describe the simulation technique. We briefly discuss the role of misfit dislocations as a mechanism for strain relaxation and present our simulation results in Section 3. Section 4 summarizes our investigations of the Stranski-Krastanov growth mode and in Section 5 we conclude with a brief outlook on perspective investigations.

2. Model and method

In the following, we address quite fundamental and general aspects of heteroepitaxy, rather than the properties of specific material systems. Hence, the primary goal is to develop a fairly simple model which still captures essential the features of a mismatched growth situation.

Following several previous studies [17, 18, 23, 24], we choose a pair potential ansatz to model interactions between the particles. To begin with, we consider a Lennard-Jones (LJ) system [25]. A strong repulsive term at small distances competes with an attractive contribution in the potential

$$U_{ij}(U_o, \sigma) \;=\; 4\,U_o \left[\left(\frac{\sigma}{r_{ij}} \right)^{12} \;-\; \left(\frac{\sigma}{r_{ij}} \right)^{6} \right]. \tag{2.1}$$

The relative distance r_{ij} of particles i and j varies continuously with their position in space. By choice of the parameters U_o and σ we can specify the different material properties in our model: interactions between two substrate or adsorbate atoms are given by the sets $\{U_s, \sigma_s\}$ and $\{U_a, \sigma_a\}$, respectively. In principle, an independent set of parameters would define the interaction of substrate with adsorbate atoms. In order to keep the number of parameters small, we follow a standard approach and set $U_{as} = \sqrt{U_s U_a}, \sigma_{as} = (\sigma_s + \sigma_a)/2$ for the inter-species potential.

The potential energy of two isolated atoms that interact via (2.1) is minimal for $r_{ij} = 2^{1/6}\sigma$. Accordingly, the lattice spacing in a Lennard-Jones crystal is proportional (and close to) σ as well. The relative lattice misfit in our model is therefore directly controlled by choice of σ_s and σ_a:

$$\epsilon \;= (\sigma_a - \sigma_s)/\sigma_s. \tag{2.2}$$

Essential features and several principled questions can already be studied in the simplifying framework of $(1+1)$-dimensional growth, where particles are deposited on a one-dimensional surface. For the simulations presented here we have prepared, at least, 6 layers of substrate particles, each containing L particles. The system sizes vary between $L = 200$ and $L = 800$ in the following, depending on the computational costs of the considered problem. We assume periodic boundary conditions in the lateral direction and fix the particle positions in the bottom layer in order to stabilize the crystal.

In our simulations of the growth kinetics, adsorbate particles are deposited at a constant rate R_d as measured in monolayers per second (ML/s). Desorption events will be completely suppressed here as they would be very unlikely anyway. Only adsorbate particles at the surface are considered mobile in the sense that they perform diffusion hops and the like. However, bulk crystal adsorbate and substrate atoms will be due to relaxation processes which modify their spatial positions and relative distances without changing the topology.

The most distinctive feature of the method is the treatment of thermally activated processes, for which we assume Arrhenius like rates, see [1, 2, 3, 5]. In lattice gas models, particles are moved from one site to another with a rate which usually depends on a small neighborhood only. In the off-lattice approach any event concerns the entire configuration and its rate depends on all particle coordinates, in principle. At a given time, the system resides in a local minimum of the total potential energy of the n particles:

$$E_{tot} = \sum_{i=1}^{n} \sum_{j=i+1}^{n} U_{ij}. \tag{2.3}$$

A possible event k takes the system to one of the neighboring minima in configuration space and for any such change the corresponding energy barrier E_k and rate R_k has to be evaluated by means of a so-called Molecular Statics calculation, see [16, 26] for examples and further references.

In a most general setting the identification of potential events, i.e., the relevant energy minima, can be difficult [26, 27, 28]. The $(1+1)$-dimensional situation simplifies these calculations to a large extent.

Figure 1 illustrates the procedure: The single particle on top of the terraced surface is virtually moved to the right, along the x-coordinate in the illustration. For every fixed value of x, the total energy (2.3) can be (locally) minimized with respect to the moving atom's z-coordinate and the positions of all other atoms including the substrate. In doing so, one can evaluate a potential energy surface (PES) as displayed in Fig. 1. Of course it is not necessary to scan the PES continuously for the Arrhenius rates, as only the energies in the initial state and the transition state are relevant. The latter corresponds to a maximum in the figure, i.e., a saddle point in the energy as a function of all coordinates. In more complex situations like $(2+1)$-dim. growth it is also possible to determine saddle points

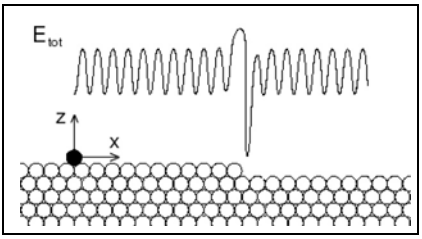

FIGURE 1. Illustration of the Molecular Statics calculations in $(1+1)$ dimensions. As the (black) adatom is virtually moved to the right, along the x-direction, the total energy of the system is locally minimized with respect to all other particle coordinates, including z for the moving adatom. The resulting potential energy surface displays an essentially periodic shape along the terraces and a pronounced Schwoebel barrier for moves along the edge.

in a PES by iterative gradient based methods [22, 26, 27, 28]. However, the identification of the physical path from one minimum to the next can be much more involved in general, e.g., for concerted moves in $(2+1)$ dimensions.

Note that the $(1+1)$-dim. system displays a strong Ehrlich-Schwoebel effect [1, 2]: hops from a terrace are hindered by a barrier which relates to the very weakly bound transition state right at the edge. The effect is also present, but much weaker in a $(2+1)$-dim. fcc-system, for instance. There, a descending particle can follow a more favorable path *between* neighboring particles at the edge.

For large misfits, exchange processes at terrace or island edges may become more frequent than downward hopping diffusion. We have checked that for the values of ϵ considered in the following, exchange diffusion can be neglected, in general. The precise barriers, however, depend in a subtle way on the misfit, the island size, and the properties of the actual interaction potential. For details we refer to [22] and forthcoming publications.

Further simplifications may be used here. First, because the LJ-potential (2.1) is very weak for distances $r_{ij} > 3\sigma$, one can effectively cut-off the interactions and consider only particles in a corresponding neighborhood region when evaluating the PES of a particular event. The so-called *frozen crystal approximation* should be employed with care: in this scheme all coordinates but those of the moving atom are considered fixed, which significantly simplifies the saddle point search. Although the scheme appears to impose a drastic restriction, it has been reported by various authors that its main effect in the LJ-system is a uniform shift of all barriers by roughly 10% [16, 17, 18, 22].

Given a configuration of the system, we set up a catalogue of all possible activated diffusion events and evaluate the rates

$$R_k = \nu_o \exp\left[-\frac{E_k}{k_B T}\right] \text{ with } \nu_o = 10^{12}/s \tag{2.4}$$

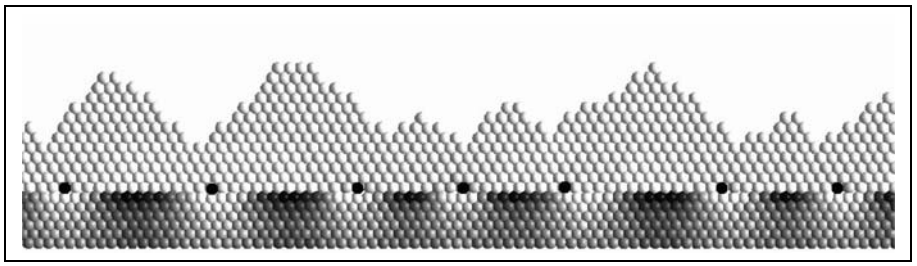

FIGURE 2. Dislocations: a film grown in the model without downhill funneling [19] for a large misfit of $\epsilon = +10\%$, section of a larger system with six layers of substrate. The lighter a particle is displayed, the smaller is its average distance to the nearest neighbors. Dislocations form right at the interface of adsorbate and substrate, as marked by the additional filled circles. Note that the elastic interaction with the film also affects the substrate.

with E_k obtained as described above. For simplicity, we choose a constant prefactor or *attempt frequency* ν_o for all diffusion processes, see [5] for a brief discussion and references. Next, one of the diffusion or deposition processes is chosen with a probability proportional to its rate. In order to facilitate an efficient bookkeeping and fast search, events are stored in a binary search tree, see [3] and references therein. After performing the particular process, the catalogue of rates has to be updated and re-evaluated. Obviously this task consumes a large portion of the computing power. Nevertheless, the rejection-free event based method is advantageous over a simple rejection-based simulation [5].

Approximations and numerical inaccuracies, and even more so the use of the *frozen crystal* picture, result in deformations of the crystal and the accumulation of artificial strain energy. In order to avoid this effect, a relaxation of the system should be performed after each event, in the sense that the configuration is taken to the nearest local minimum of E_{tot}. In practice we perform after each diffusion or deposition a *local* relaxation within a radius 3σ about the location of the event. The full *global* procedure is applied only after a certain number of processes, which is increased whenever the relaxation changes barriers by more than, say, a few percent.

In the following sections we discuss applications in the context of two different mechanisms of strain relaxation. Their peculiarities require certain extensions and modifications. However, the basic concepts and essential ingredients have been outlined above.

3. Formation of dislocations

If the misfit is relatively small in heteroepitaxial growth, one frequently observes the initial growth of a *pseudomorphic* film. Here the substrate determines the

lateral lattice constant also in the adsorbate and strain energy accumulates in the growing film. On the other hand, for very thick adsorbate films far away from the substrate, one clearly expects to find a lattice structure and spacing as in the undisturbed bulk material. The ultimate relaxation of strain is through misfit dislocation, lattice defects which allow the adsorbate to assume its natural lattice structure, eventually. Here we address the question of how the transition from strained pseudomorphic to relaxed adsorbate growth occurs and how the lattice spacing evolves with the film thickness.

In the frame of our model we choose the same potential depth for all types of interactions, which defines the energy scale. By identifying $U_a = U_s = U_{as}$ with the value $U_o = 1.3125eV$, for instance, we obtain a barrier of $0.90eV$ for surface diffusion in the case of zero misfit. The substrate temperature was set to $T = 0.03U_o/k_B \approx 460K$ which is well below the melting temperature of a monoatomic Lennard-Jones crystal. All results presented in this section were obtained with the deposition rate $R_d = 1ML/s$.

Dislocations can be identified by constructing Voronoy polyhedra and searching for particles with a coordination number different from six in the bulk. Further information is obtained from a Burgers construction, see [19, 22] for details.

In our earlier investigations presented in [19] we considered positive and negative values of the misfit parameter in the range $-15\% \leq \epsilon \leq +11\%$. For large absolute values of ϵ the system displays the formation of misfit dislocations right at or very close to the substrate/adsorbate interface, cf. Fig. 2. The slightly oversimplifying picture is that, initially, separated islands or mounds grow on the substrate and dislocations emerge where they meet. These are then overgrown by the deposited material. Diffusion of dislocations by concerted moves of the surrounding particles are highly improbable in the LJ-system and for the low temperatures considered here. We find a mean distance between dislocations very close to $1/\epsilon$ which directly reflects the *relative periodicity* of the two lattices involved.

For smaller misfits, one observes a more interesting evolution of the surface: initially, a pseudomorphic adsorbate film grows with the same mean lateral atomic distances $\bar{a}_{\mathrm{lat}} \propto \sigma_s$ as in the substrate. At a rather well-defined film thickness, misfit dislocations appear everywhere in the surface, which are later overgrown. Snapshots of the surface evolution in the vicinity of a single dislocation are shown in Figure 3 for $\epsilon = -5\%$.

In our most recent studies of the low misfit regime, we have slightly amended the model in comparison with Section 2. Deposited particles perform a so-called *downhill funneling* upon arrival at the surface: It is assumed that its kinetic energy enables an arriving atom to move to the lowest position in the vicinity of the deposition site. Similar incorporation effects, which are clearly not thermally activated, are discussed in [5] (this volume) and in greater detail in [1, 2]. The funneling process smoothes the surface by reducing the effect of the strong Schwoebel barrier in the system. It hence allows for the simulation of thicker films without a pronounced mound structure as, for instance, in Fig. 2. Note, however, that our findings are to a large extent robust with respect to such modifications.

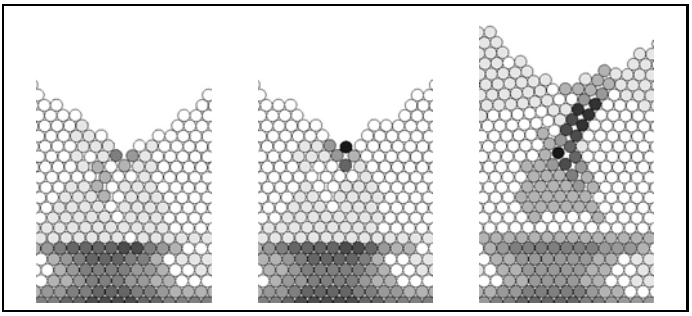

FIGURE 3. The emergence of a misfit dislocation in the model without downhill funneling [19] for $\epsilon = -5\%$, other details as in Fig. 2. The snapshots correspond to a mean film thickness of $12ML, 13ML$ and $18ML$, respectively.

For positive misfits the adsorbate is laterally compressed and it reacts by assuming a vertical lattice spacing $\bar{a}_\perp$ which is larger than in its undisturbed bulk. A simple consideration yields for small ϵ in the LJ-system a vertical spacing $\bar{a}_\perp^{\text{const}} \approx \bar{a}_{\text{lat}}\sqrt{3/4}(1 + 4/3\epsilon)$ of the atomic layers in the pseudomorphic film. After misfit dislocations have emerged, the adsorbate approaches its relaxed undisturbed bulk structure, as indicated by the decrease of $\bar{a}_\perp$ with the film thickness. Figure 4 shows the result of our simulations on average over 10 independent runs for system sizes of at least $L = 400$ and misfits in the range $1.4\% \leq \epsilon \leq 2.2\%$. The qualitative evolution of $\bar{a}_\perp$ agrees with novel measurements of this quantity in experimental studies of II-VI-semiconductor heteroepitaxy [29]. In a forthcoming publication the comparison with experimental data will be presented in greater detail.

Perhaps the most interesting result in this context concerns the *critical* film thickness h_c at which the dislocations appear in the system. In Fig. 4, it is marked by the deviation of $\bar{a}_\perp$ from its initial value. The rescaling of the thickness with $\epsilon^{-3/2}$ in Fig. 4 shows a relatively good collapse of the curves in the relevant phase of growth. It is by no means our intention to suggest that, here, a true *dynamical scaling law* exists as in, e.g., kinetic roughening [1, 2]. The small range of considered misfits would certainly not allow for such a claim. Nevertheless, our data is consistent with a critical thickness of the form

$$h_c \propto \epsilon^{-3/2}. \tag{3.1}$$

In the previous study of a slightly modified model we considered a different measure of the critical film thickness [19]. There, we found the same power law behavior for positive and negative misfits in a much wider range of misfits. Preliminary studies yield the same qualitative result for the model with other pair potentials in place of the Lennard-Jones interactions. Hence we believe that the observed dependence is robust with respect to details of the model and displays a certain degree of universality.

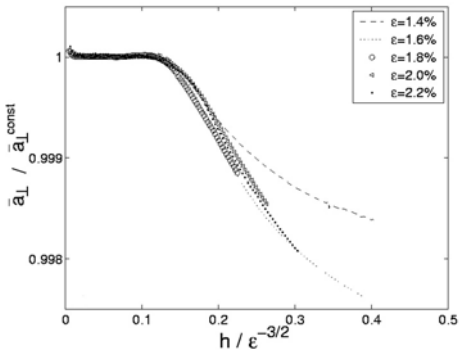

FIGURE 4. Dislocations: development of the vertical layer spacing in the model with *downhill funneling*, see text, with increasing film height for various values of the misfit. Results were obtained on average over 10 independent simulation runs and the spacing $\bar{a}_\perp$ is rescaled by its initial value. The scaling of the film thickness is according to Eq. (3.1) and results in a relatively good collapse of the curves close to the critical thickness.

Note that the power law behavior (3.1) disagrees with the results of energy or force balance considerations, as for instance the well-known and widely accepted relation derived by Matthews and Blakeslee [30]. One can argue, however, that the dislocation formation as observed here is a kinetic phenomenon far from equilibrium. Indeed, alternative approaches as suggested by Cohen-Solal and co-workers predict the power law dependence (3.1) for the critical thickness [31, 32]. Furthermore, experimental data for several IV-IV, III-V, and II-VI semiconductor systems shows very good agreement with the hypothesized power law [31, 32, 33].

In forthcoming investigations we will study the dependence of the surface evolution on the temperature and deposition rate. This should provide further evidence for the robustness of relation (3.1) and for the interpretation of misfit induced dislocation formation as an activated process.

4. Stranski-Krastanov like growth

Obviously, dislocations should dominate the strain relaxation in sufficiently thick films and for large misfits. In material systems with relatively small mismatch an alternative effect governs the initial growth of very thin films: Instead of growing layer by layer, the adsorbate aggregates in three-dimensional structures, allowing for partial relaxation. The term *3D-islands* is used to indicate that these structures are spatially separated. The effect is to be distinguished from the emergence of *mounds* due to the Ehrlich-Schwoebel instability [1, 2] which also occurs in homoepitaxy.

At least two distinct growth scenarios display 3D-island formation: In *Volmer-Weber* growth, the structures emerge immediately upon the substrate before the adsorbate even forms a closed layer [1]. The situation resembles the formation of non-wetting droplets of liquid on a surface. It is often observed in systems where adsorbate and substrate are fundamentally different, an example being Pb on a graphite substrate [1].

Here, we will focus on on the so-called *Stranski-Krastanov* (SK) growth mode, where 3D-islands are found upon a persistent pseudomorphic wetting-layer (WL) of adsorbate material [1, 6]. Most prominent examples for SK-systems are Ge/Si and InAs/GaAs where, as in almost all cases discussed in the literature, the adsorbate is under compression in the WL.

In order to avoid conflicts with more detailed or more restricted definitions of SK growth in the literature, we use the term *SK-like growth* here. It summarizes the following sequence of events during the deposition of a few monolayers (ML) of material:

1. Initial layer by layer growth of a pseudomorphic, compressed adsorbate WL.
2. The sudden appearance of 3D-islands, marking the so-called 2D-3D- or SK-transition at a *kinetic WL thickness* $h^*_{\rm WL}$.
3. Further growth of the 3D-islands, which is fed by additional deposition and by incorporation of surrounding WL atoms.
4. The observation of separated 3D-islands of similar shapes and sizes, on top of a WL with reduced *stationary thickness* $h_{\rm WL} < h^*_{\rm WL}$.

In order to avoid confusion, and since one might interpret our $(1 + 1)$-dim. model as a cross section of the full $(2 + 1)$-dim. picture, we will use the term 2D-3D-transition as usual throughout the following.

In SK growth a number of effects might play important roles, including the mixing interdiffusion of materials or the segregation of compound adsorbates. These effects are certainly highly relevant in many cases, see several contributions in [4] and [6]. However, SK-like growth is observed in a variety of material systems which may or may not display these specific features. For instance, intermixing or segregation should be irrelevant in the somewhat *exotic* case of large organic molecules like PTCDA deposited on a metal substrate. Nevertheless, this system shows SK-like growth according to the above definition [34].

This very diversity of SK-systems gives rise to the hope that this growth scenario might be explained in terms of a few basic mechanisms. Accordingly, it should be possible to capture and identify these universal features in relatively simple model systems without aiming at the reproduction of material specific details. This hope motivated the investigation of SK-growth in the frame of our off-lattice model.

An important modification beyond the description in Section 2 concerns the interlayer diffusion of adatoms. As argued above, the Ehrlich-Schwoebel effect would be much less pronounced in the physical $(2 + 1)$-dim. situation. In our investigation of the SK-like scenario we remove the ES-barrier for all interlayer

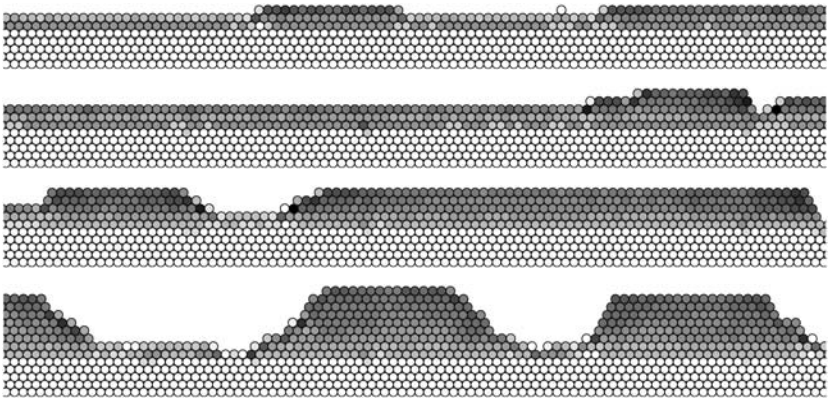

FIGURE 5. SK-like growth: A section of a simulated crystal with six layers of substrate as obtained for $\epsilon = +4\%$ and $R_d = 7.0ML/s$ at $T = 500K$ after deposition of (top to bottom) $1.5ML, 2.3ML, 3.0ML$ and $4.0ML$. In the second snapshot the critical WL thickness $h^*_{WL} \approx 2.3ML$ is reached and island formation sets in. Note how smaller islands grow and larger structures break up. Note also that WL particles contribute to the growth of islands. Eventually, the well-separated structures are located on a stationary WL with, here, $h_{WL} \approx 1$. The darker a particle is displayed, the larger is the average distance from its nearest neighbors. White represents σ_s whereas σ_a corresponds to a dark grey on this scale.

diffusion events at terrace edges *by hand*. One motivation is the above-mentioned over-estimation. More importantly, we wish to investigate strain induced island formation without interference of the ES instability. Note that the latter leads to the formation of mounds even in homoepitaxy [1, 2].

In order to favor the emergence of a wetting layer, we set $U_s > U_{as} > U_a$ in our model. As an example we have used $U_s = 1.0eV$, $U_a = 0.74eV$, and $U_{as} = 0.86eV$ accordingly. If not otherwise specified, we consider a positive misfit of $\epsilon = 4\%$ in the following. We have demonstrated before [19], cf. Section 3, that strain relaxation through dislocations is not expected for $\epsilon = 4\%$ within the first few adsorbate layers. Indeed, no misfit dislocations were observed in the simulations presented here.

In the simulation we realize a situation very similar to many experiments: a fixed amount of adsorbate material, corresponding to $4ML$, is deposited at a constant rate R_d. After deposition ends, we allow for a short relaxation period, in which atoms can still diffuse on the surface. Note however, that the essential surface properties are already determined during growth.

Our model displays a behavior along the lines of our operative definition of SK-like growth. The snapshots of an example simulation run in Figure 5 correspond

precisely to the four stages outlined above, illustrating mpeg-movies of sample simulations are available at [35].

Several properties of surface diffusion in our model are discussed in [21] in great detail. Here, we shortly summarize the essential features:

a) Adsorbate diffusion right on the substrate is relatively slow, due to the fact that U_{as} is quite large and satisfies $U_{as} > U_a$.
b) Adsorbate diffusion on a strained WL is relatively fast. The diffusion barrier decreases with the thickness, but essentially saturates at 3 or $4ML$ in our model, where the interaction with the substrate becomes negligible.
c) An adsorbate particle on top of an existing island is subject to a strong diffusion bias towards the island center. This result was already reported in [16]. The bias is due to the partial relaxation in the island and unrelated to the Ehrlich-Schwoebel effect, which has been eliminated in our model.

The first two effects, (a) and (b), clearly favor and stabilize the existence of a wetting layer. Qualitatively the same relation is obtained in experimental investigations of the Ge/Si system [36] and [6]. With the model parameters specified above we find an activation barrier of approximately $0.57eV$ for directly on the substrate and roughly $0.47eV$ for diffusion on the first wetting layer.

On the contrary, the diffusion bias (c) stabilizes existing islands by essentially confining adatoms to their top terraces. Of course this is the case for particles deposited onto the island. More importantly, we find a significant contribution of particles that jump upward, from the WL atop an island. The rate for such processes is quite small, generally, but becomes significant close to the SK-transition, see [21] for details.

In simulations with different deposition rates we observe that the kinetic WL thickness increases with R_d [20, 21]. If the formation of second or third layer nuclei by freshly deposited particles was the driving force, one would expect more frequent nucleation and an earlier 2D-3D-transition at higher growth rates. We conclude that, in the main, upward jumps trigger the SK-transition. Further evidence and a more detailed discussion of this important point is given in [21].

Our investigations suggest the following picture of the Stranski-Krastanov transition: The diffusion properties, (a) and (b), favor the formation of a wetting layer and stabilize it. As the film grows, strain accumulates in the film and upward hops from the WL become more probable. The precise spatial modulation of R_d in the film presumably determines the final island sizes and will be studied in forthcoming investigations. Once multilayer have emerged they are stabilized by the diffusion bias (c).

After the 2D-3D-transition, islands grow by incorporating newly deposited material, but also by consumption of the surrounding WL. Note that very large islands are observed to split by means of upward diffusion events onto their top layer, cf. Fig. 5. The migration of WL particles towards and onto the islands can well extend into the relaxation period after deposition ends. Eventually, a stationary WL thickness $h_{\mathrm{WL}} \approx 1$ is observed in our example scenario with $U_{as} \approx$

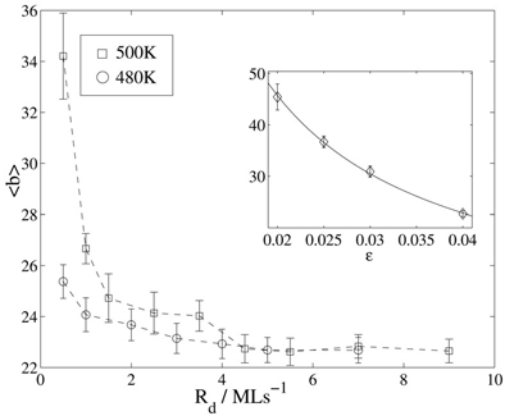

FIGURE 6. Average base size $\langle b \rangle$ of multilayer islands as a function of R_d at $T = 480$ and $T = 500K$, together with standard error bars. Results were obtained on average over 15 independent simulation runs. The inset shows the result for $T = 500K, R_d = 4.5ML/s$ and different misfit parameters, the solid line corresponds to $\langle b \rangle = 0.91/\epsilon$.

$0.86eV$. By increasing the strength of the adsorbate/substrate interaction we can achieve, e.g., $h_{\mathrm{WL}} \approx 2$ for $U_{as} \approx 2.7eV$, but it is difficult to stabilize a greater stationary thickness, due to the short range nature of the LJ-potential.

Finally, we discuss some properties of the emerging islands or SK-Dots. Figure 6 displays the average lateral size, measured as the number of particles in the island bottom layer. The results shown here were obtained at the end of a short relaxation period with $R_d = 0$. Whereas the mean values do not change significantly, fluctuations are observed to decrease in this phase.

We observe for two different temperatures that the island size decreases with increasing deposition rate. This is in accordance with several experimental observations [37]. However, the size becomes constant and independent of T for large enough deposition flux. A corresponding behavior is found for the island density and their lateral spacing, which hints at a considerable degree of spatial ordering [20, 21]. This saturation behavior further demonstrates the relevance of upward hops. Standard arguments [1, 2] show that a dominant aggregation of deposited particles on top terraces would yield an island density that continues to increase with R_d.

The inset in Fig. 6 displays the mean island size for $T = 500K$ and $R_d = 4.5ML/s$, i.e., in the saturation regime. Our result is consistent with a simple power law of the form $\langle b \rangle \propto 1/\epsilon$. Very far from equilibrium, the only relevant length scale in the system appears to be, again, the relative periodicity $1/\epsilon$ of substrate and adsorbate lattice.

5. Summary and outlook

Despite its conceptual simplicity and the small number of parameters, our model reproduces several features of heteroepitaxial growth. Strain effects are incorporated in a natural version as they emerge directly from the interaction of particles. For instance, we have demonstrated that misfit dislocations appear in the system when the film thickness exceeds a characteristic value. This characteristic height displays a power law behavior on the lattice misfit.

We furthermore believe that, with appropriately chosen interaction parameters, our model is capable of reproducing the three essential growth modes: extended layer by layer growth (for very small misfits), Volmer-Weber (for $U_{as} < U_a$ and, as demonstrated already, SK-growth for $U_{as} > U_a$. The small number of parameters should allow for determining the corresponding *phase diagram* of growth modes in the frame of our model system.

Besides the exploration of the available parameter space, we intend to extend the model conceptually in several directions. As just one example, intermixing and segregation should be included to study the relevance of these effects in the Quantum Dot formation.

In order to test the potential universality of our findings, we will introduce different types of interactions in our model. Preliminary results for, e.g., Morse potentials [25] and modifications of LJ-potentials confirm our results in the context of dislocation formation. Ultimately, we will extend our model to the physical case of growth in $(2 + 1)$ dimensions and to realistic empirical potentials for metals or semi-conductors. As a first step, we are currently investigating the sub-monolayer regime in strained heteroepitaxy of fcc materials.

In a sense, the off-lattice KMC method provides a link between traditional, lattice based methods and Molecular Dynamics. Hence, it might play a significant role in the further development of the multiscale approach.

Acknowledgment

M.B. would like to thank the organizers and all participants of the MFO Mini-Workshop on *Multiscale Modelling in Epitaxial Growth* for the most stimulating atmosphere and many useful discussions. One of us (F.M.) was supported by the Deutsche Forschungsgemeinschaft.

References

[1] A. Pimpinelli and J. Villain, *Physics of crystal growth.* Cambridge University Press (1998).

[2] T. Michely and J. Krug, *Islands, mounds and atoms. Patterns and Processes in Crystal Growth far from equilibrium.* Springer (2004).

[3] M.E.J. Newman and G.T. Barkema, *Monte Carlo Methods in Statistical Physics,* Oxford University Press (1999).

[4] M. Kotrla, N.I. Paanicolaou, D.D. Vvedensky, and L.T. Wille, *Atomistic Aspects of Epitaxial Growth.* Kluwer (2002).

[5] M. Biehl, *Lattice gas models of epitaxial growth and Kinetic Monte Carlo simulations.* This volume.

[6] B. Joyce, P. Kelires, A. Naumovets, and D.D. Vvedensky (eds.), *Quantum Dots: Fundamentals, Applications, and Frontiers.* Kluwer, to be published.

[7] D.C. Rapaport, *The Art of Molecular Dynamics Simulation.* Cambridge University Press (1995).

[8] M. Parrinello, Solid State Comm. **102** (1997) 107.

[9] K. Albe, this volume.

[10] L. Dong, J. Schnitker, R.W. Smith, D.J. Sroloviy, *Stress relaxation and misfit dislocation nucleation in the growth of misfitting films: a molecular dynamics simulation.* J. Appl. Phys. **83** (1997) 217.

[11] A.F. Voter, F. Montalenti, and T.C. Germann, *Extending the time scale in atomistic simulations of materials.* Annu. Rev. Mater. Res. **32** (2002) 321.

[12] A. Madhukar, *Far from equilibrium vapor phase growth of lattice matched III-V compound semiconductor interfaces: some basic concepts and Monte Carlo computer simulations.* Surf. Sci. **132** (1983) 344.

[13] K.E. Khor and S. Das Sarma, *Quantum Dot self-assembly in growth of strained-layer thin films: a kinetic Monte Carlo study.* Phys. Rev. **B 62** (2000) 16657.

[14] C.H. Lam, C.K. Lee, and L.M. Sander, *Competing roughening mechanisms in strained heteroepitaxy: A fast kinetic Monte Carlo study.* Phys. Rev. Lett. **89** (2002) 216102.

[15] M. Meixner, E. Schöll, V.A. Shchukin, and D. Bimberg, *Self-assembled quantum dots: crossover from kinetically controlled to thermodynamically limited growth.* Phys. Rev. Lett. **87** (2001) 236101.

[16] M. Schroeder and D.E. Wolf, *Diffusion on strained surfaces.* Surf. Sci. **375** (1997) 375.

[17] A.C. Schindler, *Theoretical aspects of growth in one and two-dimensional strained crystal surfaces.* Dissertation, Univeristät Duisburg (1999).

[18] A.C. Schindler and D.E. Wolf, *Continuous space Monte Carlo simulations in a model of strained epitaxial growth.* Preprint, Universität Duisburg (1999).

[19] F. Much, M. Ahr, M. Biehl, and W. Kinzel, *Kinetic Monte Carlo simulations of dislocations in heteroepitaxial growth.* Europhys. Lett. **56** (2001) 791–796.

[20] F. Much and M. Biehl, *Simulation of wetting-layer and island formation in heteroepitaxial growth.* Europhys. Lett. **63** (2003) 14–20.

[21] M. Biehl and F. Much, *Off-lattice Kinetic Monte Carlo simulations of Stranski-Krastanov-like growth.* In [6], in press.

[22] F. Much, *Modeling and simulation of strained heteroepitaxial growth.* Dissertation Universität Würzburg (2003).

[23] J. Kew, M.R. Wilby, and D.D. Vvedensky, *Continuous-space Monte Carlo simulations of epitaxial growth.* J. Cryst. Growth **127** (1993) 508.

[24] H. Spjut and D.A. Faux, *Computer simulation of strain-induced diffusion enhancement of Si adatoms on the Si(001) surface.* Surf. Sci. **306** (1994) 233.

[25] F. Jensen, *Introduction to Computational Chemistry,* Wiley (1999).

[26] G.T. Barkema and N. Mousseau, *Event-based relaxation of continuous disordered systems.* Phys. Rev. Lett. **77** (1996) 4358.

[27] N. Mousseau and G.T. Barkema, *Traveling through potential energy landscapes of disordered materials: the activation relaxation technique.* Phys. Rev. **E 57** (1998) 2419.

[28] R. Malek and N. Mousseau, *Dynamics of Lennard-Jones clusters: A characterization fo the activation relaxation technique.* Phys. Rev. **E 62** (2000) 7723.

[29] A.S. Bader, W. Faschinger, C. Schumacher, J. Geurts, and L.W. Molenkamp, *Real-time in situ X-ray diffraction as a method to control epitaxial growth.* Appl. Phys. Lett. **82** (2003) 4684.

[30] J.W. Matthews and A.E. Blakeslee, *Defects in epitaxial multilayers.* J. Cryst. Growth **27** (1974) 118.

[31] G. Cohen-Solal, F. Bailly, and M. Barbé, *Critical thickness of zinc-blende semiconductor compounds.* J. Cryst. Growth **138** (1994) 138.

[32] F. Bailly, M. Barbé, and G. Cohen-Solal, *Setting up of misfit dislocations in heteroepitaxial growth and critical thickness.* J. Cryst. Growth **153** (1995) 153.

[33] K. Pinardi, U. Jain, S.C. Jain, H.E. Maes, R. Van Overstraeten, and M. Willander, *Critical thickness and strain relaxation in lattice mismatched II-VI semiconductor layers.* J. Appl. Phys. **83** (1998) 4724.

[34] L. Chkoda, M. Schneider, V. Shklover, L. Kilian, M. Sokolowski, C. Heske, and E. Umbach, *Temperature-dependent morphology and structure of ordered 3,4,9,10-perylene-tetracarboxylicacid-dianhydride (PCTDA) thin films on Ag(111)*, Chem. Phys. Lett. **371** (2003) 548.

[35] Illustrations and movies of our simulations are available at http://physik.uni-wuerzburg.de/~much{biehl}.

[36] V. Cherepanov and B. Voigtländer, *Influence of strain on diffusion at Ge(111) surfaces*, Appl. Phys. Lett. **81** (2002) 4745.

[37] J. Johansson and W. Seifert, *Kinetics of self-assembled island formation: Part I – island density*, J. Cryst. Growth **234** (2002) 132, and: *Part II – island size*, same volume, 139.

Michael Biehl
University Groningen
Institute for Mathematics and Computing Science
P.O. Box 800
NL-9700 AV Groningen
The Netherlands
e-mail: `biehl@cs.rug.nl`

Florian Much and Christian Vey
Universität Würzburg
Institut für Theoretische Physik
Am Hubland
D-97074 Würzburg
Germany
e-mail: `much@physik.uni-wuerzburg.de`
e-mail: `vey@physik.uni-wuerzburg.de`

International Series of Numerical Mathematics, Vol. 149, 57–66

Quasicontinuum Monte Carlo Simulation of Multilayer Surface Growth

Jason P. DeVita, Leonard M. Sander and Peter Smereka

Abstract. We develop a method, for simulating epitaxial growth, based on coarse graining (in time) the evolution equations of the probability functions for Kinetic Monte Carlo. Our approach has the advantages offered by continuum methods but still retains enough of the fluctuations to offer good physical fidelity. We have compared our method to KMC in a number of situations and found good agreement.

Mathematics Subject Classification (2000). Primary 82B80; Secondary 35R35.

Keywords. Epitaxial Growth; Kinetic Monte Carlo; Quasicontinuum.

1. Introduction

Molecular beam epitaxy (MBE) is a popular technique for growing materials, and is also an interesting example of a statistical process out of equilibrium. Epitaxy is commonly modeled by either kinetic Monte Carlo (KMC) or by continuum methods. In KMC, discrete adatoms are deposited onto a grid (taken to be a square lattice for simplicity) at a rate F. Once on the grid, they execute nearest neighbor hops with probability $e^{(-nE_0/kT)}$, where E_0 is the bond energy between two adatoms, and n is the number of in-plane bonds. KMC automatically incorporates internal noise by representing each atom individually. However, in situations where the adatom density is high – such as near equilibrium – KMC can be slowed down considerably.

Continuum models such as those proposed by Burton et al. [1] and Ghez & Lyer[2] do not slow down for large adatom densities. In this approach, adatoms are represented as a continuous field. This type of model has been implemented using level set methods, see for example Refs. [3, 4, 5]. These models have the potential to be much faster than KMC when there are a large number of adatoms present occurs in the presence of high detachment rates [6]. In addition, there are situations where it is believed that that epitaxial growth occurs quite close to

equilibrium. In these situations there is a large number of adatoms present and such systems become very difficult to simulate using KMC. One such example is Tersoff et al. [7].

There have been other approaches that are continuum in nature but capture certain aspects of the discrete nature of the problem. E and Schulze [8] developed a formulation, in one space dimension, with discrete adatoms; the adatoms were attached deterministically to islands. Mandreoli et al. [9] presented a similar idea in two dimensions. Both of these formulations will be discussed in more detail later in the paper. We also mention that Ratsch et al. [10] were able to include finite size effects in a continuum model.

In all of the continuum formulations outlined above fluctuations which may be important are ignored. One important kind of fluctuation arises from that fact that particles are attached to the interface stochastically one at a time. This effect is responsible for the fractal-like patterns that are observed in diffusion-limited growth; see Witten and Sander [11]. In an effort to retain the advantages of the continuum approach and include fluctuations Schulze et al. [12] developed a hybrid approach in one space dimension. In this formulation the regions near the interface are treated with KMC. Non-KMC regions are course-grained in space and time and treated in the continuum field. This approach is best suited for situations with widely spaced steps and has been extended to two space dimensions by Schulze [13].

Another hybrid approach was proposed in Ref. [14]. In this work the authors considered a situation where the interface was commensurate with the underlying lattice. They then solve the diffusion equation with boundary conditions on the interface that include effects of detachment and attachment. Adatoms are added or removed as follows. The net flux of adatoms to the interface and from the interface are computed. When either of these exceeds unity adatoms are added or removed with a probability proportional to this flux. In this way effects of fluctuations are included. This approach is reminiscent of the dielectric breakdown model [16]. The advantage of this approach is that it allows large time steps because the boundary conditions naturally include the effects of rapid attachment and detachment. In addition, the speed of the algorithm is independent of the number of adatoms since adatoms are treated in terms of a probability density. The disadvantage is that the computation is at every site. To go significantly faster it is necessary to take very large time steps which entails coarse graining in time.

2. Probabilistic KMC and coarse-graining

In this section we will combine ideas from KMC, E and Schulze, Mandreoli et al. [9] and Russo et al. [14] to formulate our temporally coarse grained model for epitaxial growth. To fix ideas we first work in one dimension and consider very simple model. At each time step an adatom must hop. It will hop to the left or right with equal probability. We will consider the situation where the sites left of $j = 0$ are occupied by island atoms and there is no detachment. Note that $j = 1$

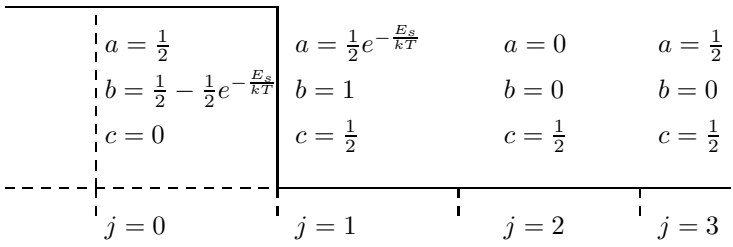

FIGURE 1. How the geometry determines a, b, and c.

is a potential attachment site. Let p_j^n represent the adatom concentration at site j at time n. The time evolution of p_j^n is then given by

$$p_j^{n+1} = \tfrac{1}{2}(p_{j+1}^n + p_{j-1}^n) + F \quad \text{for} \quad j = \ldots, -3, -2, -1 \tag{2.1}$$

$$p_0^{n+1} = \tfrac{1}{2}p_{-1}^n + F \tag{2.2}$$

$$p_1^{n+1} = p_1^n + \tfrac{1}{2}(p_2^n + p_0^n) + F \tag{2.3}$$

$$p_2^{n+1} = \tfrac{1}{2}p_3^n + F \tag{2.4}$$

$$p_j^{n+1} = \tfrac{1}{2}(p_{j+1}^n + p_{j-1}^n) + F \quad \text{for} \quad j = 3, 4, 5, \ldots. \tag{2.5}$$

Eqs. (2.1) and (2.5) describe the adatom hopping on top of the island and below the island respectively and away from the step. This can be understood from the fact that adatoms can hop into these sites from either the left or right. Since the attachment is irreversible, Eqs. (2.2) and (2.4) will not have any contribution from the attachment site ($j = 1$). Finally since $j = 1$ is an attachment site any adatoms that arrive there cannot leave. This is reflected in the first term in Eq. (2.3). Therefore, p_1^n represents the net mass of adatoms at the attachment site.

The expression for p_j^n can be written as

$$p_j^{n+1} = a_j p_{j+1}^n + b_j p_j^n + c_j p_{j-1}^n + F$$

where a_j b_j, and c_j are determined by the environment, as shown in Figure 2. A flux of adatoms has now been included with the F term. We can modify this formulation to include an Ehrlich-Schwoebel Barrier [15]. In this case, a_j, b_j and c_j are determined as shown in Figure 2. We can rewrite the evolution equation as

$$p_j^{n+1} - p_j^n = a_j p_{j+1}^n + (b_j - 1)p_j^n + c_j p_{j-1}^n + F. \tag{2.6}$$

We make the assumption that p is slowly varying in time and use the following approximation:

$$\frac{d}{dt}p_j \approx p_j^{n+1} - p_j^n$$

and write (2.6) as

$$\frac{d}{dt}p_j(t) = a_j p_{j+1}(t) + (b_j - 1)p_j(t) + c_j p_{j-1}(t) + F.$$

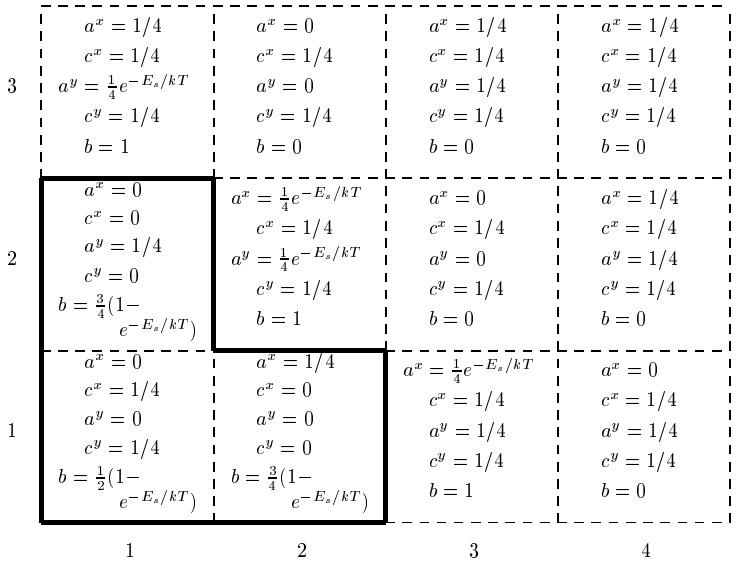

FIGURE 2. Computation of a, b and c in two dimensions.

We can easily extend this to two space dimensions, as follows:

$$\frac{d}{dt}p_{i,j} = \Delta p_{i,j} + F \tag{2.7}$$

where

$$\Delta p_{i,j} \equiv a^x_{i,j}p_{i-1,j} + c^x_{i,j}p_{i+1,j} + a^y_{i,j}p_{i,j-1} + c^y_{i,j}p_{i,j+1} + (b_{i,j} - 1)p_{i,j} + F$$

where a, b and c are determined by the environment as shown in Figure 2.

A formulation similar to this was developed in one dimension by E and Schulze [8] and by Mandreoli et al. [9]. In both these approaches an adatom is added to an island edge when the attachment probability exceeds one. Therefore these models are deterministic and consequently ignore fluctuations. Indeed, in Ref. [9] the authors report not being able to obtain fractal island shapes.

In our approach we attach adatoms probabilistically. Let A represent all potential attachment sites. Then

$$P = \sum_{(i,j)\in A} p^n_{i,j}$$

represents the total mass of adatoms in the attachment sites. When the integer part of P exceeds unity then then we add L adatoms to attachment sites where $L = [P]$ (L is the integer part of P) The attachment location is chosen at random with a probability proportional to p^n_i.

2.1. Edge diffusion and detachment

The effects of edge diffusion and detachment are incorporated by using KMC on the edge atoms (atoms with less than 4 in-plane bonds). The difficulty with this procedure is that these atoms may hop off the island at which point they should become part of the adatom sea. To incorporate these adatoms we place a source term concentrated at the point of detachment with a strength equal to $1/\Delta t$ where Δt is the time step.

2.2. Nucleation

For nucleation we use a variant of the nucleation model introduced in [4, 5]. In this model adatoms are removed at a rate $2\sigma_1 \sum_{i,j}(p^n_{i,j})^2$ from the adatom field. σ_1 is the capture rate and its computation is discussed in Refs. [17, 3, 19]. Using the approach taken in [19], the capture number typically takes on values of 3 ± 1 for situations we are simulating. Empirical results from our simulations show little dependence on σ_1 over such a variation; thus, in our computations we take $\sigma_1 = 3$. When this exceeds unity, dimer(s) are added to the surface. The location of the dimer is chosen at random with a probability proportional to $p^2(x,t)$. Due to detachment, the adatom concentration is will be high near the interface. To reduce the effects of an adatom nucleating with itself we only allow nucleation in a region at least two grid cells from the interface. We call this region Ω.

3. The algorithm

Step 1. Compute $\Delta p_{i,j}$ as described in Figure 2 and solve the diffusion equation implicitly for one time step from t_n to $t_{n+1} = t_n + \Delta t$.

$$\dot{p}_{i,j} = \Delta p_{i,j} + F - 2\sigma_1 \sum_{(i,j)\in\Omega} (p^n_{i,j})^2 + \frac{1}{\Delta t} \sum_{(i,j)\in D} \delta_{i,j} \tag{3.1}$$

the updated value of p is denoted p^{n+1} and Ω is defined in §2.2. The diffusion equation is solved implicitly using operator splitting. D is the set of detachment sites and is computed in Step 3.

Step 2. Identify all the attachment sites and then compute

$$P = P^* + \sum_{(i,j)\in A} p^{n+1}_{i,j}$$

where P^* is defined below. If $P > 1$ then $L = [P]$ adatoms are attached. The location is chosen at random with a probability distribution based on the values of p at the attachment sites. This performed using rejection Monte Carlo. Then set $P^* = P - L$ and $p_{i,j} = 0$ for $(i,j) \in A$.

Step 3. Now we execute KMC on the edge atoms. Suppose there are M edge atoms. Then we choose $M\Delta t$ edge atoms at random, and allow each to hop with probability $\exp(-nE_0/kT)$, where E_0 is the bond energy, and n is the number of in-plane nearest-neighbor bonds. If an atom hops to a site which is not adjacent

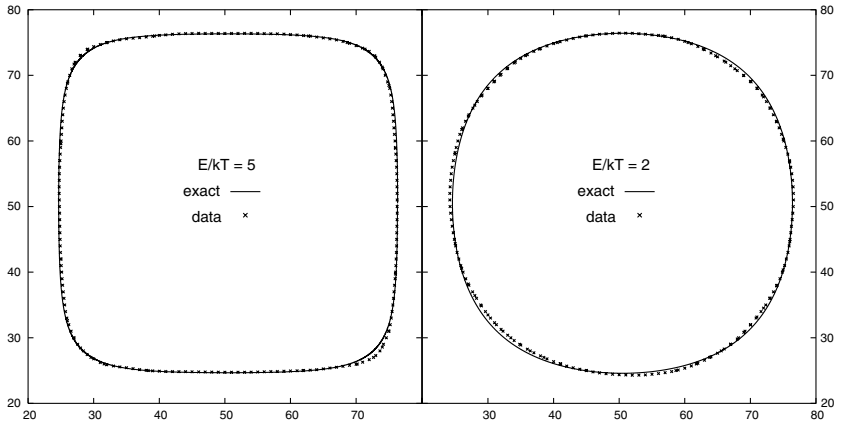

FIGURE 3. Our method produces equilibrium island shapes that closely match the exact shapes [18]. The plots are for E/kT of 5 (left) and 2 (right).

to an edge the we say it has detached. Denote the set of detachment sites by D. The set D is used in Step 1.

Step 4. Finally, we nucleate new islands, by introducing new dimers. The rate of dimer nucleation is given by the sum of $\sigma_1 p^2$ over all sites that are at least two grid point from an interface. The prefactor σ_1 represents the cross-section for adatom capture by another adatom.

4. Results

Our method produces accurate results for both submonolayer and multilayer growth.

4.1. Submonolayer growth

With the flux F set to 0 and the initial condition of a square island, we allowed the island to come to equilibrium with the surrounding adatoms. Figure 3 shows a comparison of QCMC generated equilibrium island shapes compared to exact solutions for two different temperatures. The exact solutions are according to [18]. The data is averaged over 80 and 200 realizations, for $E/kT = 5$ and $E/kT = 2$ respectively.

Figure 4 shows early growth (0.1ML) for two different growth regimes. One is grown at $E/kT = 3.5$ and produces compact islands. The other is at zero temperature, which produces dendritic islands. In both cases, QCMC compares qualitatively with KMC.

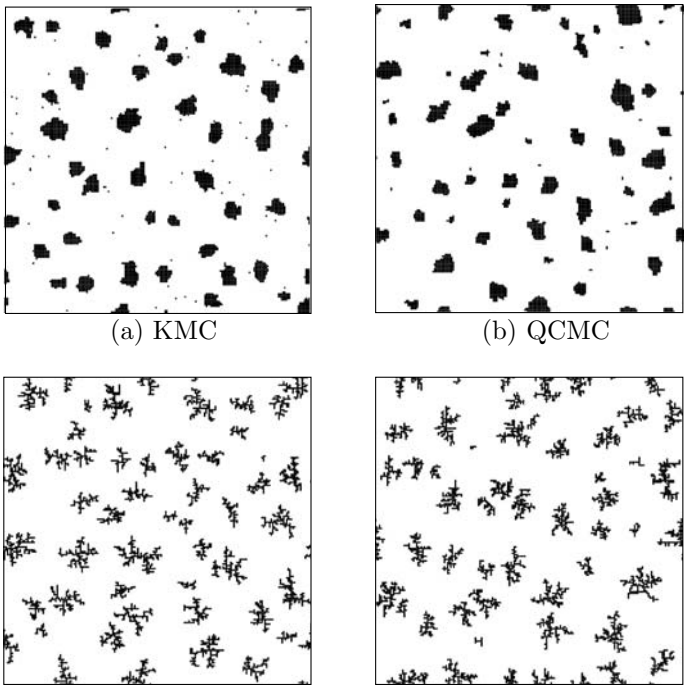

(a) KMC (b) QCMC

(c) KMC (d) QCMC

FIGURE 4. Submonolayer growth, comparing KMC to QCMC, for two different growth regimes. Figures (a) and (b) were grown at $D/F = 2.5 \times 10^5$, $E/kT = 3.5$, for 0.1ML. Figures (c) and (d) were grown at $D/F = 5 \times 10^6$, $T = 0$, for 0.1ML. QCMC and KMC produce qualitatively similar results for growth of both compact and dendritic islands.

4.2. Multilayer growth and mounding

An interesting case of multilayer growth is development in the presence of an Ehrlich-Schwoebel (ES) barrier, which can produce mounding [20, 21]. The fundamental process is that the barrier traps adatoms on the top of islands, and leads to nucleation there, so that the growth cannot be layer-by-layer. Figure 5 shows KMC and QCMC results for multilayer growth with no ES barrier. Figure 6 shows a comparison of KMC and QCMC for multilayer growth involving barrier-induced mounding. We qualitatively reproduce the KMC patterns.

Acknowledgment

This work is supported by the National Science Foundation. JPD and PS were supported by NSF grant number DMS 0207402. LMS and PS were supported by NSF grant number DMS 0244419.

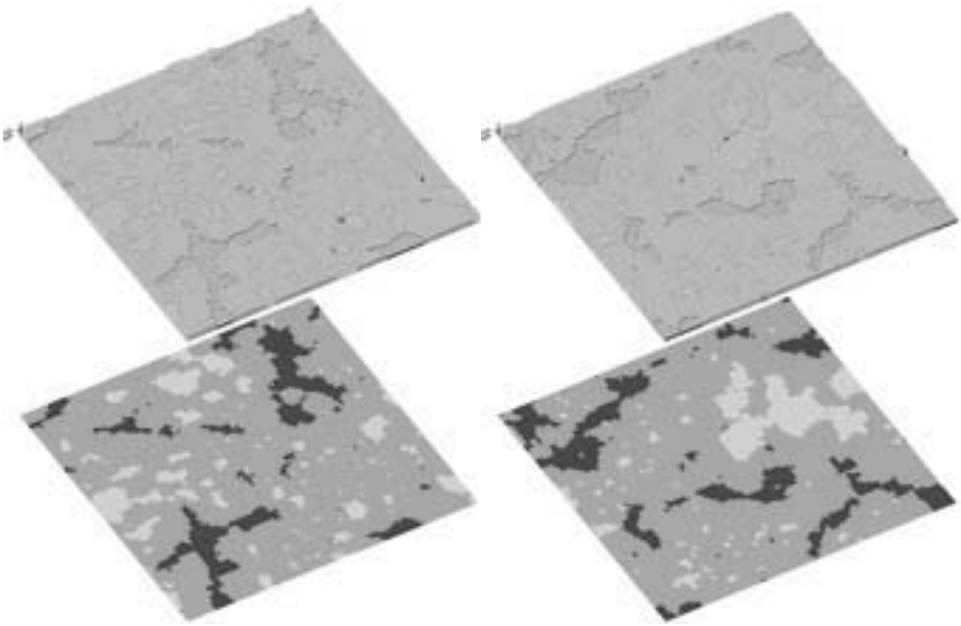

(a) KMC (b) QCMC

FIGURE 5. KMC versus QCMC for no ES barrier, $E_0/kT = 3.5$, $F = 0.5 \times 10^{-4}$, 50 monolayers.

References

[1] W.K. Burton, N. Cabrera, and F.C. Frank, *The growth of crystals and the equilibrium structure of their surfaces*, Trans. R. Soc. London Ser. A **243** (1951), 299–358.

[2] R. Ghez and S.S. Iyer, *The kinetics of fast steps on crystal surfaces and its application to molecular beam epitaxy of silicon*, IBM J. Res. Develop. **32** (1988), 804-818.

[3] M.F. Gyure, C. Ratsch, B. Merriman, R.E. Caflisch, S. Osher, J.J. Zinck, D.D. Vvedensky, *Level-set methods for the simulation of epitaxial phenomena*, Phys. Rev. E **58** R6927 (1998).

[4] S. Chen, B. Merriman, M. Kang, R.E. Caflisch, C. Ratsch, L.T. Cheng, M. Gyure, R.P. Fedkiw, C. Anderson S. Osher, *Level set method for thin film epitaxial growth*, J. of Comput. Phys. **167** (2001), 475–500.

[5] C. Ratsch, M.F. Gyure, R.E. Caflisch, F. Gibou, M. Petersen M. Kang, J. Garcia, D.D. Vvedensky, *Level-set method for island dynamics in epitaxial growth*, Phys. Rev. B **65** 195403 (2002).

[6] M. Petersen, C. Ratsch, R.E. Caflisch and A. Zangwill, *Level set approach to reversible epitaxial growth*, Phys. Rev. B **64** 061602 (2001).

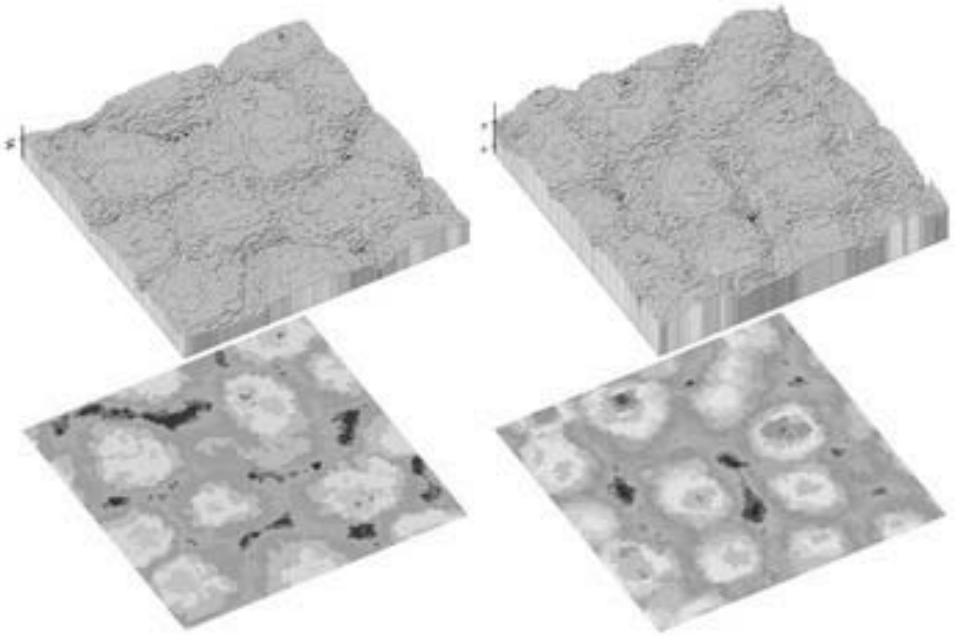

(a) KMC (b) QCMC

FIGURE 6. KMC versus QCMC for $E_s/kT = 1.26$, $E_0/kT = 3.5$, $F = 1.5 \times 10^{-4}$, 90 monolayers.

[7] J. Tersoff, M.D. Johnson, and B.G. Orr, *Adatom densities on GaAs: evidence for near-equilibrium growth*, Phys. Rev. Lett. **78** (1997), 282–285.

[8] T.P. Schulze and W. E, *A continuum model for the growth of epitaxial films*, J. Cryst. Growth, **222** (2000) 414–425.

[9] L. Mandreoli, J. Neugebauer, R. Kunert, and E. Schöll, *Adatom density kinetic Monte Carlo: A hybrid approach to perform epitaxial growth simulations*, Phys. Rev. B. **68**, 155429 (2003).

[10] C. Ratsch, M. Kang and R.E. Caflisch, *Atomic size effects in continuum modeling*, Phys. Rev. E **64** 020601(R) (2001).

[11] T.A. Witten and L.M. Sander, *Diffusion-Limited Aggregation, a Kinetic Critical Phenomenon*, Phys. Rev. Lett. **47** (1981), 1400–1403.

[12] T.P. Schulze, P. Smereka, W. E, *Coupling kinetic Monte Carlo and continuum models with application to epitaxial growth*, J. Comput. Phys. **189** (2003) 197–211.

[13] T.P. Schulze, *A hybrid method for simulating epitaxial growth*, J. Cryst. Growth, to appear.

[14] G. Russo, L.M. Sander, P. Smereka, *Quasicontinuum Monte Carlo: A method for surface growth simulations*, Phys. Rev. B **69** 121406(R) (2004).

[15] G. Ehrlich, F. Hudda, *Atomic view of surface self-diffusion: tungsten on tungsten*, J. Chem. Phys. **44** (1966), 1039–1099. R.L. Schwoebel, E. J. Shipsey, *Step motion on crystal surfaces*, J. Appl. Phys. **37** (1966) 3682–3686.

[16] L. Niemeyer, L. Pietronero, H.J. Wiesmann, *Fractal Dimension of Dielectric Breakdown* Phys. Rev. Lett. **52** (1984), 1033–1036.

[17] J.A. Venables, *Rate equation approaches to thin film nucleation kinetics.*, Phil. Mag. **27** (1973), 697–738.

[18] C. Rottman, M. Wortis, *Exact equilibrium crystal shapes at nonzero temperature in two dimensions*, Phys. Rev. B **24** (1981), 6274–6277.

[19] G.S. Bales, D.C. Chrzan, *Dynamics of irreversible island growth during submonolayer epitaxy*, Phys. Rev. B **50** (1984), 6057–6067.

[20] M.D. Johnson, C. Orme, A.W. Hunt, D. Graff, J. Sudijono, L.M. Sander, B.G. Orr, *Stable and unstable growth in molecular beam epitaxy*, Phys. Rev. Lett. **72** (1994), 116–119.

[21] J.G. Amar and F. Family, *Mound Formation, Coarsening and Instabilities in Epitaxial Growth*, Surface Rev. and Lett. **5** (1998), 851-864.

Jason P. DeVita
Department of Physics
University of Michigan
Ann Arbor, MI, 48109-1120, USA
e-mail: `jdevita@umich.edu`

Leonard M. Sander
Department of Physics
and Michigan Center for Theoretical Physics
University of Michigan
Ann Arbor, MI, 48109-1120, USA
e-mail: `lsander@umich.edu`

Peter Smereka
Department of Mathematics
and Michigan Center of Theoretical Physics
University of Michigan
Ann Arbor, MI 48109-1109, USA
e-mail: `psmereka@umich.edu`

Part 2

Step Flow Models

International Series of Numerical Mathematics, Vol. 149, 69–95

Introduction to Step Dynamics and Step Instabilities

Joachim Krug

Abstract. This paper provides an elementary introduction to the basic concepts used in describing epitaxial crystal growth in terms of the thermodynamics and kinetics of atomic steps. Selected applications to morphological instabilities of stepped surfaces are reviewed, and some open problems are outlined.

Mathematics Subject Classification (2000). Primary 80A22; Secondary 35R35.

Keywords. Crystal growth; step flow; vicinal surfaces; morphological stability.

1. Introduction

The hallmark of a crystalline solid is the discrete translational symmetry imposed by the crystal lattice. At the surface of a crystal, this leads to the existence of atomic *steps*, which separate exposed lattice planes (*terraces*) that differ in height by a single lattice spacing. At sufficiently low temperatures, steps are thermodynamically stable, in the sense that the creation of a new step segment entails a positive free energy cost per unit length of the step. Thus steps are long-lived surface defects, which makes them suitable as a basis for the description of the surface morphology on an intermediate (*mesoscopic*) scale, between atomistic and macroscopic levels of modeling.

In crystal growth, steps play a central role because they provide the *kink* sites at which new atomic units are incorporated into the crystal (see Fig. 1). The growth of a crystal surface can thus be reduced to the advancement of existing steps, the nucleation of new closed step loops (i.e., atomic height *islands*), and the annihilation of steps by the merging of islands and terraces. This point of view was pioneered by Burton, Cabrera and Frank (BCF) in their classic 1951 paper [1]. The exchange of matter between the steps and the population of adsorbed atoms

This work was supported in part by DFG within SFB 237 *Unordnung und grosse Fluktuationen* and SFB 616 *Energiedissipation an Oberflächen.*

(*adatoms*) on the terraces implies that the step motion has to be formulated as a moving boundary problem. With the advent of powerful numerical techniques for the solution of such problems, step dynamics has become an attractive alternative to atomistic modeling approaches in epitaxial crystal growth. Recent progress along these lines is described in many contributions to this volume.

The main purpose of the present article is to introduce the basic concepts used in the step-dynamical approach to crystal growth. Since this approach is most useful when the number of steps is conserved, i.e., in the absence of island nucleation and merging, we will largely restrict ourselves to the growth on stepped (*vicinal*) surfaces. In Sections 2 and 3 we will present the fundamental thermodynamic and kinetic notions in a reasonably self-contained manner, with considerable attention to physical assumptions and approximations that enter into the construction of the model. Sections 4 and 5 provide a brief overview of applications to morphological instabilities of stepped surfaces. Here the discussion will be rather cursory, but key references will be given to guide the reader into the extensive literature. In the final section we try to formulate some challenges for the future. General introductions to the subject can be found, e.g., in [2, 3, 4].

2. Thermodynamics of steps

The fundamental abstraction of the step-dynamical approach is the replacement of the microscopic step conformation, which is a (possibly very convoluted) path on the discrete surface lattice, by a smooth curve in continuous space. At least locally, the step can then be described by the graph of a function $y(x)$ (Fig. 1).

2.1. Step free energy and step stiffness

The thermodynamic properties of a single step are contained in the step free energy per unit length δ which, because of the underlying crystal structure, is generally a function $\delta(\theta)$ of the in-plane step orientation angle θ (see Fig. 1). The step is a long-lived, thermodynamically stable object as long as $\delta > 0$. At the thermal roughening transition of the surface the step free energy vanishes. Above the roughening transition temperature T_R steps proliferate and a description of the surface in terms of isolated steps and flat terraces is no longer possible. The concept of a roughening transition was first conceived by BCF [1], but the nature of the transition was clarified only much later, in the seventies of the past century [5, 6]. For applications to epitaxial growth the roughening transition is of little importance, as the growth processes of interest usually proceed far below T_R.

Given the function $\delta(\theta)$, the free energy F of an arbitrary step configuration $y(x)$ is obtained by integrating along the step,

$$F = \int ds\, \delta(\theta(s)) = \int dx\, \sqrt{1 + (dy/dx)^2}\, \delta(\theta(x)), \tag{2.1}$$

where s denotes the arc length along the step and $\theta(x) = \arctan(dy/dx)$. From (2.1) the *step chemical potential*, i.e., the free energy change upon adding an atom

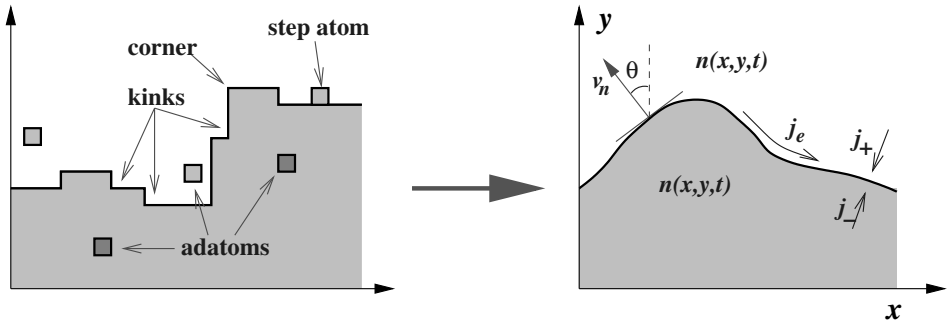

FIGURE 1. *Left panel*: Sketch of a step on a crystal surface of fourfold symmetry. The upper terrace is shaded. The step consists of straight (close packed) segments separated by kinks and corners. Adatoms diffuse on the terraces and can be incorporated into the crystal by attaching at kinks sites. An atom moving along a straight segment of the step is called a step atom. *Right panel*: In the step-dynamical treatment the discrete lattice step is replaced by a smooth curve $y(x)$. The local step orientation is described by the angle θ between the step normal and the y-axis. The step moves at speed v_n along the normal direction. The adatom diffusion field $n(x, y, t)$ is defined on both the upper and lower terrace, but it may be discontinuous across the step (see Fig. 3). Step atoms contribute to the step edge current j_e, while terrace adatoms attaching to, detaching from, or crossing the step are contained in the mass currents j_+ and j_-.

to the step, can be derived by functional differentiation. This yields the expression

$$\mu = \Omega \frac{\delta F}{\delta y} = \Omega \tilde{\delta} \kappa, \tag{2.2}$$

where Ω denotes the area occupied by a surface atom, κ is the step curvature, and the quantity $\tilde{\delta} = \delta + d^2\delta/d\theta^2$ is known as the *stiffness* of the step. The step stiffness appears in a local version of the Wulff construction, which relates the step free energy to the equilibrium shape of two-dimensional islands [4, 6]. In this formulation the equilibrium condition reads simply

$$\tilde{\delta}\kappa = \text{const.}, \tag{2.3}$$

i.e., the local curvature of the equilibrium shape is inversely proportional to the local step stiffness.

The calculation of $\delta(\theta)$ for a specific system requires the application of equilibrium statistical mechanics to a microscopic model of the surface. A popular microscopic model is the Ising lattice gas, where each site of the surface lattice is either vacant or occupied and the energy of a configuration is obtained by summing over all pairs of occupied nearest neighbor sites. A simple, model-independent

expression for the step stiffness is obtained for steps along the close-packed (= minimal energy) directions of the lattice at low temperatures. Such steps consist of straight close-packed segments interspersed by a small concentration of kinks. Elementary statistical mechanics considerations then show that [4]

$$\tilde{\delta} \approx \frac{k_{\mathrm{B}}T}{2a} e^{\epsilon/k_{\mathrm{B}}T}, \tag{2.4}$$

where k_{B} denotes Boltzmann's constant, T is the temperature, a the in-plane lattice spacing, and ϵ is the energy cost of a kink.

2.2. Step roughness

The existence of a roughening transition for two-dimensional surfaces, which was briefly mentioned in the preceding subsection, is due to the fact that steps are extended, one-dimensional objects. As a consequence the free energy of a step increases with its length (provided $\delta > 0$), and the free energy cost for the spontaneous creation of a macroscopic piece of a step becomes prohibitively large. In contrast, the creation of a kink on a one-dimensional step requires only a fixed energy amount ϵ, and hence a step contains a finite kink concentration at any nonzero temperature. This implies that the step is *rough* whenever $T > 0$: A typical step conformation looks like the graph of a one-dimensional random walk, with a diffusivity proportional to the kink concentration. Assuming that the step is on average aligned with the x-axis, the roughness can be quantified by the height-difference correlation function

$$\langle [y(x) - y(x')]^2 \rangle = \frac{k_{\mathrm{B}}T}{\tilde{\delta}} |x - x'|. \tag{2.5}$$

Here the angular brackets refer to a thermal average with respect to the equilibrium distribution. The relation (2.5) has been widely exploited to derive, via (2.4), experimental estimates for the kink energy ϵ from scanning tunnelling microscopy observations of step fluctuations [7, 8].

A thermodynamic consequence of step roughness is that the step free energy $\delta(\theta)$ cannot contain any singularities. Via the Wulff construction [1, 6], this implies that the corresponding equilibrium island shapes have finite curvature everywhere [compare to (2.3)], and hence display no corners or "facets" in the thermodynamic limit (of course, islands of a size comparable to or smaller than the mean distance between kinks nevertheless have atomically straight edges). This is in contrast to the three-dimensional case, where cusps in the Wulff-plot of the *surface* free energy lead to facets in the equilibrium crystal shape [6, 9].

2.3. Step-step interactions

So far we have considered a single atomic step in isolation. To understand the thermodynamics and kinetics of stepped surfaces, which consist of an array of parallel steps of equal sign (see Fig. 4), it is crucial to take into account also the interactions between the steps. An important source of interaction is the very fact that steps are thermally rough. As was first noted by Gruber and Mullins [10], in an array of parallel steps the thermal wandering of a given step is impeded

by collisions with its neighbors (since the steps cannot cross). This reduces the entropy of the step, thus increasing its free energy and leading to an effective repulsion between the steps.

It is straightforward to estimate the strength of the repulsion from (2.5). Suppose the average distance between the steps (along the perpendicular y-direction) is l. Then the *collision length* L_c, the distance between close encounters of two steps measured along the parallel x-direction, is obtained by setting the left-hand side of (2.5) equal to l^2 and inserting L_c for $|x - x'|$. This yields $L_c \approx \tilde{\delta} l^2/(k_{\mathrm{B}}T)$. Assuming a fixed entropy loss $k_{\mathrm{B}}C$ per collision, the free energy of the step is then increased by an amount

$$\Delta\delta \approx \frac{Ck_{\mathrm{B}}T}{L_c} = \frac{C(k_{\mathrm{B}}T)^2}{\tilde{\delta} l^2}. \tag{2.6}$$

The coefficient C can be evaluated for a model in which the steps are represented as world lines of non-interacting fermions (subject only to the non-crossing constraint), which yields $C = \pi^2/6$ [11].

The important feature of (2.6) is that the step interactions decay quite slowly with step distance, as l^{-2}. There is extensive experimental support for this interaction law from scanning tunnelling microscopy measurements of the distribution of step spacings on vicinal surfaces [7, 8]. However, the interaction strength is typically found to be considerably larger than predicted by the purely entropic expression (2.6). This is because elastic interactions between the strain fields associated with the steps, mediated through the bulk crystal, display the same l^{-2} decay law, and typically dominate the entropic interactions. Electrostatic dipoles associated with the steps also lead to an l^{-2}-interaction. A macroscopic consequence of the l^{-2}-repulsion is the singular behavior $z(y) - z(y_0) \sim (y - y_0)^{3/2}$ of the height of the equilibrium crystal shape $z(y)$ near a facet edge at $y = y_0$ [5, 6, 9].

3. Step dynamics as a moving boundary problem

Within the step dynamical picture, a step is a mathematically sharp boundary that evolves by exchanging mass with the continuous adatom concentration field $n(x, y, t)$ on the terraces. Thus the formulation of a step dynamical model requires, first, the specification of the dynamics of the adatom concentration, and, second, the formulation of boundary conditions for n at the steps. Whereas the first part is quite straightforward, the second contains a number of (explicit and implicit) assumptions about the underlying microscopic physics. As the formulation of the appropriate boundary conditions constitutes a central part of the step-dynamical modeling approach, we will discuss these issues in considerable detail.

3.1. Adatom dynamics

We want to describe physical situations where atoms arrive at the surface with a deposition flux F, diffuse over the terraces with a surface diffusion coefficient

D, and possibly desorb back into the vacuum at rate $1/\tau$. In some cases it is also of interest to include a directed force $\vec{f}$ acting on the adatoms due to an electric current in the bulk of the sample (*surface electromigration*) [12, 13, 14]. Together these processes imply the evolution equation

$$\frac{\partial n}{\partial t} = D\nabla^2 n - \frac{D}{k_{\rm B}T}\vec{f}\cdot\nabla n + F - \frac{n}{\tau} = -\nabla\cdot\vec{J} + F - \frac{n}{\tau} \tag{3.1}$$

for the adatom concentration field. Here the adatom current $\vec{J}$ has been introduced, which is generally driven by the concentration gradient as well as by the electromigration force. The coefficient $D/k_{\rm B}T$ in front of the drift term is the adatom mobility, which is related to the diffusion coefficient through the Einstein relation.

The motion of the steps is often slow compared to the time scale on which the adatom concentration changes, so that (3.1) can be solved quasistatically, setting $\partial n/\partial t = 0$. To see when this approximation is justified, consider for concreteness the case of growth, and suppose that the typical distance between steps is l. Then the step velocity is of the order $v \sim F\Omega l$, which is to be compared to the diffusion velocity $v_D \sim D/l$, the effective speed of an atom diffusing over the distance l [15]. The quasistatic approximation holds if $v \ll v_D$ or

$$l \ll (D/\Omega F)^{1/2}. \tag{3.2}$$

This condition is essentially always fulfilled, because nucleation of new islands creates steps at typical distances $l_D \sim (D/F)^\chi$, where $\chi < 1/2$ [4], and hence the step density is usually much larger than required according to (3.2). The situation is different in the presence of an electromigration force, because then also the drift velocity $v_{\rm drift} = (D/k_{\rm B}T)|\vec{f}|$ of the adatoms would be required to be large compared to V; since the electromigration force is very weak, this condition is not necessarily satisfied [16] (see also Sect. 3.8). In the following we nevertheless adhere to the quasistatic approximation.

3.2. Kinetic processes at the step

The interaction of adatoms with steps involves the following microscopic processes [17, 18, 19] (see Fig. 2):

- *Attachment and detachment.* It is important to note that these processes actually consist of two stages: When attaching to the step, an adatom first attaches to a straight step segment and then moves along the segment until it reaches a kink, where it is incorporated; similarly a detachment event requires first that an atom detaches from a kink to the straight step, and subsequently detaches from the step segment onto the terrace.
- *Step crossing.* The foregoing remark implies that an atom may also cross a step without attaching to a kink; this happens if the kink concentration is low and the binding to the straight step weak, so that the step atom detaches from the straight step before a kink is encountered.

- *One-dimensional nucleation* [20]. If two step atoms are present simultaneously on a straight segment of the step, they can meet and form a step dimer, which is essentially a pair of kinks of opposite sign. This provides a nonequilibrium mechanism for the creation of kinks, in addition to the thermally excited kinks that are present in equilibrium (see Sect. 2.2). If step atoms cannot detach onto the terrace, the typical distance between kinks created by one-dimensional nucleation is

$$l_{1\mathrm{d}} \sim \left(\frac{D_{\mathrm{e}}}{F_{1\mathrm{d}}}\right)^{1/4}, \tag{3.3}$$

  where D_{e} is the diffusion coefficient of a step atom along a straight step segment, and $F_{1\mathrm{d}}$ is the one-dimensional flux impinging onto the step from the terrace [21, 22]. Generalizations of (3.3) to other conditions can be found in [17, 20, 23].
- *Diffusion along a rough step.* Since steps always contain a finite concentration of kinks (of equilibrium or nonequilibrium origin), mass transport by step edge diffusion requires that step atoms are able to cross kinks and corners. The diffusion along a rough step is therefore considerably slower than the diffusion along a straight step segment. As indicated in Fig. 2, a step atom crossing a kink "from above" first has to round the kink and then detach from it onto the step. Kink rounding is often associated with an additional energy barrier [24, 25, 26].

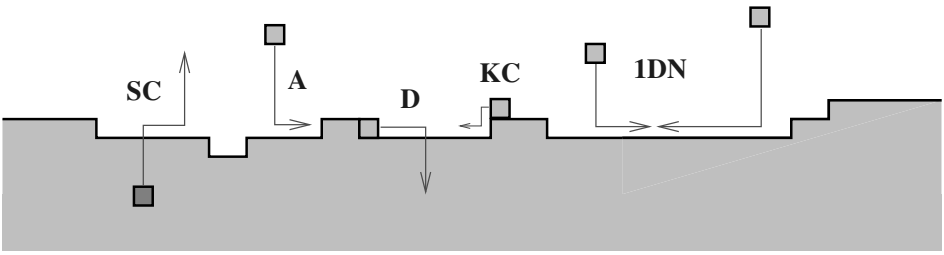

FIGURE 2. Atomic processes at a step: Attachment (A) and detachment (D) of terrace atoms; step crossing (SC); kink crossing (KC); and one-dimensional nucleation (1DN). As in Fig. 1, the upper terrace is shaded.

3.3. Linear constitutive relations

Within the step dynamical model, the diverse and rather complex processes described in the preceding subsection are lumped together into the net mass currents j_+ and j_- from the lower and upper terrace, respectively, and the edge diffusion current j_e (see Fig. 1). In the spirit of linear nonequilibrium thermodynamics, these currents are assumed to be linear in the adatom concentration gradients and

differences. Consider first the edge diffusion current j_e, which counts the number of atoms that pass a point on the step in unit time. It is of the form

$$j_e = -\sigma \frac{\partial \mu}{\partial s}, \tag{3.4}$$

a relation that can be taken to define the *mobility* σ of an edge atom along a (rough, curved) step [26, 27]. It is important to keep in mind that (3.4) includes only that part of the mass transport along the step that is induced by differences in the step chemical potential, and hence serves to restore thermal equilibrium at the step. In addition, there are genuinely nonequlibrium contributions to the current that arise from the combined effects of attachment, step edge diffusion and kink rounding barriers [24, 25, 28, 29].

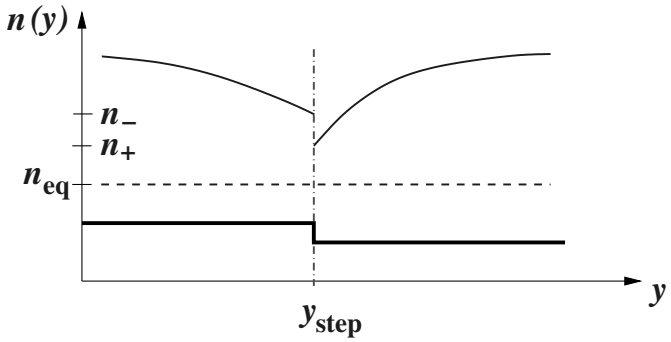

FIGURE 3. Behavior of the adatom concentration near a step.

Figure 3 illustrates how the adatom concentration changes across a step. At each point of the step, three different values of n can be defined: The limiting value n_+ (n_-) attained by the terrace concentration field $n(x, y)$ when approaching the step from the lower (upper) terrace, and the equilibrium step atom concentration $n_{\rm eq}$ which would be established in the absence of growth, through the detachment of atoms from thermally excited kinks. The mass currents j_+ and j_- that leave a terrace via the ascending and descending step, respectively, are now written as linear combinations of the differences between these adatom concentrations, in the form (see, e.g., [16])

$$j_+ = k_+(n_+ - n_{\rm eq}) + p(n_+ - n_-) \tag{3.5}$$

and

$$j_- = k_-(n_- - n_{\rm eq}) - p(n_+ - n_-). \tag{3.6}$$

The first term on the right-hand side of (3.5) is the net current of terrace atoms that attach to the step from below, while the second term is the current of atoms that cross the step without attaching to it. The first contribution is driven by the deviation of the adatom concentration from its equilibrium value, while the

second contribution is driven by the difference of the adatom concentrations on the two terraces. Similar considerations apply to the current (3.6) from the upper terrace. The kinetic coefficients k_+ and k_- are known as *attachment rates*, while the coefficient p is referred to as the *step permeability*; see Sects. 3.6 and 3.7 for further discussion of physical effects related to these quantities. Usually all kinetic coefficients are assumed to be positive, but negative values can also be meaningful under certain conditions [30] (see Sect. 4.3). The symmetry between the step crossing terms in (3.5) and (3.6) can be viewed as a consequence of the Onsager reciprocity relations [16].

The linearity of the constitutive relations (3.4, 3.5, 3.6) contains the implicit assumption that the step is close to equilibrium. There have been recent attempts to formulate kinetic models that do not require this assumption [18, 19], but the bulk of the work in the field relies on it. Detailed kinetic modeling is also needed to derive expressions for $k_\pm$ and p in terms of the rates of elementary atomic processes[1]. Here we follow the common practice and regard the kinetic coefficients in (3.5, 3.6) as phenomenological parameters.

3.4. Thermodynamic driving force

The thermodynamic driving forces that are responsible for restoring equilibrium enter (3.5, 3.6) through the equilibrium adatom concentration $n_{\rm eq}$, which is related to the (local) step chemical potential through the standard thermodynamic identity

$$n_{\rm eq} = n_{\rm eq}^0 e^{\mu/k_{\rm B}T} \approx n_{\rm eq}^0(1+\mu/k_{\rm B}T). \tag{3.7}$$

Here $n_{\rm eq}^0$ is the equilibrium adatom concentration at an isolated, straight step, and the second relation assumes that the deviations from this value are small. As was discussed in Sect. 2, the step chemical potential is affected by the step curvature [see (2.2)] and by the step-step interactions. To derive the latter contribution, we denote by $y_j(x)$ the position of the jth step in the (x,y)-plane, and assume (following Sect. 2.3) that the free energy of the step-step interaction (including both entropic and direct, elastic or electrostatic contributions) for two steps at a distance l is of the form $V(l) = A/l^2$, where A is the interaction strength. Then the contribution to the step chemical potential of step j from the interaction with the neighboring steps $j-1$ and $j+1$ is

$$\Delta\mu_j^{\rm int} = \frac{\partial}{\partial y_j}[V(y_{j+1}-y_j) + V(y_j - y_{j-1})] \tag{3.8}$$

and together with the curvature contribution the expression for the chemical potential of step j, to be inserted in (3.7), is

$$\mu_j = \Omega\tilde{\delta}\kappa_j + 2A\left[\frac{1}{(y_{j+1}-y_j)^3} - \frac{1}{(y_j-y_{j-1})^3}\right], \tag{3.9}$$

with κ_j denoting the curvature of step j. Note that all terms in (3.9) also depend on the coordinate x along the step.

[1]For the step edge mobility σ in (3.4) such a derivation has been achieved, see [26, 27].

3.5. Mass conservation

Once the mass currents $j_\pm$ have been fixed through the constitutive relations (3.5,3.6), the boundary conditions for the adatom concentration field as well as the evolution equations for the step follow simply from mass conservation. This requires, first, that the mass currents are continuous at the step, which means that the total terrace current $\vec{J}$ appearing on the right-hand side of (3.1) must be matched to the local currents $j_\pm$ at the steps. Thus

$$j_+ = D\vec{n} \cdot \left[\nabla n|_+ - \frac{1}{k_\mathrm{B}T} \vec{f} n \right] \tag{3.10}$$

and

$$j_- = -D\vec{n} \cdot \left[\nabla n|_- - \frac{1}{k_\mathrm{B}T} \vec{f} n \right], \tag{3.11}$$

where $\nabla n|_\pm$ are the values of the concentration gradient on the two sides of the step, and $\vec{n}$ is the unit vector normal to the step, which points towards the lower terrace. Together with (3.5,3.6), these equations constitute the boundary conditions for the solution of the (quasistatic) drift-diffusion equation for n.

The second consequence of mass balance is that the step moves in response to the net attachment current $j_+ + j_-$ (note that the contributions due to step crossing cancel), as well as due to the mass transport along the step. The normal velocity of the step is therefore given by

$$v_n = \Omega \left(j_+ + j_- - \frac{\partial j_e}{\partial s} \right). \tag{3.12}$$

This completes the derivation of the step-dynamical model.

3.6. The Ehrlich-Schwoebel effect

The attachment rates $k_\pm$ were introduced by Schwoebel in his seminal 1969 paper [31]. Schwoebel and Shipsey were the first to explore the consequences of attachment asymmetry ($k_+ \neq k_-$) for the stability of growing stepped surfaces [31, 32]. Their work was triggered by the field ion microscope observation of Ehrlich and Hudda that tungsten adatoms on tungsten surfaces tend to be reflected by descending step edges [33], which implies that $k_+ > k_-$. Therefore the preferential attachment to ascending steps, which is observed for many materials, is often referred to as the *(normal) Ehrlich-Schwoebel (ES) effect*.

For metal surfaces, the ubiquity of the normal ES effect is now fairly well established [4], but for semiconductor materials the situation is less clear. For example, for the Si(111)-surface, a detailed microscopy study of island nucleation near steps [34] provides evidence for an *inverse* ES effect ($k_+ < k_-$) at high temperatures, above the transition from the (7×7) to the (1×1) reconstruction, but at lower temperatures (below the transition) a study of electromigration-induced step and island motion [35] indicates that, on the contrary, $k_+ > k_-$.

3.7. Step permeability

The importance of step crossing processes for the evolution of the surface morphology has been realized only fairly recently. Step permeability in the sense of (3.5, 3.6) was first introduced in 1992 by Ozdemir and Zangwill [36]. The dimensionless ratio p/k_+, which is a measure for the probability that an atom crosses the step without being incorporated, can be quite large for semiconductor surfaces, where the incorporation process may be difficult because of reconstructions at the step. From an analysis of the relaxation of biperiodic gratings on Si(001) it was concluded that $p/k_\pm = 40 \pm 20$ for this system [37]. But also steps on metal surfaces can be highly permeable, as evidenced by the dramatic formation of steep pyramids on Al(110) [38], which cannot be explained without substantial transport across steps. In the fully permeable limit, $p \to \infty$, the finiteness of the current in (3.5, 3.6) forces the adatom concentration to be *continuous* at the steps. Some consequences of step permeability will be described in Sect. 4.3.

3.8. Kinetic lengths

Inserting the expressions (3.5) and (3.6) on the right-hand sides of (3.10) and (3.11), the boundary conditions are seen to identify gradients of the adatom concentration n, multiplied by D, with differences in n, multiplied by kinetic coefficients. As a consequence, the ratios of D to the kinetic coefficients naturally define the length scales

$$l_+ = \frac{D}{k_+}, \quad l_- = \frac{D}{k_-}, \quad l_0 = \frac{D}{p}, \tag{3.13}$$

which are collectively referred to as *kinetic lengths*. The kinetic lengths are useful in discussing the effects of step boundary conditions on the morphological evolution. For example, in assessing the importance of a conventional ES effect in growth, it is crucial to compare the typical terrace sizes to the kinetic length l_-; the ES effect is *strong*, and makes itself felt during the growth of the first few layers, if l_- is large compared to the terrace size [3, 4] (see also Sect. 4.1.1).

Similarly the comparison of the two terms inside the square brackets in (3.10) and (3.11) leads to the definition of the *electromigration length* [39]

$$\xi = \frac{k_\mathrm{B}T}{|\vec{f}|}, \tag{3.14}$$

and the discussion of non-quasistatic effects can be phrased in terms of a "Péclet-length"

$$\xi_P = \frac{D}{v}, \tag{3.15}$$

where v is the step velocity [16]. This is motivated by the fact that going to a frame moving with speed v introduces a convection term $v\nabla n$ in the stationary diffusion equation, which is of the same form as the electromigration term in (3.1). In general, the quasistatic approximation requires that all other relevant length scales are small compared to ξ_P.

4. Morphological stability

The solution of the moving boundary problem formulated in the preceding section in its full generality is a formidable challenge. For this reason much of the work in this area has been restricted to linear stability analysis of simple surface morphologies. The most important results will be summarized in this section.

4.1. Stability of growing and sublimating step trains

The basic instability modes of a regular step train – a vicinal surface with straight, equidistant steps – are illustrated in Fig. 4: Either the surface separates into regions of high step density (*step bunches*) and wide terraces, or the steps become wavy (*step meandering*). While the two modes are usually assumed to be mutually exclusive, there is experimental evidence from homoepitaxial growth that they may also coexist [40, 41].

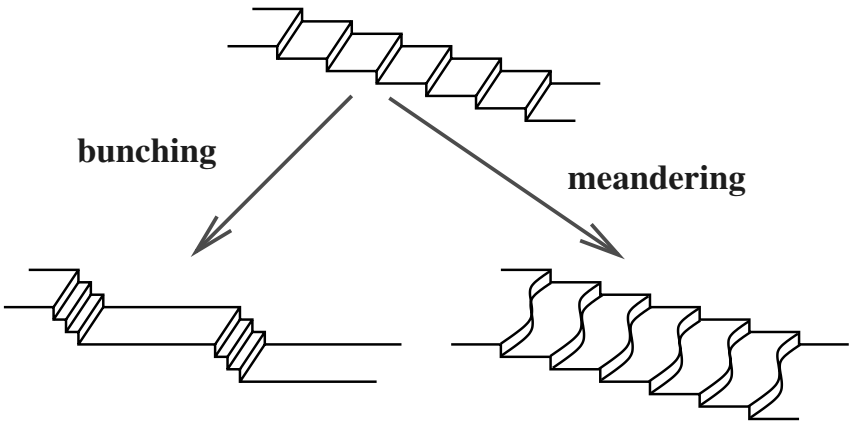

FIGURE 4. Instability modes of a vicinal surface.

4.1.1. Bunching of straight steps. The stability analysis is particularly simple if the steps can be assumed to remain straight, because then the dynamical problem reduces to a set of ordinary differential equations coupled along the y-direction. The basic stability results for straight, impermeable steps were derived by Schwoebel and Shipsey [31, 32], who showed that a growing step train is stabilized by a normal ES effect ($k_+ > k_-$) while the same effect leads to step bunching during sublimation; conversely, an inverse ES effect ($k_+ < k_-$) implies step bunching during growth. Explicitly, the equations of motion for the step positions y_j during growth are of the form

$$\frac{dy_j}{dt} = f_+(y_{j+1} - y_j) + f_-(y_j - y_{j-1}), \tag{4.1}$$

where f_+ and f_- denote the contributions from the leading and the trailing terrace, respectively, which are given by

$$f_\pm(l) = \frac{F\Omega l}{2} \frac{2l_\mp + l}{l_+ + l_- + l}. \tag{4.2}$$

Here the effects of step-step interactions arising from the step chemical potential (3.9) have been neglected. A straightforward linear stability analysis of (4.1) shows that the equidistant step train is stable provided $d[f_+(l) - f_-(l)]/dl > 0$, which, using the explicit expression (4.2), is seen to be equivalent to $k_+ > k_-$. The functional form of (4.2) illustrates the role of the kinetic lengths $l_\pm$ in gauging the strength of the attachment asymmetry: When the terrace size $l \gg l_\pm$ the attachment kinetics becomes effectively symmetric and $f_+ \approx f_- \approx F\Omega l/2$.

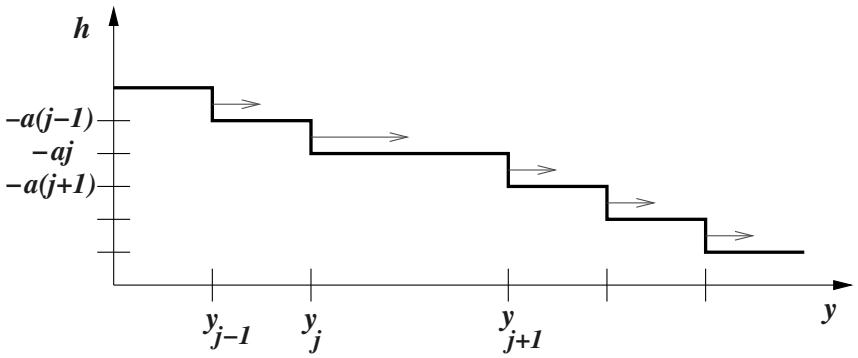

FIGURE 5. Stabilization of a configuration of equidistant, straight steps by a normal ES effect. Step j receives most of its flux from the leading terrace $y_j < y < y_{j+1}$. It therefore moves faster than the neighboring steps, and the step spacing is equalized. In our notation the terrace in front of step j, measured from an arbitrary reference level, is at height $h = -aj$, where a is the (vertical) lattice constant.

The stabilization of the growing step train by the normal ES effect is illustrated in Fig. 5. Formally it can be interpreted in terms of an effective step-step repulsion mediated by the diffusion field on the terraces. This repulsion is very efficient, in the sense that it leads to terrace width fluctuations that are much smaller than the corresponding fluctuations in thermal equilibrium [42, 43].

The fact that a normal ES effect stabilizes the regular step spacing implies that step bunching during growth – which is actually observed rather frequently in experiments – requires a separate mechanism for its explanation. It has been realized for a long time that impurities may cause step bunching during growth [44, 45, 55]. Recently it was pointed out by Pimpinelli and coworkers that step bunching can also be induced if the diffusing species that is incorporated during growth (e.g., the adatoms) is coupled to a second species, which could be a

chemical precursor in the case of chemical vapor deposition [47] or highly mobile dimers [48]. Using a two-species generalization of BCF theory, it can be shown that under suitable conditions a normal ES effect for the second species implies an effective inverse ES effect for the growth species, and hence causes step bunching. On reconstructed surfaces such as Si(001) the pronounced anisotropy of terrace diffusion can also cause step bunching [49]. Finally, through a subtle coupling to a preceding meandering instability, fast edge diffusion has been predicted to provide a mechanism for step bunching [28]. This last scenario seems consistent with the combined meandering and bunching instability observed for Cu(100) [40, 41].

4.1.2. Step meandering. Bales and Zangwill (BZ) first showed that a normal ES effect induces step meandering during growth [50]. Because of the effective step-step repulsion, the meander can be most easily accommodated if the steps meander in phase, as indicated in Fig. 4. Within the linear stability analysis, this implies that the in-phase meander is the mode with the largest growth rate [51]. A fundamental result of the BZ analysis is a prediction for the meander wavelength in the initial stage of the instability. In the absence of desorption but taking into account edge diffusion, the relevant expression reads [53]

$$\lambda_{\mathrm{BZ}} = 4\pi \sqrt{\frac{(D n_{\mathrm{eq}}^0 l/k_{\mathrm{B}}T + \sigma)\Omega\tilde{\delta}}{F l^2 f_{\mathrm{ES}}}}. \tag{4.3}$$

Here l is the step spacing of the vicinal surface, which is assumed to be small compared to the meander wavelength, and the factor $f_{\mathrm{ES}} = (l_- - l_+)/(l_+ + l_- + l) > 0$ is a measure for the strength of the ES effect. Equation (4.3) makes it clear that the meander wavelength is determined by the competition between the destabilizing flux in the denominator, and the stabilizing thermodynamic forces represented by the step stiffness in the numerator; shifting the balance towards the stabilizing/destabilizing side increases/decreases the meander wavelength. The stiffness is multiplied by the sum of two kinetic coefficients representing the two kinetic pathways that contribute to smoothening the step, terrace diffusion and step edge diffusion.

The basic mechanism underlying the BZ instability is well known from more conventional diffusional interface instabilities, e.g., in solidification [52]: The preferential attachment of adatoms to the ascending step implies that the growth of protrusions in the step is amplified. In contrast to solidification, however, here we are dealing with an infinite array of coupled "interfaces". The situation is illustrated in Fig. 6. It is clear from this figure that the essential feature needed for the instability is that the flux reaching the step from the lower terrace is larger than the corresponding flux from the upper terrace. Such an imbalance can be achieved even without an attachment asymmetry, by simply making the lower terrace larger than the upper terrace. Experiments on suitably tailored step structures on the Si(111) surface [56] (for which the existence of a ES effect is controversial, see Sect. 3.6) do indeed produce meander patterns, and confirm the prediction of the BZ linear stability analysis that the meander wavelength should scale with the inverse

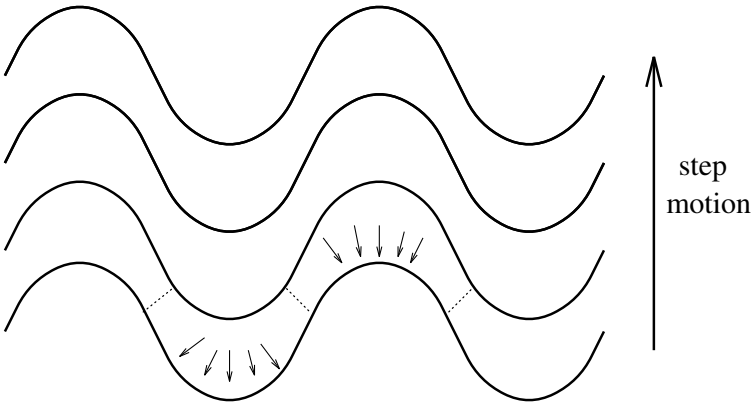

FIGURE 6. Geometric origin of the Bales-Zangwill meandering instability [54, 55]. The terraces are subdivided into lots along the dotted lines, which are drawn perpendicular to the lines of constant adatom concentration. Each lot receives the same number of atoms per unit time, which, owing to the ES effect, attach primarily to the corresponding segment of the ascending step. Because of the meander, the indented segments of the step are longer than the protruding ones. Since both receive the same total flux, the protrusions propagate faster and the meander is amplified.

square root of the flux [see (4.3)]. By the same argument, step meandering can result if the upper and lower terraces differ, e.g., in the diffusion or desorption rates for adatoms, a situation that is relevant to growth on Si(111) near the $7\times7 \rightarrow 1\times1$ transition temperature [57].

A detailed experimental study of the temperature and flux dependence of the meander wavelength was reported recently for growing surfaces vicinal to Cu(100) [41, 58, 59]. The main conclusion of this work was that the experimentally observed meander instability *cannot* be attributed to the BZ mechanism; instead, it seems that quantitative agreement can be reached [23, 60] if an alternative mechanism associated with kink rounding barriers (the *Kink-Ehrlich-Schwoebel Effect* or KESE) [24, 25, 28] is assumed to be operative. The KESE is the one-dimensional analog of the ES effect [41]. In the present case it is triggered by the disturbances created by one-dimensional nucleation events on the perfectly straight steps. Consequently the initial meander wavelength is given by the nucleation length (3.3). This changes the exponent of the flux dependence as compared to (4.3), and leads to a temperature dependence governed by the activation energy for step edge diffusion.

In contrast to the BZ instability, the KESE acts independently at each step, and hence there is no specific phase relation between the deformations of different steps in the initial regime of the instability [23]. Phase coherence develops later due to the effective step-step repulsion induced by the ES effect or, in the absence of any

attachment asymmetry, due to entropic or energetic step interactions; particularly in the last case, the synchronization of the step meanders is found in simulations to be very slow [61].

Step meandering can also occur in the absence of either a ES effect or a KESE, if edge diffusion is sufficiently fast. The phenomenon was discovered in kinetic Monte Carlo simulations [25], and it can be understood within the framework of a coarse grained continuum ("height") description of the surface, based on the notion of growth-induced surface currents [3, 4, 55, 62, 63] (see also Sect. 5). The starting point of the height description is a suitable phenomenological nonlinear partial differential equation for the surface height field $h(x, y, t)$. The stability analysis for a growing vicinal surface carried out in this setting shows that the surface is unstable towards step meandering whenever there is a net surface current in the uphill direction [27, 64]. Such a current can be argued to arise by step edge diffusion for purely geometric reasons, if the steps are already somewhat wavy; then the motion of an atom along a step, directed on average from protrusions to indentations, also has an uphill component. Because it presupposes a certain step corrugation, the effect is, in a sense, nonlinear, and it has so far not been possible to treat it within the conventional stability analysis of the step dynamical model. Kinetic Monte Carlo simulations indicate that the meander wavelength scales with flux as $\lambda \sim F^{-1/4}$, but a theoretical understanding of this result is lacking [65].

4.2. Stability of islands

We have emphasized in the preceding subsection that the BZ instability requires a larger flux to the step from the lower, compared to the upper, terrace. It is clear that this situation also arises during the growth of two-dimensional islands on a *singular* surface (a surface without preexisting steps). When the islands nucleate their radius is much smaller than the distance between islands [2, 4], and hence the adatoms that contribute to the growth of the island originate mainly from the substrate, i.e., from the lower terrace relative to the island boundary. Conversely, in the late stage of growth close to island coalescence, the island boundary is mainly fed from above, as the uncovered areas between islands are smaller than the islands themselves. One therefore expects that the island boundary should be unstable to meandering during the early stages of growth, and that it is restabilized when coalescence is approached. Of course it is also possible that the island boundary remains stable, if the island size is small compared to the characteristic meander wavelength [given, e.g., by (4.3)] throughout the growth history.

This qualitative picture is confirmed by linear stability analysis. The first study of island stability was carried out by Avignon and Chakraverty, who considered a single island growing in the presence of desorption [66]; in this case the length scale for the island size at which restabilization sets in is given by the diffusion length

$$x_s = \sqrt{D\tau}, \tag{4.4}$$

which is a measure for the range of correlations induced by the diffusion field. The first mode that becomes unstable during growth is a deformation of three-

fold symmetry[2]. A self-consistent treatment of island stability in the presence of surrounding islands was performed by Bales and Chrzan [67], who arrived at similar conclusions. Initial instability followed by restabilization has been observed experimentally for micron-sized islands on Si(111) [56].

4.3. Stability under surface electromigration

In 1989, Latyshev and collaborators reported that a direct heating current can induce step bunching on surfaces vicinal to Si(111) [68]. The bunches dissolve upon reversing the current direction, which suggested the hypothesis [12] that a current-driven directed motion of silicon adatoms – *surface electromigration* – may be responsible for the phenomenon[3]. In a seminal paper, Stoyanov included the electromigration force into the BCF theory and showed that step bunching indeed occurs, if the force is in the down-step direction [70]. Subsequent experimental work has confirmed the electromigration hypothesis, but at the same time a bewildering diversity of electromigration-induced patterns on vicinal silicon surfaces has been discovered [13, 14].

In particular, the current direction needed to induce step bunching was found to reverse three (!) times with increasing temperature. The scenario first proposed by Stoyanov [70] appears to apply to the lowest temperature regime (*regime I*), and much theoretical work has been devoted to trying to understand the reversals at higher temperatures. The simple idea that the reversals may be attributed to a sign change of the effective charge of the adatoms [71] has been ruled out by experiments [72] which show that the direction of the force coincides with the current direction at all temperatures. Other mechanisms that have been proposed to explain the reversals include strong desorption, in the sense that the diffusion length (4.4) becomes comparable to the step spacing [70], and diffusion and drift of surface vacancies [73].

While the issue is far from being settled, recent work seems to converge on the view that the resolution of the puzzle must be sought in the boundary conditions for the adatom concentration, at least as far as the first reversal (from regime I to regime II) is concerned. Stoyanov first showed that step bunching occurs, in the presence of sublimation, for a force in the up-step direction, if the steps are assumed to be perfectly permeable ($l_0 = 0$ in (3.13)) [74, 75]. Moreover, he predicted that the unstable current direction should reverse in the presence of a growth flux, in agreement with subsequent experiments [76]; at least in the absence of an attachment asymmetry, no such dependence on growth or sublimation conditions is present for impermeable steps [16]. Further support for the permeability picture comes from the observation of in-phase step meandering in regime II, when the current is in the down-step direction [77], a phenomenon that is reproduced by the linear stability analysis for permeable steps [78].

---

[2]Crystal anisotropy of the stiffness or the kinetic coefficients is not taken into account in [66, 67].
[3]For a general discussion of electromigration effects see [69] and references therein.

Nevertheless alternative explanations cannot be ruled out. For example, it has been argued that the consequences of fast attachment kinetics, in the sense of $l_+, l_- \ll l$, can hardly be distinguished from those of step permeability [16]. Evidence for step bunching due to an uphill force in the case of fast attachment kinetics has been found in kinetic Monte Carlo simulations, and the effect has been reproduced in a linear stability analysis assuming an electric field dependence of the kinetic coefficients and the equilibrium adatom concentration in the boundary conditions (3.5, 3.6) [79]. A particularly elegant recently proposed scenario for the stability reversal is based on the observation that the effective kinetic coefficients $k_\pm$ entering the boundary conditions may become *negative*, if the step is treated as a spatially extended region in which the diffusion of adatoms is enhanced rather than hindered relative to diffusion on the terraces [30]. Indeed, noting that the basic stability criterion derived by Stoyanov in his 1991 paper [70] involves the *product* of the electromigration force and the attachment coefficient, it is clear that a sign reversal of the kinetic coefficient is tantamount to a reversal of the direction of the force.

Additional complications, not discussed here, arise when the current direction is varied continuously relative to the orientation of the steps [62, 80, 81].

5. Nonlinear evolution

5.1. Step bunching

Numerical integration of the step dynamical equations in the nonlinear regime has been largely restricted to the bunching of straight steps, where the problem reduces to a one-dimensional array of coupled ordinary differential equations; representative examples out of a large number of publications are [82, 83, 84, 85]. The main interest in these studies has been to characterize the shape of individual bunches, as well as the time evolution of the typical bunch size due to bunch coarsening and coalescence. For both aspects quantitative information is available from experiments on electromigration-induced step bunching of surfaces vicinal to Si(111) [86, 87, 88].

Some of the bunch properties can be derived analytically by passing from the discrete step dynamics to a continuum description of the one-dimensional height profile $h(y,t)$ perpendicular to the steps [62]. The continuum limit is rather straightforward for the case of step flow growth, because the creation and annihilation of steps by island nucleation and coalescence does not have to be taken into account. We sketch the derivation for a particularly simple situation, thus providing an illustration of how the step dynamical model can be related to the continuum height equations discussed elsewhere in this volume [63].

Specifically, consider step bunching in the regime of a strong inverse ES effect, such that the typical step spacing l satisfies $l_+ \gg l \gg l_-$. Then the equations of

motion (4.1,4.2) become *linear*,

$$\frac{dy_j}{dt} = \hat{F}(y_j - y_{j-1}), \tag{5.1}$$

where $\hat{F} = F\Omega$. Clearly $y_j(t)$ can be replaced by a continuous function $y(h,t)$, where $h = -aj$ (compare to Fig. 5), by simply expanding the difference on the right-hand side of (5.1). To second order this yields[4]

$$\frac{\partial y}{\partial t} = \hat{F}\left[-a\frac{\partial y}{\partial h} - \frac{a^2}{2}\frac{\partial^2 y}{\partial h^2}\right]. \tag{5.2}$$

Applying the chain rule in the form

$$\frac{\partial h}{\partial t} = -\frac{\partial h}{\partial y}\frac{\partial y}{\partial t} \tag{5.3}$$

appropriate for the negatively sloped surface, we obtain a nonlinear evolution equation for $h(y,t)$ [89],

$$\frac{\partial h}{\partial t} + \frac{\partial}{\partial y}\left[-\frac{\hat{F}a^2}{2}\left(\frac{\partial h}{\partial y}\right)^{-1}\right] = \hat{F}a. \tag{5.4}$$

The right-hand side of this equation is naturally interpreted as a conservation law with a *growth-induced current* [3, 4, 55, 62, 63], which is inversely proportional to the surface slope and directed downhill (recall that $\partial h/\partial y < 0$).

The step-step interaction terms arising from (3.9) can be handled in a similar way [90]. Putting together the destabilizing and stabilizing effects, the resulting surface evolution equation takes the general form

$$\frac{\partial h}{\partial t} + \frac{\partial}{\partial y}\left[-A\left(\frac{\partial h}{\partial y}\right)^{-1} + B\left(\frac{\partial h}{\partial y}\right)^{-1}\frac{\partial^2}{\partial y^2}\left(\frac{\partial h}{\partial y}\right)^{2}\right] = \text{const.} \tag{5.5}$$

where the coefficients A and B are positive, and the constant on the right-hand side is the deposition flux. The same evolution equation has been obtained for step bunching induced by a normal ES effect during sublimation [62] and for electromigration-induced step bunching in the limit of slow attachment/detachment kinetics ($l_\pm \gg l$) [83]. It applies whenever the destabilizing part of the step dynamical equations, which is responsible for the step bunching instability, becomes linear in the step spacings [as in (5.1)].

The scaling properties of stationary step bunches can be derived from (5.5) by setting the current inside the square brackets to a constant and investigating the resulting ordinary differential equation for the slope $\partial h/\partial y$ [83, 90, 91]. One finds, in particular, that the minimal terrace size $l_{\min}$ inside the step bunch (the inverse of the maximal slope) scales with the number of steps N in the bunch as $l_{\min} \sim N^{-2/3}$, which is close to the behavior observed in experiments [87, 88]. At present it is not clear to what extent continuum equations like (5.5) are capable of also describing the time-dependent behavior of step bunches [62].

[4]The expansion has to be carried to third order in the symmetric case $k_+ = k_-$ [89].

Equation (5.5) is a representative of a larger class of evolution equations which have been proposed within a general classification scheme for step bunching phenomena [92]. All these equations are highly nonlinear, in the sense that the typical nonlinearities have the form of inverse powers of the slope. A different kind of evolution equations with polynomial nonlinearities arises when the derivation is carried out close to the threshold of the step bunching instability [93].

Finally, we note that all continuum equations discussed so far in this subsection have the form of a local conservation law [broken only by a constant flux on the right-hand side, see (5.4) and (5.5)]. One might expect that this reflects the absence of desorption from the surface, which generally violates the property of volume (hence height) conservation [55, 62, 63, 94]. However, the explicit derivation of an equation of the form (5.5) for sublimation-induced step bunching [90] shows that the structure of the conservation law is retained even in this case, provided desorption is a weak effect, in the sense of the diffusion length (4.4) being large compared to the other relevant length scales. In the presence of *strong* desorption one obtains instead an evolution equation with polynomial singularities of Kuramoto-Sivashinsky type, which displays spatiotemporal chaos rather than coarsening behavior [95] (see [62] for a general discussion).

5.2. Step meandering

The nonlinear evolution of growth-induced step meandering has been studied mostly within the framework of *local* approximations to the nonlocal moving boundary problem, which can be systematically derived using multiscale techniques. The result of such a calculation is a one-dimensional, nonlinear partial differential equation which (depending on the situation of interest) describes either a single step interacting with the diffusion field [96] or the collective step coordinate of a step train with an in-phase meander [53, 97, 98]. As in the preceding subsection, evolution equations of nonconserved type [96, 97] (displaying spatiotemporal chaos) and conserved type [53, 98] may be distinguished. To give an example of the latter kind, the evolution equation [99]

$$\frac{\partial y}{\partial t} = -\frac{\partial}{\partial x}\left\{\frac{\alpha y_x}{1+y_x^2} + \frac{\beta}{(1+y_x^2)^\nu}\frac{\partial}{\partial x}\left[\frac{y_{xx}}{(1+y_x^2)^{3/2}}\right]\right\} \tag{5.6}$$

with positive coefficients α, β describes the collective step meander for the Bales-Zangwill instability; the exponent ν depends on whether the dominant step smoothing mechanism is terrace diffusion ($\nu = 1$) or step edge diffusion ($\nu = 1/2$). In both cases the equation displays unbounded amplitude growth, with $\langle y\rangle \sim t^{1/2}$, while the lateral wavelength of the pattern remains fixed. Related equations with other nonlinear terms may also display unbounded lateral coarsening [100] or interrupted coarsening limited to a finite time interval [101] (see also [62]).

6. Open problems

At the end of these introductory notes, it seems appropriate to formulate some open questions that could be, and should be, addressed in the near future.

6.1. Microscopic basis of kinetic coefficients

For the step dynamical model to attain predictive power, it is mandatory to achieve a good understanding of the relationship between the kinetic coefficients entering the boundary conditions and the underlying atomistic rates. There has been encouraging progress in this direction (see, e.g., [23]), but the problem is clearly not solved in full generality. Presumably it will be necessary to go beyond the assumption of equilibrium at the steps, along the lines of [18, 19].

6.2. Crystal anisotropy

In the same vein, it is essential to take account of the fact that both thermodynamic and kinetic properties of steps on crystal surfaces are generally strongly anisotropic; still crystal anisotropy is ignored in most of the work in the field. As was recently demonstrated for the case of step meandering, anisotropy may *qualitatively* alter the evolution of morphological instabilities [101]. An attractive application for a numerical step-dynamical scheme incorporating crystal anisotropy would be to reproduce the sequence of island shapes that is observed experimentally as a function of temperature on metal surfaces such as Pt(111) [4].

6.3. Exotic step instabilities

We have briefly mentioned two novel step instabilities related to edge diffusion, which cannot be captured by straightforward linear stability analysis, and which thus may be termed *exotic*: The meandering instability caused by fast edge diffusion without attachment asymmetry or kink rounding barriers [25], and the step bunching instability induced by edge diffusion on steps with a preexisting meander [28]. So far evidence for the existence of these instabilities comes mainly from kinetic Monte Carlo simulations [25, 65]. A fully nonlinear treatment within the step dynamical model (including, in particular, the appropriate edge diffusion currents) would provide important guidance towards an analytic understanding, which is ultimately needed to assess the relevance of these effects for real surfaces.

6.4. Synchronization of the step meander

As was discussed above in Sect. 5.2, the nonlinear evolution of the step meandering instability has so far been treated under the assumption that the in-phase meander is fully coherent, so that the whole pattern can be described by a single step conformation $y(x,t)$. With the availability of powerful numerical algorithm for the solution of the full moving boundary problem for multiple steps, it will soon be possible to address also the initial phase of the instability, where the phase relation between different steps is established. Gaining a better understanding of the synchronization process is important, because the phase defects in the meander pattern have been shown to act as seeds for secondary instabilities which eventually

lead to the proliferation of steps of a sign opposite to the initial vicinality, and hence to the breakdown of step flow [64, 102]. Kinetic Monte Carlo simulations indicate that the breakdown is mediated by the formation of closed step loops deep in the fjords of the meander [102]. To handle such topology changes within the step dynamical model will require the use of approaches that avoid explicit tracking of the steps, such as phase field or level set methods, which are described elsewhere in this volume.

Acknowledgment

I would like to thank Jouni Kallunki and Stoyan Stoyanov for fruitful interactions, and John Weeks for making [30] available prior to publication.

References

[1] W.K. Burton, N. Cabrera, F.C. Frank, *The Growth of Crystals and the Equilibrium Structure of their Surfaces.* Phil. Trans. Roy. Soc. A **243** (1951), 299–358.

[2] A. Pimpinelli, J. Villain, *Physics of Crystal Growth.* Cambridge University Press, 1998

[3] P. Politi, G. Grenet, A. Marty, A. Ponchet, J. Villain, *Instabilities in Crystal Growth by Atomic or Molecular Beams.* Phys. Rep. **324** (2000), 271–404.

[4] T. Michely, J. Krug, *Islands, Mounds and Atoms. Patterns and Processes in Crystal Growth Far from Equilibrium.* Springer, Heidelberg 2004.

[5] H. van Beijeren, I. Nolden, *The Roughening Transition.* In W. Schommers, P. von Blanckenhagen (Eds.), *Structure and Dynamics of Surfaces II.* (Springer, Heidelberg 1987), pp. 259–300.

[6] P. Nozières, *Shape and Growth of Crystals.* In C. Godrèche (Ed.), *Solids Far from Equilibrium* (Cambridge University Press, 1991), pp. 1–154.

[7] H.-C. Jeong, E.D. Williams, *Steps on Surfaces: Experiment and Theory.* Surf. Sci. Rep. **34** (1999), 171–294.

[8] M. Giesen, *Step and island dynamics at solid/vacuum and solid/liquid interfaces.* Prog. Surf. Sci. **68** (2001), 1–153.

[9] H.P. Bonzel, *3D Equilibrium Crystal Shapes in the New Light of STM and AFM.* Phys. Rep. **385** (2003), 1–67.

[10] E.E. Gruber, W.W. Mullins, *On the Theory of Anisotropy of Crystalline Surface Tension.* J. Phys. Chem. Solids **28** (1967), 875–887.

[11] B. Joós, T.L. Einstein, N.C. Bartelt, *Distribution of terrace widths on a vicinal surface within the one-dimensional free-fermion model.* Phys. Rev. B **43** (1991), 8153–8162.

[12] S. Stoyanov, *Heating Current Induced Conversion between* 2×1 *and* 1×2 *Domains at Vicinal (001) Si Surfaces – Can it be Explained by Electromigration of Si Adatoms?* Jap. J. Appl. Phys. **29** (1990), L659–L662.

[13] K. Yagi, H. Minoda, M. Degawa, *Step bunching, step wandering and faceting: self-organization at Si surfaces.* Surf. Sci. Repts. **43** (2001) 45–126.

[14] H. Minoda, *Direct current heating effects on Si(111) vicinal surfaces.* J. Phys.-Cond. Matter **15** (2003), S3255–S3280.

[15] R. Ghez, S.S. Iyer, *The Kinetics of Fast Steps on Crystal Surfaces and its Application to the Molecular Beam Epitaxy of Silicon.* IBM J. Res. Dev. **32**, 804 (1988)

[16] O. Pierre-Louis, *Step bunching with general kinetics: stability analysis and macroscopic models.* Surf. Sci. **529** (2003), 114–134.

[17] C. Roland, G.H. Gilmer, *Epitaxy on surfaces vicinal to Si(001). II. Growth properties of Si(001) steps.* Phys. Rev. B **46** (1992) 13437–13451.

[18] R.E. Caflisch, W. E, M.F. Gyure, B. Merriman, C. Ratsch, *Kinetic model for a step edge in epitaxial growth.* Phys. Rev. B **59** (1999), 6879–6887.

[19] S.N. Filimonov, Yu.Yu. Hervieu, *Terrace-edge-kink model of atomic processes at the permeable steps.* Surf. Sci. **553** (2004), 133–144.

[20] V.V. Voronkov, *The movement of an elementary step by means of the formation of one-dimensional nuclei.* Sov. Phys. Crystallogr. **15** (1970), 8–13.

[21] M.C. Bartelt, J.W. Evans, *Scaling analysis of diffusion-mediated island growth in surface adsorption processes.* Phys. Rev. B **46** (1992), 12675–12687.

[22] J. Villain, A. Pimpinelli, L. Tang, D. Wolf, *Terrace sizes in molecular beam epitaxy.* J. Phys. I France **2** (1992), 2107–2121.

[23] J. Kallunki, J. Krug, *Competing mechanisms for step meandering in unstable growth.* Phys. Rev. B **65** (2002), 205411.

[24] O. Pierre-Louis, M.R. D'Orsogna, T.L. Einstein, *Edge Diffusion during Growth: The Kink Ehrlich-Schwoebel Effect and Resulting Instabilities.* Phys. Rev. Lett. **82** (1999), 3661–3664.

[25] M.V. Ramana Murty, B.H. Cooper, *Instability in Molecular Beam Epitaxy due to Fast Edge Diffusion and Corner Diffusion Barriers.* Phys. Rev. Lett **83** (1999), 352–355.

[26] J. Kallunki, J. Krug, *Effect of kink-rounding barriers on step edge fluctuations.* Surf. Sci. **523** (2003) L53–L58.

[27] J. Krug, H.T. Dobbs, S. Majaniemi, *Adatom mobility for the solid-on-solid model.* Z. Phys. B **97** (1995), 281–291.

[28] P. Politi, J. Krug, *Crystal symmetry, step-edge diffusion, and unstable growth.* Surf. Sci. **446** (2000), 89–97.

[29] M. Rusanen, I.T. Koponen, T. Ala-Nissila, C. Ghosh, T.S. Rahman, *Morphology of ledge patterns during step flow growth of metal surfaces vicinal to fcc(001).* Phys. Rev. B **65** (2002), 041404.

[30] T. Zhao, J.D. Weeks, D. Kandel, *A unified treatment of current-induced instabilities on Si surfaces.* (preprint, `cond-mat/0403488`).

[31] R.L. Schwoebel, *Step Motion on Crystal Surfaces. II.* J. Appl. Phys. **40** (1969), 614–618.

[32] R.L. Schwoebel, E.J. Shipsey, *Step Motion on Crystal Surfaces.* J. Appl. Phys. **37** (1966), 3682–3686.

[33] G. Ehrlich, F.G. Hudda, *Atomic View of Surface Self-Diffusion: Tungsten on Tungsten.* J. Chem. Phys. **44** (1966), 1039–1055.

[34] W.F. Chung, M.S. Altman, *Kinetic length, step permeability, and kinetic coefficient asymmetry on the Si(111) (7 × 7) surface.* Phys. Rev. B **66** (2002), 075338.

[35] A. Saúl, J.-J. Métois, A. Ranguis, *Experimental evidence for an Ehrlich-Schwoebel effect on Si(111).* Phys. Rev. B **65** (2002) 075409.

[36] M. Ozdemir, A. Zangwill, *Morphological equilibration of a facetted crystal.* Phys. Rev. B **45** (1992), 3718–3729.

[37] S. Tanaka, N.C. Bartelt, C.C. Umbach, R.M. Tromp, J.M. Blakely, *Step Permeability and the Relaxation of Biperiodic Gratings on Si(001).* Phys. Rev. Lett. **78** (1997) 3342–3345.

[38] F. Buatier de Mongeot, W. Zhu, A. Molle, R. Buzio, C. Boragno, U. Valbusa, E. G. Wang, Z. Zhang, *Nanocrystal Formation and Faceting Instability in Al(110) Homoepitaxy: True Upward Adatom Diffusion at Step Edges and Island Corners.* Phys. Rev. Lett. **91** (2003), 016102.

[39] O. Pierre-Louis, T.L. Einstein, *Electromigration of single-layer clusters.* Phys. Rev. B **62** (2000), 13697–13706.

[40] N. Néel, T. Maroutian, L. Douillard, H.-J. Ernst, *From Meandering to Faceting, Is Step Flow Growth Ever Stable?* Phys. Rev. Lett. **91** (2003) 226103.

[41] N. Néel, T. Maroutian, L. Douillard, H.-J. Ernst, *Spontaneous structural pattern formation at the nanometer scale in kinetically restricted homoepitaxy on vicinal surfaces.* J. Phys.: Condens. Matter **15** (2003), S3227–S3240.

[42] J. Krug, M. Schimschak, *Metastability of Step Flow Growth in* $1+1$ *Dimensions.* J. Phys. I France **5** (1995), 1065–1086.

[43] O. Pierre-Louis, C. Misbah, *Dynamics and fluctuations during MBE on vicinal surfaces. I. Formalism and results of linear theory.* Phys. Rev. B **58** (1998), 2259–2275.

[44] N. Cabrera, D.A. Vermilyea, *The Growth of Crystals from Solution.* In: *Growth and Perfection of Crystals*, ed. by R. Doremus, B. Roberts, D. Turnbull (Wiley, New York 1958) pp. 393–408.

[45] D. Kandel, J. Weeks: *Theory of impurity-induced step bunching.* Phys. Rev. B **49** (1994), 5554–5564.

[46] J. Krug, *New mechanism for impurity-induced step bunching.* Europhys. Lett. **60** (2002), 788–794.

[47] A. Pimpinelli, A. Videcoq, *Novel mechanism for the onset of morphological instabilities during chemical vapour epitaxial growth.* Surf. Sci. **445** (2000), L21–L28.

[48] M. Vladimirova, A. De Vita, A. Pimpinelli, *Dimer diffusion as a driving mechanism of the step bunching instability during homoepitaxial growth.* Phys. Rev. B **64** (2001), 245420.

[49] J. Mysliveček, C. Schelling, F. Schäffler, G. Springholz, P. Šmilauer, J. Krug, B. Voigtländer, *On the microscopic origin of the kinetic step bunching instability on vicinal Si(001).* Surf. Sci. **520** (2002), 193–206.

[50] G.S. Bales, A. Zangwill, *Morphological instability of a terrace edge during step-flow growth.* Phys. Rev. B **41** (1990), 5500–5508.

[51] A. Pimpinelli, I. Elkinani, A. Karma, C. Misbah, J. Villain, *Step motions on high-temperature vicinal surfaces.* J. Phys.: Condens. Matter **6** (1994), 2661–2680.

[52] B. Caroli, C. Caroli, B. Roulet, *Instabilities of planar solidification fronts.* In C. Godrèche (Ed.), *Solids Far from Equilibrium* (Cambridge University Press, 1991), pp.155–296.

[53] F. Gillet, O. Pierre-Louis, C. Misbah, *Non-linear evolution of the step meander during growth of a vicinal surface with no desorption.* Eur. Phys. J. B **18** (2000), 519–534.

[54] J. Kallunki, *Growth instabilities of vicinal crystal surfaces during Molecular Beam Epitaxy.* (PhD dissertation, University of Duisburg-Essen, 2003).

[55] J. Krug, *Four lectures on the physics of crystal growth.* Physica A **313** (2002), 47–82.

[56] Y. Homma, P. Finnie, M. Uwaha, *Morphological instability of atomic steps observed on Si(111) surfaces.* Surf. Sci. **492** (2001), 125–136.

[57] R. Kato, M. Uwaha, Y. Saito, *Step wandering due to the structural difference of the upper and lower terraces.* Surf. Sci. **550** (2004), 149–165.

[58] T. Maroutian, L. Douillard, H.-J. Ernst, *Morphological instability of Cu vicinal surfaces during step-flow growth.* Phys. Rev. B **64** (2001), 165401.

[59] T. Maroutian, *Étude expérimentale d'instabilités de croissance des faces vicinales* (PhD dissertation, Université Paris 7, 2001).

[60] M. Rusanen, I. T. Koponen, J. Heinonen, T. Ala-Nissila, *Instability and wavelength selection during step flow growth of metal surfaces vicinal to fcc(001).* Phys. Rev. Lett. **86** (2001), 5317–5320.

[61] J. Kallunki (unpublished).

[62] J. Krug, *Kinetic Pattern Formation at Solid Surfaces.* In G. Radons, P. Häussler, W. Just (Eds.), *Collective Dynamics of Nonlinear and Disordered Systems* (Springer, Berlin 2004).

[63] M. Rost, (this volume)

[64] M. Rost, P. Šmilauer, J. Krug, *Unstable epitaxy on vicinal surfaces.* Surf. Sci. **369** (1996), 393–402.

[65] A. Videcoq, *Auto-organisation de surfaces cristallines pendant la croissance épitaxiale: une étude théorique* (PhD dissertation, Université Blaise Pascal, Clermont-Ferrand 2002).

[66] M. Avignon, B.K. Chakraverty, *Morphological stability of a two-dimensional nucleus.* Proc. Roy. Soc. A **310** (1969), 277–296.

[67] G.S. Bales, D.C. Chrzan, *Transition from Compact to Fractal Islands during Submonolayer Epitaxial Growth.* Phys. Rev. Lett. **74** (1995), 4879–4882.

[68] A.V. Latyshev, A.L. Aseev, A.B. Krasilnikov, S.I. Stenin, *Transformations on clean Si(111) stepped surface during sublimation.* Surf. Sci. **213** (1989) 157–169.

[69] P. Kuhn, J. Krug, (this volume)

[70] S. Stoyanov, *Electromigration Induced Step Bunching on Si Surfaces - How Does It Depend on the Temperature and Heating Current Direction?* Jap. J. Appl. Phys. **30** (1991), 1–6.

[71] D. Kandel, E. Kaxiras, *Microscopic Theory of Electromigration on Semiconductor Surfaces.* Phys. Rev. Lett. **76** (1996), 1114–1117.

[72] M. Degawa, H. Minoda, Y. Tanishiro, K. Yagi, *Direct-current-induced drift direction of silicon adatoms on Si(111)-(*1×1*) surfaces.* Surf. Sci. **461** (2000), L528–L536.

[73] C. Misbah, O. Pierre-Louis, A. Pimpinelli, *Advacancy-induced step bunching on vicinal surfaces.* Phys. Rev. B **51** (1995), 17283–17286.

[74] S. Stoyanov, *Current-induced step bunching at vicinal surfaces during crystal sublimation.* Surf. Sci. **370** (1997), 345–354.

[75] S. Stoyanov, *New type of step bunching instability at vicinal surfaces in crystal evaporation affected by electromigration.* Surf. Sci. **416** (1998), 200–213.

[76] J.J. Métois, S. Stoyanov, *Impact of growth on the stability-instability transition at Si(111) during step bunching induced by electromigration.* Surf. Sci. **440** (1999), 407–419.

[77] H. Minoda, I. Morishima, M. Degawa, Y. Tanishiro, K. Yagi, *Time evolution of DC heating-induced in-phase step wandering on Si(111) vicinal surfaces.* Surf. Sci. **493** (2001), 487–493.

[78] M. Sato, M. Uwaha, Y. Saito, *Instabilities of steps induced by the drift of adatoms and effect of the step permeability.* Phys. Rev. B **62** (2000), 8452–8472.

[79] N. Suga, J. Kimpara, N.-J. Wu, H. Yasunaga, A. Natori: *Novel Transition Mechanism of Surface Electromigration Induced Step Structure on Vicinal Si(111) Surfaces.* Jpn. J. Appl. Phys. **39** (2000), 4412–4416.

[80] H. Dobbs, J. Krug, *Current Induced Faceting in Theory and Simulation.* J. Phys. I France **6** (1996), 413–430.

[81] M. Degawa, H. Minoda, Y. Tanishiro, K. Yagi, *In-phase step wandering on Si(111) vicinal surfaces: Effect of direct current heating tilted from the step-down direction.* Phys. Rev. B **63** (2001), 045309.

[82] S. Stoyanov, V. Tonchev, *Properties and dynamic interaction of step density waves at a crystal surface during electromigration affected sublimation.* Phys. Rev. B **58** (1998), 1590–1600.

[83] D.-J. Liu, J.D. Weeks, *Quantitative theory of current-induced step bunching on Si(111).* Phys. Rev. B **57** (1998), 14891–14900.

[84] M. Sato, M. Uwaha, *Growth of step bunches formed by the drift of adatoms.* Surf. Sci. **442** (1999), 318–328.

[85] M. Sato, M. Uwaha, *Growth law of step bunches induced by the Ehrlich-Schwoebel effect in growth.* Surf. Sci. **493** (2001), 494–498.

[86] Y.-N. Yang, E.S. Fu, E.D. Williams, *An STM study of current-induced step bunching on Si(111).* Surf. Sci. **356** (1996), 101–111.

[87] K. Fujita, M. Ichikawa, S.S. Stoyanov, *Size-scaling exponents of current-induced step bunching on silicon surfaces.* Phys. Rev. B **60** (1999), 16006–16012.

[88] Y. Homma, N. Aizawa, *Electric-current-induced step bunching on Si(111).* Phys. Rev. B **62** (2000), 8323–8329.

[89] J. Krug, *Continuum Equations for Step Flow Growth.* In D. Kim, H. Park, B. Kahng (Eds.), *Dynamics of Fluctuating Interfaces and Related Phenomena* (World Scientific, Singapore 1997), pp. 95–113.

[90] J. Krug, V. Tonchev, S. Stoyanov, A. Pimpinelli, *Scaling properties of step bunches induced by Ehrlich-Schwoebel barriers during sublimation.* (in preparation)

[91] P. Nozières, *On the motion of steps on a vicinal surface.* J. Physique **48** (1987), 1605–1608.

[92] A. Pimpinelli, V. Tonchev, A. Videcoq, M. Vladimirova, *Scaling and Universality of Self-Organized Patterns on Unstable Vicinal Surfaces.* Phys. Rev. Lett. **88** (2002), 206103.

[93] F. Gillet, Z. Csahok, C. Misbah, *Continuum nonlinear surface evolution equation for conserved step-bunching dynamics.* Phys. Rev. B **63** (2001), 241401.

[94] P. Šmilauer, M. Rost, J. Krug, *Fast coarsening in unstable expitaxy with desorption.* Phys. Rev. E **59** (1999), R6263–R6266.

[95] M. Sato, M. Uwaha, *Step Bunching as Formation of Soliton-like Pulses in Benney Equation.* Europhys. Lett. **32** (1995), 639–644.

[96] I. Bena, C. Misbah, A. Valance, *Nonlinear evolution of a terrace edge during step-flow growth.* Phys. Rev. B **47** (1993), 7408–7419.

[97] O. Pierre-Louis, C. Misbah, *Dynamics and fluctuations during MBE on vicinal surfaces. II. Nonlinear analysis.* Phys. Rev. B **58** (1998), 2276–2288.

[98] O. Pierre-Louis, C. Misbah, Y. Saito, J. Krug, P. Politi, *New Nonlinear Evolution Equation for Steps during Molecular Beam Epitaxy on Vicinal Surfaces.* Phys. Rev. Lett. **80** (1998), 4221–4224.

[99] J. Kallunki, J. Krug, *Asymptotic step profiles from a nonlinear growth equation for vicinal surfaces.* Phys. Rev. E **62** (2000), 6229–6232.

[100] P. Politi, C. Misbah, *When Does Coarsening Occur in the Dynamics of One-Dimensional Fronts?* Phys. Rev. Lett. **92** (2004), 090601.

[101] G. Danker, O. Pierre-Louis, K. Kassner, C. Misbah, *Interrupted coarsening of anisotropic step meander.* Phys. Rev. E **68** (2003), 020601(R).

[102] J. Kallunki, J. Krug, *Breakdown of step-flow growth in unstable homoepitaxy.* Europhys. Lett. **66** (2004), 749–755.

Joachim Krug
Universität zu Köln
Institut für Theoretische Physik
Zülpicher Strasse 77
D-50937 Köln, Germany
e-mail: `krug@thp.uni-koeln.de`

International Series of Numerical Mathematics, Vol. 149, 97–114

A Finite Element Framework for Burton-Cabrera-Frank Equation

Frank Haußer and Axel Voigt

Abstract. A finite element framework is presented for the Burton-Cabrera-Frank (BCF) equation. The model is a $2+1$-dimensional step flow model, discrete in the height but continuous in the lateral directions. The problem consists of adatom diffusion equations on terraces of different atomic height; boundary conditions at steps (terrace boundaries); and a normal velocity law for the motion of such boundaries determined by a two-sided flux, together with one-dimensional edge-diffusion. Two types of boundary conditions, modeling either diffusion limited growth or growth governed by attachment-detachment kinetics at the steps, are considered. We review the basic ideas of the algorithms, already described in [1, 2] and extent it to incorporate anisotropy of the step free energy, the edge mobility and the kinetic coefficients (attachment-detachment rates). The problem is solved using two independent meshes: a two-dimensional mesh for the adatom diffusion and a one-dimensional mesh for the step dynamics governed by an anisotropic geometric evolution law. Finally results on the anisotropic growth of single layer islands are presented.

Mathematics Subject Classification (2000). Primary 80A22; Secondary 35R35.

Keywords. step-flow model; anisotropic geometric evolution laws; parametric finite elements; discrete-continuous coupling.

1. Introduction

The Burton-Cabrera-Frank (BCF) equations [3] serve as a prototype of discrete-continuous step flow models, discrete in the height resolving the atomic layers in the growth direction, but coarse grained in the lateral direction. The steps, separating terraces of different height, are assumed to be smooth curves and serve as free boundaries for an adatom diffusion on terraces. Mathematically such a model is a free boundary problem that consists of a diffusion equation for the adatom density on the terraces, boundary conditions at the steps and a velocity

law for the motion of the steps. A detailed description of step flow dynamics is given in the review article of Krug [4] (this volume).

The evolution of the steps can be used to describe the surface morphology of the growing film on a mesoscopic scale. For this aim the dynamics of a large number of steps has to be determined. During the last years powerful numerical techniques for the solution of such problems have been developed and make step dynamics an attractive alternative to atomistic modeling approaches in epitaxial crystal growth.

Recently, level-set based finite difference methods have been developed to solve the BCF-equations in the diffusion limited regime [5, 6, 7, 8, 9]. In particular, in a layer-by-layer growth mode quantitative agreement with kinetic Monte Carlo simulations could be demonstrated. In the attachment-detachment limited regime a level-set based method is introduced in [10]. An alternative method to level-sets is the phase-field approach. In the diffusion limited regime this method has been introduced in [11, 12, 13]. For attachment-detachment limited growth phase-field models are developed in [14, 15, 16, 17]. With both, the level-set and the phase-field method, topological changes like coalescence of islands can be handled very efficiently. But until now, the (anisotropic) step energies and (anisotropic) edge diffusion have not been built in accurately. In particular it is not straight-forward how to discretize the fourth-order derivative occurring in the edge-diffusion term. Very recently, level-set approaches based on semi-implicit methods to describe such fourth order evolution laws have been developed in [18, 19], but have not yet been applied to solve the BCF equations. A phase-field model which includes isotropic edge diffusion is introduced in [20] (this volume). A front-tracking finite element approach for epitaxial growth was developed in [1, 2]. This approach will be reviewed and extended to treat anisotropic step free energies, edge adatom mobilities and kinetic coefficients.

2. Burton-Cabrera-Frank equation

We denote by $\Omega \subset \mathbb{R}^2$ the projected domain of a film surface in a two-dimensional Cartesian coordinate system, and assume that Ω is independent of time t. We denote also by $\Omega_i = \Omega_i(t) \subset \mathbb{R}^2$, $i = 0, \dots, N$, islands or terraces of discrete height i. Thus, $N + 1$ is the total number of layers that are exposed on the film surface. Note that, since the height of neighboring terraces differs only by one atomic layer, we conclude that

$$\overline{\Omega_i(t)} \cap \overline{\Omega_j(t)} = \emptyset \quad \text{if and only if} \quad |i - j| \geq 2.$$

We denote further the corresponding steps (or terrace boundaries) by

$$\Gamma_i(t) = \overline{\Omega_i(t)} \cap \overline{\Omega_{i-1}(t)}, \qquad i = 1, \dots, N.$$

Denote by $\rho_i = \rho_i(x, t)$ the adatom density on terrace $\Omega_i(t)$ $(i = 0, \dots N)$ at time t. The adatom diffusion on a terrace is described by the diffusion equation for the

adatom density

$$\partial_t \rho_i - \nabla \cdot (D \nabla \rho_i) = F - \tau^{-1} \rho_i \qquad \text{in } \Omega_i(t), \quad i = 0, \ldots, N, \tag{2.1}$$

where D is the diffusion coefficient, F is the deposition flux rate, and τ^{-1} is the desorption rate. The fluxes of adatoms to the steps are given by

$$q_i^+ := -D \nabla \rho_i \cdot \vec{n}_i - v_i \rho_i, \tag{2.2}$$

$$q_i^- := D \nabla \rho_{i-1} \cdot \vec{n}_i + v_i \rho_{i-1}, \tag{2.3}$$

where q_i^+ is the flux from the upper terrace $\Omega_i(t)$ and q_i^- the flux from the lower terrace $\Omega_{i-1}(t)$ to the boundary $\Gamma_i(t)$, $\vec{n}_i$ is the unit normal of the step $\Gamma_i(t)$ pointing from the upper to the lower terrace, and v_i is the normal velocity of the step $\Gamma_i(t)$ with the convention that $v_i > 0$ if the movement of $\Gamma_i(t)$ is in the direction of $\vec{n}_i$. Boundary conditions for the adatom density at the steps $\Gamma_i(t)$ are given in terms of the thermodynamic equilibrium density

$$\rho_i^{eq} = \rho^* \left(1 + \frac{\mu_i}{k_B T} \right), \tag{2.4}$$

with μ_i the step chemical potential. The adatom density satisfies one of the following boundary conditions on the steps $\Gamma_i(t)$ for $i = 1, \ldots, N$:

Diffusion limited regime

$$\rho_i = \rho_{i-1} = \rho_i^{eq} \tag{2.5}$$

Attachment-detachment kinetics

$$q_i^+ = k_+(\rho_i - \rho_i^{eq}), \tag{2.6}$$

$$q_i^- = k_-(\rho_{i-1} - \rho_i^{eq}), \tag{2.7}$$

where θ denotes the angle between the outer normal of the step $\Gamma_i(t)$ and the x-axis, and $k_+ = k_+(\theta)$, $k_- = k_-(\theta)$ are the kinetic attachment rates from the upper and lower terrace to the step $\Gamma_i(t)$, respectively. In general, we have $0 < k_+ \leq k_-$ by our notation, where the strict inequality $k_+ < k_-$ models the Ehrlich-Schwoebel effect. In the case of attachment-detachment kinetics the adatom density is discontinuous at the steps. In the limit $k_+, k_- \to \infty$ the adatom density becomes continuous at the steps and the diffusion limited boundary condition is recovered. Denoting by γ the orientation dependent step free energy divided by $k_B T$ and neglecting any elastic or entropic interactions between steps, the step chemical potential μ_i is given in terms of the curvature κ_i of the step $\Gamma_i(t)$ as $\mu_i / k_B T = \tilde{\gamma} \kappa_i$, where $\tilde{\gamma}(\theta) = \gamma(\theta) + \gamma''(\theta)$. This yields the following Gibbs-Thomson type relation for the equilibrium density ρ_i^{eq}

$$\rho_i^{eq} = \rho^* \left(1 + \tilde{\gamma} \kappa_i \right). \tag{2.8}$$

For the motion of the moving boundaries, we assume the following law for the normal velocity v_i of the step $\Gamma_i(t)$:

$$v_i = q_i^+ + q_i^- + \partial_s(\nu \partial_s(\tilde{\gamma} \kappa_i)), \tag{2.9}$$

where $\nu = \nu(\theta)$ is the mobility for diffusion along the steps and ∂_s denotes the tangential derivative along the steps. The term $\partial_s(\nu\partial_s(\tilde{\gamma}\kappa_i))$ represents the one-dimensional edge diffusion. We assume either periodic or flux-free boundary conditions for the adatom densities at the boundary of the film domain, and assume that the initial terraces $\Omega_i(0)$ $(i = 0, \dots, N)$ along with their corresponding steps $\Gamma_i(0)$ $(i = 1, \dots, N)$ are given. Moreover, we assume that initial adatom densities are given by

$$\rho_i(x, 0) = \bar{\rho}_i(x) \qquad \forall x \in \Omega_i(0), \quad i = 0, \dots, N \tag{2.10}$$

for some given function $\bar{\rho}_i$.

3. Finite element discretization

We describe a weak formulation for the time-dependent diffusion equations and use an implicit scheme to discretize in time. In each time step:

1. We update the discrete boundaries by solving the anisotropic geometric partial differential equations (PDE) based on the adatom densities and the discrete boundaries from the previous time step;
2. We solve the adatom diffusion equations to update the adatom densities using the adatom densities from the previous time step and the computed discrete boundaries.

We will start with describing the discretization for the adatom diffusion.

3.1. Adatom diffusion

Assume that ρ_i is smooth in $\Omega_i = \Omega_i(t)$. Multiplying both sides of the diffusion equation in (2.1) by a smooth, time-independent, test function ϕ, and integrating by parts, we get

$$\begin{aligned}\int_{\Omega_i} \partial_t \rho_i \phi + \int_{\Omega_i} D\nabla\rho_i \cdot \nabla\phi - \int_{\Gamma_i} D\nabla\rho_i \cdot \vec{n}_i \phi + \int_{\Gamma_{i+1}} D\nabla\rho_i \cdot \vec{n}_{i+1}\phi \\ = \int_{\Omega_i} F\phi - \int_{\Omega_i} \tau^{-1}\rho_i\phi.\end{aligned} \tag{3.1}$$

In the case of *diffusion limited growth* we can define a global continuous adatom density by setting $\rho(x, y, t) = \rho_i(x, y, t)$ for $(x, y) \in \Omega_i(t)$ and get

$$\int_\Omega \partial_t\rho\phi + \int_\Omega D\nabla\rho\cdot\nabla\phi + \sum_{i=1}^N \int_{\Gamma_i} D[\nabla\rho\cdot\vec{n}_i]_i\phi = \int_\Omega F\phi - \int_\Omega \tau^{-1}\rho\phi, \tag{3.2}$$

with $[\nabla\rho\cdot\vec{n}_i]_i := \nabla\rho_i\cdot\vec{n}_i - \nabla\rho_{i-1}\cdot\vec{n}_i$. The boundary conditions at the steps (2.5) are now incorporated by a penalty method

$$\int_\Omega \partial_t\rho\phi + \int_\Omega D\nabla\rho\cdot\nabla\phi + \frac{1}{\epsilon}\sum_{i=1}^N \int_{\Gamma_i} (\rho - \rho^*(1+\tilde{\gamma}\kappa_i))\phi = \int_\Omega F\phi - \int_\Omega \tau^{-1}\rho\phi$$

with $\epsilon \ll 1$. Thus (in a weak sense) $D[\nabla\rho\cdot\vec{n}_i]_i = \frac{1}{\epsilon}(\rho - \rho^*(1+\tilde{\gamma}\kappa_i))$. Now, split the time interval by discrete time instants $0 = t_0 < t_1 < \cdots$ and define the time

steps $\triangle t_m := t_{m+1} - t_m$ $(m = 0, 1, \ldots)$. Using the approximations $\Gamma_i^m \approx \Gamma_i(t_m)$, we have the following formulation of the time discretization problem.

$$\int_\Omega \frac{\rho^{m+1} - \rho^m}{\triangle t_m}\phi + \int_\Omega D\nabla\rho^{m+1} \cdot \nabla\phi + \frac{1}{\epsilon}\sum_{i=1}^{N}\int_{\Gamma_i^{m+1}} (\rho^{m+1} - \rho^*(1 + \tilde{\gamma}\kappa_i^{m+1}))\phi$$
$$= \int_\Omega F\phi - \int_\Omega \tau^{-1}\rho^{m+1}\phi$$

where κ_i^{m+1} denotes the curvature of Γ_i^{m+1}.

In the case of *attachment-detachment kinetics* notice that for a moving smooth domain $\omega(t)$ and a smooth function $\xi(x,t)$ for $x \in \omega(t)$,

$$\frac{d}{dt}\int_{\omega(t)} \xi = \int_{\omega(t)} \partial_t\xi + \int_{\partial\omega(t)} \xi u,$$

where u is the normal velocity of the moving boundary $\partial\omega(t)$. Applying this formula to the corresponding term in (3.1) and using the boundary conditions (2.6) and (2.7), we obtain

$$\frac{d}{dt}\int_{\Omega_i(t)} \rho_i\phi + \int_{\Omega_i(t)} D\nabla\rho_i \cdot \nabla\phi + \int_{\Omega_i(t)} \tau^{-1}\rho_i\phi + \int_{\Gamma_i(t)} k_+(\rho_i - \rho^*(1 + \tilde{\gamma}\kappa_i))\phi$$
$$+ \int_{\Gamma_{i+1}} k_-(\rho_i - \rho^*(1 + \tilde{\gamma}\kappa_{i+1}))\phi = \int_{\Omega_i(t)} F\phi.$$

Let $\triangle t > 0$ be a small time step. Then,

$$\frac{d}{dt}\int_{\Omega_i(t)} \rho_i\phi \approx \frac{1}{\triangle t}\left[\int_{\Omega_i(t)} \rho_i(x,t)\phi(x) - \int_{\Omega_i(t-\triangle t)} \rho_i(x, t-\triangle t)\phi(x)\right].$$

Again, split the time interval by discrete time instants $0 = t_0 < t_1 < \cdots$ and define the time steps $\triangle t_m := t_{m+1} - t_m$ $(m = 0, 1, \ldots)$. Using the approximations $\Omega_i^m \approx \Omega_i(t_m)$ and $\Gamma_i^m \approx \Gamma_i(t_m)$, we have the following formulation of the time discretization problem.

$$\frac{1}{\triangle t_m}\left[\int_{\Omega_i^{m+1}} \rho_i^{m+1}\phi - \int_{\Omega_i^m} \rho_i^m\phi\right] + \int_{\Omega_i^{m+1}} D\nabla\rho_i^{m+1} \cdot \nabla\phi + \int_{\Omega_i^{m+1}} \tau^{-1}\rho_i^{m+1}\phi$$
$$+ \int_{\Gamma_i^{m+1}} k_+(\rho_i^{m+1} - \rho^*(1 + \tilde{\gamma}\kappa_i^{m+1}))\phi + \int_{\Gamma_{i+1}^{m+1}} k_-(\rho_i^{m+1} - \rho^*(1 + \tilde{\gamma}\kappa_{i+1}^{m+1}))\phi$$
$$= \int_{\Omega_i^{m+1}} F\phi,$$

where κ_i^{m+1} and κ_{i+1}^{m+1} denote the curvature of Γ_i^{m+1} and Γ_{i+1}^{m+1}, respectively. At each time step, we need to solve an elliptic problem with curved boundaries. To avoid the complexity in the spatial discretization near such curved boundaries, we use the method of composite finite elements. Therefore let ρ_i^m $(m \geq 0)$ be the trivial extension of ρ_i to the whole domain Ω, i.e.,

$$\rho_i^m(x) = \rho_i(x) \quad \text{for } x \in \Omega_i^m \qquad \text{and} \qquad \rho_i^m(x) = 0 \quad \text{for } x \in \Omega\backslash\Omega_i^m.$$

Furthermore, define for each $m \geq 0$ and $0 \leq i \leq N$

$$\Big(D_{i,m}(x), F_{i,m}(x), \tau^{-1}_{i,m}(x)\Big) = \begin{cases} (D, F, \tau^{-1}) & : x \in \bar{\Omega}^m_i \\ (0,0,0) & : x \in \Omega \setminus \Omega^m_i \end{cases}$$

Extend also the initial densities $\bar{\rho}_i$, still denoted by $\bar{\rho}_i$, by $\bar{\rho}_i = 0$ in $\Omega \setminus \Omega_i(0)$. Now, replace D, τ^{-1}, F, and Ω^m_i by $D_{i,m+1}$, $\tau^{-1}_{i,m+1}$, $F_{i,m+1}$, and Ω, and solve the corresponding problem on the whole domain for all test function ϕ defined on Ω

$$\begin{aligned}\int_\Omega \frac{\rho^{m+1}_i - \rho^m_i}{\triangle t_m}\phi + \int_\Omega D_{i,m+1}\nabla\rho^{m+1}_i \cdot \nabla\phi + \int_\Omega \tau^{-1}_{i,m+1}\rho^{m+1}_i\phi \\ + \int_{\Gamma^{m+1}_i} k_+(\rho^{m+1}_i - \rho^*(1+\tilde{\gamma}\kappa_i))\phi + \int_{\Gamma^{m+1}_{i+1}} k_-(\rho^{m+1}_i - \rho^*(1+\tilde{\gamma}\kappa_{i+1}))\phi \\ = \int_\Omega F_{i,m+1}\phi.\end{aligned}$$

To discretize in space, let T^m_h be a triangulation of Ω at time instant t_m. We will use the finite element space of globally continuous, piecewise linear elements

$$\mathbb{V}^m_h = \left\{v_h \in C^0(\overline{\Omega}) \ : \ v_h|_T \in \mathbb{P}_1 \ \ \forall T \in T^m_h\right\},$$

where $\mathbb{P}_1$ denotes the set of all polynomials of total degree ≤ 1. Denote by $P_m : C^0(\overline{\Omega}) \to \mathbb{V}^m_h$ the usual Lagrange interpolation operator. With this setting, the space discretization of the *diffusion limited problem* reads

$$\begin{aligned}\int_\Omega \frac{\rho^{m+1}_h - \rho^m_h}{\triangle t_m}\phi_h + \int_\Omega D\nabla\rho^{m+1}_h \cdot \nabla\phi_h + \frac{1}{\epsilon}\sum_{i=1}^N \int_{\Gamma^{m+1}_i} (\rho^{m+1}_h - \rho^*(1+\tilde{\gamma}\kappa^{m+1}_{i,h}))\phi_h \\ = \int_\Omega F\phi_h - \int_\Omega \tau^{-1}\rho^{m+1}_h\phi_h\end{aligned}$$

and the discretization in the case of *attachment-detachment kinetics* reads

$$\begin{aligned}&\int_\Omega \frac{\rho^{m+1}_{i,h} - \rho^m_{i,h}}{\triangle t_m}\phi_h + \int_\Omega D_{i,m+1}\nabla\rho^{m+1}_{i,h} \cdot \nabla\phi_h + \int_{\Gamma^{m+1}_{i,h}} k_+(\rho^{m+1}_{i,h} - \rho^*(1+\tilde{\gamma}\kappa^{m+1}_{i,h}))\phi_h \\ &+ \int_{\Gamma^{m+1}_{i+1,h}} k_-(\rho^{m+1}_{i,h} - \rho^*(1+\tilde{\gamma}\kappa^{m+1}_{i+1,h}))\phi_h + \int_\Omega \tau^{-1}_{i,m+1}\rho^{m+1}_{i,h}\phi_h = \int_\Omega F_{i,m+1}\phi_h\end{aligned}$$

for all $\phi_h \in \mathbb{V}^{m+1}_h$ with $\kappa^{m+1}_{i,h}$ the discrete curvatures of $\Gamma^{m+1}_{i,h}$. Let $(\phi_k)_{k=1}^L$ be the standard nodal basis of the finite element space $\mathbb{V}_h$, where L is the dimension of $\mathbb{V}_h$. Expand ρ^{m+1}_h and $\rho^{m+1}_{i,h}$ as

$$\rho^{m+1}_h = \sum_{k=1}^L r_k\phi_k, \quad \rho^{m+1}_{i,h} = \sum_{k=1}^L r_{i,k}\phi_k,$$

for some $R = (r_1, \ldots, r_L)^t \in \mathbb{R}^L$ and $R_i = (r_{i,1}, \ldots, r_{i,L})^t \in \mathbb{R}^L$. Define the following mass and stiffness matrices and load vectors:

$$\begin{aligned}
\boldsymbol{M} &= (M_{kl}), & M_{kl} &= (\phi_k, \phi_l)\,; \\
\boldsymbol{M}^{\Gamma_i} &= (M_{kl}^{\Gamma_i}), & M_{kl}^{\Gamma_i} &= \langle \phi_k, \phi_l \rangle_{\Gamma_i}; \\
\boldsymbol{M}_{\pm}^{\Gamma_i} &= (M_{\pm,kl}^{\Gamma_i}), & M_{\pm,kl}^{\Gamma_i} &= \langle k_{\pm}\phi_k, \phi_l \rangle_{\Gamma_i}; \\
\boldsymbol{M}_i &= (M_{i,kl}), & M_{i,kl} &= \left(\tau_i^{-1}\phi_k, \phi_l\right); \\
\boldsymbol{A} &= (A_{kl}), & A_{kl} &= (D\nabla\phi_k, \nabla\phi_l)\,; \\
\boldsymbol{A}_i &= (A_{i,kl}), & A_{i,kl} &= (D_i\nabla\phi_k, \nabla\phi_l)\,; \\
\boldsymbol{F} &= (F_l), & F_l &= (F, \phi_l)\,; \\
\boldsymbol{F}_i &= (F_{i,l}), & F_{i,l} &= (F_i, \phi_l)\,; \\
\boldsymbol{F}^{\Gamma_i} &= (F_l^{\Gamma_i}), & F_l^{\Gamma_i} &= \langle \rho^*(1 + \tilde{\gamma}\kappa_{i,h}), \phi_l \rangle_{\Gamma_i}; \\
\boldsymbol{F}_{\pm}^{\Gamma_i} &= (F_{\pm,l}^{\Gamma_i}), & F_{\pm,l}^{\Gamma_i} &= \langle k_{\pm}\rho^*(1 + \tilde{\gamma}\kappa_{i,h}), \phi_l \rangle_{\Gamma_i};
\end{aligned}$$

where the index ranges are $1 \le k, l \le L$ and $\langle \cdot, \cdot \rangle_{\Gamma_i}$ stands for the L^2 inner product over the current interface $\Gamma_i = \Gamma_{i,h}$ and $(\cdot, \cdot)$ stands for the L^2 inner product over the domain Ω. In matrix form the *diffusion limited case* reads

$$\begin{aligned}
\frac{1}{\triangle t_m}\boldsymbol{M}R^{m+1} + \boldsymbol{A}R^{m+1} + \tau^{-1}\boldsymbol{M}R^{m+1} + \frac{1}{\epsilon}\sum_{i=1}^{N}\boldsymbol{M}^{\Gamma_i}R^{m+1} \\
= \boldsymbol{F} + \frac{1}{\epsilon}\sum_{i=1}^{N}\boldsymbol{F}^{\Gamma_i} + \frac{1}{\triangle t_m}\boldsymbol{M}R^m.
\end{aligned}$$

For *attachment-detachment kinetics* one obtains

$$\begin{aligned}
\frac{1}{\triangle t_m}\boldsymbol{M}R_i^{m+1} + \boldsymbol{A}_iR_i^{m+1} + \boldsymbol{M}_iR_i^{m+1} + \boldsymbol{M}_+^{\Gamma_i}R_i^{m+1} + \boldsymbol{M}_-^{\Gamma_{i+1}}R_i^{m+1} \\
= \boldsymbol{F}_i + \boldsymbol{F}_+^{\Gamma_i} + \boldsymbol{F}_-^{\Gamma_{i+1}} + \frac{1}{\triangle t_m}\boldsymbol{M}R_i^m, \qquad i = 0, \ldots, N.
\end{aligned}$$

Note that in the *diffusion limited case* only one linear system has to be solved, whereas in the case of *attachment-detachment kinetics* $N + 1$ linear systems need to be solved. However, in actual computations, the number can be reduced to at most 2 because odd-labeled (or even-labeled) terraces are non-contiguous, and it is enough to work with a single function ρ_{odd} for all odd i's and a single function ρ_{even} for all even i's.

The assembly of the matrices involves several nonstandard integrals. The line integration over a boundary $\Gamma_{i,h}$ in the adatom diffusion problem is treated by subdividing the boundary into polygons, see Figure 3.1. A polygon is defined by the intersection points of $\Gamma_{i,h}$ and boundaries of the element T, and points of $\Gamma_{i,h}$, where the parameterization changes. The integration can then be performed in a standard way by calculating integrals of piecewise linear functions. See [21] for further details. Integrals involving coefficients that are discontinuous within

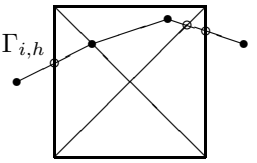

FIGURE 1. Element T, boundary $\Gamma_{i,h}$, and line integration path.

one element are treated as in [22]. These integrals are of the form $\int \phi\,\lambda$ with ϕ a smooth function and λ a discontinuous function,

$$\lambda = \begin{cases} \lambda_{i-1} & \text{in } T \cap \overline{\Omega_{i-1}} \\ \lambda_i & \text{in } T \cap \overline{\Omega_i} \end{cases}$$

with some $\lambda_{i-1}, \lambda_i \in \mathbb{R}$, cf. Figure 2. We use the following integral approximation, cf. Figure 2:

$$\begin{aligned} \int_T \lambda\,\phi &\approx \int_{\triangle(DBE)} \lambda_i \phi + \int_{\square(ADEC)} \lambda_{i-1}\phi \\ &= \int_{\triangle(DBE)} \lambda_i \phi + \int_T \lambda_{i-1}\phi - \int_{\triangle(DBE)} \lambda_{i-1}\phi. \end{aligned}$$

Note that this formula avoids the explicit integration over quadrilaterals and requires only integration over triangles, and thus can be performed in a nearly standard way. We introduce the following quantities defined on the nodes on the

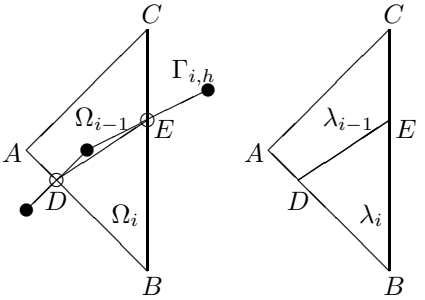

FIGURE 2. Element T, boundary $\Gamma_{i,h}$, and definition of λ.

boundaries $\Gamma_{i,h}$: in the *diffusion limited case*

$$f_i := \frac{1}{\epsilon}(\rho_h|_{\Gamma_{i,h}} - \rho^*) \tag{3.3}$$

and in the case of *attachment-detachment kinetics*

$$f_i := k_+(\rho_{i,h}|_{\Gamma_{i,h}} - \rho^*) + k_-(\rho_{i-1,h}|_{\Gamma_{i,h}} - \rho^*). \tag{3.4}$$

These quantities will enter in the subproblem of moving boundaries.

3.2. Step evolution

In order to use the velocity law (2.9) for numerical computation it needs to be reformulated. Using the identity $D[\nabla\rho\cdot\vec{n}_i]_i = \frac{1}{\epsilon}(\rho-\rho^*(1+\tilde{\gamma}\kappa_i))$, see Section 3.1, the evolution law in the *diffusion limited case* reads

$$v_i = \frac{1}{\epsilon}(\rho-\rho^*) - \frac{1}{\epsilon}\rho^*\tilde{\gamma}\kappa_i + \partial_s(\nu\partial_s(\tilde{\gamma}\kappa_i)). \tag{3.5}$$

In the case of *attachment-detachment kinetics* we add the two boundary conditions (2.6) and (2.7) at $\Gamma_i(t)$ and obtain together with the velocity formula (2.9)

$$v_i = k_+(\rho_i-\rho^*) + k_-(\rho_{i-1}-\rho^*) - (k_++k_-)\rho^*\tilde{\gamma}\kappa_i + \partial_s(\nu\partial_s(\tilde{\gamma}\kappa_i)). \tag{3.6}$$

Both equations are of the form

$$v_i = f_i - \beta\tilde{\gamma}\kappa_i + \partial_s(\nu\partial_s(\tilde{\gamma}\kappa_i)) \tag{3.7}$$

and can be interpreted as an equation for anisotropic surface diffusion with lower order terms, with f_i given by (3.3) and (3.4) and $\beta = \frac{1}{\epsilon}\rho^*$ in the *diffusion limited case* and $\beta = (k_++k_-)\rho^*$ in the case of *attachment-detachment kinetics*. To discretize this nonlinear 4th order equation, we adapt with modification a variational formulation introduced for isotropic surface diffusion in [23], cf. also [24]. By introducing the position vector $\vec{x}_i$, the curvature vector $\vec{\kappa}_i$, and the velocity vector $\vec{v}_i$, a system of equations for $\vec{\kappa}_i$, $\tilde{\kappa}_i := \tilde{\gamma}\kappa_i$, v_i, and $\vec{v}_i$ can be derived from (3.7). In order to account for the anisotropy in $\tilde{\gamma}$, the weighted curvature $\tilde{\kappa}_i$ is treated as an unknown. By the geometric expression $\vec{\kappa}_i = -\partial_{ss}\vec{x}_i$, the velocity law (3.7), and the relations between the vector-valued and scalar quantities $\tilde{\kappa}_i = \tilde{\gamma}\vec{\kappa}_i\cdot\vec{n}_i$ and $\vec{v}_i = v_i\vec{n}_i$, we obtain

$$\begin{aligned}
\vec{\kappa}_i &= -\partial_{ss}\vec{x}_i, && (3.8)\\
\tilde{\kappa}_i &= \tilde{\gamma}\vec{\kappa}_i\cdot\vec{n}_i, && (3.9)\\
v_i &= f_i - \beta\tilde{\kappa}_i + \partial_s(\nu\partial_s(\tilde{\kappa}_i)), && (3.10)\\
\vec{v}_i &= v_i\vec{n}_i. && (3.11)
\end{aligned}$$

Consider the discrete time instant t_m and time step $\triangle t_m := t_{m+1}-t_m$. We represent the next boundary Γ_i^{m+1} in terms of the current boundary Γ_i^m by updating the position vectors

$$\vec{x}_i^{\,m+1} \leftarrow \vec{x}_i^{\,m} + \triangle t_m\vec{v}_i^{\,m+1}. \tag{3.12}$$

In the time discretization, all the geometric quantities such as $\vec{n}_i$ and the differentiation ∂_s are evaluated on the *current* boundary Γ_i^m. In contrast to the geometric quantities, the unknowns $\vec{\kappa}_i$, $\tilde{\kappa}_i$, v_i, and $\vec{v}_i$ are treated implicitly. In particular, in view of (3.12), we define

$$\vec{\kappa}_i^{\,m+1} := -\partial_{ss}(\vec{x}_i^{\,m} + \triangle t_m\vec{v}_i^{\,m+1}). \tag{3.13}$$

To derive a weak formulation, we multiply (3.9), (3.10), (3.11), and (3.13) by test functions $\vec{\psi} \in \vec{H}^1(\Gamma_i)$ and $\psi \in H^1(\Gamma_i)$, and use integration by parts. Using the

notation $\langle\cdot,\cdot\rangle$ for the L^2 inner product over the current interfaces Γ_i^m, we arrive at the following set of semi-implicit equations:

$$\begin{aligned}
\langle\vec{\kappa}_i^{m+1},\vec{\psi}\rangle - \triangle t_m\langle\partial_s\vec{v}_i^{m+1},\partial_s\vec{\psi}\rangle &= \langle\partial_s\vec{x}_i^m,\partial_s\vec{\psi}\rangle && \forall\vec{\psi}\in\vec{H}^1(\Gamma_i^m),\\
\langle\tilde{\kappa}_i^{m+1},\psi\rangle - \langle\tilde{\gamma}\vec{\kappa}_i^{m+1}\cdot\vec{n}_i,\psi\rangle &= 0 && \forall\psi\in H^1(\Gamma_i^m),\\
\langle v_i^{m+1},\psi\rangle + \langle\nu\partial_s(\tilde{\kappa}_i^{m+1}),\partial_s\psi\rangle + \langle\beta\tilde{\kappa}_i^{m+1},\psi\rangle &= \langle f_i,\psi\rangle && \forall\psi\in H^1(\Gamma_i^m),\\
\langle\vec{v}_i^{m+1},\vec{\psi}\rangle - \langle v_i^{m+1}\vec{n}_i,\vec{\psi}\rangle &= 0 && \forall\vec{\psi}\in\vec{H}^1(\Gamma_i^m).
\end{aligned}$$

Note that in the above formulation, the adatom densities are needed only for computing f_i. To discretize in space, we consider a polygonal curve $\Gamma_{i,h}^m$ approximating Γ_i at time t_m. The polygonal segments are thought of as finite elements. We denote by $\vec{n}_{i,h}$ the unit normal to $\Gamma_{i,h}^m$ pointing to the lower terrace. Denote by $\mathbb{W}_h^m\subseteq H^1(\Gamma_{i,h}^m)$ the finite element space of globally continuous, piecewise linear functions with corresponding nodal basis functions $(\psi_k)_{k=1}^K$, where K is the number of degrees of freedom. By $\vec{\mathbb{W}}_h^m\subseteq\vec{H}^1(\Gamma_{i,h}^m)$ we denote the finite element space of vector-valued functions with nodal basis functions $(\vec{\psi}_k^q)_{k=1,\dots,K}^{q=1,2}$, where $\vec{\psi}_k^q=\psi_k\vec{e}_q$ with ψ_k the scalar basis function defined above and $(\vec{e}_1,\vec{e}_2)$ the standard basis in $\mathbb{R}^2$. Upon expanding the functions $\vec{\kappa}_i^{m+1}$, $\tilde{\kappa}_i^{m+1}$, v_i^{m+1}, $\vec{v}_i^{m+1}$ in terms of the basis functions and testing against all discrete test functions, a discretization reads

$$\begin{aligned}
\langle\vec{\kappa}_{i,h}^{m+1},\vec{\psi}_h\rangle - \triangle t_m\langle\partial_s\vec{v}_{i,h}^{m+1},\partial_s\vec{\psi}_h\rangle &= \langle\partial_s\vec{x}_i^m,\partial_s\vec{\psi}_h\rangle && \forall\vec{\psi}_h\in\vec{\mathbb{W}}_h^m,\\
\langle\tilde{\kappa}_{i,h}^{m+1},\psi_h\rangle - \langle\tilde{\gamma}\vec{\kappa}_{i,h}^{m+1}\cdot\vec{n}_{i,h},\psi_h\rangle &= 0 && \forall\psi_h\in\mathbb{W}_h^m,\\
\langle v_{i,h}^{m+1},\psi_h\rangle + \langle\nu\partial_s(\tilde{\kappa}_{i,h}^{m+1}),\partial_s\psi_h\rangle + \langle\beta\tilde{\kappa}_{i,h}^{m+1},\psi_h\rangle &= \langle f_i,\psi_h\rangle && \forall\psi_h\in\mathbb{W}_h^m,\\
\langle\vec{v}_{i,h}^{m+1},\vec{\psi}_h\rangle - \langle v_{i,h}^{m+1}\vec{n}_{i,h},\vec{\psi}_h\rangle &= 0 && \forall\vec{\psi}_h\in\vec{\mathbb{W}}_h^m.
\end{aligned}$$

In order to show uniqueness of the discrete system it is sufficient to show that if $(\vec{\kappa}_{i,h}^{m+1},\tilde{\kappa}_{i,h}^{m+1},\vec{v}_{i,h}^{m+1},v_{i,h}^{m+1})$ satisfies

$$\langle\vec{\kappa}_{i,h}^{m+1},\vec{\psi}_h\rangle - \triangle t_m\langle\partial_s\vec{v}_{i,h}^{m+1},\partial_s\vec{\psi}_h\rangle = 0 \qquad \forall\vec{\psi}_h\in\vec{\mathbb{W}}_h^m, \tag{3.14}$$

$$\langle\tilde{\kappa}_{i,h}^{m+1},\psi_h\rangle - \langle\tilde{\gamma}\vec{\kappa}_{i,h}^{m+1}\cdot\vec{n}_{i,h},\psi_h\rangle = 0 \qquad \forall\psi_h\in\mathbb{W}_h^m, \tag{3.15}$$

$$\langle v_{i,h}^{m+1},\psi_h\rangle + \langle\nu\partial_s(\tilde{\kappa}_{i,h}^{m+1}),\partial_s\psi_h\rangle + \langle\beta\tilde{\kappa}_{i,h}^{m+1},\psi_h\rangle = 0 \qquad \forall\psi_h\in\mathbb{W}_h^m, \tag{3.16}$$

$$\langle\vec{v}_{i,h}^{m+1},\vec{\psi}_h\rangle - \langle v_{i,h}^{m+1}\vec{n}_{i,h},\vec{\psi}_h\rangle = 0 \qquad \forall\vec{\psi}_h\in\vec{\mathbb{W}}_h^m. \tag{3.17}$$

then $(\vec{\kappa}_{i,h}^{m+1},\tilde{\kappa}_{i,h}^{m+1},\vec{v}_{i,h}^{m+1},v_{i,h}^{m+1})=0$. In the following we drop the time step in the notation. Inserting $\vec{\psi}_h=\vec{\kappa}_{i,h}$ in (3.14) and using an inverse inequality one obtains

$$\begin{aligned}
\|\vec{\kappa}_{i,h}\|^2_{L^2(\Gamma_{i,h}^m)} &\leq \triangle t_m\|\partial_s\vec{v}_{i,h}\|_{L^2(\Gamma_{i,h}^m)}\|\partial_s\vec{\kappa}_{i,h}\|_{L^2(\Gamma_{i,h}^m)}\\
&\leq C\triangle t_m h^{-2}\|\vec{v}_{i,h}\|_{L^2(\Gamma_{i,h}^m)}\|\vec{\kappa}_{i,h}\|_{L^2(\Gamma_{i,h}^m)},
\end{aligned}$$

where h is a lower bound on the lengths of the segments of $\Gamma_{i,h}^m$ and C is a generic constant. With $\vec{\psi}_h=\vec{v}_{i,h}$ in (3.17) one gets $\|\vec{v}_{i,h}\|_{L^2(\Gamma_{i,h}^m)}\leq\|v_{i,h}\|_{L^2(\Gamma_{i,h}^m)}$ and

therefore

$$\|\vec{\kappa}_{i,h}\|_{L^2(\Gamma^m_{i,h})} \leq C\triangle t_m h^{-2}\|v_{i,h}\|_{L^2(\Gamma^m_{i,h})}. \tag{3.18}$$

Using $\psi_h = v_{i,h}$ in (3.16) and applying again an inverse inequality one gets

$$\|v_{i,h}\|^2_{L^2(\Gamma^m_{i,h})} \leq C(1+h^{-2})\|v_{i,h}\|_{L^2(\Gamma^m_{i,h})}\|\tilde{\kappa}_{i,h}\|_{L^2(\Gamma^m_{i,h})},$$

where we assume $\max(\nu,\beta) \leq C$. With $\psi_h = \tilde{\kappa}_{i,h}$ in (3.15) one gets $\|\tilde{\kappa}_{i,h}\|_{L^2(\Gamma^m_{i,h})} \leq \|\tilde{\gamma}\vec{\kappa}_{i,h}\|_{L^2(\Gamma^m_{i,h})} \leq C\|\vec{\kappa}_{i,h}\|_{L^2(\Gamma^m_{i,h})}$, where we assume $\tilde{\gamma} \leq C$ and therefore get

$$\|v_{i,h}\|_{L^2(\Gamma^m_{i,h})} \leq C(1+h^{-2})\|\vec{\kappa}_{i,h}\|_{L^2(\Gamma^m_{i,h})}.$$

Inserting this into (3.18) yields $\vec{\kappa}_{i,h} = 0$ provided that $C\triangle t_m h^{-2}(1+h^{-2}) < 1$. This indicates that the parameters $\triangle t_m$ and h may not be chosen independently of each other and the way in which they are related certainly will influence the stability of the scheme. The timestep restriction following from this rough estimations is $\Delta t \sim h^4$, which is not needed in practice, see Section 4. From $\vec{\kappa}_{i,h} = 0$ it follows $\tilde{\gamma}\kappa_{i,h} = 0$, $\vec{v}_{i,h} = 0$ and $v_{i,h} = 0$.

The discrete scheme is now translated into a matrix-vector system by using the nodal bases (ψ_k) and $(\vec{\psi}^q_k)$ to obtain the mass, stiffness, and normal matrices, and the load vector

$$\begin{aligned}
&\boldsymbol{M} = (M_{kl}), \quad M_{kl} = \langle \psi_k, \psi_l\rangle; && \boldsymbol{M}_\beta = (M_{\beta,kl}), M_{\beta,kl} = \langle \beta\psi_k, \psi_l\rangle;\\
&\vec{\boldsymbol{M}} = (\vec{M}_{kl}), \quad \vec{M}_{kl} = (M^{qr}_{kl}) = (\delta_{qr}M_{kl}); && \boldsymbol{A} = (A_{kl}), \quad A_{kl} = \langle \partial_s\psi_k, \partial_s\psi_l\rangle;\\
&\boldsymbol{A}_\nu = (A_{\nu,kl}), \quad A_{\nu,kl} = \langle \nu\partial_s\psi_k, \partial_s\psi_l\rangle; && \vec{\boldsymbol{A}} = (\vec{A}_{kl}), \quad \vec{A}_{kl} = (A^{qr}_{kl}) = (\delta_{qr}A_{kl});\\
&\vec{\boldsymbol{N}} = (\vec{N}_{kl}), \quad \vec{N}_{kl} = (N^q_{kl}) = (\langle \psi_k, \psi_l n^q_{i,h}\rangle); && F = (F_k), \quad F_k = \langle f_i, \psi_k\rangle;\\
&\vec{\boldsymbol{N}}_{\tilde{\gamma}} = (\vec{N}_{\tilde{\gamma},kl}), \ \vec{N}_{\tilde{\gamma},kl} = (N^q_{\tilde{\gamma},kl}) = (\langle \psi_k, \tilde{\gamma}\psi_l n^q_{i,h}\rangle);
\end{aligned}$$

where the index ranges are $1 \leq k,l \leq K$ and $1 \leq q,r \leq 2$, $\delta_{qr} = \vec{e}_q \cdot \vec{e}_r$ is the Kronecker symbol, and $n^q_{i,h} = \vec{n}_{i,h} \cdot \vec{e}_q$ is the qth spatial component of the normal. The linear system takes now the following matrix form.

$$\begin{pmatrix} \vec{\boldsymbol{M}} & \boldsymbol{0} & \boldsymbol{0} & -\vec{\boldsymbol{N}} \\ \boldsymbol{0} & \boldsymbol{M} & -\vec{\boldsymbol{N}}^t_{\tilde{\gamma}} & \boldsymbol{0} \\ -\triangle t_m\vec{\boldsymbol{A}} & \boldsymbol{0} & \vec{\boldsymbol{M}} & \boldsymbol{0} \\ \boldsymbol{0} & \boldsymbol{A}_\nu + \boldsymbol{M}_\beta & \boldsymbol{0} & \boldsymbol{M} \end{pmatrix} \begin{pmatrix} \vec{V}_i \\ \vec{K}_i \\ \vec{K}_i \\ V_i \end{pmatrix} = \begin{pmatrix} 0 \\ 0 \\ \vec{\boldsymbol{A}}\vec{X}^m_i \\ F \end{pmatrix}$$

With this arrangement, a Schur complement equation for $\vec{K}_i, V_i$ reads

$$\boldsymbol{S}\begin{pmatrix} \vec{K}_i \\ V_i \end{pmatrix} = \begin{pmatrix} \vec{\boldsymbol{A}}\vec{X}^m_i \\ F \end{pmatrix},$$

where

$$\boldsymbol{S} = \begin{pmatrix} \vec{\boldsymbol{M}} & \boldsymbol{0} \\ \boldsymbol{0} & \boldsymbol{M} \end{pmatrix} - \begin{pmatrix} -\triangle t_m \vec{\boldsymbol{A}} & \boldsymbol{0} \\ \boldsymbol{0} & \boldsymbol{A}_\nu + \boldsymbol{M}_\beta \end{pmatrix} \begin{pmatrix} \vec{\boldsymbol{M}} & \boldsymbol{0} \\ \boldsymbol{0} & \boldsymbol{M} \end{pmatrix}^{-1} \begin{pmatrix} \boldsymbol{0} & -\vec{\boldsymbol{N}} \\ -\vec{\boldsymbol{N}}_{\tilde{\gamma}}^t & \boldsymbol{0} \end{pmatrix}$$
$$= \begin{pmatrix} \vec{\boldsymbol{M}} & -\triangle t_m \vec{\boldsymbol{A}} \vec{\boldsymbol{M}}^{-1} \vec{\boldsymbol{N}} \\ (\boldsymbol{A}_\nu + \boldsymbol{M}_\beta) \boldsymbol{M}^{-1} \vec{\boldsymbol{N}}_{\tilde{\gamma}}^t & \boldsymbol{M} \end{pmatrix}.$$

The above formulation in turn gives rise to the final Schur complement equation for the single unknown V_i:

$$\left(\triangle t_m (\boldsymbol{A}_\nu + \boldsymbol{M}_\beta) \boldsymbol{M}^{-1} \vec{\boldsymbol{N}}_{\tilde{\gamma}}^t \vec{\boldsymbol{M}}^{-1} \vec{\boldsymbol{A}} \vec{\boldsymbol{M}}^{-1} \vec{\boldsymbol{N}} + \boldsymbol{M} \right) V_i$$
$$= F - (\boldsymbol{A}_\nu + \boldsymbol{M}_\beta) \boldsymbol{M}^{-1} \vec{\boldsymbol{N}}_{\tilde{\gamma}}^t \vec{\boldsymbol{M}}^{-1} \vec{\boldsymbol{A}} \vec{X}_i^m. \quad (3.19)$$

Once V_i is obtained, the unknown $\vec{V}_i$ is easily computed by solving

$$\vec{\boldsymbol{M}} \vec{V}_i = \vec{\boldsymbol{N}} V_i, \quad (3.20)$$

$\vec{\boldsymbol{M}}$ being invertible, and then $\vec{X}_i$ is updated through

$$\vec{X}_i \leftarrow \vec{X}_i + \triangle t_m \vec{V}_i. \quad (3.21)$$

The weighted curvature, which is needed as data in the adatom diffusion problem, is now computed for accuracy reasons on the new interface $\Gamma_{i,h}^{m+1}$ instead of the old interface $\Gamma_{i,h}^m$. To this end, we use the same formulation as above but with all the geometric quantities defined for $\Gamma_{i,h}^{m+1}$ replacing $\Gamma_{i,h}^m$. We obtain the following problem

$$\langle \vec{\kappa}_{i,h}, \vec{\psi}_h \rangle = \langle \partial_s \vec{x}_i^{m+1}, \partial_s \vec{\psi}_h \rangle \qquad \forall \vec{\psi}_h \in \vec{\mathbb{W}}_h^{m+1},$$
$$\langle \tilde{\kappa}_{i,h}, \psi_h \rangle - \langle \tilde{\gamma} \vec{\kappa}_{i,h} \cdot \vec{n}_{i,h}, \psi_h \rangle = 0 \qquad \forall \psi_h \in \mathbb{W}_h^{m+1}.$$

Again, the system can be written equivalently in matrix form, where the matrices are now defined in terms of the basis functions on $\Gamma_{i,h}^{m+1}$

$$\begin{pmatrix} \boldsymbol{M} & -\vec{\boldsymbol{N}}_{\tilde{\gamma}}^t \\ 0 & \vec{\boldsymbol{M}} \end{pmatrix} \begin{pmatrix} \tilde{K}_i \\ \vec{K}_i \end{pmatrix} = \begin{pmatrix} 0 \\ \vec{\boldsymbol{A}} \vec{X}_i^{m+1} \end{pmatrix}.$$

This leads to

$$\tilde{K}_i = -\boldsymbol{M}^{-1} \vec{\boldsymbol{N}}_{\tilde{\gamma}} \vec{\boldsymbol{M}}^{-1} \vec{\boldsymbol{A}} \vec{X}_i^{m+1}. \quad (3.22)$$

In summary, the subproblem of boundary evolution consists of solving N decoupled problems one for each interface $\Gamma_{i,h}$, $i = 1, \ldots, N$. For the adatom diffusion problem the new interfaces $\Gamma_{i,h}^{m+1}$ and the weighted curvatures $\tilde{\kappa}_{i,h}^{m+1} = \tilde{\gamma} \kappa_{i,h}^{m+1}$ will enter.

3.3. Implementation

The method is implemented in ALBERT [25]. The two-dimensional diffusion problem and the one-dimensional boundary evolution problem are coupled via a TCP/IP port. Adaptivity in space and time is used for the adatom diffusion as well as the boundary evolution. Thereby heuristic criteria are employed which ensure that the 1d and 2d meshes are locally of the same size. In order to trace the height of the terraces we mark all 2d elements by the discrete height according to the initial condition and update this marking in each time step.

4. Numerical results

Numerical tests of the algorithms described in Section 3 have been presented in [1, 2, 27]. In [26], the algorithm is used to simulate Ostwald ripening using 400 islands. Here we will demonstrate, how the method can be used to investigate the influence of anisotropy on the shape of growing monolayer islands.

STM topographs of adatom islands on Pt(111) exhibit a dramatic variability [28] (Fig. 3.1, p. 62). In our numerical study we qualitatively analyze the interplay between energetic and kinetic effects on the shape of such growing islands. We consider an underlying sixfold symmetry in the edge free energy γ. Different diffusion coefficients along A- and B-steps (see [28] (Fig. 2.1, p. 15)) are modeled by an anisotropic step edge mobility ν with threefold symmetry. Furthermore we consider different attachment-detachment rates on A- and B-steps, modeled by ansiotropic attachment-detachment rates $k_\pm$ also exhibiting a threefold symmetry in the kinetic coefficients.

4.1. Anisotropies

The anisotropic mobility ν, the anisotropic attachment/detachment rates k_+, k_- and the anisotropic edge energy γ are given in terms of an orientation dependent anisotropy function $f(\theta)$ as:

$$\nu(\theta) = \nu_0 f(\theta), \tag{4.1}$$

$$k_+(\theta) = k_-(\theta) = k_0 f(\theta), \tag{4.2}$$

$$\gamma(\theta) = \gamma_0 f(\theta). \tag{4.3}$$

We will use anisotropy functions of the following form:

$$f_1(\theta) = \frac{1 + a\cos^2(\frac{k}{2}(\theta + \alpha))}{1 + a}, \tag{4.4}$$

$$f_2(\theta) = 1 + a\cos(k(\theta + \alpha)), \tag{4.5}$$

where α is the angle between the symmetry axes and the coordinate system, k is the number of symmetry axes and $a \geq 0$ is a measure for the strength of the anisotropy. An anisotropy of the type f_1 is used for the edge diffusion mobility and the attachment-detachment rates, whereas f_2 is used to model the anisotropic edge energy γ, see Fig. 3 and Fig. 4.

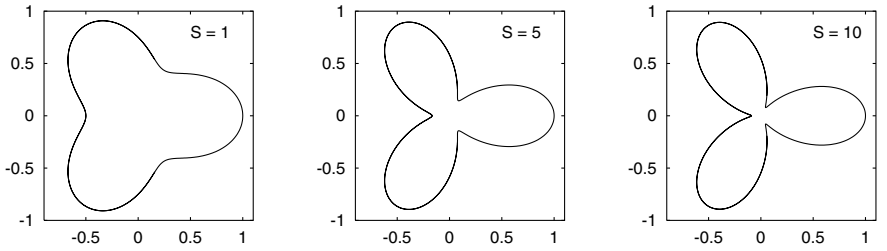

FIGURE 3. Polar plot of the anisotropy function given in Eq. (4.4) with threefold symmetry ($k = 3$), $\alpha = 0$ and $a = 1$, 5, 10. This anisotropy will be used to model the anisotropic attachment-detachment rates k_+, k_- and the anisotropic mobility ν of the edge diffusion.

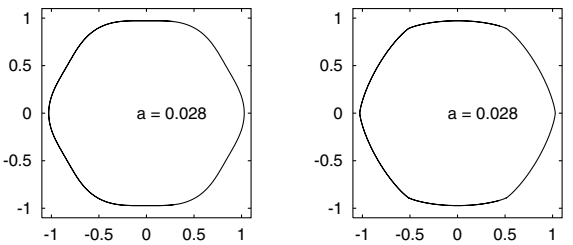

FIGURE 4. Polar plot of the anisotropy function given in Eq. (4.5) with sixfold symmetry ($k = 6$), $\alpha = 0$ and strength $a = 0.028$ (left); corresponding Wulff shape (right). This anisotropy will be used to model the anisotropic edge energy γ.

4.2. Simulations

The following parameters are used in the simulations:

- Initial geometry: a single island with area 4π is sitting on a substrate of size 10×10. The initial shape of the island is the Wulff shape defined by the anisotropic edge energy γ.
- Model parameters: Deposition flux $F = 1$, Diffusion constant $D = 10^5$, equilibrium density at a straight step $\rho^* = 10^{-4}$, $\gamma_0 = 0.1$, $\nu_0 = 1.0$, $k_0 = 10^4$.
- Anisotropies (see Eqs. (4.4,4.5)):
  - Edge energy $\gamma(\theta) = \gamma_0 f_2(\theta)$, with $k = 6$, $a = 0.028$.
  - Edge mobility $\nu(\theta) = \nu_0 f_1(\theta)$, with $k = 3$ and different values of the strength a.
  - Attachment-detachment rates $k_+(\theta) = k_-(\theta) = k_0 f_1(\theta)$, with $k = 3$ and different values for the strength a.

  For the mobility ν and for $k_\pm$ we always use the same anisotropy strength a.

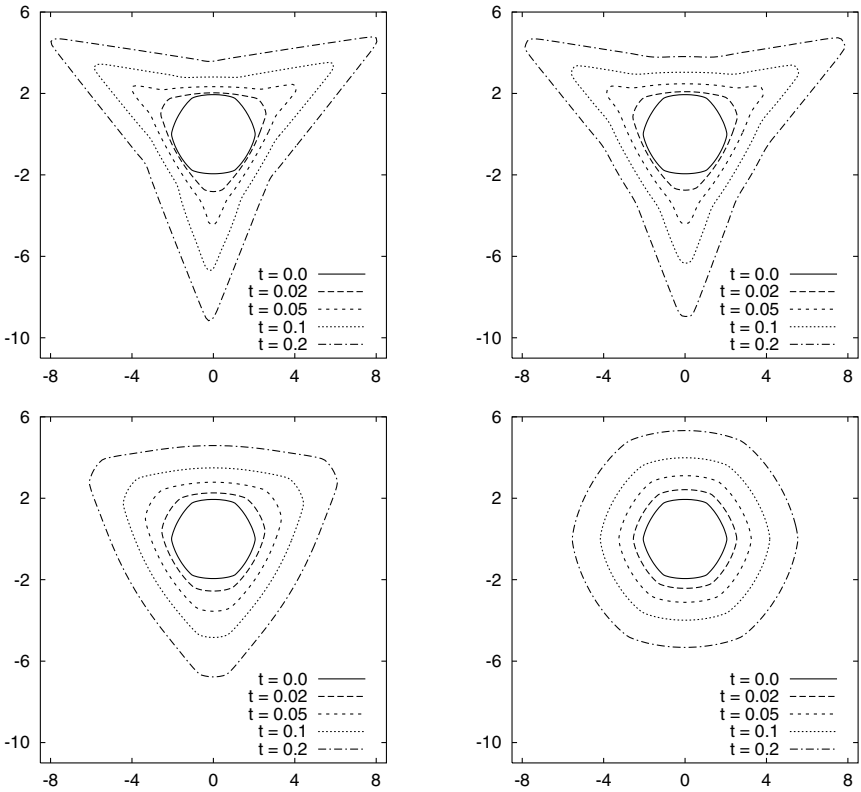

FIGURE 5. Anisotropic growth of a single island: the shape evolution depends strongly on the strength a (see Eq. (4.4)) of the attachment-detachment anisotropy. From top left to bottom right: $a = 10$, $a = 5$, $a = 1$, and $a = 0$.

- Discretization: The timestep during growth is $\Delta t = 10^{-4}$. During relaxation the time step is chosen adaptively depending on the maximum of the velocity of the boundary. The initial 1d-mesh has 128 grid points, i.e., the 1d-mesh size $h \approx 0.1$. The 1d-mesh size is kept approximately constant during growth. The 2d-mesh is refined along the step edge such that the 1d-mesh size is about three times larger then the 2d-mesh size, i.e., a 1d-element intersects approximately three 2d-elements.

As shown in Fig. 5, the shape of the growing island depends strongly on the strength a of the attachment-detachment ansisotropy. If $a = 0$, i.e., the attachment-detachment rates are constant, the shape of the island does stay close to the Wulff shape defined by the anisotropic edge energy γ. With growing anisotropy of the

attachment-detachment rates, the shape becomes triangular and even convex, resembling the pictures known from experiments.

If the deposition flux is turned off, the island relaxes to its equilibrium shape, as shown in Fig. 6. As expected, the adatom density is discontinuous at the island boundaries, see Fig. 7.

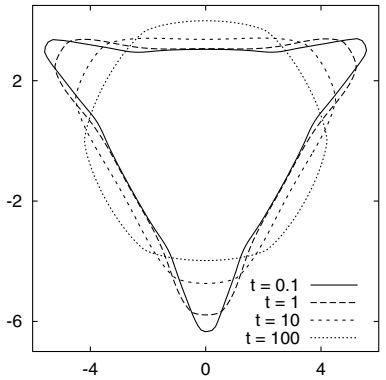

FIGURE 6. Anisotropic growth and relaxation of a single island: the deposition flux is turned off at $t = 0.1$. Attachment anisotropy with strength $a = 5$

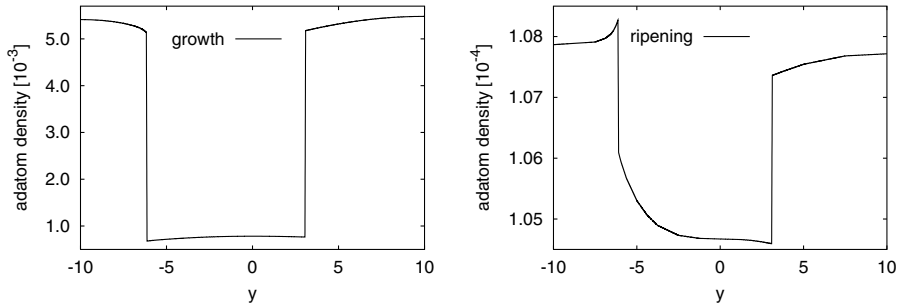

FIGURE 7. Adatom density profile at $x = 0.0$: the density is discontinuous at the island boundary. During growth ($t = 0.1$), the sum of the normal fluxes is always positive but is higher at the corner of the island (at $y \approx -6.1$), see left figure. During relaxation ($t = 0.14$) the sum of the normal fluxes is negative at the corner (at $y \approx -6.1$) but positive at the flat site ($y \approx 3.1$), as shown in the right figure.

Acknowledgment

We would like to thank Joachim Krug for the stimulating discussions we had at the MFO Mini-Workshop on *Multiscale Modelling in Epitaxial Growth* about the interplay of the different anisotropies on the island shape.

References

[1] E. Bänsch, F. Haußer, O. Lakkis, B. Li, A. Voigt, *Finite element method for epitaxial growth with attachment-detachment kinetics* J. of Comput. Phys. **194** (2004), 409–434.

[2] E. Bänsch, F. Haußer, A. Voigt, *Finite Element Method for Epitaxial Growth with thermodynamic boundary conditions* SIAM J. Sci. Comput. (2005), (to appear).

[3] W.K. Burton, N. Cabrera, F.C. Frank, *The growth of crystals and the equilibrium of their surfaces* Phil. Trans. Roy. Soc. London Ser. A **243** (1951), 299–358.

[4] J. Krug, (this volume).

[5] M.F. Gyure, C. Ratsch, B. Merriman, R.E. Caflisch, S. Osher, J. Zinck, D. Vvedensky, *Level set method for the simulation of epitaxial phenomena.* Phys. Rev. E **58** (1998), R6931.

[6] R.E. Caflisch, M.F. Gyure, B. Merriman, S. Osher, C. Ratsch, D. Vvedensky, J. Zink, *Island dynamics and the level set method for epitaxial growth.* Appl. Math. Lett. **12** (1999), 13–22.

[7] S. Chen, B. Merriman, M. Kang, R.E. Caflisch, C. Ratsch, L.-T. Cheng, M. Gyure, R.P. Fedkiw, C. Anderson, S. Osher, *Level Set Method for Thin Film Epitaxial Growth.* J. Comp. Phys. **167** (2001), 475–500.

[8] M. Peterson, C. Ratsch, R.E. Caflisch, A. Zangwill, *Level set approach to reversible epitaxial growth.* Phys. Rev. E **64** (2001), 061602.

[9] C. Ratsch, M.F. Gyure, R.E. Caflisch, F. Gibou, M. Peterson, M. Kang, J. Garcia, D.D. Vvedensky, *Level-set method for island dynamics in epitaxial growth.* Phys. Rev. B **65** (2002), 195403.

[10] D.L. Chopp, *A level-set method for simulating island coarsening.* J. Comp. Phys. **162** (2000), 104–122.

[11] F. Liu, H. Metiu, *Stability and kinetics of step motion on crystal surfaces* Phys. Rev. E **49** (1997), 2601–2616.

[12] A. Karma, M. Plapp, *Spiral surface growth without desorption* Phys. Rev. Lett. **81** (1998), 4444–4447.

[13] A. Rätz, A. Voigt, *Phase-Field Model for Island Dynamics* Appl. Anal. **83** (2004), 1015–1025.

[14] O. Pierre-Louis, *Phase-field models for step flow* Phys. Rev. E **68** (2003), 020601.

[15] F. Otto. P. Penzler, A. Rätz, T. Rump, A. Voigt, *A diffuse-interface approximation for step flow in epitaxial growth.* Nonlin. **17** (2004), 477–491.

[16] F. Otto. P. Penzler, T. Rump, (this volume).

[17] A. Rätz, A. Voigt, *A Phase-Field Model for attachment-detachment kinetics in epitaxial growth.* Euro. J. Appl. Math. (2004), (to appear).

[18] P. Smereka, *Semi-implicit level set methods for motion by mean curvature and surface diffusion* J. Sci. Comp. **19** (2003), 439–456.

[19] U. Clarenz, F. Haußer, M. Rumpf, A. Voigt, U. Weikard, (this volume).

[20] A. Rätz, A. Voigt, (this volume).

[21] A. Schmidt, *Computation of three dimensional dendrites with finite elements* J. of Comput. Phys. **125** (1996), 293–312.

[22] A.-K. Tornberg, *Interface tracking methods with applications to multiphase flow* PhD thesis, NADA, KTH, Stockholm, Sweden (2000).

[23] E. Bänsch, P. Morin, R.H. Nochetto, *A Finite Element Method for surface diffusion: the parametric case* J. of Comput. Phys. **203** (2005), 321–343.

[24] G. Dziuk, *An algorithm for evolutionary surfaces* Numer. Math. **58** (1991), 603–611.

[25] A. Schmidt, K.G. Siebert, *Albert – software for scientific computations and applications* Acta Math. Univ. Comenianae **70** (2001), 205–122.

[26] F. Haußer, A. Voigt, (this volume).

[27] F. Haußer, A. Voigt, *Finite element method for epitaxial island growth.* J. Crys. Growth **266** (2004), 381–387.

[28] M. Michely, J. Krug, *Island, Mounds and Atoms.* Springer, 2004

Frank Haußer and Axel Voigt
Crystal Growth group
research center caesar
Ludwig-Erhard-Allee 2
D-53175 Bonn, Germany
e-mail: hausser@caesar.de
e-mail: voigt@caesar.de

International Series of Numerical Mathematics, Vol. 149, 115–125

Edge Diffusion in Phase-Field Models for Epitaxial Growth

Andreas Rätz and Axel Voigt

Abstract. A phase-field model is proposed to describe step-flow in epitaxial growth. In this model the motion of steps or island boundaries of discrete atomic layers on an epitaxial growing film is determined by the time evolution of an introduced phase-field variable. We use formally matched asymptotic expansion to determine the asymptotic limit of vanishing interfacial thickness and show the reduction to classical sharp interface models of Burton-Cabrera-Frank type with edge diffusion.

Mathematics Subject Classification (2000). Primary 35R35; Secondary 80A22.

Keywords. step-flow model; phase-field approximation; edge diffusion.

1. Model description

In the classical Burton-Cabrera-Frank model [3] step-edges are assumed to act as a perfect sink, i.e., the kinetics of attachment of an adatom at a step-edge is infinitely fast. We will concentrate on this assumption and only additionally include edge-diffusion, diffusion of edge-adatoms along step-edges. One can think of step-edges as an energy sink along which edge-adatoms are able to diffuse. Edge-adatoms then tend to attach to kinks, a site, at which point they can be considered as being part of the crystal. The mechanism of edge-diffusion suppresses the onset of an instability leading to fractal-like growth. Thus edge-diffusion yields a smoothing of the step-edges. For a detailed description of step flow dynamics we refer to [8].

Denote by $\rho_i = \rho_i(x, y, t)$ the adatom density on island or terrace $\Omega_i \subset \mathbb{R}^2$ ($i = 0, \ldots, N$ the discrete height of the layers). The adatom diffusion on an island or terrace is described by the diffusion equation for the adatom density

$$\partial_t \rho_i - \nabla \cdot (D \nabla \rho_i) = F - \tau^{-1} \rho_i \qquad \text{in } \Omega_i(t), \quad i = 0, \ldots, N, \tag{1.1}$$

where D is the diffusion coefficient, F is the deposition flux rate, and τ^{-1} is the desorption rate. We assume that the adatom density satisfies the following

thermodynamic boundary condition on the step-edges or island boundaries $\Gamma_i = \overline{\Omega}_i \cap \overline{\Omega}_{i-1}$ for $i = 1, \ldots, N$:

$$\rho_i = \rho_{i-1} = \rho^*(1 + \tilde{\gamma}\kappa_i), \tag{1.2}$$

where κ_i is the curvature of the boundary $\Gamma_i(t)$; ρ^* and $\tilde{\gamma}$ are two positive constants. The constant ρ^* is a thermodynamic equilibrium value for straight steps, and the constant $\tilde{\gamma}$ is proportional to the stiffness of the boundary $\Gamma_i(t)$. For the description of the moving boundaries, we assume the following law for the normal velocity v_i of the step-edges or island boundary $\Gamma_i(t)$:

$$v_i = -D\nabla\rho_i \cdot \vec{n}_i + D\nabla\rho_{i-1} \cdot \vec{n}_i + \nu\partial_{s_i s_i}\kappa_i, \tag{1.3}$$

where $\vec{n}_i$ is the unit normal pointing from the upper to lower terrace and v_i the normal velocity of the boundary $\Gamma_i(t)$ with the convention that $v_i > 0$ if the movement of $\Gamma_i(t)$ is in the direction of $\vec{n}_i$. Furthermore $\partial_{s_i s_i}\kappa_i$ denotes the second tangential derivative of the curvature κ_i, and ν is a mobility coefficient. This surface diffusion term models edge-diffusion, diffusion of edge-adatoms along step-edges and yields a smoothing of step-edges with nonconstant curvature and is furthermore mass conserving.

Various numerical approaches are discussed in the literature for this system. In [1, 2] a front tracking algorithm is introduced. Thereby the geometric evolution law (1.3) is solved by parametric finite elements and coupled to the adatom diffusion on terraces via a penalty approach. A level-set method where the surface diffusion term in (1.3) is approximated by $\nu(\kappa_i - \overline{\kappa}_i)$, with $\overline{\kappa}_i$ the averaged curvature, is used in [13]. We will introduce a phase-field model. Phase-field models for diffusion limited situations of epitaxial growth without edge-diffusion were already used in [10, 7, 12, 11]. In this paper edge-diffusion is incorporated into the model described in [12]. This is done by a mobility function, which increases the mobility at the step-edges. The treatment in the asymptotic analysis is similar to the one introduced in [6] for a modified Mullins-Sekerka model. The idea of an increased mobility was also introduced in [4, 5] for a Cahn-Hillard approximation for motion by surface diffusion. The outline of the paper is as follows: Section 2 describes the phase-field model. Afterwards, in Section 3 it is demonstrated that the Burton-Cabrera-Frank model with thermodynamic boundary conditions and edge-diffusion (1.1)–(1.3) may be obtained by formal asymptotics.

2. Phase-field approximation

Let $\Omega = \cup_{i=0}^{N}\overline{\Omega}_i$ denote the film domain. We will introduce an adatom density ρ^ϵ on Ω and treat each step Γ_i as a diffuse interface of interfacial thickness ϵ. Each terrace Ω_i^ϵ can now be seen as a phase of the system and can be described by a phase-field variable ϕ^ϵ. In this context ϕ^ϵ can be interpreted as a continuous height function of the growing film, cf. Figure 1.

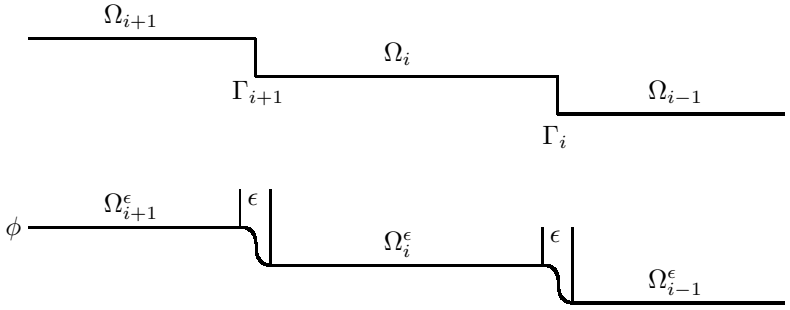

FIGURE 1. Relation between the terraces Ω_i and the phase-field variable ϕ.

We introduce a phase-field model consisting of the following coupled system for ρ^ϵ and ϕ^ϵ,

$$\partial_t \rho^\epsilon + \partial_t \phi^\epsilon = \nabla \cdot M(\phi^\epsilon, \epsilon) \nabla \rho^\epsilon + F - \tau^{-1} \rho^\epsilon \quad \text{in} \quad \Omega, \tag{2.1}$$

$$\alpha \epsilon^2 \partial_t \phi^\epsilon = \epsilon^2 \Delta \phi^\epsilon - G'(\phi^\epsilon) + \frac{\epsilon}{\rho^* \tilde{\gamma}} (\rho^\epsilon - \rho^*) \quad \text{in} \quad \Omega \tag{2.2}$$

with the approximated adatom density and the phase-field variable

$$\rho^\epsilon = \rho^\epsilon(x, y, t; \epsilon),$$
$$\phi^\epsilon = \phi^\epsilon(x, y, t; \epsilon).$$

In the following we will drop the dependence on ϵ in the nomenclature and use ρ and ϕ also in the phase-field context. α is a constant, G is a multiwell potential, cf. Figure 2

$$G(\phi) = c(\phi - i)^2 (i + 1 - \phi)^2, \quad \phi \in [i, i+1], \quad i = 0, \ldots, N-1, \tag{2.3}$$

where c is a constant defined later and each minimum of G corresponds to a phase (terrace height) of the system. One obtains $G \in C^2(\mathbb{R})$, the periodicity

$$G(\phi + 1) = G(\phi) \quad \text{for} \quad \phi \in [0, N-1] \tag{2.4}$$

and the symmetry

$$G\left(i + \frac{1}{2} + \phi\right) = G\left(i + \frac{1}{2} - \phi\right) \qquad \text{for} \quad i = 0, \ldots, N-1. \tag{2.5}$$

By choosing a potential of this form we assume phase transition to occur only between terraces Ω_i and Ω_j with $|i - j| = 1$. The mobility function $M(\phi, \epsilon)$ is used for modeling the edge-diffusion. M is defined as

$$M(\phi, \epsilon) := D + \epsilon^{-1} N(\phi). \tag{2.6}$$

Here the periodic function N is assumed to satisfy

$$\mathrm{supp}N \subset \bigcup_{i=-\infty}^{+\infty} (i, i+1),$$

cf. Figure 2. So we choose

$$I := \bigcup_{i=0}^{N-1} \mathrm{supp}N\big|_{[i,i+1]}.$$

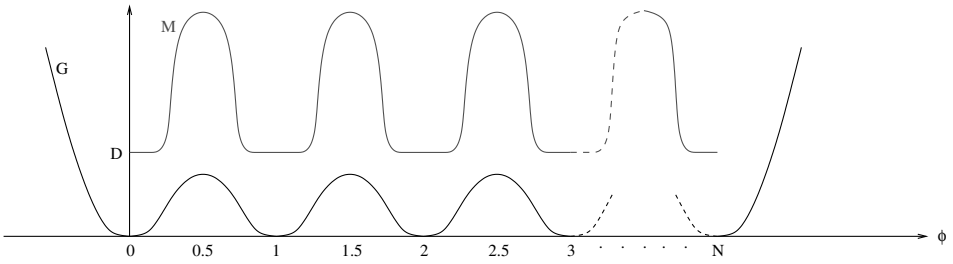

FIGURE 2. Double well potential G, mobility M.

Initial and boundary conditions for ρ and ϕ are set to be

$$\begin{aligned} \rho(x,y,0;\epsilon) &= \tilde{\rho}(x,y;\epsilon), \qquad \phi(x,y,0;\epsilon) = \tilde{\phi}(x,y;\epsilon), \qquad (x,y) \in \Omega, \\ \frac{\partial}{\partial n}\rho(x,y,t;\epsilon) &= 0, \qquad \frac{\partial}{\partial n}\phi(x,y,t;\epsilon) = 0, \qquad (x,y) \in \partial\Omega \end{aligned}$$

where $\tilde{\rho}$ and $\tilde{\phi}$ satisfy certain compatibility conditions. The interfaces are now defined by

$$\Gamma_i(t;\epsilon) := \left\{ (x,y) \in \Omega : \phi(x,y,t;\epsilon) = i - \frac{1}{2} \right\}, \quad i = 1, \ldots, N. \tag{2.7}$$

We will show that in the asymptotic limit for $\epsilon \to 0$ and $\alpha \to 0$ one obtains from this phase-field model the original sharp interface Burton-Cabrera-Frank model with thermodynamic boundary conditions and edge-diffusion (1.1)–(1.3).

3. Matched asymptotic expansion

3.1. Preliminaries

New coordinates are established in the neighborhoods of the curves Γ_i. To this end $r_i = r_i(x,y,t;\epsilon)$ is defined as the signed distance of (x,y) from $\Gamma_i(t;\epsilon)$, where $r_i < 0$, if $(x,y) \in \Omega_i$ and $r_i > 0$, if $(x,y) \in \Omega_{i-1}$. Then for $0 < \delta_i \ll 1$ there exists a neighborhood

$$U_i(t;\epsilon) = \{(x,y) \in \Omega : |r_i(x,y,t;\epsilon)| < \delta_i\} \tag{3.1}$$

of $\Gamma_i(t;\epsilon)$ such that a orthogonal curvilinear coordinate system (r_i, s_i) in U_i can be defined, where for $(x, y) \in \Gamma(t;\epsilon)$ one defines $s_i = s_i(x, y, t;\epsilon)$ to be the arc length along $\Gamma_i(t;\epsilon)$ to (x, y) from some point $(x_i, y_i) \in \Gamma_i(t;\epsilon)$ moving in the direction normal to Γ_i for proceeding time.

Now one chooses $\delta := \min_{i\in\{1,\dots,N\}} \delta_i$ and in addition $\delta > 0$ small enough in order to ensure the sets U_i being disjunct for all considered times. Then U_i is redefined by replacing in (3.1) δ_i by δ. Now one transforms ρ and ϕ to the new coordinate system:

$$\hat{\rho}(r_i, s_i, t;\epsilon) := \rho(x, y, t;\epsilon), \qquad (x, y) \in U_i(t;\epsilon),$$
$$\hat{\phi}(r_i, s_i, t;\epsilon) := \phi(x, y, t;\epsilon), \qquad (x, y) \in U_i(t;\epsilon).$$

Furthermore a stretched variable is introduced

$$z_i := \frac{r_i}{\epsilon}, \qquad i = 1, \dots, N, \tag{3.2}$$

and one defines

$$P(z_i, s_i, t;\epsilon) := \hat{\rho}(r_i, s_i, t;\epsilon),$$
$$\Phi(z_i, s_i, t;\epsilon) := \hat{\phi}(r_i, s_i, t;\epsilon).$$

In addition the following Taylor expansion approximations for small ϵ are assumed to be valid:

$$\rho(x, y, t;\epsilon) = \rho_0(x, y, t) + \epsilon\rho_1(x, y, t) + \cdots, \tag{3.3}$$
$$\hat{\rho}(r_i, s_i, t;\epsilon) = \hat{\rho}_0(r_i, s_i, t) + \epsilon\hat{\rho}_1(r_i, s_i, t) + \cdots, \qquad i = 1, \dots, N, \tag{3.4}$$
$$P(z_i, s_i, t;\epsilon) = P_0(z_i, s_i, t) + \epsilon P_1(z_i, s_i, t) + \cdots, \qquad i = 1, \dots, N, \tag{3.5}$$

and similarly

$$\phi(x, y, t;\epsilon) = \phi_0(x, y, t) + \epsilon\phi_1(x, y, t) + \cdots, \tag{3.6}$$
$$\hat{\phi}(r_i, s_i, t;\epsilon) = \hat{\phi}_0(r_i, s_i, t) + \epsilon\hat{\phi}_1(r_i, s_i, t) + \cdots, \qquad i = 1, \dots, N, \tag{3.7}$$
$$\Phi(z_i, s_i, t;\epsilon) = \Phi_0(z_i, s_i, t) + \epsilon\Phi_1(z_i, s_i, t) + \cdots, \qquad i = 1, \dots, N. \tag{3.8}$$

(3.3), (3.4), (3.6) and (3.7) are called outer expansions while (3.5) and (3.8) are called inner expansions. It is assumed that these hold simultaneously in some overlapping region and represent the same functions, which yields the matching conditions

$$\lim_{r_i\to\pm 0} \hat{\rho}_0(r_i, s_i, t) = \lim_{z_i\to\pm\infty} P_0(z_i, s_i, t), \qquad i = 1, \dots, N, \tag{3.9}$$
$$\lim_{r_i\to\pm 0} \partial_{r_i}\hat{\rho}_0(r_i, s_i, t) = \lim_{z_i\to\pm\infty} \partial_{z_i} P_1(z_i, s_i, t), \qquad i = 1, \dots, N, \tag{3.10}$$
$$\lim_{r_i\to\pm 0} \hat{\phi}_0(r_i, s_i, t) = \lim_{z_i\to\pm\infty} \Phi_0(z_i, s_i, t), \qquad i = 1, \dots, N, \tag{3.11}$$
$$\lim_{r_i\to\pm 0} \partial_{r_i}\hat{\phi}_0(r_i, s_i, t) = \lim_{z_i\to\pm\infty} \partial_{z_i}\Phi_1(z_i, s_i, t), \qquad i = 1, \dots, N. \tag{3.12}$$

Note that the functions ρ_j, $\hat{\rho}_j$, ϕ_j, $\hat{\phi}_j$, $j = 0, 1, 2, \dots$, need not to be smooth for $r_i = 0$. Only the existence of the one-sided limits is required. The transform of the

derivatives into the new coordinates (r_i, s_i) lead:

$$\partial_t \quad \text{is replaced by} \quad \partial_t + \partial_t r_i \partial_{r_i} + \partial_t s_i \partial_{s_i}, \tag{3.13}$$

$$\nabla \quad \text{is replaced by} \quad \nabla r_i \partial_{r_i} + \nabla s_i \partial_{s_i}, \tag{3.14}$$

$$\Delta \quad \text{is replaced by} \quad \partial_{r_i r_i} + |\nabla s_i|^2 \partial_{s_i s_i} + \Delta r_i \partial_{r_i} + \Delta s_i \partial_{s_i}, \tag{3.15}$$

where $|\nabla r_i| = 1$ was used. Let $n_i = n_i(s_i, t; \epsilon)$, $v_i = v_i(s_i, t; \epsilon)$ and $\kappa_i = \kappa_i(s_i, t; \epsilon)$ denote the normal, the normal velocity and the curvature, where the normal is pointing from the subset of $U_i(t; \epsilon)$ where $\phi > i - 1/2$ to the subset of $U_i(t; \epsilon)$ where $\phi < i - 1/2$, i.e., from the upper to the lower terrace as before. Then one has on $\Gamma_i(t, \epsilon)$:

$$\partial_t r_i(x, y, t; \epsilon) = -v_i(s_i(x, y, t; \epsilon), t; \epsilon), \qquad i = 1, \dots, N, \tag{3.16}$$

$$\Delta r_i(x, y, t; \epsilon) = \kappa_i(s_i(x, y, t; \epsilon), t; \epsilon), \qquad i = 1, \dots, N, \tag{3.17}$$

which yields in the coordinate system (z_i, s_i):

$$\partial_t \quad \text{is replaced by} \quad \partial_t - \frac{1}{\epsilon} v_i \partial_{z_i} + \partial_t s_i \partial_{s_i}, \tag{3.18}$$

$$\nabla \quad \text{is replaced by} \quad \frac{1}{\epsilon} \nabla r_i \partial_{z_i} + \nabla s_i \partial_{s_i}, \tag{3.19}$$

$$\Delta \quad \text{is replaced by} \quad \frac{1}{\epsilon^2} \partial_{z_i z_i} + |\nabla s_i|^2 \partial_{s_i s_i} + \frac{1}{\epsilon} \kappa_i \partial_{z_i} + \Delta s_i \partial_{s_i}. \tag{3.20}$$

3.2. Outer approximation

Inserting the outer expansions into the system (2.1)–(2.2) leads to:
$\mathcal{O}(\epsilon^{-1})$**:**

$$\nabla \cdot (N(\phi_0) \nabla \rho_0) = 0; \tag{3.21}$$

$\mathcal{O}(1)$**:**

$$\partial_t \rho_0 + \partial_t \phi_0 = \nabla \cdot ((N'(\phi_0)\phi_1 + D) \nabla \rho_0) + F - \tau^{-1} \rho_0, \tag{3.22}$$

$$G'(\phi_0) = 0. \tag{3.23}$$

The solutions to equation (3.23) are

$$\phi_0 = i - 1, \quad \phi_0 = i - \frac{1}{2}, \quad \phi_0 = i, \qquad i = 1, \dots, N. \tag{3.24}$$

By appropriate initial conditions this reduces to $\phi_0 \in \{0, 1, \dots, N\}$ and therefore $N(\phi_0) = N'(\phi_0) = 0$, from which one obtains that (3.21) does not contain any information and that by (3.22)

$$\partial_t \rho_0 = D \Delta \rho_0 + F - \tau^{-1} \rho_0 \qquad \text{in} \quad \Omega \setminus \bigcup_{i=1}^{n} \Gamma_i(t; 0)$$

as desired.

3.3. Inner approximation

Plugging (3.5) and (3.8) into (2.1) and (2.2), using (3.18), (3.19) as well as (3.20) one obtains for

$\mathcal{O}(\epsilon^{-3})$**:**

$$\partial_{z_i}\left(N(\Phi_0)\partial_{z_i}P_0\right)=0; \tag{3.25}$$

$\mathcal{O}(\epsilon^{-2})$**:**

$$\partial_{z_i}\left((N'(\Phi_0)\Phi_1+D)\partial_{z_i}P_0\right)+\partial_{z_i}\left(N(\Phi_0)\partial_{z_i}P_1\right)+\kappa_i N(\Phi_0)\partial_{z_i}P_0=0, \tag{3.26}$$

$$\partial_{z_iz_i}\Phi_0-G'(\Phi_0)=0; \tag{3.27}$$

$\mathcal{O}(\epsilon^{-1})$**:**

$$\begin{aligned}-v_i\partial_{z_i}P_0-v_i\partial_{z_i}\Phi_0&=\partial_{z_i}\left(N(\Phi_0)\partial_{z_i}P_2\right)+\partial_{z_i}\left((N'(\Phi_0)\Phi_1+D)\partial_{z_i}P_1\right)\\&\quad+\frac{1}{2}\partial_{z_i}\left((N''(\Phi_0)\Phi_1^2+2N'(\Phi_0)\Phi_2)\partial_{z_i}P_0\right)+|\nabla s_i|^2\partial_{s_i}(N(\Phi_0)\partial_{s_i}P_0)\\&\quad+\Delta s_i N(\Phi_0)\partial_{s_i}P_0+\kappa_i(N(\Phi_0)\partial_{z_i}P_1+(N'(\Phi_0)\Phi_1+D)\partial_{z_i}P_0),\end{aligned} \tag{3.28}$$

$$-\alpha v_i\partial_{z_i}\Phi_0=\partial_{z_iz_i}\Phi_1+\kappa_i\partial_{z_i}\Phi_0-G''(\Phi_0)\Phi_1+\frac{1}{\rho^*\tilde{\gamma}}\left(P_0-\rho^*\right). \tag{3.29}$$

From the matching condition (3.11) one obtains

$$\lim_{z_i\to+\infty}\Phi_0(z_i)=\lim_{r_i\to+0}\hat{\phi}_0=i, \tag{3.30}$$

$$\lim_{z_i\to-\infty}\Phi_0(z_i)=\lim_{r_i\to-0}\hat{\phi}_0=i+1. \tag{3.31}$$

Because of (3.27) this yields

$$\lim_{z_i\to\pm\infty}\partial^2_{z_i}\Phi_0(z_i)=\lim_{z_i\to\pm\infty}G'(\Phi_0(z_i))=0. \tag{3.32}$$

Now by (3.30), (3.31) and (3.32) we get

$$\lim_{z_i\to\pm\infty}\partial_{z_i}\Phi_0(z_i)=0. \tag{3.33}$$

Multiplying (3.27) by $\partial_{z_i}\Phi_0$, integrating from $-\infty$ to z_i and using (3.31) as well as (3.33) we arrive at

$$\partial_{z_i}\Phi_0=-\sqrt{2G(\Phi_0)} \tag{3.34}$$

the negative root resulting from the fact that $\lim_{z_i\to+\infty}\Phi_0(z_i)=0$ as well as $\lim_{z_i\to-\infty}\Phi_0(z_i)=1$, so the monotone decreasing solution of (3.27) is needed. By definition we have

$$\Phi_0(0)=i+1/2,$$

and so for $z_i=0$ the solution Φ_0 of (3.27) is independent of s_i and t, from which we get

$$\partial_{s_i}\Phi_0=\partial_t\Phi_0=0. \tag{3.35}$$

By (3.25) there exists a constant $c_i=c_i(s_i,t)$ such that

$$N(\Phi_0)\partial_{z_i}P_0=c_i. \tag{3.36}$$

Because of

$$\lim_{z_i \to \pm\infty} N(\Phi_0)\partial_{z_i} P_0 = 0$$

we obtain $c_i = 0$ and therefore

$$N(\Phi_0)\partial_{z_i} P_0 = 0 \qquad \text{for} \quad z_i \in \mathbb{R} \tag{3.37}$$

as well as

$$\partial_{z_i} P_0 = 0 \qquad \text{for} \quad \Phi_0 \in I.$$

Defining $\tilde{I} := \Phi_0^{-1}(I)$ this reads

$$\partial_{z_i} P_0 = 0 \qquad \text{for} \quad z_i \in \tilde{I}. \tag{3.38}$$

Because of $N(\Phi_0) = 0$ for $z_i \notin \tilde{I}$ we have

$$N'(\Phi_0)\partial_{z_i} P_0 = 0 \qquad \text{for} \quad z_i \in \mathbb{R}. \tag{3.39}$$

Now we use (3.26) to obtain with these properties (3.37) and (3.39)

$$\partial_{z_i}(D\partial_{z_i} P_0) + \partial_{z_i}(N(\Phi_0)\partial_{z_i} P_1) = 0.$$

This in turn yields

$$D\partial_{z_i} P_0 + N(\Phi_0)\partial_{z_i} P_1 = d_i = d_i(s_i, t).$$

One therefore gets

$$\lim_{z_i \to \pm\infty} \partial_{z_i} P_0 = \frac{d_i}{D},$$

and since we assume ρ_0 to be bounded at the interface, we obtain from matching condition (3.9)

$$\lim_{z_i \to \pm\infty} \partial_{z_i} P_0 = \frac{d_i}{D} = 0.$$

From this it follows that

$$N(\Phi_0)\partial_{z_i} P_1 + D\partial_{z_i} P_0 = 0 \qquad \text{for} \quad z_i \in \mathbb{R}. \tag{3.40}$$

By definition of I we therefore have

$$\partial_{z_i} P_0 = 0 \qquad \text{for} \quad z_i \in \mathbb{R} \setminus \tilde{I}$$

resulting together with (3.38) in

$$\partial_{z_i} P_0 = 0 \qquad \text{for} \quad z_i \in \mathbb{R}$$

or

$$P_0 = a_i = a_i(s_i, t), \tag{3.41}$$

which in turn yields together with (3.40)

$$\partial_{z_i} P_1 = 0 \qquad \text{for} \quad z_i \in \tilde{I}. \tag{3.42}$$

Just as above one gets

$$N(\Phi_0)\partial_{z_i} P_1 = 0 \qquad \text{for} \quad z_i \in \mathbb{R} \tag{3.43}$$

and

$$N'(\Phi_0)\partial_{z_i} P_1 = 0 \qquad \text{for} \quad z_i \in \mathbb{R}. \tag{3.44}$$

Now we use (3.41), (3.43), (3.44) and (3.35) in (3.28) as well as

$$\Delta s_i = \mathcal{O}(\epsilon) \quad \text{and} \quad |\nabla s_i|^2 = 1 + \mathcal{O}(\epsilon)$$

and obtain

$$-v_i \partial_{z_i} \Phi_0 = \partial_{z_i} \left(N(\Phi_0) \partial_{z_i} P_2 \right) + \partial_{z_i} \left(D \partial_{z_i} P_1 \right) + N(\Phi_0) \partial_{s_i s_i} P_0. \tag{3.45}$$

Integration of this equation along the whole z_i-axis yields

$$v_i = D \left(\lim_{z_i \to \infty} \partial_{z_i} P_1 - \lim_{z_i \to -\infty} \partial_{z_i} P_1 \right) + \int_{-\infty}^{+\infty} N(\Phi_0)\, dz_i\, \partial_{s_i s_i} a_i. \tag{3.46}$$

Using matching condition (3.10) and (3.34) as well as the transformation rule we get

$$\begin{aligned} v_i &= D \left(\lim_{r_i \to +0} \partial_{r_i} \hat{\rho}_0 - \lim_{r_i \to -0} \partial_{r_i} \hat{\rho}_0 \right) + \int_0^1 \frac{N(\phi)}{\sqrt{2G(\phi)}}\, d\phi\, \partial_{s_i s_i} a_i \\ &= D(\nabla \rho_0^- |_{\Gamma_i} - \nabla \rho_0^+ |_{\Gamma_i}) \cdot \vec{n}_i + \int_0^1 \frac{N(\phi)}{\sqrt{2G(\phi)}}\, d\phi\, \partial_{s_i s_i} a_i. \end{aligned} \tag{3.47}$$

Now in order to compute a_i we solve (3.29) for P_0 and obtain

$$-\rho^* \tilde{\gamma} \left(\partial_{z_i z_i} \Phi_1 - G''(\Phi_0) \Phi_1 + \kappa_i \partial_{z_i} \Phi_0 + \alpha v_i \partial_{z_i} \Phi_0 \right) = P_0 - \rho^*. \tag{3.48}$$

Testing (3.48) with $\partial_{z_i} \Phi_0$ and integrating along the whole real z_i-axis we arrive at

$$\begin{aligned} &- \rho^* \tilde{\gamma} \int_{-\infty}^{+\infty} \partial_{z_i} \Phi_0 (\partial_{z_i z_i} \Phi_1 - G''(\Phi_0) \Phi_1)\, dz_i - \rho^* \tilde{\gamma} \left(\kappa_i + \alpha v_i \right) \int_{-\infty}^{+\infty} \partial_{z_i} \Phi_0 \partial_{z_i} \Phi_0\, dz_i \\ &\quad = (P_0 - \rho^*) \int_{-\infty}^{+\infty} \partial_{z_i} \Phi_0\, dz_i, \end{aligned} \tag{3.49}$$

Integrating by parts and using (3.33) one obtains

$$\begin{aligned} &\int_{-\infty}^{+\infty} \partial_{z_i} \Phi_0 (\partial_{z_i z_i} \Phi_1 - G''(\Phi_0) \Phi_1)\, dz_i \\ &\quad = \int_{-\infty}^{+\infty} (\partial_{z_i}^3 \Phi_0 - G''(\Phi_0) \partial_{z_i} \Phi_0) \Phi_1\, dz_i + [\partial_{z_i} \Phi_0 \partial_{z_i} \Phi_1]_{-\infty}^{+\infty} - [\partial_{z_i z_i} \Phi_0 \Phi_1]_{-\infty}^{+\infty} \\ &\quad = \int_{-\infty}^{+\infty} \partial_{z_i} (\partial_{z_i z_i} \Phi_0 - G'(\Phi_0)) \Phi_1\, dz_i = 0. \end{aligned}$$

In the last step we have used (3.27). By transformation rule and (3.34) we have

$$\begin{aligned} \int_{-\infty}^{+\infty} (\partial_{z_i} \Phi_0)^2\, dz_i &= - \int_{-\infty}^{+\infty} \sqrt{2G(\Phi_0)} \partial_{z_i} \Phi_0\, dz_i = - \int_{\Phi_0(-\infty)}^{\Phi_0(+\infty)} \sqrt{2G(\phi)}\, d\phi, \\ &= \int_i^{i+1} \sqrt{2G(\phi)}\, d\phi = \int_0^1 \sqrt{2G(\phi)}\, d\phi. \end{aligned}$$

Inserting these results into (3.49) and using matching relation (3.9) one arrives at

$$\rho_0 - \rho^* = \rho^* \tilde{\gamma}(\kappa_i + \alpha v_i) \int_0^1 \sqrt{2G(\phi)}\, d\phi \qquad \text{on} \quad \Gamma_i(t). \tag{3.50}$$

Furthermore we choose G such that

$$\int_0^1 \sqrt{2G(\phi)}\, d\phi = 1. \tag{3.51}$$

This yields

$$\rho_0 - \rho^* = \rho^* \tilde{\gamma}(\kappa_i + \alpha v_i) \qquad \text{on} \quad \Gamma_i(t). \tag{3.52}$$

In the limit $\alpha \to 0$ we obtain (1.2) as desired and using the matching condition (3.9) and (3.41) one gets

$$\partial_{s_i s_i} a_i(s_i, t) = \rho^* \tilde{\gamma} \partial_{s_i s_i} \kappa_i(s_i, t)$$

and by appropriate choice of the function N:

$$\nu = \rho^* \tilde{\gamma} \int_0^1 \frac{N(\phi)}{\sqrt{2G(\phi)}}\, d\phi$$

we get by (3.47) the correct velocity formula (1.3). We remark that the normalization (3.51) yields

$$G(\phi) = 18(\phi - i)^2 (i + 1 - \phi)^2. \tag{3.53}$$

4. Conclusions

A phase-field model is introduced as an approximation of the Burton-Cabrera-Frank equation with thermodynamic boundary conditions and edge diffusion. The edge diffusion is thereby modeled through an enhanced mobility function in the diffuse interface region. Formal matched asymptotics are used to show the convergence to the Burton-Cabrera-Frank model for vanishing interfacial thickness.

Acknowledgment

We would like to thank Felix Otto for fruitful discussions.

References

[1] E. Bänsch, F. Haußer and A. Voigt, *Finite element method for epitaxial growth with thermodynamic boundary conditions.* SIAM J. Sci. Comput. (2005), to appear.

[2] F. Haußer and A. Voigt, (this volume).

[3] W.K. Burton, N. Cabrera and F.C. Frank, *The growth of crystals and the equilibrium structure of their surfaces.* Phil. Trans. Roy. Soc. London Ser. A **243** (1951), 299–358.

[4] J.W. Cahn, C.M. Elliott and A. Novick-Cohen, *The Cahn-Hilliard equation with a concentration dependent mobility: motion by minus the Laplacian of the mean curvature.* Euro. J. Appl. Math. **7** (1996), 287–301.

[5] C.M. Elliott, H. Garcke, *E*xistence results for diffusive surface motion laws. Adv. Math. Sci. Appl. **7** (1997), 465–488.

[6] P.C. Fife and O. Penrose, *Interfacial dynamics for thermodynamically consistent phase-field models with nonconserved order parameter.* Electron. J. Differential Equations **16** (1995), 1–49.

[7] A. Karma and M. Plapp, *Spiral surface growth without desorption.* Phys. Rev. Lett. **81** (1998), 4444–4447

[8] J. Krug, (this volume).

[9] J. Krug, *Four lectures on the physics of crystal growth.* Physica A **318** (2002), 47–82.

[10] F. Liu and H. Metiu, *Stability and kinetics of step motion on crystal surfaces.* Phys. Rev. E **49** (1994), 2601–2616.

[11] O. Pierre-Louis, *Phase field models for step flow.* Phys. Rev. E **68** (2003), 021604.

[12] A. Rätz and A. Voigt *Phase-field model for island dynamics in epitaxial growth.* Appl. Anal. **83** (2004), 1015–1025.

[13] C. Ratsch, M.F. Guyre, R.E. Caflisch, et al., *Level-set method for island dynamics in epitaxial growth.* Phys. Rev. B **65** (2002), 195403.

Andreas Rätz and Axel Voigt
Crystal Growth group
research center caesar
Ludwig-Erhard-Allee 2
D-53175 Bonn, Germany
e-mail: `raetz@caesar.de`
e-mail: `voigt@caesar.de`

International Series of Numerical Mathematics, Vol. 149, 127–158

Discretisation and Numerical Tests of a Diffuse-Interface Model with Ehrlich–Schwoebel Barrier

Felix Otto, Patrick Penzler and Tobias Rump

Abstract. We consider a step flow model for epitaxial growth, as proposed by Burton, Cabrera and Frank [3]. This type of model is discrete in the growth direction but continuous in the lateral directions. The effect of the Ehrlich–Schwoebel barrier, which limits the attachment rate of adatoms to a step from an upper terrace, is included. Mathematically, this model is a dynamic free boundary problem for the steps. In [6], we proposed a diffuse-interface approximation which reproduces an arbitrary Ehrlich–Schwoebel barrier. It is a version of the Cahn–Hilliard equation with variable mobility.

In this paper, we propose a discretisation for this diffuse-interface approximation. Our approach is guided by the fact that the diffuse-interface approximation has a conserved quantity and a Liapunov functional. We are lead to an implicit finite volume discretisation of symmetric structure.

We test the discretisation by comparison with the matched asymptotic analysis carried out in [6]. We also test the diffuse-interface approximation itself by comparison with theoretically known features of the original free boundary problem. More precisely, we investigate quantitatively the phenomena of step bunching and the Bales–Zangwill instability.

Mathematics Subject Classification (2000). Primary 65M06; Secondary 82D37.

Keywords. epitaxial growth; Ehrlich–Schwoebel barrier; phase-field model.

1. Introduction

1.1. Epitaxial growth

Epitaxial growth is the layer-by-layer growth of a crystalline thin film on a substrate. We think of the thin film as a landscape of terraces which are separated by steps. The growth process is a combination of various microscopic processes: e.g., the deposition of atoms on the terraces, the diffusion of adsorbed atoms

("adatoms") on the terraces, the attachment of adatoms to steps and the detachment of adatoms from steps (see Figure 1). The incorporation of adatoms into

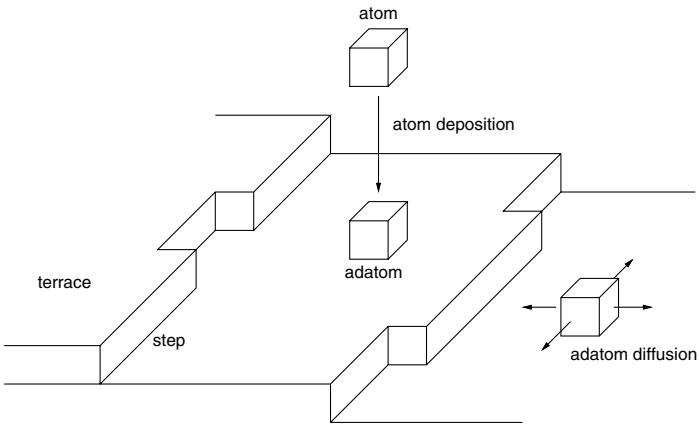

FIGURE 1. Microscopic processes in epitaxial growth.

steps changes the step position. This induces a flow of the steps in the horizontal direction and thereby a growth of the film in the vertical direction.

In this paper, we are interested in the effect of the *Ehrlich–Schwoebel (ES) barrier* [4]. It is an energy barrier which an adatom has to overcome in order to attach to a step coming from the upper terrace. This leads to different attachment rates at a step up and at a step down, respectively.

The ES barrier has two important consequences on the morphology of the surface:

- It counteracts *step bunching* and thus stabilizes a vicinal surface under growth [9], see Section 3.1.
- It favors *step meandering*, also known as the Bales–Zangwill instability [1], see Section 3.2.

1.2. BCF model

We consider a semi-discrete Burton–Cabrera–Frank (BCF) type model [3] for step flow. It is discrete in the growth direction, but continuous in the horizontal direction. The location of a step is described by a continuous curve and the adatom density on each terrace is modeled by a continuous function ρ. In the regime we are interested in, the adatom density has enough time to relax to its quasi-stationary equilibrium on the terraces, so that in a non-dimensionalised setting

$$-\Delta w \;=\; f \qquad \text{on terraces,} \tag{1.1a}$$

where $w := \rho - \rho^*$ is the excess density. Here, ρ^* denotes the thermodynamic equilibrium density at a straight step and f the deposition rate.

The ES barrier is incorporated into the boundary condition of the model: We consider the case of finite attachment rate $\sim 1/\zeta_0$ at a step down and infinite rate at a step up, so that

$$0 = w^+ - \kappa \qquad \text{at a step up,} \tag{1.1b}$$

$$\zeta_0 \frac{\partial w^-}{\partial \nu} = -(w^- - \kappa) \qquad \text{at a step down,} \tag{1.1c}$$

where ν denotes the normal of a step in direction of the lower terrace and κ the curvature of a step with the convention that $\kappa \geq 0$ if the upper terrace is convex. The notations $+$ and $-$ refer to values of w at a step up and at a step down, respectively.

The normal velocity of the step is determined by the adatom flux into the step:

$$V = \frac{\partial w^+}{\partial \nu} - \frac{\partial w^-}{\partial \nu} \qquad \text{at steps.} \tag{1.1d}$$

Note that (1.1) defines a free boundary problem for the step position.

1.3. Diffuse-interface approximation

While the BCF model has a discrete height function for the terraces, the diffuse-interface approximation introduces a continuous height function ϕ which counts the atomic monolayers and which is smeared out on a small length scale ε (see Figure 2).

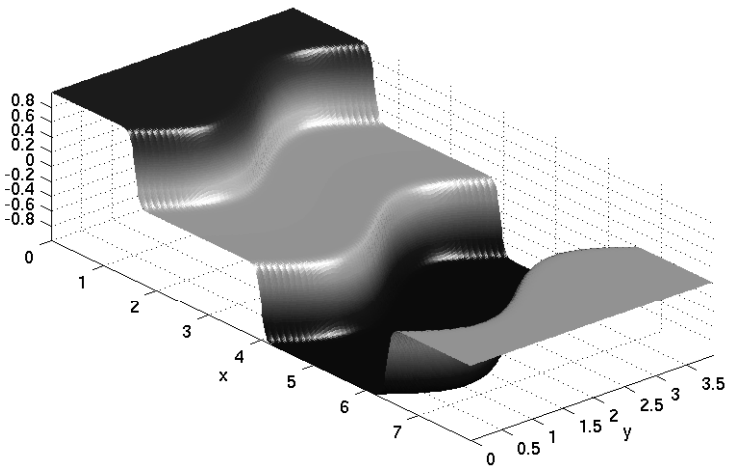

FIGURE 2. The smeared-out height function ϕ.

In [6], we proposed the following variable mobility Cahn–Hilliard-type equation:

$$\partial_t \phi - \nabla \cdot M(\phi) \nabla \left(-\varepsilon \Delta \phi + \varepsilon^{-1} G'(\phi) \right) = f \tag{1.2}$$

with a mobility function which degenerates near the steps:

$$M(\phi) := \frac{1}{1+\varepsilon^{-1}\zeta(\phi)}. \tag{1.3}$$

Sometimes, we expand (1.2) in terms of the flux J and the chemical potential w as

$$\begin{aligned} \partial_t \phi + \nabla \cdot J &= f, && \text{(1.4a)} \\ J &= -M(\phi)\nabla w, && \text{(1.4b)} \\ w &= -\varepsilon\Delta\phi + \varepsilon^{-1}G'(\phi). && \text{(1.4c)} \end{aligned}$$

The key idea of [6] is to choose the asymmetric friction function $\zeta(\phi)$. For the numerical simulations we choose

$$\zeta(\phi) := 6\zeta_0(p+5)(p+4)\phi^{p+2}(1-\phi)^2 \text{ for } \phi \in [0,1], \text{ periodically extended,} \tag{1.5}$$

where $p \gg 1$ is an additional numerical parameter. For the multi-well potential, we make the Ansatz

$$G(\phi) := 18\phi^2(1-\phi)^2 \text{ for } \phi \in [0,1], \text{ periodically extended} \tag{1.6}$$

(see Figure 3). The function w in (1.4c) coincides with the excess density from the BCF model.

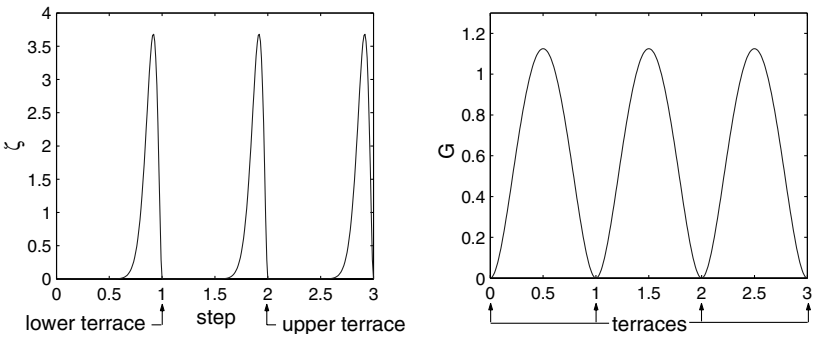

FIGURE 3. The numerical choices for the friction function ζ for $\zeta_0 = 1$ and $p = 20$ (left) and the multi-well potential G (right).

As shown in [6], asymptotic analysis yields

$$\begin{aligned} -\Delta w &= f && \text{on terraces,} && \text{(1.7a)} \\ V &= \frac{\partial w^+}{\partial \nu} - \frac{\partial w^-}{\partial \nu} && \text{at steps,} && \text{(1.7b)} \\ \begin{pmatrix} \zeta^+ & \zeta^m \\ \zeta^m & \zeta^- \end{pmatrix} \begin{pmatrix} \frac{\partial w^+}{\partial \nu} \\ \frac{\partial w^-}{\partial \nu} \end{pmatrix} &= \begin{pmatrix} w^+ - \kappa \\ -(w^- - \kappa) \end{pmatrix} && \text{at steps,} && \text{(1.7c)} \end{aligned}$$

with

$$\begin{aligned}\zeta^+ &= \int_0^1 \zeta(\phi)(1-\phi)^2 \frac{d\phi}{\sqrt{2G(\phi)}},\\ \zeta^m &= \int_0^1 \zeta(\phi)(1-\phi)\phi \frac{d\phi}{\sqrt{2G(\phi)}},\\ \zeta^- &= \int_0^1 \zeta(\phi)\phi^2 \frac{d\phi}{\sqrt{2G(\phi)}}.\end{aligned} \tag{1.8}$$

With the choices (1.5) and (1.6) we have

$$\zeta^- = \zeta_0, \qquad \zeta^+ = \frac{6\zeta_0}{(p+2)(p+3)} = \mathcal{O}(p^{-2}) \quad \text{and} \quad \zeta^m = \frac{2\zeta_0}{p+3} = \mathcal{O}(p^{-1}). \tag{1.9}$$

Thus, in the limit $p \uparrow \infty$ (1.7) yields the BCF model (1.1). In the following we refer to (1.7) & (1.9) as the "p-BCF" model.

The numerical advantage of the diffuse-interface approximation is that both the excess adatom density w and the height function ϕ, which determines the step position, can be discretised with respect to the same grid. Also topological changes of terraces can be naturally treated.

For further details of the BCF model and its diffuse-interface approximation we refer to [6].

2. Discretisation

The discretisation should preserve the following two features of the continuum evolution:

- In absence of f, $\int \phi \, dx$ is a conserved quantity. More precisely, we have
$$\partial_t \phi + \nabla \cdot J = 0.$$
- In absence of f, $E(\phi) := \int \left(\varepsilon \frac{1}{2}|\nabla\phi|^2 + \varepsilon^{-1} G(\phi)\right)$ is a Liapunov functional. In fact, we have
$$\frac{d}{dt}\int \left(\varepsilon \frac{1}{2}|\nabla\phi|^2 + \varepsilon^{-1} G(\phi)\right) dx = -\int \frac{1}{M(\phi)}|J|^2 \, dx.$$

Preserving conservation of mass and thermodynamic consistency are the guiding principles for our discretisation.

2.1. Time discretisation

2.1.1. Field report. The Newton method for implicit time discretisations relies on the linearisation of the operator. In our subsequent discussion of the discretisation strategies and in their implementation, we simplify the true linearisation of the operator in two ways:

- Partial Linearisation. We linearise the nonlinear evolution operator

$$F(\phi) := \nabla \cdot \left(M(\phi)\nabla\left(\varepsilon\Delta\phi - \varepsilon^{-1}G'(\phi)\right)\right) - f \tag{2.1}$$

in the potential G only (not in the mobility M):

$$A(\phi)\,\delta\phi = \nabla \cdot \left(M(\phi)\nabla\left(\varepsilon\Delta\delta\phi - \varepsilon^{-1}G''(\phi)\delta\phi\right)\right). \tag{2.2}$$

- Constant coefficients. We replace the non-constant coefficient $G''(\phi)$ and $M(\phi)$ by their values $G''(0) > 0$ and $M(0) = 1$ on the terraces:

$$A_0\,\delta\phi = \varepsilon\Delta^2\delta\phi - \varepsilon^{-1}G''(0)\Delta\delta\phi. \tag{2.3}$$

The theoretical advantage is that we have a good understanding of the spectrum of the constant coefficient operator A_0. In particular, the largest eigenvalue of A_0 scales as $\varepsilon\frac{1}{\Delta x^4} + \varepsilon^{-1}\frac{1}{\Delta x^2}$, where Δx is the typical spatial mesh size. The practical advantage is that (2.3) can be easily inverted by Fast Fourier Transform and used as a preconditioner for (2.2), see Section 2.4.1.

Consider the **Explicit Euler** method:

$$\frac{1}{\tau}(\phi^{k+1} - \phi^k) + F(\phi^k) \;=\; 0. \tag{2.4}$$

The simplified linearisation (in the above sense) for the evolution of a infinitesimal perturbation $\{\delta\phi^k\}_k$ is given by

$$\frac{1}{\tau}(\delta\phi^{k+1} - \delta\phi^k) + A_0\,\delta\phi^k \;=\; 0.$$

We infer that (2.4) suffers from the time step restriction for

$$\tau \;\ll\; \frac{1}{\text{largest eigenvalue of } A_0} \;\sim\; \varepsilon^{-1}\Delta x^4 + \varepsilon\Delta x^2. \tag{2.5}$$

In order to resolve the interfacial layer of width ε without wasting too many degrees of freedom, $\Delta x \sim \varepsilon$ is a good assumption. Hence (2.5) turns into the restriction

$$\tau \;\ll\; \varepsilon^3,$$

which is prohibitive.

On the other hand, the simplified linearisation

$$\frac{1}{\tau}(\delta\phi^{k+1} - \delta\phi^k) + A_0\,\delta\phi^{k+1} \;=\; 0$$

of the **Implicit Euler** method is unconditionally stable. We experimentally verified this prediction in the nonlinear setting: The scheme

$$\frac{1}{\tau}(\phi^{k+1} - \phi^k) + A_0\,(\phi^{k+1} - \phi^k) + F(\phi^k) \;=\; 0 \tag{2.6}$$

did indeed not show signs of a time step restriction for stability. Notice that (2.6) is the first Newton step in the Implicit Euler scheme

$$\frac{1}{\tau}(\phi^{k+1} - \phi^k) + F(\phi^{k+1}) \;=\; 0$$

with simplified linearisation. Despite the fact that the scheme is stable, solutions were physically unacceptable even for fairly small τ, see Figure 4. As can be seen,

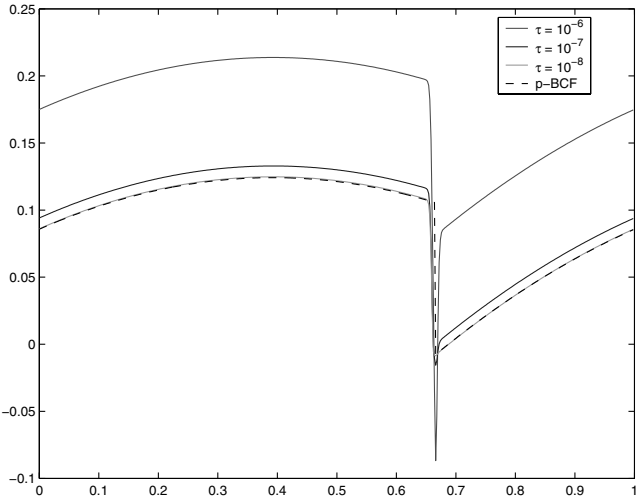

FIGURE 4. Comparison of w for different τ for the first order scheme (2.6).

the error originates at the interfacial layer; it persists when increasing the spatial resolution.

Therefore we consider second order schemes. A standard choice for a second order method is the **Crank–Nicolson** scheme

$$\frac{1}{\tau}(\phi^{k+1} - \phi^k) + \frac{1}{2}(F(\phi^k) + F(\phi^{k+1})) \;=\; 0.$$

Its first Newton step with simplified linearisation is given by

$$\frac{1}{\tau}(\phi^{k+1} - \phi^k) + \frac{1}{2}\, A_0\, (\phi^{k+1} - \phi^k) + F(\phi^k) \;=\; 0. \tag{2.7}$$

Infinitesimal perturbations evolve according to

$$\frac{1}{\tau}(\delta\phi^{k+1} - \delta\phi^k) + \frac{1}{2}\, A_0\, (\delta\phi^{k+1} + \delta\phi^k) \;=\; 0. \tag{2.8}$$

The iteration matrix $\delta\phi^{k+1} = T\delta\phi^k$ of (2.8) is given by

$$T \;=\; (\mathrm{id} - \frac{\tau}{2}A_0)(\mathrm{id} + \frac{\tau}{2}A_0).$$

Notice that the eigenvalue of T approaches -1 as the corresponding eigenvalue of A_0 approaches ∞. Hence (2.8) does barely damp the high modes, which would rapidly decay in the time continuous setting. This deficiency shows clearly up in numerical experiments on (2.7): A peak on the terrace, coming from the initial

position of the interfacial layer, is not diffused away. Hence the Crank–Nicolson scheme is inadequate for Cahn–Hilliard type evolutions.

A better choice for a second order method is the **θ-scheme** (see [2] and [10]). This scheme yields an iteration matrix which eigenvalues are uniformly bounded away from ± 1.

2.1.2. The θ-scheme. We will now explain the θ-scheme. Let F be defined as in (2.1). The θ-scheme needs three intermediate steps per time step. For given α, β, θ with $\theta \in (0, \frac{1}{2})$, $\alpha + \beta = 1$, $\alpha > 0, \beta > 0$ and the time step size τ, it reads as

$$\begin{aligned}
\frac{\phi^{k+\theta} - \phi^k}{\theta\tau} &= -(\alpha F(\phi^{k+\theta}) + \beta F(\phi^k)),\\
\frac{\phi^{k+1-\theta} - \phi^{k+\theta}}{(1-2\theta)\tau} &= -(\beta F(\phi^{k+1-\theta}) + \alpha F(\phi^{k+\theta})),\\
\frac{\phi^{k+1} - \phi^{k+1-\theta}}{\theta\tau} &= -(\alpha F(\phi^{k+1}) + \beta F(\phi^{k+1-\theta})).
\end{aligned}$$

As shown in [2], the choice

$$\theta = 1 - \frac{\sqrt{2}}{2}, \quad \alpha = \frac{1-2\theta}{1-\theta} = 2 - \sqrt{2}, \quad \beta = \frac{\theta}{1-\theta} = \sqrt{2} - 1$$

yields an unconditionally stable second order scheme.

In each θ-step we solve the time discrete problem by Newton's method. Considering for example the first θ-step, we have to solve

$$\underbrace{\phi^{k+\theta} - \phi^k + \theta\tau(\alpha F(\phi^{k+\theta}) + \beta F(\phi^k))}_{=:\mathcal{F}(\phi^{k+\theta}, \phi^k)} = 0,$$

so in the ith Newton step we have to solve

$$\mathcal{F}(\phi^{k+\theta,i-1}, \phi^k) + D_1\mathcal{F}(\phi^{k+\theta,i-1}, \phi^k)(\phi^{k+\theta,i} - \phi^{k+\theta,i-1}) = 0$$

for $\phi^{k+\theta,i}$. Here, $\phi^{k+\theta,0} = \phi^k$ and $\phi^{k+\theta,\infty} = \phi^{k+\theta}$. Obviously, we set $\phi^{k+\theta} := \phi^{k+\theta,j}$ when j is large enough meaning $\phi^{k+\theta,j}$ is close enough to the exact solution. Since Newton's method converges quadratically, two Newton steps are sufficient in our case.

By definition of $\mathcal{F}$, the differential $D_1\mathcal{F}(\phi^{k+\theta,i-1}, \phi^k)$ is

$$\mathrm{id} + \theta\tau\alpha DF(\phi^{k+\theta,i-1}).$$

As mentioned above, we do not linearise in the mobility M, but use

$$DF(\phi^{k+\theta,i-1}) \approx \nabla \cdot (-M(\phi^{k+\theta,i-1})\nabla[-\varepsilon\Delta + \varepsilon^{-1}G''(\phi^{k+\theta,i-1})]).$$

This might slightly slow down the convergence of Newton's method, but permits us to use a solver for symmetric problems (see Section 2.2).

We can now state the time discrete formulation of our problem. We introduce the notations

$$\mathcal{L} := -\theta\alpha M(\phi^{k+\theta,i-1})\nabla[-\varepsilon\Delta + \varepsilon^{-1}G''(\phi^{k+\theta,i-1})], \tag{2.9}$$

$$w^k = -\varepsilon\Delta\phi^k + \varepsilon^{-1}G'(\phi^k),$$
$$w^{k+\theta,i-1} = -\varepsilon\Delta\phi^{k+\theta,i-1} + \varepsilon^{-1}G'(\phi^{k+\theta,i-1})$$

and finally

$$J^{k+\theta,i} := \mathcal{L}(\phi^{k+\theta,i} - \phi^{k+\theta,i-1}) - \theta(\alpha M(\phi^{k+\theta,i-1})\nabla w^{k+\theta,i-1} + \beta M(\phi^k)\nabla w^k).$$

With these notations, the ith Newton step leads to the following equation for $\phi^{k+\theta,i}$:

$$\frac{1}{\tau}(\phi^{k+\theta,i} - \phi^{k+\theta,i-1}) + \nabla\cdot J^{k+\theta,i} = -\frac{1}{\tau}(\phi^{k+\theta,i-1} - \phi^k) + \theta f \tag{2.10}$$

$$\iff \frac{1}{\tau}(\phi^{k+\theta,i} - \phi^k) + \nabla\cdot J^{k+\theta,i} = \theta f. \tag{2.11}$$

As opposed to (2.6), the θ-scheme shows much better convergence, see Figure 5. Already for $\tau = 10^{-4}$, the θ-scheme yields a smaller approximation error than

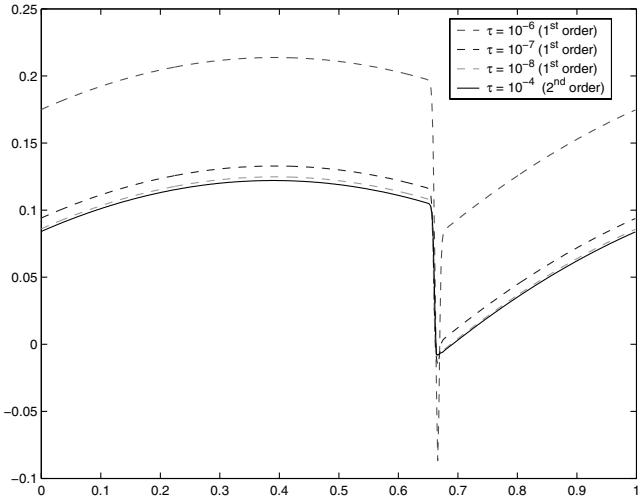

FIGURE 5. Comparison of w for first and second order scheme.

the implicit Euler scheme for $\tau = 10^{-8}$.

2.2. Symmetrisation via flux

Note that the fourth order elliptic equation (2.11) for $\phi^{k+\theta,i}$ is not symmetric due to the mobility M. Instead of solving (2.11) to get $\phi^{k+\theta,i}$, we will rewrite the problem as an equation for $J^{k+\theta,i}$. This will give rise to a symmetric iteration matrix. After solving the symmetric problem, we can then regain $\phi^{k+\theta,i}$ from (2.11).

2.2.1. Idea. We illustrate the idea in the case of a single Newton step in a semi-implicit Euler scheme without deposition, i.e., (2.6), which reads as

$$\left(\frac{1}{\tau}\mathrm{id} + \nabla \cdot M(\phi^k)\nabla(\varepsilon\Delta - \varepsilon^{-1}G''(\phi^k))\right)(\phi^{k+1} - \phi^k) + F(\phi^k) = 0,$$

where F is defined as in (2.1). By defining the discrete flux analogous to the previous section

$$\widetilde{J}^{k+1} := M(\phi^k)\nabla\left[\varepsilon\Delta\phi^{k+1} - \varepsilon^{-1}(G'(\phi^k) + G''(\phi^k)(\phi^{k+1} - \phi^k))\right],$$

this equation can be rewritten as

$$\frac{1}{\tau}(\phi^{k+1} - \phi^k) + \nabla \cdot \widetilde{J}^{k+1} = 0. \tag{2.12}$$

Applying the operator

$$\tilde{\mathcal{L}} := \varepsilon\nabla\Delta - \varepsilon^{-1}\nabla G''(\phi^k)$$

to (2.12) yields

$$\begin{aligned} \frac{1}{\tau}\tilde{\mathcal{L}}(\phi^{k+1} - \phi^k) + \tilde{\mathcal{L}}\nabla \cdot \widetilde{J}^{k+1} &= 0 \\ \iff \frac{1}{\tau}\left(\varepsilon\nabla\Delta\phi^{k+1} - \varepsilon^{-1}\nabla G''(\phi^k)(\phi^{k+1} - \phi^k)\right) + \tilde{\mathcal{L}}\nabla \cdot \widetilde{J}^{k+1} &= \frac{1}{\tau}(\varepsilon\nabla\Delta\phi^k) \\ \iff \left(\frac{1}{\tau M(\phi^k)}\mathrm{id} + \tilde{\mathcal{L}}\nabla\cdot\right)\widetilde{J}^{k+1} &= -\frac{1}{\tau}\nabla w^k. \end{aligned}$$

The last equation can be seen as a discrete (and regularised) version of (1.4b) with a symmetric fourth order operator. Indeed,

$$\left(\frac{1}{\tau M(\phi^k)}\mathrm{id} + \tilde{\mathcal{L}}\nabla\cdot\right) = \left(\frac{1}{\tau M(\phi^k)}\mathrm{id} + \varepsilon(\nabla\nabla\cdot)^2 - \varepsilon^{-1}\nabla G''(\phi^k)\nabla\cdot\right). \tag{2.13}$$

We now argue why we expect (2.13) to be not only symmetric but also positive definite for $\tau \ll 1$.

We take the point of view of the asymptotic analysis [6] that ϕ^k is a modulation of the 1-d transition profile

$$\phi_*(x) = \frac{1}{2}\left(1 - \tanh\left(\frac{x}{2\varepsilon}\right)\right), \qquad x \in \mathbb{R}.$$

This 1-d transition profile is the *minimizer* of our Liapunov functional

$$E_{1-d}(\phi) := \int_{-\infty}^{+\infty} \frac{\varepsilon}{2}\left|\frac{d}{dx}\phi\right|^2 + \varepsilon^{-1}G(\phi)\, dx$$

under the boundary conditions of

$$\lim_{x\to\pm\infty}\phi(x) = \left\{\begin{array}{c} 1 \\ 0 \end{array}\right\}.$$

Hence the second variation under the infinitesimal perturbation $\delta\phi$ of the profile is nonnegative:

$$\int_{-\infty}^{+\infty} \varepsilon \left| \frac{d}{dx}\delta\phi \right|^2 + \varepsilon^{-1} G''(\phi_*)(\delta\phi)^2 \, dx \geq 0,$$

which means that the corresponding operator

$$\mathcal{E}(\phi_*)\delta\phi = -\varepsilon \frac{d^2}{dx^2}\delta\phi + \varepsilon^{-1} G''(\phi_*)\delta\phi$$

is positive semidefinite. Therefore also the conjugate operator $\frac{d}{dx}\mathcal{E}(\phi_*)(\frac{d}{dx})^t = -\frac{d}{dx}\mathcal{E}(\phi_*)\frac{d}{dx}$, i.e.,

$$\varepsilon \frac{d^4}{dx^4} - \varepsilon^{-1} \frac{d}{dx} G''(\phi_*) \frac{d}{dx}$$

is positive semidefinite. This implies that at least the 1-d version of our operator (2.13)

$$\frac{1}{\tau M(\phi_*)}\mathrm{id} + \varepsilon \frac{d^4}{dx^4} - \varepsilon^{-1} \frac{d}{dx} G''(\phi_*) \frac{d}{dx}$$

is positive definite for any $\tau > 0$.

The algebraic relationship

$$\frac{1}{\tau M(\phi^k)}\mathrm{id} + \varepsilon(\nabla\nabla\cdot)^2 - \varepsilon^{-1}\nabla G''(\phi^k)\nabla\cdot = \frac{1}{\tau M(\phi^k)}\mathrm{id} - \nabla\left(\text{Hessian of } E \text{ in } \phi^k\right)\nabla\cdot$$

holds in general. Since ϕ^k is a modulation of the 1-d transition profile ϕ_* along the sharp step Γ^k, we expect in view of the above

$$\text{Hessian of } E \text{ in } \phi^k \gtrsim \text{Hessian of step length in } \Gamma^k$$

in the sense of bilinear forms for $\varepsilon \ll 1$. Since we expect BCF solutions to be generically smooth, the latter has only a finite dimensional negative subspace. Since

$$\frac{1}{\tau M(\phi^k)}\mathrm{id} = \frac{(1 + \varepsilon^{-1}\zeta(\phi^k))}{\tau}\mathrm{id} \geq \frac{1}{\tau}\mathrm{id},$$

we expect that, independently of ε, $\tau \ll 1$ is sufficient to ensure that (2.13) is positive definite.

2.2.2. Application to full problem. Again, we display only the formula for the first θ-step, the formulas for the other two θ-steps are analogue. We apply $\mathcal{L}$ as defined

in (2.9) to both side of (2.11) which leads to

$$\begin{aligned}\left[\frac{1}{\theta\tau M(\phi^{k+\theta,i-1})}\mathrm{id}+\alpha\left(\varepsilon(\nabla\nabla\cdot)^2-\frac{1}{\varepsilon}\nabla G''(\phi^{k+\theta,i-1})\nabla\cdot\right)\right]J^{k+\theta,i}\\ =-\frac{1}{\tau}\alpha\left(\varepsilon\nabla\Delta-\frac{1}{\varepsilon}\nabla G''(\phi^{k+\theta,i-1})\right)(\phi^{k+\theta,i-1}-\phi^k)\\ -\frac{1}{\tau}\left(\alpha\nabla w^{k+\theta,i-1}+\beta\frac{M(\phi^k)}{M(\phi^{k+\theta,i-1})}\nabla w^k\right)\\ -\theta\alpha\frac{1}{\varepsilon}\nabla G''(\phi^{k+\theta,i-1})f.\end{aligned}\tag{2.14}$$

The part in the square brackets gives rise to a symmetric iteration matrix. The advantage is now that we can use a solver for symmetric problems, e.g., the conjugate gradient method. In addition, we often use a periodic sequence of steps down as initial data. Then ϕ is only periodic modulo the number of steps in an unit cell, while J is really periodic, which is more convenient.

2.3. Spatial discretisation

For the spatial discretisation, we plan to use a finite element scheme in the future, see Section 4.1. So far, we use a finite volume scheme on an equidistant grid: To keep the symmetry of the discretised operator, i.e., the symmetry of the iteration matrix, we must discretise the operators $\nabla\cdot$ and ∇ such that they are dual to each other. Functions and the divergence of vector fields live on the volumes (▲), both the x-components (×) and the y-components (○) of fluxes and gradients live on the edges of the grid (see Figure 6 for one and two dimensions).

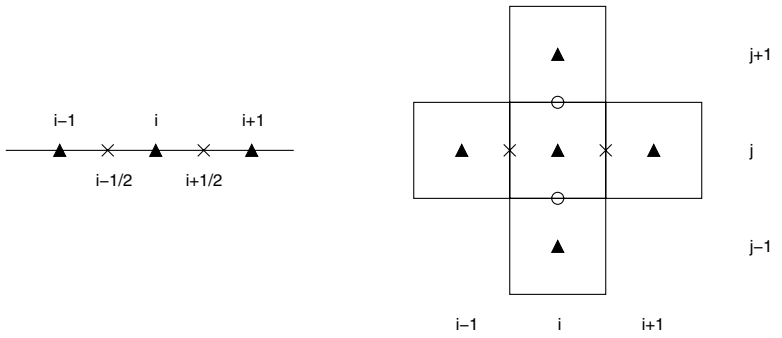

FIGURE 6. The functions ϕ and $\nabla\cdot J$ live on the volumes (▲), the fluxes J and the gradients $\nabla\phi$ on the edges (x-component (×) numbered by index i and y-component (○) numbered by j).

We choose for the divergence in one dimension

$$(\nabla^h\cdot J)(i)=\tfrac{1}{h}(J(i+\tfrac{1}{2})-J(i-\tfrac{1}{2}))$$

and in two dimensions ($J = (J_x, J_y)$)

$$(\nabla^h \cdot J)(i,j) = \tfrac{1}{h}(J_x(i+\tfrac{1}{2},j) - J_x(i-\tfrac{1}{2},j) + J_y(i,j+\tfrac{1}{2}) - J_y(i,j-\tfrac{1}{2})).$$

The suitable dual discrete gradient for this choice is given in one dimension by

$$(\nabla^h \phi)_x(i+\tfrac{1}{2}) = \tfrac{1}{h}(\phi(i+1) - \phi(i))$$

and in two dimensions by

$$(\nabla^h \phi)_x(i+\tfrac{1}{2},j) = \tfrac{1}{h}(\phi(i+1,j) - \phi(i,j)),$$

$$(\nabla^h \phi)_y(i,j+\tfrac{1}{2}) = \tfrac{1}{h}(\phi(i,j+1) - \phi(i,j)).$$

For the mobility we follow [5] and take the average of the friction ζ instead of the average of the mobility:

$$\begin{aligned} M_x(i+\tfrac{1}{2},j) &= \frac{1}{1+\frac{1}{2\varepsilon}\left(\zeta(\phi(i+1,j)) + \zeta(\phi(i,j))\right)}, \\ M_y(i,j+\tfrac{1}{2}) &= \frac{1}{1+\frac{1}{2\varepsilon}\left(\zeta(\phi(i,j+1)) + \zeta(\phi(i,j))\right)}. \end{aligned}$$

From the physical point of view, this choice is reasonable, since the movement of an adatom "over the grid" is affected by the sum of the frictions (instead of the sum of the mobilities).

2.4. Linear solver

As we have a symmetric positive definite iteration matrix, we can use the conjugate gradient method. Instead of using one of the standard preconditioners, we chose a preconditioner which is guided by the structure of the problem.

2.4.1. Preconditioning. To find a cheap approximate inverse, we note that the mobility only affects the flux in proximity of the step, so only on a fraction of the whole grid. If we set $M = M(\text{terrace}) \equiv 1$ and use $G'' \equiv G''(\text{terrace})$, as mentioned in 2.1.1, the operator in the square brackets in equation (2.14) is a linear operator with constant coefficients. Since we prescribe periodic boundary conditions for J and use an equidistant grid, we can use Fast Fourier Transformation for inversion.

Even despite the fact that matrix inversion is a non-local operation, we hope that the inverse of the simplified operator will be close to the inverse of the operator in (2.14).

As a first test, we compared our preconditioner to the case without preconditioning and to the simple method of multiplying the diagonal with $\tau M(\phi)$. As expected, computing times are significantly shorter with our preconditioner. Only for relatively small systems with about $2 \cdot 10^4$ degrees of freedom, FFT preconditioning is slower than the two other ones. See Figure 7 for a comparison of running times. Obviously, we will have to compare the computing times to more elaborate preconditioners.

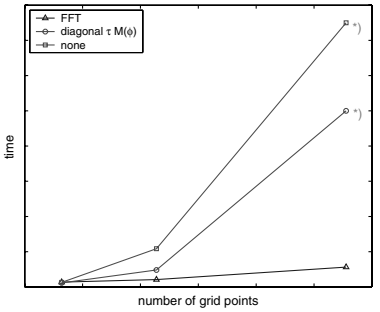

FIGURE 7. Comparison of running times vs. number of degrees of freedom for different preconditioners. Times marked with *) are extrapolated.

2.5. Accuracy

In this section we want to compare the numerical results with the analytical predictions. The difference between the BCF model (1.1) and the p-BCF model (1.7) shows the effect of nonzero ζ^+ and ζ^m (since p is finite) and the difference between the p-BCF model and the numerical data shows the effect of a nonzero ε (and possibly of the discretisation):

$$\text{diffuse-interface} \quad \xrightarrow{\varepsilon \downarrow 0} \quad p\text{-BCF} \quad \xrightarrow{p \uparrow \infty} \quad \text{BCF}.$$

Thus, we will most of the time compare the numerical data to the p-BCF model (1.7) and therefore focus on the ε-convergence of our diffuse-interface model.

2.5.1. Outer solution. We first solve the p-BCF model (1.7) in one space dimension for a step train, i.e., coming from $-\infty$ there is a step down every L_x units. So for a unit cell with a step down at $x = 0$, the next step down is at $x = L_x$. If we set $w^+ = w(0)$ and $w^- = w(L_x)$, equations (1.7) turn into

$$\begin{aligned} -w'' &= f, && \text{(2.15a)}\\ V &= w'(0) - w'(L_x), && \text{(2.15b)}\\ \zeta^+ w'(0) + \zeta^m w'(L_x) &= w(0), && \text{(2.15c)}\\ \zeta^m w'(0) + \zeta^- w'(L_x) &= -w(L_x). && \text{(2.15d)} \end{aligned}$$

The solution is

$$\begin{aligned} w(x) = &-\frac{1}{2} f x^2 + f L_x \left(\frac{\zeta^m + \zeta^- + \frac{1}{2} L_x}{2\zeta^m + \zeta^+ + \zeta^- + L_x} \right) x \\ &+ f L_x \left(\frac{\frac{1}{2} L_x (\zeta^+ - \zeta^m) + \zeta^- \zeta^+ - (\zeta^m)^2}{2\zeta^m + \zeta^+ + \zeta^- + L_x} \right). \end{aligned} \tag{2.16}$$

Figure 8 shows the result of a 1+1-dimensional numerical simulation for a system of size $L_x = 8$. The first graph compares the numerical solution of the

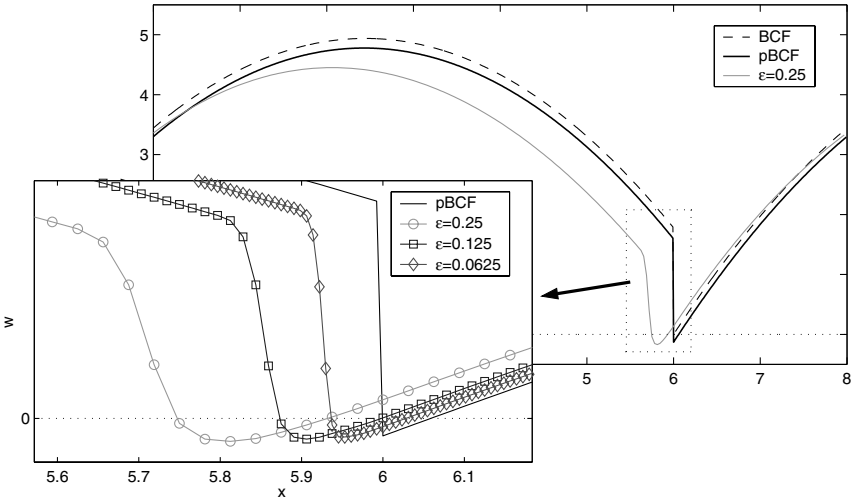

FIGURE 8. Linear convergence of the diffuse-interface approximation to the approximated BCF model.

diffuse-interface approximation (1.4) for $\varepsilon = 0.25$, $p = 20$ to the exact solution of (1.1) (BCF) and the exact solution of (1.7) (p-BCF). For the latter we use

$$\begin{pmatrix} \zeta^+ & \zeta^m \\ \zeta^m & \zeta^- \end{pmatrix} \approx \begin{pmatrix} 0.011 & 0.087 \\ 0.087 & 1 \end{pmatrix} \zeta_0$$

according to (1.9). The second graph zooms in at the step and shows the linear convergence of the method as $\varepsilon \downarrow 0$. We note that the discretisation error for our choices $h = 1/128$ and $\tau = 10^{-4}$ is negligible compared to the ε-error.

As can be seen, the diffuse-interface solution lags behind the BCF solution. This is because the excess density w in the BCF model instantaneously has the shape of a travelling wave, whereas the excess density in the diffuse-interface model starts with $w \equiv 0$ and needs some time to reach its travelling wave shape (see Figure 9).

This time is the shorter the smaller ε is, thus for smaller ε the step position is more accurate. Once w reaches its final shape, the step velocity of the diffuse-interface model matches the step velocity of the BCF model for any ε as it should be because of volume conservation.

2.5.2. Inner solution. Our numerical simulation shows an undershoot (see Figure 10) in the diffuse-interface-w. We argue here that it is a feature of the exact ε-solution and not an effect of the discretisation.

To derive the inner solution, we introduce a new coordinate z,

$$z = \frac{x - \text{step position}}{\varepsilon},$$

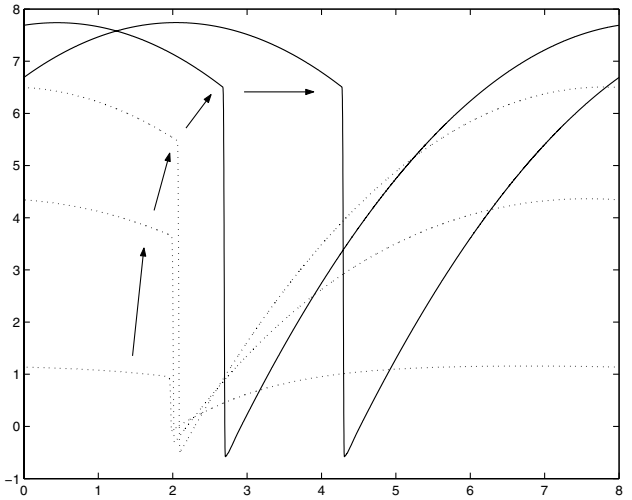

FIGURE 9. The diffuse-interface excess density w at different times: it needs some time to build up.

and denote the zeroth order terms of asymptotic expansions of ϕ and w by Φ_0 and W_0, respectively. Applying asymptotic analysis, we obtain the equations [6, (5.16)–(5.18)]

$$\lambda = -w'(0), \tag{2.17a}$$

$$V = -w'(0) - w'(L_x), \tag{2.17b}$$

$$\partial_z \Phi_0 = -\sqrt{2G(\Phi_0)}, \tag{2.17c}$$

$$\partial_z W_0 = -\zeta(\phi)(V\Phi_0 - \lambda). \tag{2.17d}$$

The explicit outer solution (2.16) allows us to identify the right-hand sides of (2.17a) and (2.17b). We integrate (2.17c) and (2.17d) numerically. The integration constant is fixed by the matching condition

$$\lim_{z\to-\infty} W_0(z) = \lim_{x\to 0} w^-(x) = w(L_x)$$

and by $\Phi_0(0) = \frac{1}{2}$.

Figure 10 shows the comparison between the exact inner solution W_0 and a numerical simulation for $\varepsilon = 1/128$, $h = 1/8192$ and $L_x = 1$. By definition of z, the step position is at $z = 0$ (i.e., $\phi(z = 0) = \frac{1}{2}$).

So we see that the analysis indeed predicts such sign changes of w' near a step down and the numerics reproduce the inner solution. The depth of the undershoot depends on L_x.

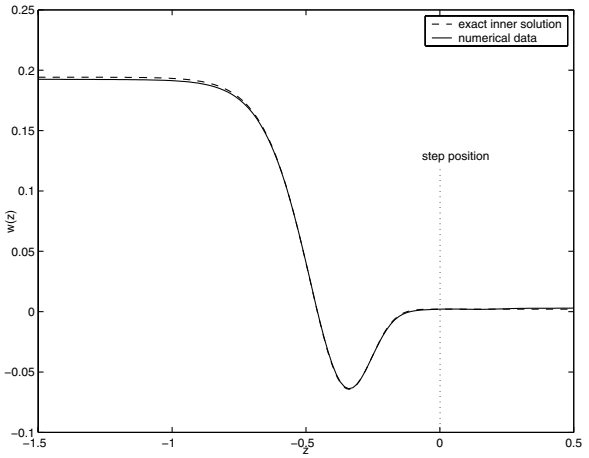

FIGURE 10. The exact inner solution for the excess density w and the numerical data in stretched coordinates z. They both show the same undershoot near the step.

3. Numerical simulations

In this paragraph we want to show that the diffuse-interface model can reproduce certain phenomena predicted by the BCF model, especially effects arising from the ES barrier. For this purpose, we focus on the $1+1$-d effect of step bunching and the $2+1$-d effect of step meandering, which is also known as the Bales–Zangwill instability (cf. [1]).

3.1. Step bunching

To introduce the $1+1$-d effect of step bunching we consider a periodic step train, which is a periodic sequence of a number of descending steps, and analyse the change in the terrace lengths. For the simplest case of two steps, the terrace lengths do not change at all if there is no barrier. So for our investigation, we focus on a step train consisting of three different terrace lengths as shown in Figure 11. The evolution of the terrace lengths under growth depends on the attachment rates at the steps (see next section). We will speak of *step bunching* when at least one terrace length becomes zero, i.e., the terrace vanishes.

3.1.1. Analysis. From the BCF model (1.1), the velocity of a step at position ξ_i is given by

$$\dot{\xi}_i = f\left(\frac{\zeta l_i + \frac{1}{2}l_i^2}{\zeta + l_i} + \frac{\frac{1}{2}l_{i-1}^2}{\zeta + l_{i-1}}\right), \tag{3.1}$$

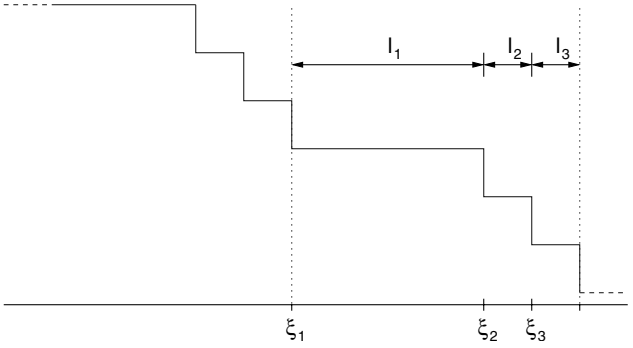

FIGURE 11. Unit cell of a step train with three terraces and total length $L_x = l_1 + l_2 + l_3$.

so that the terrace length l_i obeys

$$\dot{l}_i = \dot{\xi}_{i+1} - \dot{\xi}_i = f\left(\frac{\zeta l_{i+1} + \frac{1}{2}l_{i+1}^2}{\zeta + l_{i+1}} - \frac{\zeta l_i}{\zeta + l_i} - \frac{\frac{1}{2}l_{i-1}^2}{\zeta + l_{i-1}}\right). \tag{3.2}$$

As mentioned above, we consider a unit cell with three terraces. In the following, the system

$$\begin{aligned}
\dot{l}_1 &= f\left(\frac{\zeta l_2 + \frac{1}{2}l_2^2}{\zeta + l_2} - \frac{\zeta l_1}{\zeta + l_1} - \frac{\frac{1}{2}l_3^2}{\zeta + l_3}\right),\\
\dot{l}_2 &= f\left(\frac{\zeta l_3 + \frac{1}{2}l_3^2}{\zeta + l_3} - \frac{\zeta l_2}{\zeta + l_2} - \frac{\frac{1}{2}l_1^2}{\zeta + l_1}\right),\\
\dot{l}_3 &= f\left(\frac{\zeta l_1 + \frac{1}{2}l_1^2}{\zeta + l_1} - \frac{\zeta l_3}{\zeta + l_3} - \frac{\frac{1}{2}l_2^2}{\zeta + l_2}\right),
\end{aligned} \tag{3.3}$$

is written as $(\dot{l}_1, \dot{l}_2, \dot{l}_3) = \mathbf{L}(l_1, l_2, l_3)$. It preserves the total length $l_1 + l_2 + l_3 = L_x$ and has equidistant steps (i.e., $l_1 = l_2 = l_3 =: l_*$) as stationary point.

The Jacobian $D\mathbf{L}$ in (l_*, l_*, l_*) is given by

$$D\mathbf{L}(l_*, l_*, l_*) = \frac{f}{(\zeta + l_*)^2}\begin{pmatrix} -\zeta^2 & \zeta^2 + \zeta l_* + \frac{1}{2}l_*^2 & -(\zeta l_* + \frac{1}{2}l_*^2) \\ -(\zeta l_* + \frac{1}{2}l_*^2) & -\zeta^2 & \zeta^2 + \zeta l_* + \frac{1}{2}l_*^2 \\ \zeta^2 + \zeta l_* + \frac{1}{2}l_*^2 & -(\zeta l_* + \frac{1}{2}l_*^2) & -\zeta^2 \end{pmatrix}. \tag{3.4}$$

It has the eigenvalues $\lambda_1 = 0$ (due to the conservation of $l_1 + l_2 + l_3$) and

$$\lambda_{2/3} = -\frac{3f\zeta^2}{2(\zeta + 3l_*)^2} \pm i\frac{\sqrt{3}f}{2}. \tag{3.5}$$

Hence, for a "switched-on" ES barrier $\zeta > 0$, we get $\mathrm{Re}(\lambda_{2/3}) < 0$, which means that equidistant steps are locally (asymptotically) stable. Hence (l_*, l_*, l_*) is an attractor of the system, so the terrace lengths will tend to l_* under growth. Loosely

spoken, the barrier favors equidistant steps under growth and counteracts step bunching.

The same considerations are valid for the p-BCF model (1.7), where equation (3.2) reads as

$$\dot{l}_i = f\Big(l_{i+1}\frac{\zeta^- + \zeta^m + \frac{1}{2}l_{i+1}}{\zeta^- + 2\zeta^m + \zeta^+ + l_{i+1}} + l_i\frac{\zeta^+ - \zeta^-}{\zeta^- 2\zeta^m + \zeta^+ + l_i} - l_{i-1}\frac{\zeta^m + \zeta^+\frac{1}{2}l_{i-1}}{\zeta^- + 2\zeta^m + \zeta^+ + l_{i-1}}\Big).$$

The impact of the approximation parameter p is minimal. The graphs of the lengths are nearly indistinguishable.

In the case of no ES barrier, i.e., $\zeta = 0$, (3.1) and (3.2) read as

$$\dot{\xi}_i = \tfrac{f}{2}(l_i + l_{i-1}) \text{ and} \tag{3.6a}$$

$$\dot{l}_i = \tfrac{f}{2}(l_{i+1} - l_{i-1}), \tag{3.6b}$$

so that step bunching is not prevented. Figure 12 shows an example where step bunching occurs. The initial lengths are $l_1 = 4.5$, $l_2 = 0.5$ and $l_3 = 1$, so $L_x = 6$. Considering the system (3.6), the length of the center terrace l_2 decreases and

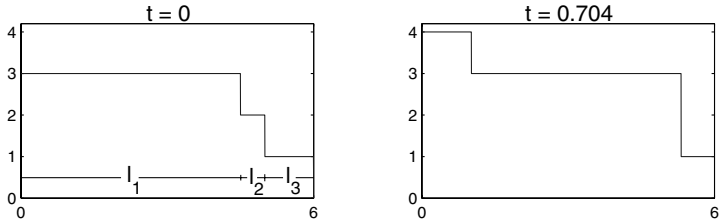

FIGURE 12. The terrace with length l_2 vanishes after time $t_b = 0.704$. The height of the step at $\xi_2 = \xi_3$ is 2 in atomic units.

becomes zero at a time t_b, so the two adjacent steps coincide and form a big step of two atomic units height (see Figure 12). Since we do not allow for overhangs in our model, we have to reinterpret the equations (3.6) in the time period where l_2 would become negative, i.e., from t_b on as long as $\dot{l}_2 < 0$. Once $\dot{l}_2 = \frac{f}{2}(l_3 - l_1)$ becomes positive again at a time t_r, we switch back to the original system (3.6) and the center terrace reappears. Our reinterpretation of (3.6) in case of $l_2 = 0$ goes as follows: For the new big step, two adatoms are needed for the step to grow one atomic unit, so the speed is only half of (3.6a):

$$\dot{\xi}_2 = \dot{\xi}_3 = \tfrac{f}{4}(l_1 + l_3).$$

Consequently, the ODEs for the remaining lengths l_1 and l_3 turn into

$$\begin{aligned} \dot{l}_1 &= -\tfrac{f}{4}(l_1 + l_3), \\ \dot{l}_3 &= \tfrac{f}{4}(l_1 + l_3), \end{aligned}$$

so the change of l_1 and l_3 speeds up. Figure 13 shows a plot of the three lengths l_1, l_2 and l_3 of the terraces versus time. At time t_b (the first dotted line) the center

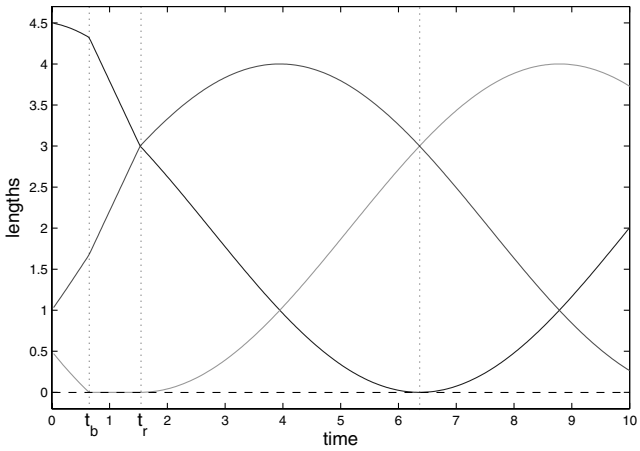

FIGURE 13. The terrace with length l_2 vanishes at time t_b and reappears at t_r.

terrace vanishes, so the two adjacent steps bunch and we switch to the intermediate ODE system until $l_3 \geq l_1$ (the second dotted line). We then switch back to the original system. After that, the terraces vanish one after another periodically, but the corresponding lengths only "touch" the value zero, so no change in the ODEs is necessary.

3.1.2. Numerical results. For the numerical simulations we choose the same initial lengths as in the previous example (i.e., $l_1 = 4.5$, $l_2 = 0.5$ and $l_3 = 1$). The numerical parameters are $\varepsilon = 3/64$ and $p = 20$. For the case of no ES barrier (i.e., $\zeta = 0$) step bunching occurs as predicted by the preceding considerations (see Figure 14). One difference is of course that terraces bunch earlier in the diffuse-interface model, because the terraces cannot vanish completely due to the nonzero ε (see Figure 15). Note that in the diffuse-interface model, step bunching is naturally treated and no intervention by hand to prevent negative step lengths is necessary.

Figure 16 shows the comparison of the diffuse-interface model with the BCF model for the stable case $\zeta = 1$, i.e., with ES barrier. As can be seen, the lengths tend to the stationary value l_*.

3.2. Step meandering

As a second example for the effects of the ES barrier, we turn to step meandering. This is a $2 + 1$-d effect. We consider a planar equidistant descending step train.

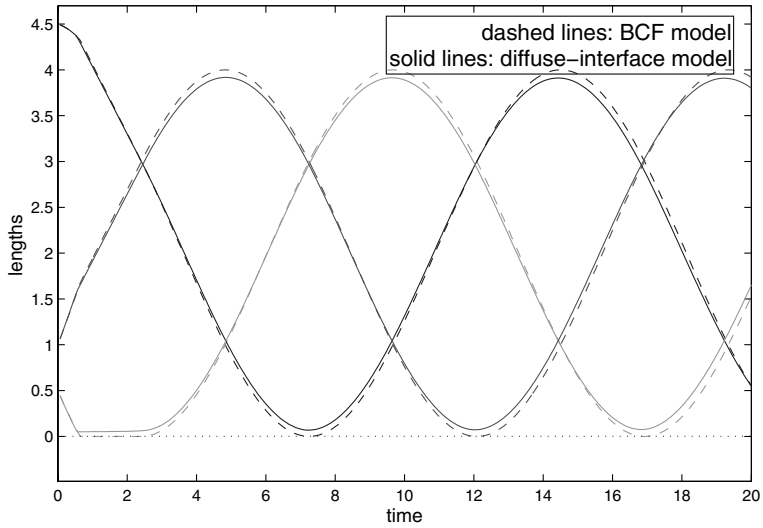

FIGURE 14. Without ES barrier, step bunching occurs periodically.

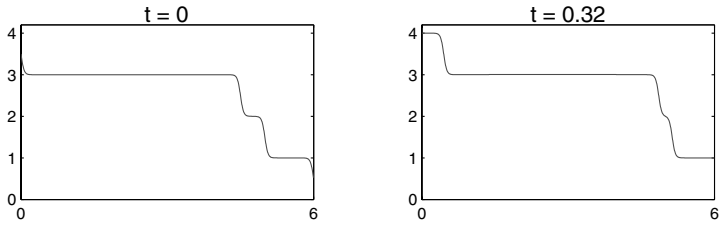

FIGURE 15. The terrace with length l_2 vanishes at time $t_b = 0.32$ due to the nonzero ε. The lengths at $t = 0$ are the same as in Figure 12.

We investigate small lateral perturbation of the steps. These perturbations are in-phase, i.e., identical for each step. Hence it is natural to work in a periodic setup with periodic cell $[0, L_x] \times [0, L_y]$, where L_x is the step spacing and L_y is a period of the perturbation (see Figure 17). We will speak of *step meandering* when the initial perturbation increases under growth, so that the steps do not stay straight.

The linear stability analysis of the BCF model has been carried out in [1]: The presence of an ES barrier leads to the *Bales–Zangwill instability* which is at the onset of step meandering.

3.2.1. Linear stability analysis. The following linear stability analysis is based on the original BCF model (1.1) and follows that of [1].

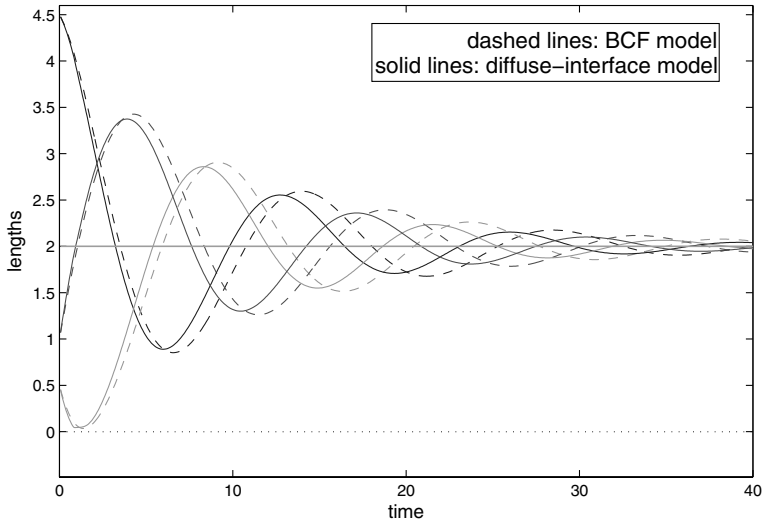

FIGURE 16. The ES barrier prevents step bunching: $l_* = 2$ is an attractor.

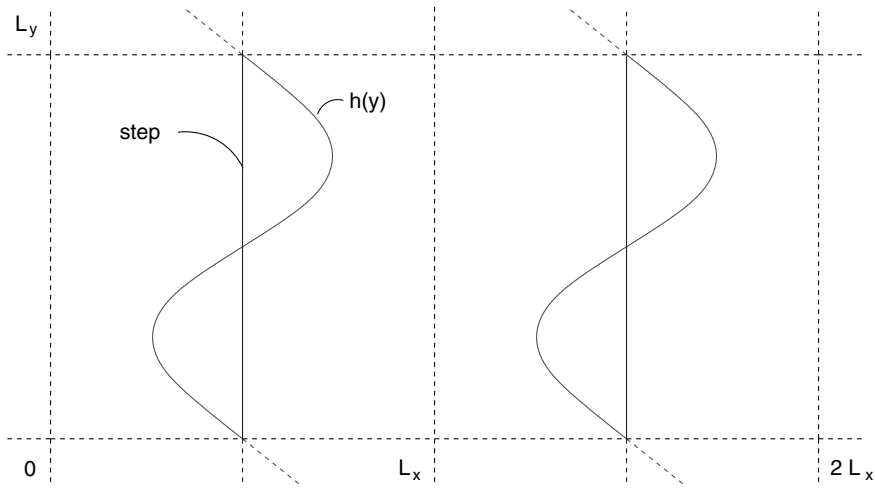

FIGURE 17. Top view of the unit cell $[0, L_x] \times [0, L_y]$: each step is perturbed by the same function $h(y)$ of order δ.

First, we insert an δ-expansion of w, i.e., $w = w_0 + \delta w_1 + \mathcal{O}(\delta^2)$, in the equations in order to derive the δ-order evolution of the boundary, which is the

evolution of the perturbation h. The resulting $\mathcal{O}(\delta)$-equations are

$$\begin{aligned} -\Delta w_1 &= 0 && \text{on terrace,}\\ \frac{d}{dt}h &= \frac{\partial w_1^+}{\partial x} - \frac{\partial w_1^-}{\partial x} && \text{at step,}\\ w_1^+ &= -ch - \frac{dh^2}{dy^2} && \text{at step up,}\\ \zeta_0\frac{\partial w_1^-}{\partial x} + w_1^- &= -(c - fL_x - f\zeta_0)h - \frac{dh^2}{dy^2} && \text{at step down,} \end{aligned}$$

where $c = f(\zeta_0 L_x + \frac{1}{2}L_x^2)/(\zeta_0 + L_x)$. Fourier transformation in y yields

$$\begin{aligned} -\frac{\partial^2 w_1}{\partial x^2} + |k|^2 w_1 &= 0,\\ \frac{d}{dt}h_k &= \frac{\partial w_1^+}{\partial x} - \frac{\partial w_1^-}{\partial x},\\ w_1^+ &= (|k|^2 - c)h_k,\\ \zeta_0\frac{\partial w_1}{\partial x} + w_1^- &= (f\zeta_0 - c + fL_x + |k|^2)h_k. \end{aligned}$$

This motivates the Ansatz

$$w_1(x, |k|) := c_1 \exp(|k|x) + c_2 \exp(-|k|x).$$

Tedious calculations for c_1 and c_2 finally yield for each wave vector k

$$\frac{d}{dt}h_k(t) = c_1|k|(1 - \exp(|k|L_x)) - c_2|k|(1 - \exp(-|k|L_x)) = \omega(k)h_k(t) \tag{3.7}$$

with the dispersion relation

$$\begin{aligned} \omega(k) =& \frac{-|k|(|k|^2 - c)|k|\zeta_0 \sinh(|k|L_x)}{\sinh(|k|L_x) + |k|\zeta_0 \cosh(|k|L_x)}\\ &- \frac{|k|(2(|k|^2 - c) + f(\zeta_0 + L_x))(\cosh(|k|L_x) - 1)}{\sinh(|k|L_x) + |k|\zeta_0 \cosh(|k|L_x)}. \end{aligned} \tag{3.8}$$

The calculations for the p-BCF model (1.7) are analogous. The resulting dispersion relation is given by

$$\begin{aligned} \omega(k) =& \frac{-|k|^2 \sinh(|k|L_x)\left[(|k|^2 - c_p)(\zeta^+ + 2\zeta^m + \zeta^-) + fL_x(\zeta^m + \zeta^+)\right]}{\sinh(|k|L_x)(\zeta^+\zeta^-|k|^2 - (\zeta^m|k|)^2 + 1) + |k|\cosh(|k|L_x)(\zeta^- + \zeta^+) + 2\zeta^m|k|}\\ &- \frac{|k|(\cosh(|k|L_x) - 1)\left[2(|k|^2 - c_p) + f(\zeta^- - \zeta^+ + L_x)\right]}{\sinh(|k|L_x)(\zeta^+\zeta^-|k|^2 - (\zeta^m|k|)^2 + 1) + |k|\cosh(|k|L_x)(\zeta^- + \zeta^+) + 2\zeta^m|k|} \end{aligned} \tag{3.9}$$

with $c_p := fL_x \frac{\zeta^- + \zeta^m + L_x/2}{\zeta^- + 2\zeta^m + \zeta^+ + L_x}$.

Note that due to the linearisation, the dispersion relation for a given wave number $|k|$ is independent of all other wave numbers. This permits us to decompose

the perturbation in perturbations of just a single wave number and analyse only one of those.

As can be seen from (3.8), for $\zeta = 0$ or $f = 0$ we have $\omega(k) < 0$ for all k, so that any initial perturbation will flatten out during growth. Only if $\zeta > 0$ and $f > 0$, there is a region of wave numbers for which $\omega(k) > 0$. In this case an instability will develop. This means that the ES barrier favors step meandering under growth.

The diffuse-interface model has a similar structure: There is a 1-d travelling wave solution ϕ_*. By conservation of volume, its speed has to be fL_x. If $\xi := x - fL_x t$ denotes the normal variable in a moving frame, ϕ_* is characterised by

$$\begin{aligned} -fL_x\partial_\xi\phi_* + \partial_\xi(M(\phi_*)\partial_\xi(\varepsilon\partial_\xi^2\phi_* - \tfrac{1}{\varepsilon}G'(\phi_*))) = f,\\ \phi_*(\xi + L_x) = \phi_*(\xi) - 1. \end{aligned} \tag{3.10}$$

It is a stationary point of the full diffuse-interface model in moving frame variables, i.e.,

$$\partial_t\phi = fL_x\partial_\xi\phi - \nabla_{(\xi,y)}\cdot(M(\phi)\nabla_{(\xi,y)}(\varepsilon\Delta_{(\xi,y)}\phi - \tfrac{1}{\varepsilon}G'(\phi))) + f,$$

which we think of as

$$\partial_t\phi = \mathcal{N}(\phi),$$

where $\mathcal{N}$ is a nonlinear 2-d fourth-order operator.

The evolution of a small perturbation $\delta\phi = \phi - \phi_*$ around ϕ_* is described by the linearisation

$$\partial_t\delta\phi = A(\phi_*)\delta\phi, \tag{3.11}$$

where $A(\phi_*)$ is a linear 2-d fourth-order operator. Notice that $\delta\phi$ is periodic in both ξ and y.

Since ϕ_* only depends on ξ, (3.11) can be Fourier transformed in y:

$$\partial_t\delta\phi_k = A_k(\phi_*)\delta\phi_k,$$

where $A_k(\phi_*)$ is a linear 1-d fourth-order operator.

We expect that in the regime $\varepsilon \ll 1$, its spectrum $\sigma(A_k(\phi_*))$ is of the following form: It has one eigenvalue close to $\omega(k)$ and the remainder of the spectrum is very negative. This would for instance imply that the total energy $H_k(t) := \int_0^{L_x} |\delta\phi_k(t)|^2\, d\xi$ contained in the wave number k at time t grows approximately as $\exp(2\omega(k)t)$:

$$H_k(t) \;\propto\; \exp(2\omega(k)t). \tag{3.12}$$

We check this hypothesis numerically directly on the nonlinear diffuse-interface model for small perturbations $\delta\phi$ of wave number k of ϕ_*, see the following section.

3.2.2. Numerical results. Let us first describe how we construct the initial small perturbation of wave number k of the travelling wave profile ϕ_*.

- As an approximation to the travelling wave profile ϕ_* (which is defined through (3.10) but not explicitly known), we take

$$\widetilde{\phi}_*(x) = \frac{1}{2}\left(1 - \tanh\left(\frac{x - L_x/2}{2\varepsilon}\right)\right), \quad x \in (0, L_x),$$

which we extend "periodically" (i.e., as $\widetilde{\phi}_*(x+L_x) = \widetilde{\phi}_*(x) - 1$). Notice that $\widetilde{\phi}_*$ is exponentially close to ϕ_*.

- In order to control which modes are excited, we consider an additive perturbation

$$\phi(t=0,x,y) = \widetilde{\phi}_*(x) + \sum_k \delta_k \sin\left(\frac{2\pi k}{L_y} y\right). \tag{3.13}$$

We monitor the total energy in its nonlinear version

$$H_k(t) = \int_0^{L_x} |(\phi - \phi_*)_k(t)|^2 \, dx = \int_0^{L_x} |\phi_k(t)|^2 \, dx.$$

We use the Fast Fourier Transform to compute $H_k(t)$ in the discrete setting. In order to probe exponential growth we evaluate

$$\omega_t^\varepsilon(k) = \frac{\ln\left(\frac{H_k(t)}{H_k(t-\Delta t)}\right)}{2\Delta t}.$$

In theory, $\omega_t^\varepsilon(k)$ should be independent of t and close to $\omega(k)$ for small ε. In practice, $\omega_t^\varepsilon(k)$ depends on t, as can be seen from Figure 18. The reasons for this

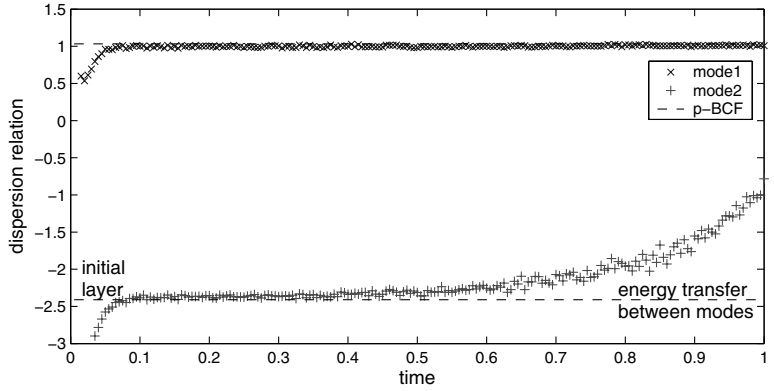

FIGURE 18. After the initial layer, the dispersion relation of the diffuse-interface model matches the predicted values. When the first mode gets larger and the second mode gets small, we can see the energy transfer between the modes due to nonlinear effects.

behavior are the following:

- As outlined in Section 2.5.1, the diffuse-interface-w needs some time to reach its final shape. This is at the origin of the initial layer.
- As time proceeds, perturbations grow in the unstable case. Hence one leaves the linear regime with its decoupled modes. As one can see in Figure 18, there is a transfer of energy from the growing mode 1 (i.e., $|k| = \frac{2\pi}{L_y}$), which

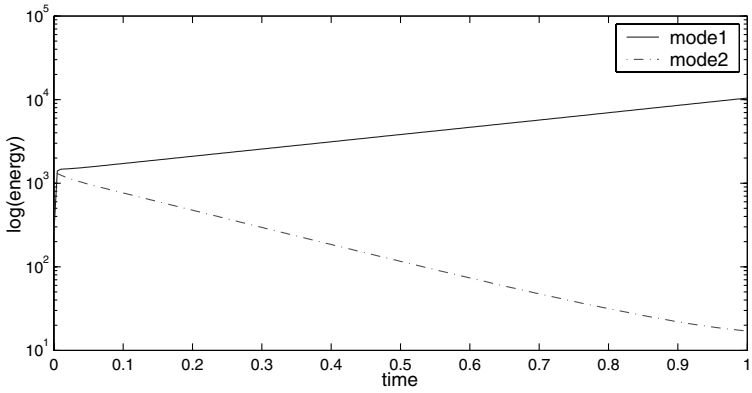

FIGURE 19. Total energy in logarithmic plot: The growing mode 1 contains most of the energy.

contains most of the energy (see Figure 19), to the decaying mode 2 (i.e., $|k| = \frac{4\pi}{L_y}$), which only contains little energy.

Nonetheless, there is always a plateau value $\omega^\varepsilon(k)$ for $\omega_t^\varepsilon(k)$. Our numerical simulations show linear convergence of $\omega^\varepsilon(k)$ to $\omega(k)$ as $\varepsilon \downarrow 0$, see Figure 20 for an unstable case and Figure 21 for a stable case.

3.3. Boundary condition of w

We present some numerical results of $2+1$-d simulations based on the diffuse-interface approximation (1.4). All the main features given by the BCF model (1.1) can be found in the pictures.

As numerical setup we use a 2-d unit cell of size $L_x = L_y = 7$ (see Figure 17) with the numerical parameters $p = 20$ and $\varepsilon = \frac{7}{32}$. We perturb planar initial data with a single wave vector k with $|k| = 2\pi/L_y$ according to (3.13).

In Figure 22 we set $f = 0$ and $\zeta = 0$. Following (1.1a), (1.1b) and (1.1c), w is the harmonic continuation of its boundary values at the step, which are determined by the curvature κ of the step. This property is clearly visible in the figure.

In Figure 23, we switch on the deposition ($f = 0.1$) and the ES barrier ($\zeta = 5$). The upper terrace is to the left, the position of the step is a slight perturbation of a straight line. We can observe

- the concave shape of w on the terraces due to deposition,
- the jump of w at the step due to the ES barrier,
- the variation in the jump height due to curvature.

The discontinuity in w is well resolved.

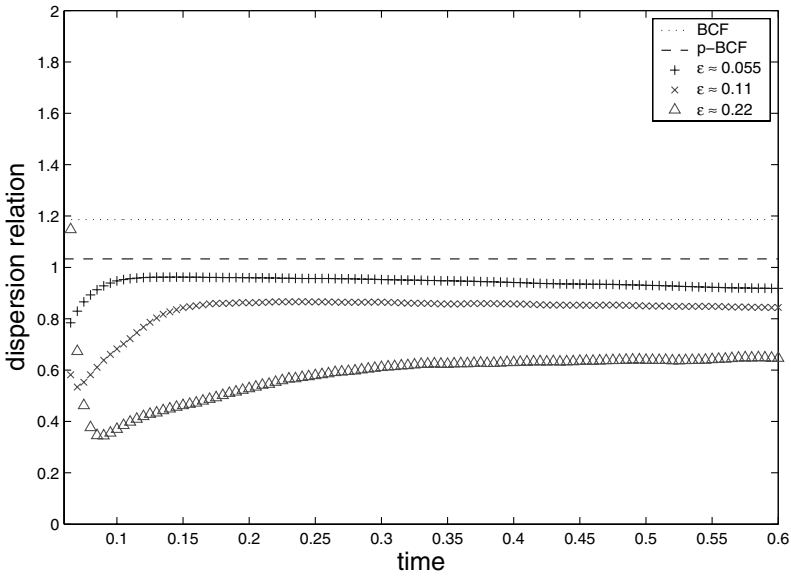

FIGURE 20. Dispersion relation ω^ε vs. time for different values of ε. Linear convergence in ε can be seen.

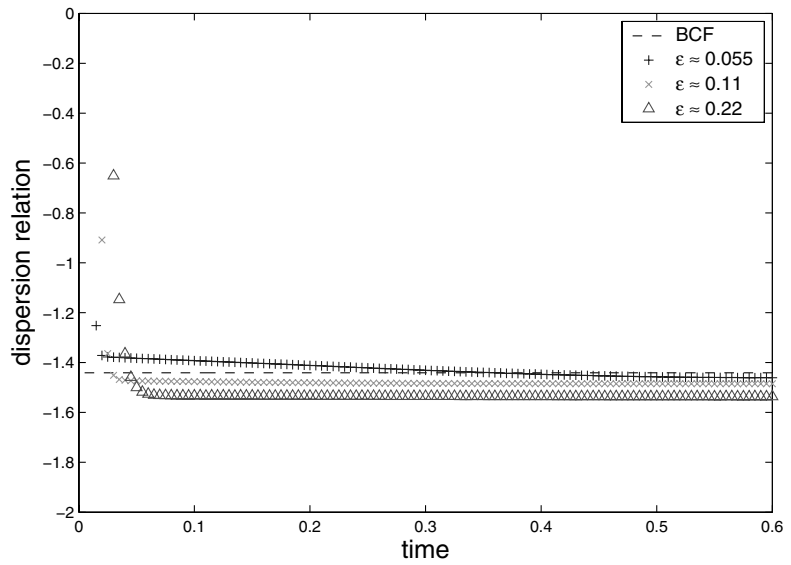

FIGURE 21. Dispersion relation ω^ε vs. time for different values of ε in the stable case $f = \zeta = 0$.

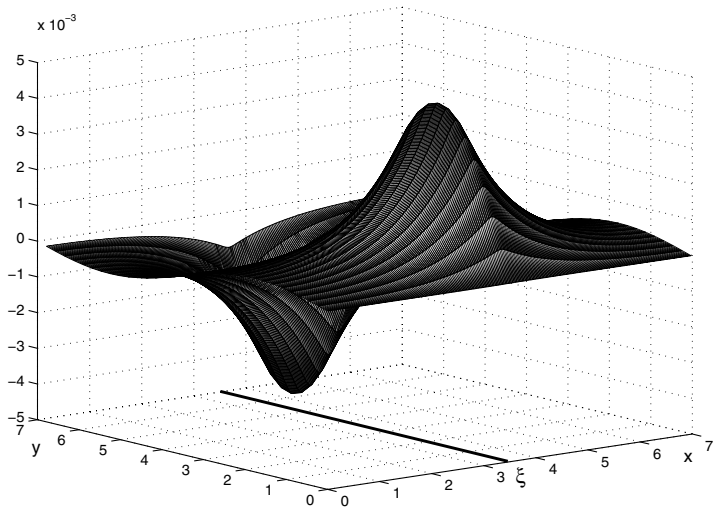

FIGURE 22. The excess density w with no deposition and no barrier is the harmonic continuation of the boundary values for a slightly perturbed step ξ.

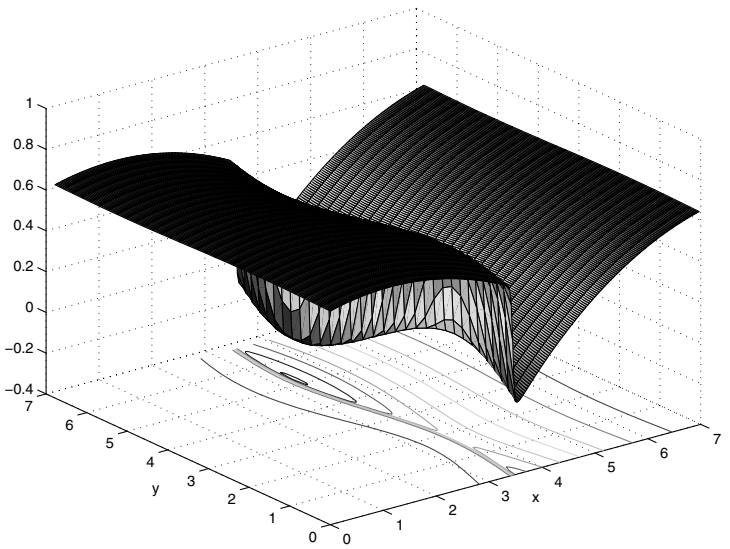

FIGURE 23. Excess density w under growth with ES barrier.

4. Outlook

4.1. Finite element formulation

We propose a finite element formulation for the time discrete problem (2.14), which we simplify for the following discussion to

$$\left[\frac{1}{\tau M(\phi)}\mathrm{id} + \varepsilon(\nabla\nabla\cdot)^2 - \frac{1}{\varepsilon}\nabla G''(\phi)\nabla\cdot\right] J = -\nabla w. \tag{4.1}$$

4.1.1. Weak formulation. The weak formulation of (4.1) is given by

$$\int_\Omega \frac{1}{\tau M(\phi)} J\cdot\widetilde{J} + \int_\Omega \varepsilon(\nabla\nabla\cdot J)\cdot(\nabla\nabla\cdot\widetilde{J}) + \int_\Omega \frac{1}{\varepsilon}G''(\phi)(\nabla\cdot J)(\nabla\cdot\widetilde{J}) = -\int_\Omega \nabla w\cdot\widetilde{J}$$

for test fields $\widetilde{J}$. To avoid high-order finite elements, we introduce an auxiliary quantity K defined by

$$K := -\nabla\nabla\cdot J.$$

We can then rewrite the weak formulation as

$$\int_\Omega K\cdot\widetilde{J} = \int_\Omega (\nabla\cdot J)(\nabla\cdot\widetilde{J}), \tag{4.2a}$$

$$\int_\Omega \frac{1}{\tau M(\phi)} J\cdot\widetilde{J} + \int_\Omega \varepsilon(\nabla\cdot K)(\nabla\cdot\widetilde{J}) + \int_\Omega \frac{1}{\varepsilon}G''(\phi)(\nabla\cdot J)(\nabla\cdot\widetilde{J}) = -\int_\Omega \nabla w\cdot\widetilde{J}, \tag{4.2b}$$

which only requires $J, K \in H(\nabla\cdot,\Omega) := \{J \in (L^2(\Omega))^2 \mid \nabla\cdot J \in L^2(\Omega)\}$. Suitable $H(\nabla\cdot,\Omega)$-conforming elements are the Raviart–Thomas (RT) elements [8]. For a given triangulation $\mathcal{T}$ of Ω, they are defined by

$$\begin{aligned}\mathrm{RT}(\mathcal{T}) := \{J \in (L^2(\Omega))^2 \mid \forall T \in \mathcal{T}\ \exists a_T \in \mathbb{R}^2 \text{ and } b_T \in \mathbb{R}:\\ \forall x \in T\ J(x) = a_T + b_T x \ \text{ and } \forall \text{ edges } E : [J]_E\cdot\nu_E = 0\},\end{aligned} \tag{4.3}$$

where $[J]_E$ denotes the jump of J across the edge E. The continuity of the normal component at the boundary provides the $H(\nabla\cdot,\Omega)$-conformity.

In order to derive w (according to (1.4c)), we define the weak gradient of ϕ, $g \in \mathrm{RT}(\mathcal{T})$, by

$$\int_\Omega g\cdot\widetilde{J} = -\int_\Omega \phi\nabla\cdot\widetilde{J}, \qquad \forall\widetilde{J} \in \mathrm{RT}(\mathcal{T}), \tag{4.4}$$

so that

$$w = -\varepsilon\nabla\cdot g + \tfrac{1}{\varepsilon}G'(\phi). \tag{4.5}$$

We use an analogous definition for the gradient of w in the right-hand side of (4.2b).

Assuming ϕ is piecewise constant, a cubature formula e.g., for $\int_\Omega \frac{1}{\varepsilon}G''(\phi)(\nabla\cdot J)(\nabla\cdot\widetilde{J})$ is not needed. RT elements go with this assumption, since the divergence of a RT element is by definition piecewise constant and ϕ is given by $\partial_t\phi + \nabla\cdot J = f$. Thus, due to (4.5), w is piecewise constant, too.

In terms of mass and stiffness matrices, problem (4.2) reads as

$$\begin{aligned} B_0 K &= A_0 J, \\ \tfrac{1}{\tau} B_1 J + \varepsilon A_0 K + \tfrac{1}{\varepsilon} A_1 J &= Cw. \end{aligned}$$

where C denotes the gradient operator defined by (4.4) after mass lumping. Thus we have to solve

$$\left(\tfrac{1}{\tau} B_1 + \varepsilon A_0 B_0^{-1} A_0 + \tfrac{1}{\varepsilon} A_1\right) J = Cw. \tag{4.6}$$

We lump masses in B_0 and B_1, so that B_0 can be easily inverted.

4.1.2. Construction of basis functions for RT elements. We use an *edge-oriented basis* for $\mathrm{RT}(\mathcal{T})$, i.e., one basis element for each edge E of the triangulation. The two triangles which share the edge E are denoted by $T_\pm$, the vertex of $T_\pm$ which does not belong to E is denoted by $P_\pm$ (see Figure 24). An edge-oriented basis

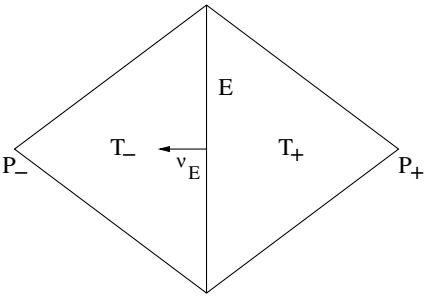

FIGURE 24. Edge E shared by two triangles T_+ and T_- with nodes P_+ and P_-, respectively. ν_E is the outer normal of T_+.

element ψ_E is then defined by

$$\psi_E(x) := \begin{cases} \pm \frac{|E|}{2|T_\pm|}(x - P_\pm) & \text{for } x \in T_\pm \\ 0 & \text{elsewhere.} \end{cases} \tag{4.7}$$

This choice provides:

- The normal component is constant along an arbitrary edge F, namely

$$\psi_E \cdot \nu_F(x) \equiv \delta_{EF}.$$

- $\{\psi_E\}_E$ is basis of $\mathrm{RT}(\mathcal{T}) \subset H(\nabla\cdot, \Omega)$.

Hence, each $J \in \mathrm{RT}(\mathcal{T})$ has the representation $J = \sum_E (J \cdot \nu_E)\psi_E$.

4.1.3. Comparison with FV scheme in 1-d. Let $h_\pm$ be the height of $T_\pm$, so that $|T_\pm| = \frac{1}{2}|E||h_\pm|$. Then, definition (4.7) reads as $\psi_E(x) = \pm(x - P_\pm)/|h_\pm|$ for $x \in T_\pm$ which in turn yields

$$\psi_i(x) = \begin{cases} \pm\frac{1}{h}(x - x_{i\pm1}) & \text{for } x \in T_\pm \\ 0 & \text{elsewhere} \end{cases}$$

in one dimension. So in 1-d, the Raviart–Thomas basis functions are just the usual linear basis functions, see Figure 25. Additionally, the operator yields in

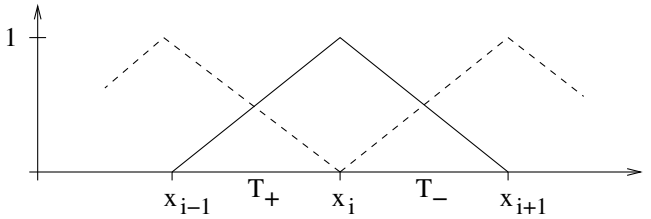

FIGURE 25. In the 1-d case, the Raviart–Thomas elements coincide with standard piecewise linear elements.

one dimension the same matrices A_0, A_1, B_0 and B_1 as the finite volume scheme introduced in Section 2.3 (after mass lumping B_0 and B_1). The stiffness matrices are tridiagonal matrices

$$\frac{1}{h}A_0 = \frac{1}{h^2}\Big(-1\ ,\ 2\ ,\ -1\Big),$$
$$\frac{1}{h}A_1 = \frac{1}{h^2}\Big(-G''(\phi_i)\ ,\ G''(\phi_i) + G''(\phi_{i+i})\ ,\ -G''(\phi_{i+1})\Big)$$

and the lumped mass matrices are

$$\frac{1}{h}B_0 = \mathrm{id}, \qquad \frac{1}{h}B_1 = \mathrm{diag}\Big(1 + \frac{1}{2\varepsilon}\big(\zeta(\phi_i) + \zeta(\phi_{i+1})\big)\Big).$$

It is noteworthy that the treatment of the mobility advocated in [5] is a natural consequence of a conformal discretisation of the symmetric formulation in J. Since w is piecewise constant (i.e., $w_{|T_i} \equiv w_i$), the vector-valued right-hand side reads as

$$\frac{1}{h}Cw = \frac{1}{h}(w_i - w_{i+1}),$$

which coincides with the (negative) discrete gradient operator of the FV scheme.

Acknowledgment

FO, PP and TR acknowledge support from the Deutsche Forschungsgemeinschaft through the SFB "Singular Phenomena and Scaling in Mathematical Models" at the University of Bonn.

References

[1] G. Bales and A. Zangwill. *Morphological instability of a terrace edge during step-flow growth.* Phys. Rev. B **41(9)** (1990), 5500–5508.

[2] M.O. Bristeau, R. Glowinski, and J. Périaux. Numerical methods for the Navier-Stokes equations. Applications to the simulation of compressible and incompressible viscous flows. In *Finite elements in physics (Lausanne, 1986)*, pages 73–187. North-Holland, Amsterdam, 1987.

[3] W.K. Burton, N. Cabrera, and F.C. Frank. *The growth of crystals and the equilibrium structure of their surfaces.* Philos. Trans. Roy. Soc. London. Ser. A. **243** (1951), 299–358.

[4] G. Ehrlich and F.G. Hudda. *Atomic view of surface diffusion: tungsten on tungsten.* J. Chem. Phys. **44** (1966), 1036–1099.

[5] G. Grün and M. Rumpf. *Nonnegativity preserving convergent schemes for the thin film equation.* Numer. Math. **87(1)** (2000), 113–152.

[6] F. Otto, P. Penzler, A. Rätz, T. Rump, and A. Voigt. *A diffuse-interface approximation for step flow in epitaxial growth. Nonlin.* **17(2)** (2004), 477–491

[7] F. Otto, P. Penzler, T. Rump. Discretisation and numerical test of a diffuse-interface model with Ehrlich–Schwoebel barrier. SFB preprint, 2004.

[8] P.-A. Raviart and J.M. Thomas. A mixed finite element method for 2nd order elliptic problems. In *Mathematical aspects of finite element methods (Proc. Conf., Consiglio Naz. delle Ricerche (C.N.R.), Rome, 1975)*, pages 292–315. Lecture Notes in Math., Vol. 606. Springer, Berlin, 1977.

[9] R.L. Schwoebel and E.J. Shipsey. *Step motion on crystal surfaces.* J. Appl. Phys. **37** (1966), 3682–3686.

[10] U. Weikard. Numerische Lösungen der Cahn-Hilliard-Gleichung und der Cahn-Larché-Gleichung. Dissertation, Rheinische Friedrich-Wilhelms-Universität Bonn, Oct. 2002.

Felix Otto, Patrick Penzler and Tobias Rump
Institut für Angewandte Mathematik
Universität Bonn
Wegelerstr. 10, Bonn, Germany
e-mail: `otto@iam.uni-bonn.de`
e-mail: `penzler@iam.uni-bonn.de`
e-mail: `rump@iam.uni-bonn.de`

International Series of Numerical Mathematics, Vol. 149, 159–173

Islands in the Stream: Electromigration-Driven Shape Evolution with Crystal Anisotropy

Philipp Kuhn and Joachim Krug

Abstract. We consider the shape evolution of two-dimensional islands on a crystal surface in the regime where mass transport is exclusively along the island edge. A directed mass current due to surface electromigration causes the island to migrate in the direction of the force. Stationary shapes in the presence of an anisotropic edge mobility can be computed analytically when the capillary effects of the line tension of the island edge are neglected, and conditions for the existence of non-singular stationary shapes can be formulated. In particular, we analyse the dependence of the direction of island migration on the relative orientation of the electric field to the crystal anisotropy, and we show that no stationary shapes exist when the number of symmetry axes is odd. The full problem including line tension is solved by time-dependent numerical integration of the sharp-interface model. In addition to stationary shapes and shape instability leading to island breakup, we also find a regime where the shape displays periodic oscillations.

Mathematics Subject Classification (2000). Primary 53C44; Secondary 82C24.

Keywords. Two-dimensional shape evolution; surface electromigration; crystal steps; crystal anisotropy.

1. Introduction

The interest of researchers in the phenomenon of electromigration has in the past mainly been guided by the technological implications of this effect, namely the degeneration of integrated circuits [1, 2, 3]. A large body of experimental work has been devoted to the study of electromigration-induced failure of metallic conductor lines under accelerated testing conditions [2, 4, 5, 6]. At least for simple geometries

This work was supported by DFG within SFB 616 *Energiedissipation an Oberflächen.*

(e.g., a single void in a single crystal grain), such experiments have been successfully modeled using a macroscopic continuum theory of shape evolution [5, 7] (see Sect. 2). On the other hand, theorists have conducted a lively (and still ongoing) debate on the microscopic driving force of electromigration [8, 9].

What appears to be largely missing in the field is experimental and theoretical work on the mesocopic level, addressing the evolution of simple atomic-scale structures such as individual steps and single-layer islands. This could help to bridge the gap between the elementary moves of single atoms and the failure behavior of polycrystalline conductor lines with a complex internal geometry. In the present paper we address the electromigration-induced shape evolution of single, atomic-height islands on a crystal surface. We work in a continuum setting first introduced, in this context, by Pierre-Louis and Einstein [10]. Among the different kinetic regimes considered in their work, we focus here on the particularly simple case where mass transport is exclusively along the island edge, so that the area of the island is strictly conserved and the evolution law for the island boundary is local. Our new contribution consists of including crystal anisotropy, which is clearly necessary to make contact with island electromigration on real crystal surfaces (such as silicon [11, 12]) and in lattice Monte Carlo simulations [10, 13, 14].

The continuum model is introduced in the next section, and previous work on the problem is described. In Section 3 we show how stationary shapes can be explicitly computed when the smoothening effects of the edge free energy is neglected, and numerical results for the full, time-dependent problem are presented in Section 4.

2. Continuum model of shape evolution

The physical system consists of an island of monoatomic height on an otherwise flat crystal surface in interaction with the flow of the electrons. The island should be large enough to allow for a coarse grained description where the individual particles of the assembly are blurred into a continuous entity. To put this into a mathematical setting we represent the spatial conformation by a closed curve in the xy-plane parametrised by the arclength s. All geometrical and physical quantities can now be expressed as functions of s. We describe the local orientation of the island edge by the angle θ between the normal and the y-axis (counted positive in the clockwise direction). The derivative of θ with respect to s is then the local curvature κ. The force F acting on an atom at the island edge is composed of two contributions:

$$F = -\frac{\partial}{\partial s}(\tilde{\gamma}\kappa) + F_{el}. \tag{2.1}$$

Here $\tilde{\gamma}\kappa$ is the chemical potential of the island edge[1], with $\tilde{\gamma}$ denoting the edge stiffness, which is related to the step free energy $\gamma(\theta)$ by $\tilde{\gamma} = \gamma + d^2\gamma/d\theta^2$ [15]. The gradient of the chemical potential on the right hand side of (2.1) accounts for the

[1]Throughout we work in units where the atomic area and the lattice spacing are set to unity.

effect of capillarity which tends to minimize the free energy by driving material away from regions of high curvature. The second term is the force that actually causes electromigration. It is conventionally written in the form $F_{el} = eZ^*E_t$, where e is the elementary charge, E_t is the component of the local electric field which acts tangentially to the step edge, and Z^* is the effective valence of the step atom. On this level of modeling, all microscopic aspects of electromigration are lumped into the quantity Z^*. To give an example, the effective valence for a copper atom moving along a close-packed step on the Cu(100) surface has been calculated to be $Z^* \approx -31$ [14]. The form of the tangential electric field to be used in this work will be specified later.

The motion of the atoms along the edge can now be described by a mass current j that is proportional to the acting force, with the factor of proportionality defining the orientation-dependent step edge mobility $\sigma(\theta)$,

$$j = \sigma(\theta)F. \tag{2.2}$$

If we assume that atoms can neither detach from the island nor attach to it, the equation of shape evolution is simply the continuity equation that relates the divergence of the mass current to the normal velocity v_n of the island edge, as

$$v_n = -\frac{\partial}{\partial s}j = \frac{\partial}{\partial s}\sigma(\theta)[\frac{\partial}{\partial s}(\tilde{\gamma}\kappa) - eZ^*E_t]. \tag{2.3}$$

By dimensional analysis, the comparison of the two terms inside the square brackets on the right hand side of (2.3) defines the characteristic length scale [10, 16, 17]

$$l_E = \sqrt{\frac{\tilde{\gamma}}{|eZ^*E_0|}}, \tag{2.4}$$

where E_0 is a typical value of the electric field strength. For islands small compared to l_E the capillary forces dominate the evolution, while for islands large compared to l_E the evolution is dominated by the electromigration force. Thus l_E sets the length scale on which electromigration-induced shape instabilities can be expected.

As formulated so far, the model is identical to the one that has been used extensively to model the evolution of quasi-two-dimensional (cylindrical) voids in current-carrying metallic thin films [5, 7, 16, 18, 19, 20, 21, 22, 23, 24, 25, 26, 27, 28]. In that context it is essential to take into account the effect of *current crowding*, which refers to the fact that current lines cannot pass through the insulating void, and hence the electric field is enhanced in the remaining parts of the conductor. As it is necessary to monitor the changes in the electric current configuration that occur in response to the shape changes of the void, the dynamical evolution becomes manifestly nonlocal. In the physical situation of interest in the present paper, this complication does not arise, since a single-layer island is not expected to significantly modify the electric current configuration in the underlying substrate film. We may therefore assume a constant electric field of strength E_0 directed at an angle ϕ with respect to the x-axis, and set $E_t = E_0 \cos(\theta + \phi)$ in (2.3).

A model that interpolates between the case of a completely insulating void and the case of a constant electric field considered here is obtained by assigning a conductivity Σ' to the void which differs from the conductivity Σ of the bulk material [18, 19]. The two limiting cases then correspond to $\Sigma'/\Sigma = 0$ and $\Sigma'/\Sigma = 1$. The local model with $\Sigma'/\Sigma = 1$ has also been used to describe the electromigration-driven evolution of dislocation loops [29, 30].

Our primary aim in this paper will be to determine the stationary shapes of the drifting island. The condition for an island to move at constant velocity V along the x-axis without changing its shape is

$$v_n = V \sin(\theta). \tag{2.5}$$

It has been shown long ago that in the absence of anisotropy ($\tilde{\gamma}$ and σ independent of θ) a circle is a stationary solution of (2.3), for general conductivity ratio Σ'/Σ [18]. In the following we try to find corresponding results for the anisotropic case.

3. Analysis in the absence of capillarity

Combining the equation of motion (2.3) and the stationarity condition (2.5) gives

$$\frac{\partial}{\partial s}\sigma(\theta)[\frac{\partial}{\partial s}(\tilde{\gamma}\kappa) - F_0 \cos(\theta + \phi)] = V \sin(\theta) \tag{3.1}$$

with $F_0 = eZ^*E_0$. This is a nonlinear ordinary differential equation of fourth order for the shape, or alternatively of second order, when viewed as an equation for the curvature as a function of θ (using $\frac{\partial}{\partial s} = \kappa\frac{\partial}{\partial \theta}$). In this section the capillarity term proportional to the stiffness $\tilde{\gamma}$ will be neglected. While it is true that the effects of capillarity become small for large islands (island radius $\gg l_E$), it can hardly be justified to drop this term altogether, because it contains the highest order derivative in the equation. In fact islands that are large compared to l_E break apart, rather than reaching a steadily drifting shape [10] (see Sect. 4).

Nevertheless the analysis of the capillarity-free case $\tilde{\gamma} = 0$ is rather instructive. It is accessible to an analytical treatment, because the unknown curvature enters (3.1) only through the derivative $\frac{\partial}{\partial s}$ which can be eliminated by the following substitution: From the two geometrical relations

$$(ds)^2 = (dx)^2 + (dy)^2 \Leftrightarrow \left(\frac{\partial x}{\partial s}\right)^2 + \left(\frac{\partial y}{\partial s}\right)^2 = 1 \tag{3.2}$$

and

$$\tan(\theta) = -\frac{dy}{dx} = -\frac{\frac{\partial y}{\partial s}}{\frac{\partial x}{\partial s}} \tag{3.3}$$

we conclude that $\frac{\partial y}{\partial s} = -\sin(\theta)$. Replacing $\sin(\theta)$ in (3.1) using this relation we find that the derivative of $Vy - j$ is zero and therefore [29] $Vy = j + \text{const}$. The constant

of integration can be set to zero, since it generates only a vertical displacement. Hence the y-coordinate of the island shape as a function of θ is

$$y(\theta) = \frac{F_0}{V}\sigma(\theta)\cos(\theta+\phi) \tag{3.4}$$

and using $\frac{dy}{dx} = -\tan(\theta)$ once more, we obtain

$$x(\theta) = -\int_0^\theta \cot(\theta')\frac{\partial y}{\partial \theta'}\,d\theta'. \tag{3.5}$$

In order to derive stationary island shapes from (3.4) and (3.5) one has to specify the mobility $\sigma(\theta)$. To mimic the anisotropy of a crystal surface with a certain discrete rotational symmetry, we choose [16]

$$\sigma(\theta) = \frac{\sigma_0[1+S\cos^2(D(\theta+\alpha))]}{1+S\cos^2(D\alpha)} \tag{3.6}$$

where α is the angle between the symmetry axes and the coordinate system[2], $2D$ is the number of symmetry axes, and $S \geq 0$ is a measure for the strength of the anisotropy; see Fig. 6 for an illustration of (3.6). The denominator ensures that the mobility at $\theta = 0$ is σ_0.

3.1. Existence of stationary shapes

When calculating the shape by means of (3.4) and (3.5) with a given choice of D, S, α and ϕ, one encounters two types of irregularities: (i) The curve is generally not closed, and (ii) it can contain self-intersections. To get a closed shape one has to demand that x and y are 2π-periodic functions of θ. Because $y(\theta)$ is always 2π-periodic it suffices to have

$$\int_0^{2\pi} dx(\theta) = \int_0^{2\pi} d\theta\ \cot(\theta)[\frac{d\sigma}{d\theta}\cos(\theta+\phi) - \sigma\sin(\theta+\phi)] = 0. \tag{3.7}$$

For integer values of D (even rotational symmetry) the mobility is π-periodic and hence the integrand in (3.7) is odd under shifts $\theta \to \theta+\pi$. As a consequence (3.7) is always fulfilled. For half-integer D (odd rotational symmetry) the evaluation of the integral in (3.7) yields $2D\cos(\phi)\cos(2D\alpha) - \sin(\phi)\sin(2D\alpha)$ times a nonzero factor, so that (3.7) requires that

$$\tan(2D\alpha)\tan(\phi) = 2D. \tag{3.8}$$

The generation of self-intersections is illustrated in Fig. 1. Because the self-intersections are always accompanied by singularities (sign changes) of the curvature, they can be avoided by requiring that

$$\frac{1}{\kappa} = -\frac{1}{\sin(\theta)}\frac{\partial y}{\partial \theta} > 0 \tag{3.9}$$

[2]The reason why we do not choose a symmetry axis to coincide with one of the coordinate axes is that the stationarity condition (2.5) becomes particularly simple when the direction of motion coincides with the x-direction.

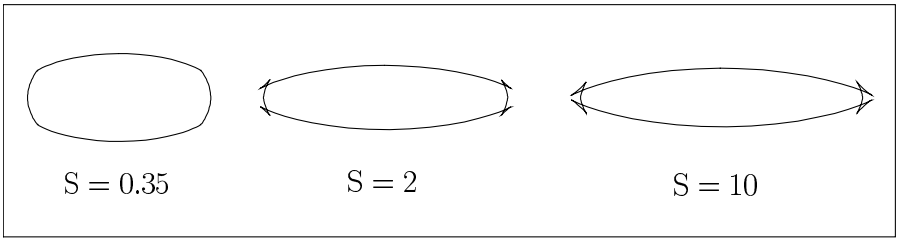

FIGURE 1. Formation of self-intersections in the capillarity-free case. The figure shows stationary shapes for $D = 3$ and $\alpha - \phi = 0$, where the critical anisotropy strength is $S_c \approx 0.35$.

everywhere. Thus the smoothness condition is related to the existence of extrema of $y(\theta)$. If $\frac{\partial y}{\partial \theta}$ is nonzero at 0 or π, the integral in (3.5) diverges because it contains the singularity of the cotangent function; the shape is then not bounded. If $\frac{\partial y}{\partial \theta}$ is zero somewhere else (3.9) is violated. If D is half-integer, the condition $\frac{\partial y}{\partial \theta}(0) = \frac{\partial y}{\partial \theta}(\pi) = 0$ requires $\alpha = \phi = 0$, which violates (3.8). In other words: For half-integer values of D the shape is either not closed or not bounded. While this result has been derived using the specific functional form (3.6) for the mobility, we expect it to be true in general that *in the capillarity-free case, no stationary shapes exist when the number of symmetry axes is odd.*

In the following we may therefore restrict ourselves to anisotropies of even symmetry. In this case $\frac{\partial y}{\partial \theta}(0) = \frac{\partial y}{\partial \theta}(\pi)$ because of the π-periodicity of y and we end up with two conditions,

$$\frac{\partial y}{\partial \theta}(0) = 0 \quad \Leftrightarrow \quad \frac{SD\sin(2D\alpha)}{1 + S\cos^2(D\alpha)} = -\tan(\phi) \tag{3.10}$$

$$\frac{\partial y}{\partial \theta}(\theta) \neq 0 \quad \Leftrightarrow \quad \frac{SD\sin(2D(\theta+\alpha))}{1 + S\cos^2(D(\theta+\alpha))} \neq -\tan(\theta+\phi) \text{ if } \theta \neq 0, \pi. \tag{3.11}$$

For a given value of the angle $\alpha - \phi$ between the symmetry axes and the field, (3.10) determines the direction of motion of the island, and the inequality (3.11) determines the values of S for which a smooth shape exists. For $S = 0$ there is always such a shape for every choice of $\alpha - \phi$, namely the circle which moves in the direction of the applied field. Increasing the anisotropy strength S the circle elongates along the field direction and finally at some critical value S_c sharp corners develop as precursors of self-intersections (see Fig. 1). For $S > S_c$ no stationary shapes exist. Figure 2 shows the array of possible shapes for the case of sixfold symmetry ($D = 3$). Note that in the absence of capillarity the characteristic scale (2.4) disappears from the problem, and hence the shapes are independent of island size (the island size determines however the migration speed, see Sect. 3.3).

It is straightforward to derive the critical anisotropy strength S_c for the special case $\alpha = \pi/2D$, $\phi = 0$, where the direction of island motion and the field

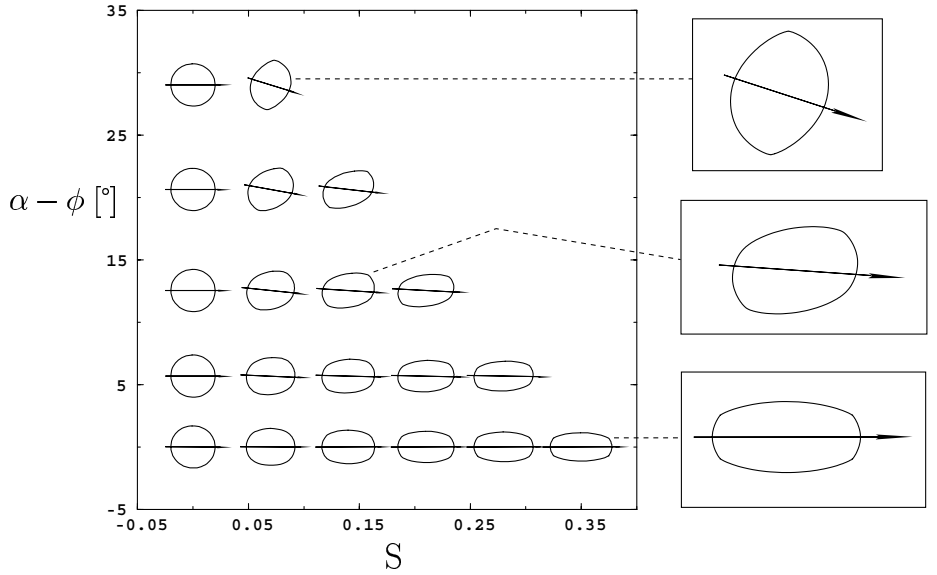

FIGURE 2. Stationary island shapes without capillarity, for sixfold crystal anisotropy and different values of the angle $\alpha - \phi$ between the symmetry axis of the anisotropy and the field, and the anisotropy strength S. In this figure the field direction is horizontal, and the arrows indicate the direction of island migration. In the empty part of the $(S, \alpha - \phi)$-plane no stationary shapes exist.

direction coincide with the direction of *minimal* mobility. The island then elongates perpendicular to the field and the self-intersections are forced by symmetry to appear at $\theta = 0$ and π. The condition of vanishing curvature radius reads simply $d^2y/d\theta^2|_{\theta=0} = 0$, which implies $[\sigma - d^2\sigma/d\theta^2]|_{\theta=0} = 0$. For our choice (3.6) of the mobility function this yields

$$S_c = \frac{1}{2D^2} \quad \text{for} \quad \alpha = \frac{\pi}{2D},\ \phi = 0. \tag{3.12}$$

This is the minimal value of S_c; the maximum range of smooth shapes appears at $\alpha = \phi = 0$, where the island moves along the direction of maximal mobility (Fig. 2).

3.2. Direction of island migration

An important consequence of anisotropy, which remains true also when capillary forces are turned on, is that the direction of island motion does not generally coincide with the direction of the electromigration force when $\alpha - \phi \neq 0$. This effect was previously observed for the nonlocal model [16]. The relationship (3.10) shows that α and ϕ have opposite signs, which implies that the direction of island motion lies between the field direction and the symmetry axis.

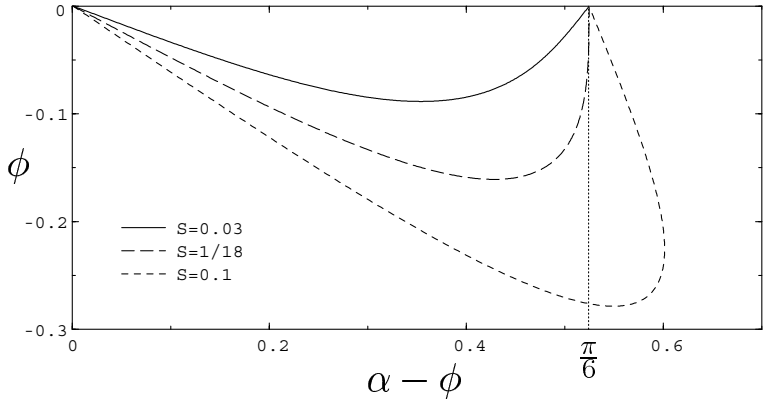

FIGURE 3. Relative angle ϕ between the field direction and the direction of island motion as a function of the angle $\alpha - \phi$ between the field and the axis of maximal mobility, as computed from (3.10) with $D = 3$. The vertical line marks the minimal mobility direction $\alpha = \pi/6$.

Figure 3 shows the angle between the direction of island motion and the field, ϕ, as a function of $\alpha - \phi$, which is the physical control parameter determined by the experimental setup. The island moves in the direction of the field, $\phi = 0$, both when the field is along the maximal mobility direction ($\alpha - \phi = 0$) and along the minimal mobility direction ($\alpha - \phi = \pi/2D$). With increasing anisotropy strength the graph becomes strongly skewed towards the minimal mobility direction until, at a critical anisotropy strength S_c which turns out to coincide with the expression (3.12) at which self-intersections first appear, the function becomes multi-valued. Beyond this point ϕ approaches a nonzero limit as $\alpha - \phi \to \pi/2D$, despite the fact that $\phi = 0$ exactly at $\alpha - \phi = \pi/2D$. The physical consequence is that the direction of island motion, as well as the island shape, change *discontinuously* as the field direction is moved across the direction of minimal mobility.

3.3. Migration speed

Since both coordinates of the parametrization (3.4) and (3.5) are multiplied by $1/V$ it is clear that the velocity is inversely proportional the extension of the island; for a circular island of radius R it is well known that $V \sim 1/R$ [18]. In other words, for every allowed choice of $\alpha - \phi$ and S, (3.4) and (3.5) generate a whole family of similar shapes moving with different velocities. To determine the dependence of V on the island size we calculate the area A of the island as follows:

$$A = \int_0^{2\pi} y(\theta)\, dx(\theta) = -\frac{1}{2}\int_0^{2\pi} d\theta\ \cot(\theta)\frac{d}{d\theta}y(\theta)^2$$
$$= -\frac{1}{2}\left(\frac{F_0}{V}\right)^2 \int_0^{2\pi} d\theta\ \cot(\theta)\frac{d}{d\theta}\sigma(\theta)^2\cos^2(\theta+\phi).$$

Inserting the form (3.6) for the mobility, it follows that the migration speed is of the form

$$V = \frac{F_0 \sigma_0}{\sqrt{A}} \frac{\sqrt{aS^2 + bS + \pi}}{1 + S\cos^2(D\alpha)}, \tag{3.13}$$

where the coefficients a and b are integrals of combinations of trigonometric functions which depend on α, ϕ and D. For the special case $\alpha = \phi = 0$ and $D = 3$ illustrated in the bottom row of Fig. 2, we find $a = 39\pi/8$ and $b = 7\pi$, which implies that the speed increases by about a factor of 1.5 when the anisotropy is increased from $S = 0$ to the critical value $S_c \approx 0.35$. The speed increase is related to the elongation of the island shape, which brings the orientation of the edge closer to the maximum mobility direction $\theta = 0$. When the island moves along the direction of minimal mobility ($\alpha = \pi/2D, \phi = 0$) the coefficients in (3.13) are negative, $a = -9\pi/8$ and $b = -5\pi$, which implies that the island slows down with increasing anisotropy.

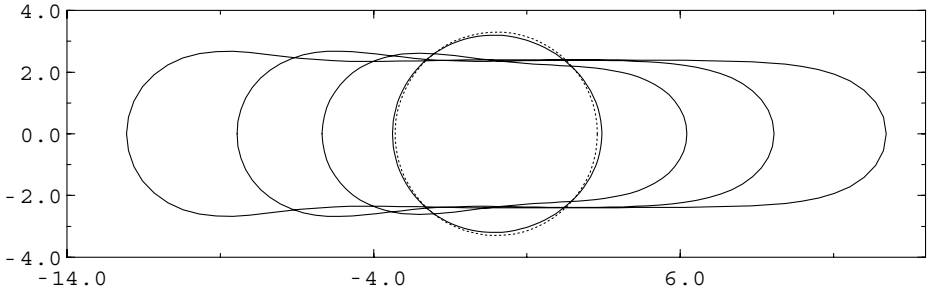

FIGURE 4. Stationary shapes without anisotropy. The dimensionless initial radii of the different shapes are $\rho_0 = 3.3$, 4, 5 and 6, and the computation was done with 100 discretization nodes. The dotted line shows the circular shape which constitutes the stable stationary solution for $\rho_0 < \rho_c \approx 3.26$.

4. Numerical integration of the time-dependent problem

We now integrate the full dynamical problem (2.3) by means of the sharp interface method described in [16, 31]. The evolution equations are discretized and integrated using a variable-step variable-order predictor-corrector method [32]. To avoid frequent remeshing an additional tangential velocity was introduced which keeps the nodes equidistant and which has to be computed implicitly.

Again we are mainly interested in the long time behavior of the system. As initial condition we take a circular island, usually imposed with a slight deformation to trigger a certain mode of motion[3]. We restrict ourselves to the case of a

[3]Unless stated otherwise, for the examples described here the asymptotic mode of evolution is independent of the precise initial condition.

mobility with six-fold symmetry ($D = 3$) with the field aligned parallel to a symmetry axis. The stiffness $\tilde{\gamma}$ is assumed to be isotropic[4]. The tunable parameters are then the initial radius R_0 and the strength S of the anisotropy. All lengths are expressed in units of the characteristic scale l_E, and the dimensionless initial radius is $\rho_0 = R_0/l_E$.

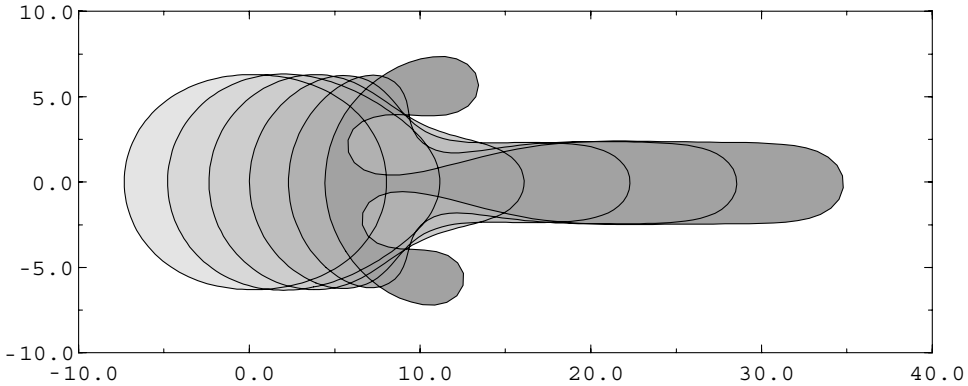

FIGURE 5. Breakup of an island in the isotropic case. The figure shows a time sequence of shapes, with a shading that darkens with increasing time. The initial shape is an ellipse elongated in the direction of island motion, with an area corresponding to a circle of dimensionless radius $\rho_0 = 7$. The computation used 150 discretization nodes. The breaking of the up-down symmetry is due to numerical noise.

To link our investigation to previous work we start with the isotropic case $S = 0$. Here we find circular stationary solutions for small radii. At the critical dimensionless radius $\rho_c = 3.26$ the circular solution loses its stability [19] and a bifurcation to non-circular stationary shapes occurs. In [30] this bifurcation was investigated by numerically solving the stationarity condition (3.1), and two branches of post-bifurcation shapes were found. In our time-dependent integration we only observe one branch, referred to as 'mode I' in [30]. To linear order in the distance from the bifurcation, the second 'mode II' branch is the symmetrical counterpart with respect to the circle, in the sense that $\kappa_I(\theta) + \kappa_{II}(\theta) = \text{const.}$; mode I is elongated in the direction of the field, mode II perpendicular to it. The mode II shapes which move at a smaller velocity seem not to be selected by the dynamics.

Some noncircular stationary shapes for $S = 0$ are shown in Fig. 4. We see that for $\rho_0 \geq 3.5$ the shapes become non-convex. These shapes were not found in [30], because the numerical calculation was stopped at the point where $1/\kappa$ approaches zero. Increasing the dimensionless island size further above $\rho_0 \simeq 6.2$

[4]This is motivated mainly by the desire to separate effects of kinetic anisotropy (in σ) from those of energetic anisotropy (in $\tilde{\gamma}$). Preliminary calculations including anisotropy in $\tilde{\gamma}$ indicate that the scenarios described here remain qualitatively the same [33].

causes the island to break. It first evolves a long finger, which corresponds to the 'slit'-solution described in [17], and subsequently invaginations ('negative' fingers) propagate in the backward direction, eventually disconnecting the island (Fig. 5). Similar breakups occur in the presence of anisotropy, so that the range of ρ_0 is generally restricted towards large values. The critical island size for breakup depends somewhat on the initial condition. For example, for the case $\rho_0 = 7$ shown in Fig. 5, it is possible to reach a stable stationary shape if the island is initially prepared in an elongated shape of appropriate width [34].

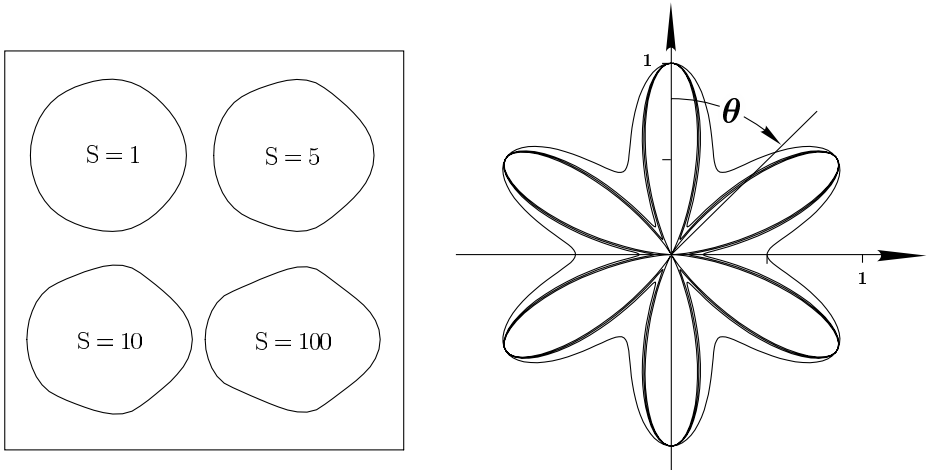

FIGURE 6. Left panel: Stationary shapes with anisotropic mobility of sixfold symmetry ($D = 3$). The initial shape was a circle of dimensionless radius $\rho_0 = 2.5$, and the anisotropy strength is $S = 1$, 5, 10 and 100. The computation used 50 discretization nodes. Right panel: Polar plot of the mobility corresponding to the shapes in the left panel.

For the anisotropic case there are no circular stationary shapes anymore. The deviation from the circle increases with increasing size ρ_0 and strength of anisotropy S. For strong anisotropy the islands evolve facet-like features, i.e., regions of the edge where the radius of curvature is very large. Figure 6 shows some examples. As was already discussed in Sect. 3.2, the direction of motion generally differs from the field direction, when the latter is not aligned with the symmetry axes of the anisotropy. Here we find that, with increasing island size, the symmetry of the direction of motion with respect to the field and anisotropy direction is *spontaneously broken*, i.e., we observe stationary island migration off the field direction even when the latter coincides with a symmetry axis of the anisotropy [34]. This behavior may perhaps be related to the discontinuity of the direction of motion when the field direction crosses the direction of minimal mobility, which was described in Sect. 3.2 for the capillarity-free case.

With increasing S the range of ρ_0 for which stationary solutions exist shrinks toward smaller values and is replaced by a domain where a qualitatively new behavior appears. Here the time evolution neither runs into a steady state nor into a breakup event but instead becomes oscillatory. A typical sequence is shown in Fig. 7: First the island elongates along the field direction, then one side of it bends so that the conformation becomes nonconvex. This leads to an acceleration of the mass transport which then shrinks the shape back to its original state. The oscillatory shape evolution in Fig. 7 is moreover seen to break the symmetry with respect to the field and anisotropy direction (recall that the field is directed along the x-axis which corresponds to a direction of maximal mobility, see the right panel in Fig. 6). The solution shown in Fig. 7 coexists with one obtained by reflection at the x-axis, in which the island travels to the right and down. Which of the two solutions is realized depends on the initial conditions. For other parameter values we have also observed solutions that switch between periods of upward and downward motion [34].

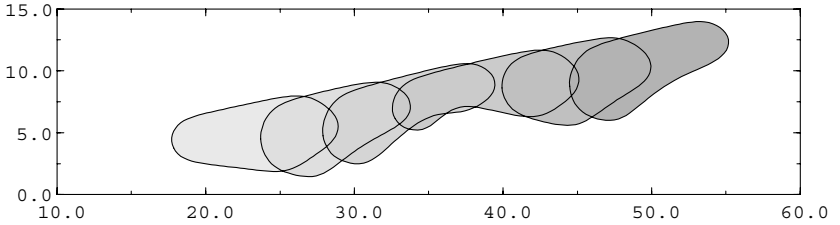

FIGURE 7. Oscillatory island motion. The dimensionless initial radius was $\rho_0 = 4$ and the anisotropy strength $S = 1$. Note that the upper boundary is stable, while the lower boundary supports a traveling wave. The computation used 100 discretization nodes.

The conditions for the appearance of stationary and oscillatory shapes largely remain to be clarified. On a qualitative level, we have observed that the "facets" that dominate the stationary shapes for large S tend to be close to orientations of maximal stability in the sense of linear stability analysis [35]. In contrast, the oscillatory shapes are typically bounded by one stable and one unstable orientation, and the shape oscillation can be viewed as the propagation of a wave along the unstable side of the island (see Fig. 7).

For the reasons described in Sect. 3, a quantitative comparison between the shapes computed numerically for the full problem and the analytically derived capillarity-free shapes is not meaningful. On a qualitative level, the most apparent difference between the shapes in Fig. 2 and Figs. 4, 6 is that in the presence of capillarity the direction of motion can clearly be discerned from the shape, while the capillarity-free shapes in Fig. 2 are front/back symmetric. This can be seen directly from (3.1). If $\tilde{\gamma} = 0$ the equation reduces to (again using $\frac{\partial}{\partial s} = \kappa \frac{\partial}{\partial \theta}$)

$$-F_0 \kappa \frac{d}{d\theta} \sigma(\theta) \cos(\theta + \phi) = V \sin(\theta) \tag{4.1}$$

which possesses two symmetries: First, reversing the direction of the field and the velocity simultaneously leaves the equation invariant. The second symmetry is the π-periodicity of the equation[5] which results in periodicity of the solution. Both symmetries are destroyed for nonzero stiffness.

5. Conclusions

It is interesting to compare the local ($\Sigma'/\Sigma = 1$) and nonlocal ($\Sigma'/\Sigma < 1$) boundary evolution problems in the light of our work[6]. For the isotropic case, it is known that the circular solution becomes linearly unstable for sufficiently large radius when $\Sigma'/\Sigma > 0$ [19], while it retains its stability (but becomes *nonlinearly* unstable under a sufficiently large perturbation [22, 27]) when $\Sigma'/\Sigma = 0$ [19, 20]. Furthermore it has been shown by complex variable techniques that noncircular stationary shapes cannot exist for $\Sigma'/\Sigma = 0$ [27], hence a void is forced to break up when it becomes unstable [22]. Here we have shown that breakup occurs for sufficiently large islands also in the local case, but in addition there is an intermediate regime, between the linear instability of the circular solution and breakup, where noncircular stationary solutions are stable[7].

Perhaps our most remarkable finding is that crystal anisotropy may induce complex, oscillatory evolution modes in the local problem. An example of oscillatory void evolution was previously reported by Gungor and Maroudas in the nonlocal case [37]. Future work should address the robustness and generality of the phenomenon. For this purpose it should be useful to employ numerical methods that are complementary to the sharp interface algorithm adopted here, such as finite element [21], phase-field [23, 26, 28], level set [24] and kinetic Monte Carlo [10, 13, 14] approaches, and to extend the study of the additional kinetic regimes (other than the case of edge diffusion considered here) in [10] to include crystal anisotropy.

Acknowledgment

We would like to thank Martin Schimschak for helpful correspondence.

References

[1] C.V. Thompson, J.R. Lloyd, *Electromigration and IC interconnects.* MRS Bulletin **18**, No. 12 (1993), 19–25.

[2] K.N. Tu, *Recent advances on electromigration in very-large-scale-integration of interconnects.* J. Appl. Phys. **94** (2003), 5451–5473.

[5] The mobility is π-periodic only for integer D, which is also the reason why we always get closed forms in this case (see Sect. 3).

[6] For a similar comparison in the substrate geometry see [36].

[7] Note that in [30] the stability and dynamical relevance of the noncircular stationary solutions was not addressed.

[3] Z. Suo, *Reliability of Interconnect Structures.* In: *Comprehensive Structural Integrity*, I. Milne, R.O. Ritchie, B. Karihaloo, Editors-in-Chief, Vol. 8: *Interfacial and Nanoscale Failure*, W. Gerberich, W. Yang, Editors (Elsevier, Amsterdam 2003), 265–324.

[4] E. Arzt, O. Kraft, W.D. Nix, J.E. Sanchez, Jr., *Electromigration failure by shape change of voids in bamboo lines.* J. Appl. Phys. **76** (1994), 1563–1571.

[5] O. Kraft, *Untersuchung und Modellierung der Elektromigrationsschädigung in miniaturisierten Aluminiumleiterbahnen.* PhD Dissertation (University of Stuttgart, 1995).

[6] Y.-C. Joo, S.P. Baker, E. Arzt, *Electromigration in single-crystal aluminum lines with fast diffusion paths made by nanoindentation.* Acta Mater. **46** (1998) 1969–1979.

[7] M.R. Gungor, D. Maroudas, *Theoretical analysis of electromigration-induced failure of metallic thin films due to transgranular void propagation.* J. Appl. Phys. **85** (1999) 2233–2246.

[8] A.H. Verbruggen, *Fundamental questions in the theory of electromigration.* IBM J. Res. Develop. **32** (1988) 93–98.

[9] R.S. Sorbello, *Theory of electromigration.* Solid State Phys. **51** (1998), 159–231.

[10] O. Pierre-Louis, T.L. Einstein, *Electromigration of single-layer clusters.* Phys. Rev. B **62** (2000) 13697–13706.

[11] J.-J. Métois, J.C. Heyraud, A. Pimpinelli, *Steady-state motion of silicon islands driven by a DC current.* Surf. Sci. **420** (1999), 250–258.

[12] A. Saúl, J.-J. Métois, A. Ranguis, *Experimental evidence for an Ehrlich-Schwoebel effect on Si(111).* Phys. Rev. B **65** (2002) 075409.

[13] H. Mehl, O. Biham, O. Millo, M. Karimi, *Electromigration-induced flow of islands and voids on the Cu(100) surface.* Phys. Rev. B **61** (2000), 4975–4982.

[14] P.J. Rous, *Theory of surface electromigration on heterogeneous metal surfaces.* Appl. Surf. Sci. **175-176** (2001) 212–217.

[15] J. Krug, *Introduction to Step Dynamics and Step Instabilities* (this volume).

[16] M. Schimschak and J. Krug, *Electromigration-driven shape evolution of two-dimensional voids.* J. Appl. Phys. **87** (2000) 695–703.

[17] Z. Suo, W. Wang and M. Yang, *Electromigration instabilities: transgranular slits in interconnects.* Appl. Phys. Lett. **64** (1994) 1944–1946.

[18] P.S. Ho, *Motion of an inclusion induced by a direct current and a temperature gradient.* J. Appl. Phys. **41** (1970) 64–68.

[19] W. Wang, Z. Suo, T.-H.Hao, *A simulation of electromigration-induced transgranular slits.* J. Appl. Phys. **79** (1996) 2394–2403.

[20] M. Mahadevan, R.M. Bradley, *Stability of a circular void in a passivated, current-carrying metal film.* J. Appl. Phys. **79** (1996), 6840–6847.

[21] L. Xia, A.F. Bower, Z. Suo, C.F. Shih, *A finite element analysis of the motion and evolution of voids due to strain and electromigration induced surface diffusion.* J. Mech. Phys. Solids **45** (1997) 1473–1493.

[22] M. Schimschak, J. Krug, *Electromigration-Induced Breakup of Two-Dimensional Voids.* Phys. Rev. Lett. **80** (1998) 1674–1677.

[23] M. Mahadevan, R.M. Bradley, *Simulations and theory of electromigration-induced slit formation in unpassivated single-crystal metal lines.* Phys. Rev. B **59** (1999), 11037–11046.

[24] Z. Li, H. Zhao, H. Gao, *A Numerical Study of Electro-migration Voiding by Evolving Level Set Functions on a Fixed Cartesian Grid.* J. Comp. Phys. **152** (1999), 281–304.

[25] M. Ben Amar, L.J. Cummings, G. Richardson, *A theoretical treatment of void electromigration in the strip geometry.* Comp. Mater. Sci. **17** (2000), 279–289.

[26] D.N. Bhate, A. Kumar, A.F. Bower, *Diffuse interface model for electromigration and stress voiding.* J. Appl. Phys. **87** (2000) 1712–1721.

[27] L.J. Cummings, G. Richardson, M. Ben Amar, *Models of void electromigration.* Eur. J. Appl. Math. **12** (2001), 97–134.

[28] J.H. Kim, P.R. Cha, D.H. Yeon, J.K. Yoon, *A phase field model for electromigration-induced surface evolution.* Metals and Materials International **9** (2003), 279–286.

[29] Z. Suo, *Electromigration-induced dislocation climb and multiplication in conducting lines.* Acta metall. mater. **42** (1994), 3581–3588.

[30] W. Yang, W. Wang, Z. Suo, *Cavity and dislocation instability due to electric current.* J. Mech. Phys. Solids **42** (1994) 897–911.

[31] M. Schimschak, *Numerische Untersuchungen zur Elektromigration auf metallischen Oberflächen*, PhD Dissertation (University of Essen, 1999).

[32] L.F. Shampine, M.K. Gordon, *Computer Solution of Ordinary Differential Equations – The Initial Value Problem* (W.H. Freeman, San Francisco, 1975).

[33] F. Hausser, A. Voigt (private communication).

[34] P. Kuhn, J. Krug (unpublished).

[35] J. Krug, H.T. Dobbs, *Current-Induced Faceting of Crystal Surfaces.* Phys. Rev. Lett. **73** (1994), 1947–1950.

[36] M. Schimschak, J. Krug, *Surface Electromigration as a Moving Boundary Value Problem.* Phys. Rev. Lett. **78** (1997), 278–281.

[37] M.R. Gungor, D. Maroudas, *Current-induced non-linear dynamics of voids in metallic thin films: morphological transition and surface wave propagation.* Surf. Sci. **461** (2000), L550–L556.

Philipp Kuhn
Fachbereich Physik
Universität Duisburg-Essen
D-45117 Essen, Germany
e-mail: philipp@theo-phys.uni-essen.de

Joachim Krug
Institut für Theoretische Physik
Universität zu Köln
Zülpicher Strasse 77
D-50937 Köln, Germany
e-mail: krug@thp.uni-koeln.de

International Series of Numerical Mathematics, Vol. 149, 175–192

Simulation of Ostwald Ripening in Homoepitaxy

Frank Haußer and Axel Voigt

Abstract. Ostwald ripening in homoepitaxy in the submonolayer regime is studied by means of numerical simulations. The simulations indicate, that the coarsening kinetics of the average island radius is described by a $t^{1/a}$ power law, where $2 \leq a \leq 3$. Here a approaches 2, if the ripening is purely kinetics limited (low attachment rate at the island boundaries) and increases with increasing attachment rate – taking the value $a = 3$ if the ripening is purely diffusion limited (infinite attachment rate at the island boundaries). For the two limiting cases the classical LSW theory is reviewed and compared with the numerical simulations. Besides the scaling law we also investigate the asymptotic scaled island size distribution function and analyse the influence of anisotropic edge energies and the effect of edge diffusion.

Mathematics Subject Classification (2000). Primary 74A50; Secondary 82C26.

Keywords. Ostwald ripening; numerical simulation.

1. Introduction

In general, a two phase mixture composed of a dispersed second phase in a matrix is not in thermodynamic equilibrium. The total energy of the two phase system can be decreased via an increase in the size scale of the second phase and thus decreasing the free energy associated with the interfaces between the two phases. When the second phase is present in form of a distribution of clusters of different size, the large clusters are growing at the expense of the small ones. This type of coarsening is known as Ostwald ripening.

The kinetics of Ostwald ripening is governed by two different processes: the mass transport between the clusters via a diffusion field in the matrix and the attachment/detachment process at the cluster boundaries. Thus, two limiting kinetic regimes are considered: in the *diffusion limited* regime (DL) the attachment/detachment of particles at the cluster boundaries is fast compared with the diffusion in the matrix, thus diffusion is the limiting process; in the *attachment*

limited regime (AL), the attachment/detachment at the cluster boundaries is slow compared with the diffusion in the matrix and therefore attachment/detachment is the limiting process.

A major advance in the quantitative description of Ostwald ripening was made by Lifshitz, Slyozov and Wagner (LSW) [10, 19]. Here, the ripening process is described in terms of a particle size distribution function of the second phase. The LSW theory predicts, that the particle size distribution function asymptotically evolves to a unique form being self similar under scaling of the average particle size. Moreover, the average particle size asymptotically obeys a temporal power law. Both results are valid in the limit of vanishing volume fraction of the second phase. Meanwhile quite a few extensions of the LSW-theory have been proposed, which take into account finite volume fractions, see, e.g., [12, 20]. For a review on theoretical work on Ostwald ripening we refer to [18, 17].

The main part of analytical and numerical work on Ostwald ripening is concerned with the three-dimensional diffusion limited regime. In two dimensions there are only a few investigations on diffusion limited ripening. The case of finite coverage is theoretically considered, e.g., in [13, 20] and numerically investigated in [20, 7]. Ostwald ripening in homoepitaxy is simulated in [16] using the level set method. Also this work only considers the diffusion limited regime. In the attachment limited regime, to our knowledge there exist no mean field theory for finite coverage in two dimensions. For the intermediate regime, which seems to be the regime of interest in many applications in epitaxial growth, neither analytical nor numerical work exists.

In this paper we consider two-dimensional Ostwald ripening in homoepitaxy in the sub monolayer regime. We analyse the *diffusion limited*, *attachment limited* and intermediate regimes numerically. In Section 2 we shortly review the Burton-Cabrera-Frank type model (BCF) for step flow in epitaxy, for a detailed description see [9]. The LSW analysis in the formulation of Wagner [19] is reviewed in Section 3 for the two limiting regimes *diffusion limited* and *attachment limited*. In Section 4, we present our numerical results. The simulations show, that the coarsening kinetics of the average island radius is described by a $t^{1/a}$ power law, where $2 \leq a \leq 3$. Here a approaches 2, if the ripening is purely kinetics limited (low attachment rate at the island boundaries) and increases with increasing attachment rate - taking the value $a = 3$ if the ripening is purely diffusion limited (infinite attachment rate at the island boundaries). Moreover we obtain a time independent island size distribution also in the mixed regime. Finally, the simulations indicate, that weak anisotropic edge energies do not alter the scaling behavior.

2. Step flow model

We shortly review the BCF-type step flow model, as described in more detail in [9]. Let $\Omega \subset \mathbb{R}^2$ be the substrate with $\Omega_i \subset \Omega, \quad i = 0, 1$ denoting the region of atomic height i (we are only considering the submonolayer regime) and $\Gamma = \overline{\Omega_0} \cap \overline{\Omega_1}$

the island boundaries. Thus the minority phase is represented by the monolayer islands Ω_1. Denote by $\rho_i = \rho_i(x,t)$ the adatom density on terrace $\Omega_i(t)$ $(i = 0, 1)$ at time t. The adatom diffusion on a terrace is described by the diffusion equation for the adatom density

$$\partial_t \rho_i - \nabla \cdot (D \nabla \rho_i) = 0, \qquad \text{in } \Omega_i(t), \tag{2.1}$$

where $D > 0$ is the surface diffusivity. Note that we have neglected desorption and that there would also be a deposition flux if epitaxial growth is modeled. Throughout the paper the unit of length will be the substrate lattice spacing a. Thus the adatom density ρ denotes the number of adatoms per adsorption site. Now let j^+, j^- be the adatom flux at the boundary Γ from the upper and lower terrace, respectively, which are given by

$$j^+ := -D \nabla \rho_1 \cdot \vec{n} - v \rho_1, \tag{2.2}$$

$$j^- := D \nabla \rho_0 \cdot \vec{n} + v \rho_0, \tag{2.3}$$

where $\vec{n}$ and v are the unit normal pointing from the upper to the lower terrace and the normal velocity of the step $\Gamma(t)$, respectively, with the convention that $v > 0$, if the movement of $\Gamma(t)$ is in the direction of $\vec{n}$. Assuming first order kinetics for the attachment/detachment at the island boundaries ("reaction kinetics"), the adatom density satisfies the following *kinetic boundary conditions* at the island boundaries $\Gamma(t)$

$$j^+ = k_+(\rho_1 - \rho_{eq}), \quad j^- = k_-(\rho_0 - \rho_{eq}), \tag{2.4}$$

where ρ_{eq} is the equilibrium density at Γ. With this notation $0 < k_+ < k_-$ models the Ehrlich-Schwoebel effect. If $k_+, k_- \to \infty$, Eqs. (2.4) pass into the *thermodynamic boundary condition*

$$\rho_1 = \rho_0 = \rho_{eq} \quad \text{at } \Gamma. \tag{2.5}$$

In this limit, the island boundaries act as perfect sinks for the adatom density and the growth/shrinking of islands is purely diffusion limited.

The equilibrium adatom density ρ_{eq} is described by the Gibbs-Thomson-type relation

$$\rho_{eq} = \rho^*(1 + \tilde{\gamma}\kappa), \quad \tilde{\gamma}(\theta) = \gamma(\theta) + \gamma_{\theta\theta}(\theta), \tag{2.6}$$

where γ denotes the orientation dependent step free energy divided by $k_B T$, κ is the curvature of the boundary $\Gamma(t)$, and θ the angle between the outer normal and the x-axis.

For the motion of the steps, we assume the following law for the normal velocity v of the island boundaries $\Gamma(t)$

$$v = j^+ + j^- + \partial_s(\nu \partial_s(\tilde{\gamma}\kappa)), \tag{2.7}$$

where ν is a positive function denoting the (in general orientation dependent) mobility of the edge diffusion, and ∂_s denotes the tangential derivative along the steps. The last term in Eq. (2.7) represents step edge diffusion of edge-adatoms along the steps, whereas the first two terms ensure the adatom mass conservation.

3. Two-dimensional LSW-Analysis

In this section we will review the LSW-analysis in the formulation of Wagner [19]. The results for two-dimensional systems are somewhat spread over the literature. So it seems to be worth to give a common treatment of the *diffusion limited* and *attachment limited* ripening adapted to the step flow model as described in Section 2. We will strongly follow the exposition given in [17]. Being aware of the limitations of the Wagner analysis it still offers a very compact formulation and is therefore chosen here to derive the theoretical scaling laws and size distribution functions in the limit of vanishing coverage (area fraction). The two-dimensional attachment limited case has been treated in a similar fashion by [8]. The diffusion limited case is treated in [20, 13], where a mean field theory for finite coverage is developed and the LSW-distribution is obtained in the limit of vanishing coverage. Both derivations rely on a cutoff of the diffusion field at some ad hoc chosen distance from the island to circumvent the difficulties arising from the logarithmic singularities of the fundamental solution for a single island in two dimensions. Here however, a very nice argument given (and also derived rigorously) in [14] is used, which allows to directly go through the Wagner analysis as in the three-dimensional case.

The first basic assumption of LSW-theory is, that the coverage ϕ (area fraction) of the second phase is very small. Hence, in the notation given in Section 2, the region Ω_1 consists of many disconnected islands far away from each other. Moreover, the islands are assumed to be radially symmetric with immobile centers. Thus the morphology of the dispersed spherical second phase may be characterized in terms of a particle radius distribution function $F(R,t)$. The number of particles per unit area is then given by $n(t) = \int_0^\infty F(R,t)\,dR$. Assuming that no nucleation and coalescence of particles takes place, F obeys the continuity equation

$$\partial_t F + \partial_R\big(\dot{R}F\big) = 0. \tag{3.1}$$

The flux of particles in size space is controlled by the function $\dot{R}(R)$. This function embodies much of the physics of the ripening problem, and thus must be constructed carefully, as will be done below.

Since in epitaxy, the diffusion constant is very large, we may pass to the quasi stationary approximation, i.e., we neglect the time derivative in Eq. (2.1) and the convective terms in Eqs. (2.2). Moreover, we assume isotropic edge energies. The edge diffusion term in Eq. (2.7) vanishes since all islands are assumed to be circular. We also assume for simplicity, that there is no Ehrlich-Schwoebel barrier, i.e., $k := k_+ = k_-$. Passing to the excess density $u := \rho - \rho^*$, Eqs. (2.1)-(2.7) become

$$\Delta u_i = 0, \quad \text{in}\,\Omega_i, \quad i = 0,1 \tag{3.2}$$

$$-D\nabla u_1\,\vec{n} = k(u_1 - \rho^*\tilde{\gamma}\kappa) \quad \text{on}\,\Gamma \tag{3.3}$$

$$D\nabla u_0\,\vec{n} = k(u_0 - \rho^*\tilde{\gamma}\kappa) \quad \text{on}\,\Gamma \tag{3.4}$$

$$v = D(\nabla u_1 - \nabla u_0)\,\vec{n} \quad \text{on}\,\Gamma. \tag{3.5}$$

To obtain an explicit solution for $\dot{R}(R)$ from the above model, LSW make the following second assumption: Far away from the islands, the excess density u may be approximated by a spatially constant *mean field* $\bar{u}(t)$. Under these assumptions, the growth rate of an island is determined by the growth rate of an isolated island obeying Eq. (3.2)–(3.5) supplemented by the boundary condition

$$u_0(\infty, t) = \bar{u}. \tag{3.6}$$

However, in contrast to the 3-dimensional case, (3.6) does not lead to a solution of the system (3.2)–(3.5) due to the logarithmic divergence of the fundamental solution of (3.2). Following [14] we introduce the typical particle distance d, the typical particle radius R, and assume $R \ll d$ such that $\phi := \pi(R/d)^2$ is the coverage. Now consider an island of radius R centered at the origin. Eq. (3.6) is substituted by

$$u_0(d, t) = \bar{u}. \tag{3.7}$$

The solution of (3.2)–(3.5) is then given by ($r = |x|$)

$$u_1(r) = \frac{\rho^* \tilde{\gamma}}{R}, \qquad (r \le R) \tag{3.8}$$

$$u_0(r) = \bar{u}(t) + \big(\frac{\rho^* \tilde{\gamma}}{R} - \bar{u}(t)\big) \frac{\ln(\frac{d}{r})}{\frac{D}{kR} + \ln(\frac{d}{R})} \qquad (r > R). \tag{3.9}$$

Thus, by (3.5) and using $\phi = \pi(R/d)^2$, the growth law for a single island is

$$\dot{R}(t) = \big(\bar{u} - \frac{\rho^* \tilde{\gamma}}{R}\big) \frac{kD}{D + kR \ln \frac{1}{\phi^{1/2}}}. \tag{3.10}$$

In view of Eq. (3.10), the critical radius R_c of a particle that neither grows nor shrinks is expressed in terms of the mean field $\bar{u}$ as

$$R_c = \rho^* \tilde{\gamma} / \bar{u}. \tag{3.11}$$

To proceed further, two limiting cases of Eq. (3.10) are considered:

- Diffusion limited ripening ($D \ll k\bar{R} \ln(\frac{1}{\phi^{1/2}})$):

$$\dot{R}(t) = K_{DL} \frac{1}{R^2} \Big(\frac{R}{R_c} - 1 \Big), \quad K_{DL} = \frac{D \rho^* \tilde{\gamma}}{\ln(\frac{1}{\phi^{1/2}})} \tag{3.12}$$

- Attachment limited ripening ($D \gg k\bar{R} \ln(\frac{1}{\phi^{1/2}})$):

$$\dot{R}(t) = K_{AL} \frac{1}{R} \Big(\frac{R}{R_c} - 1 \Big), \quad K_{AL} = k \rho^* \tilde{\gamma} \tag{3.13}$$

where $\bar{R}$ denotes the average island radius.

We now proceed in the spirit of Wagner [19] as described in [17]. Introducing the new variables

$$z = \frac{R}{R_c}, \qquad \tau = \ln(\frac{R_c(t)}{R_c(0)}), \tag{3.14}$$

Eqs. (3.12), (3.13) become

$$\frac{dz}{d\tau} = \nu \frac{z-1}{z^\lambda} - z, \quad \text{where} \tag{3.15}$$

$$\text{DL:} \quad \lambda = 2,\ \nu = \frac{K_{DL}}{R_c^2\, \dot{R}_c(t)}; \qquad \text{AL:} \quad \lambda = 1,\ \nu = \frac{K_{AL}}{R_c\, \dot{R}_c(t)}. \tag{3.16}$$

The continuity equation (3.1) for $f(z,\tau) := F\big(R_c z, t(\tau)\big)\, R_c$ is given in the new coordinates as

$$\partial_\tau f + \partial_z\Big(\frac{dz}{d\tau} f\Big) = 0. \tag{3.17}$$

Moreover, following Wagner, we make the simplifying assumption that the coverage ϕ is a conserved quantity at late times, which yields the following mass conservation constraint

$$\phi = \pi R_c^2 \int_0^\infty z^2 f(z,\tau)\, dz, \quad \text{for } \tau \text{ large.} \tag{3.18}$$

To find a unique solution $f(z,\tau)$ of Eqs.(3.15)–(3.18), the essential point of the LSW-analysis is, to argue, that ν becomes constant and takes a unique value at late times (i.e., $\tau \to \infty$), which in turn implies a scaling law for the critical radius R_c by solving the ODEs for $R_c(t)$ given in Eq. (3.16).

To argue, that ν is asymptotically constant, Eq. (3.17) is solved by a separation ansatz

$$f(z,\tau) = g(\tau)h(z). \tag{3.19}$$

First, the continuity equation (3.17) implies, that the temporal decrease of the number of particles is given by the particles with a (scaled) radius approaching $z = 0$, i.e.,

$$\frac{d}{d\tau}\int_0^\infty f(z,\tau)\, dz = \lim_{z\to 0}\big(\frac{dz}{d\tau} f\big). \tag{3.20}$$

Now note, that for $z \ll 1$ Eq. (3.15) becomes

$$\frac{dz}{d\tau} = -\frac{\nu}{z^\lambda}. \tag{3.21}$$

Plugging Eq. (3.21) into (3.20) and using the ansatz (3.19), we obtain

$$\frac{dg}{d\tau}\int_0^\infty h(z)\, dz = -g(\tau)\nu \lim_{z\to 0}\big(z^{-\lambda} h(z)\big). \tag{3.22}$$

Thus, assuming the decrease of the number of islands per unit area to be finite and positive, $h(z)$ has to be of the form $h(z) = h_0 z^\lambda + O(z^3)$ for $z \ll 1$ for some constant h_0 and therefore (3.22) becomes

$$\frac{dg}{d\tau}\frac{1}{g(\tau)} = -\frac{\nu h_0}{\int h(z)\, dz} \tag{3.23}$$

To show, that the left-hand side of (3.23) is a constant – which in turn implies, that ν does not depend on τ and is therefore also constant, the separation ansatz

(3.19) is plugged into the mass conservation constraint (3.18) to obtain

$$g(\tau) = \frac{\phi}{\pi R_c^2 \int z^2 h(z)\, dz}. \tag{3.24}$$

This implies

$$\frac{dg}{d\tau}\frac{1}{g(\tau)} = -\frac{2}{R_c}\frac{dR_c}{d\tau} = -2, \tag{3.25}$$

where we used that $\frac{dR_c}{d\tau} = R_c$, following from Eq. (3.14), and therefore ν is constant.

Given this result, the continuity equation (3.17) may be integrated straightforward using the separation ansatz (3.19). We obtain

$$-\frac{1}{g}\frac{dg}{d\tau} = \frac{1}{h}\frac{d}{dz}\Big(\frac{dz}{d\tau}h\Big) =: \beta \tag{3.26}$$

with a separation constant β, since the left-hand side does only depend on τ and, by Eq. (3.15), the right-hand side only on z. The assumption of constant coverage yields by Eq. (3.25), that $\beta = 2$, i.e.,

$$g(\tau) \sim \exp(-2\tau) \sim R_c^{-2}. \tag{3.27}$$

Finally we integrate the equation for $h(z)$, which by (3.26) becomes

$$\frac{dh}{dz} = \Big(\frac{dz}{d\tau}\Big)^{-1}\Big(2 - \frac{d}{dz}\big(\frac{dz}{d\tau}\big)\Big)h =: l(z)h, \tag{3.28}$$

with the solution

$$h(z) = h_0 \exp\Big[\int l(z)\Big]. \tag{3.29}$$

Using $\int (\frac{dz}{d\tau})^{-1}\frac{d}{dz}(\frac{dz}{d\tau}) = \ln(\frac{dz}{d\tau})$, we obtain

$$h(z) = h_0 \Big(\frac{dz}{d\tau}\Big)^{-1} \exp\Big[\int \Big(\frac{dz}{d\tau}\Big)^{-1}\Big]. \tag{3.30}$$

To explicitly calculate the function $h(z)$ from Eq. (3.30), the final step of the Wagner analysis consists in arguing, that there exists a cutoff value z_0 (i.e., $h(z) = 0$ for $z \geq z_0$) and to uniquely determine z_0 and the value of ν in the coarsening rate (3.15). Instead of repeating the partly heuristical arguments of Wagner, we give some arguments taken from [8, 17] by examining how the function $\frac{dz}{d\tau}$ varies with z and τ. As depicted in Fig. 1, four qualitative different cases may be distinguished: For negative ν-values the relative growth rate is positive for small relative island radii z and negative for bigger ones which is clearly opposite to the real physical process. Now, if ν is positive, $dz/d\tau$ generally has a maximum and can have two zeroes with the x-axes. In the case of two zeroes, $z_1 < z_2$, islands with a relative radius z such that $z_1 < z < z_2$ would grow until $z = z_2$ and islands bigger than z_2 would shrink until $z = z_2$, i.e., we would end with an ensemble of islands having all the same radius $z = z_2$, that would be stable against coarsening, which is in contradiction to thermodynamics. If $dz/d\tau$ has no interception with the x-axis, all islands would have negative growth rate and thus all islands would finally disappear. There is exactly one value of ν such that only the islands with a specific

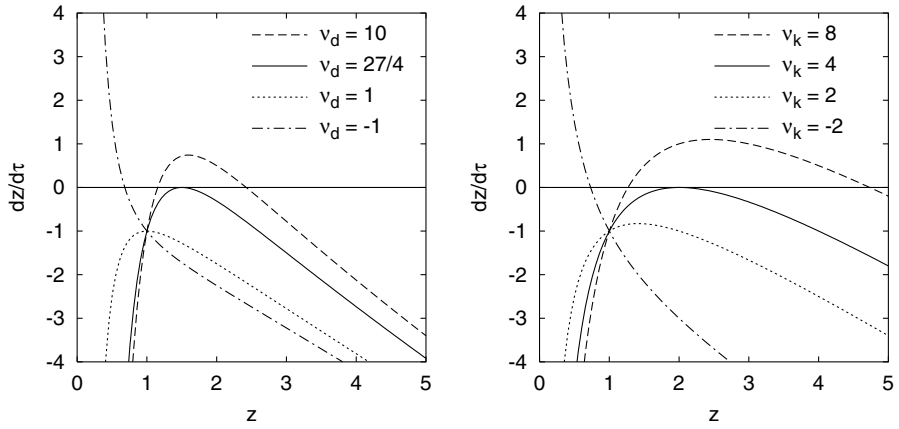

FIGURE 1. Dependence of $dz/d\tau$ on ν: DL (left); AL (right).

relative radius $z =: z_{\max}$ have a zero growth rate, which occurs, if the maximum of $dz/d\tau$ touches the x-axis. Choosing this value for ν and a cutoff value z_0 of $h(z)$ as $z_0 = z_{\max}$ yields a physical reasonable process. These considerations lead to two conditions for the function $dz/d\tau$, which fix the value of both ν and z_0:

$$\frac{dz}{d\tau}(z_0) = 0, \quad \frac{d}{dz}\frac{dz}{d\tau}(z_0) = 0.$$

Using Eq. (3.15) yields

$$\text{DL:} \quad z_0 = 3/2,\ \nu = 27/4; \qquad \text{AL:} \quad z_0 = 2,\ \nu = 4. \tag{3.31}$$

Having fixed the value of ν, the spatial distribution function $h(z)$ may be calculated explicitly from Eqs. (3.30), (3.15). Normalizing $h(z)$, one obtains the *scaled normalized island size distribution function* $h(z)$:

- Diffusion limited:

$$h_{DL}(z) = \begin{cases} 72e^{2/3}z^2(z+3)^{-17/9}(2z-3)^{-28/9}\exp\left(\frac{-2}{3-2z}\right) & : \quad z \le \frac{3}{2} \\ 0 & : \quad z > \frac{3}{2} \end{cases} \tag{3.32}$$

- Attachment limited:

$$h_{AL}(z) = \begin{cases} 8e^2 z(2-z)^{-4}\exp\left(\frac{-4}{2-z}\right) & : \quad z \le 2 \\ 0 & : \quad z > 2 \end{cases} \tag{3.33}$$

For diffusion limited ripening, the distribution (3.32) has also been obtained in [7, 20]. In the attachment limited case, the formula (3.33) is found also in [8]. To compare with experiments or numerical simulations, it is more convenient, to express the island size distribution function $h(z)$ in terms of the variable $r = R/\bar{R}$,

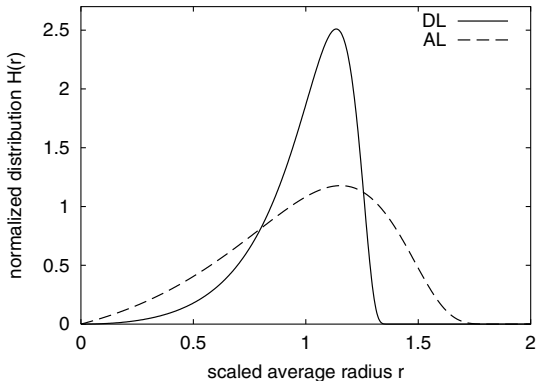

FIGURE 2. LSW normalized scaled island size distribution function $H(r)$ as defined in (3.34); diffusion limited (DL, solid) and attachment limited (AL, dashed).

i.e., to use the scaled normalized island size distribution function

$$H(r) := z_{av} h(z_{av} r), \quad \text{where } z_{av} = \int_0^\infty z h(z)\, dz\,. \tag{3.34}$$

The temporal scaling law is calculated by integrating Eq. (3.16). The *scaling law for the critical particle radius* R_c reads:

- Diffusion limited:

$$R_c(t) = \left(R_c(0)^3 + \frac{4}{9} \frac{D\rho^* \tilde{\gamma}}{\ln(\frac{1}{\phi^{1/2}})} t \right)^{\frac{1}{3}}. \tag{3.35}$$

- Attachment limited:

$$R_c(t) = \left(R_c(0)^2 + \frac{1}{2} k \rho^* \tilde{\gamma} t \right)^{\frac{1}{2}}. \tag{3.36}$$

Finally, we note that the average island radius $\bar{R}$ is given in terms of the critical radius R_c as:

$$\text{DL:} \quad \bar{R} = 1.0665 R_c; \qquad \text{AL:} \quad \bar{R} = R_c. \tag{3.37}$$

One should be aware, that the above results are valid only in the limit of small coverages ϕ and at late times. The Wagner analysis has been criticized since it is not self consistent due to the assumption of a constant coverage, see Eq. (3.18). Indeed, in a self consistent treatment the mean field $\bar{u}$ has to be determined by the mass conservation constraint

$$\bar{u}(t) + \pi \int_0^\infty R^2 f(R,t)\, dR = \text{const.}$$

Using a different approach, Marqusee and Ross [11, 12] showed, that the assumption of a fixed coverage ϕ is not necessary for the derivation of a temporal scaling

law and the self similar distribution function. Moreover they demonstrate, that the effect of changes of the coverage does not alter the zeroth order result but enters only in the first and higher order corrections in ϕ. Note that the LSW-Analysis is a one particle approximation since the growth rate of a particle does only depend on its size, which is not true for finite coverage ϕ. Quite a few mean field theories have been proposed, which account for finite coverage see, e.g., [12, 13, 20]. Most of them are concerned with 3-dimensional ripening and all of them treat the diffusion limited case. These theories predict a temporal scaling law of the form $\bar{R}(t) = (\bar{R}(0) + K(\phi)t)^{1/3}$, where the coarsening rate $K(\phi)$ increases with increasing coverage ϕ. Moreover all of them obtain a time independent scaled island size distribution function, which in general broadens with increasing coverages. However, the values of $K(\phi)$ and the specific form of the distribution function differ considerably in these theories. In most of the LSW-type analysis, it is also argued, that the particle size distribution function as obtained above is independent of the initial distribution of the particle ensemble. However, this *universality property*, predicting that the steady state solution f is a unique attractor, is not quite true in view of the results obtained in [15]. We finally note, that a rigorous treatment of two-dimensional diffusion limited Ostwald ripening in the limit of vanishing coverage is given in [14].

4. Numerical results

In this section, we present numerical results for systems with finite coverage. Since we numerically solve the full two-dimensional free boundary problem given in Eqs. (2.1)–(2.7), we are not restricted to any of the idealizing assumptions of the previous section. Thus it is possible to investigate the influence of edge diffusion, ansisotropic edge energies and the effect of finite coverage. Moreover, we do not have to stick to either the diffusion limited or the attachment limited regime, but may also explore the mixed regime, which would be much more complicated to treat within a mean-field theory.

4.1. Numerical method

The numerical method is based on adaptive linear finite elements, and Eqs.(2.1)-(2.7) are discretized using an operator splitting approach: We use two independent numerical grids: a two-dimensional grid for the adatom diffusion on the terraces and a one-dimensional grid for the step evolution. A first order implicit scheme is time is used. In each time step: (i) we update the discrete step boundaries by solving a geometric partial differential equation based on the adatom densities and the discrete step boundaries from the previous time step; (ii) we solve the diffusion equation to update the adatom densities using the adatom densities from the previous time step and the computed discrete representation of the steps. Adaptivity in space and time is indispensable for this approach to be efficient, especially if long time behavior as in Ostwald ripening is considered. For a detailed description of the algorithm see [4, 6, 5].

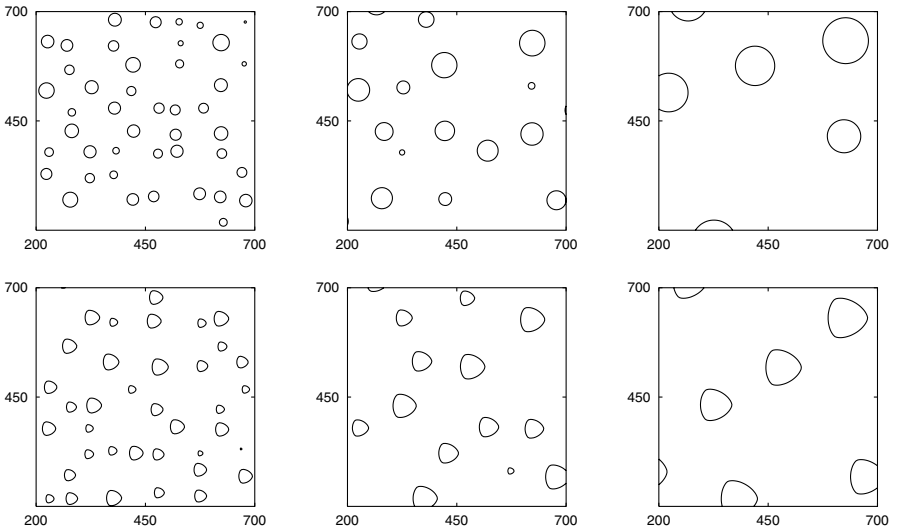

FIGURE 3. Isotropic and anisotropic Ostwald ripening: Island boundaries at times $t = 600s, 3000s, 15000s$ (from left to right); the coverage is $\phi = 0.085$ and the attachment rate is $k = 10^4$.

In the numerical simulation, the initial setup is as follows: 400 islands are placed on a 1000×1000 periodic domain. To avoid overlapping, the midpoints of the islands are placed on a regular grid and are then shifted randomly. The radii of the islands are chosen randomly according to the diffusion limited LSW ($\phi = 0$) distribution function as given in Eq. (3.32). Finally, the islands are projected onto the Wulff shape (with the same area) corresponding to the chosen anisotropy. If not otherwise stated, the following parameters are used:

$$D = 10^5, \quad \rho^* = 10^{-4}, \quad \nu = 0.0, \quad \gamma(\theta) = 1.0.$$

If ansiotropy is taken into account, we use the anisotropic edge energy

$$\gamma(\theta) = 1.0 + 0.1\cos(3\theta). \tag{4.1}$$

4.2. Movements of islands and influence of edge diffusion

To investigate the influence of edge diffusion, we have compared simulations with the same initial configuration but choosing the edge diffusion mobility ν either to be $\nu = 0.0$ or $\nu = 1.0$. For isotropic as well as an anisotropic edge energy of the form given in Eq. (4.1), there is no influence of edge diffusion seen in the simulations! I.e., the island shapes remain the Wulff shape during coarsening also without edge diffusion. This is different in the growth regime, where at least some deviation from the Wulff shape is observed and the island shape stays closer to the Wulff shape if edge diffusion is present, see [6].

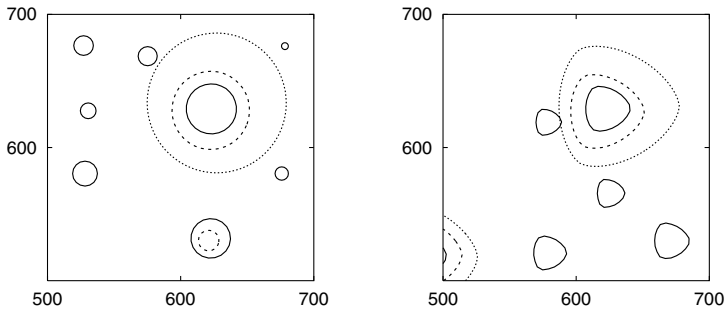

FIGURE 4. Movement of islands during ripening: Island boundaries at $t = 600$ (solid), $t = 3000$ (dashed) and $t = 15000$ (dotted) for isotropic (left) and anisotropic (right) edge energies. Same simulations as in Fig. 3.

Thus there is also no influence on the scaling behavior and the island size distribution function. Therefore in the following we will always neglect edge diffusion, i.e., we chose $\nu = 0.0$.

Some stages of isotropic and anisotropic ripening are depicted in Fig. 3. A zooming in is shown in Fig. 4. The assumption of mean field theories, that the center of the islands is fixed, can clearly be seen to be not satisfied. Also, the ripening of an individual island depends strongly on the surrounding islands ("competitive effects").

4.3. Scaling of the average island size

To determine the scaling exponent for diffusion limited ripening in the asymptotic regime, the log-log plot of the average island radius versus time is presented in Fig. 5. Here the number of island decreases from 400 to 50. For each value of ϕ, the results of five simulations with different randomly chosen initial configurations have been averaged. An affine linear fit of the data yields the scaling exponents. The values for the exponents are 0.332 and 0.325 for coverages $\phi = 0.085$ and $\phi = 0.01$, respectively, and are in very good agreement with the theoretical value of $1/3$. We like to remark that the number of particles is halved three times in the simulations, which corresponds to a simulation time $\tau = 3$ on the self-similar time scale. Thus any comparison with the asymptotic results of the mean-field theory has to be taken with some care and is a bit speculative. Assuming a temporal power law for the average island radius $\bar{R}(t)$ of the form

$$\bar{R}(t) = \left[\bar{R}(0)^3 + K(\phi)t\right]^{1/3},$$

the coarsening rate $K(\phi)$ is determined as shown in Fig. 6 by an affine linear fit of the numerical data yielding $K(0.01) = 2.6$ and $K(0.085) = 4.4$, which seem to be in reasonable agreement with the predicted values given in [20] (Fig. 8(b))

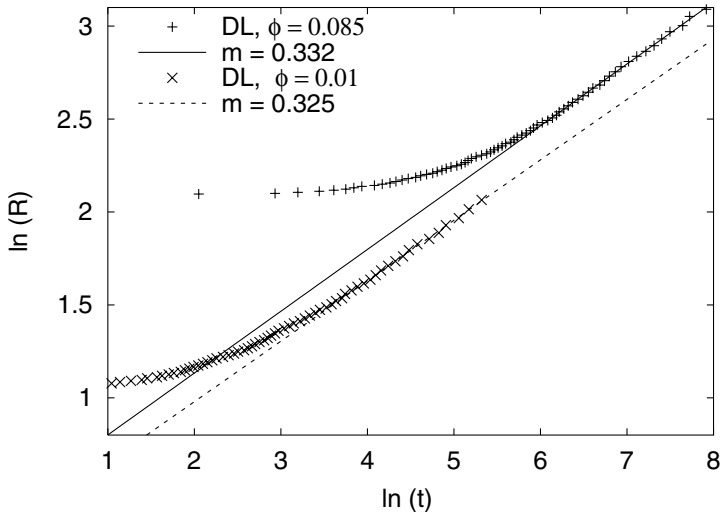

FIGURE 5. Diffusion limited ripening: Scaling of average island radius R for coverages $\phi = 0.085$ and $\phi = 0.01$. The scaling exponent is determined by an affine linear fit in the late stage as 0.332 for coverage $\phi = 0.085$ (solid line) and 0.325 for $\phi = 0.01$.

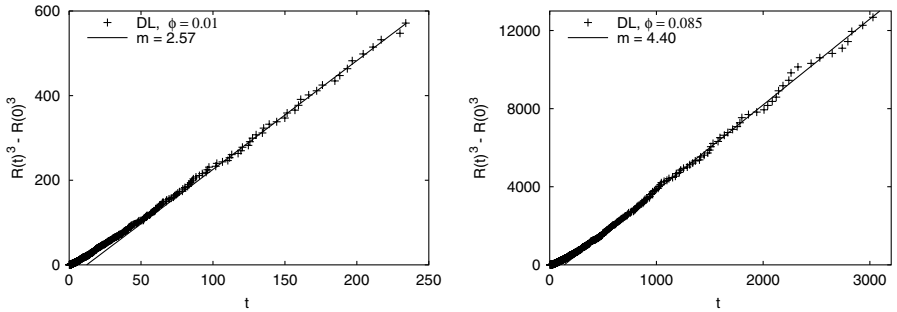

FIGURE 6. Diffusion limited ripening: Time evolution of the average island radius $\bar{R}(t)$. The plot of the numerical results for both coverages $\phi = 0.01$ (left) and $\phi = 0.085$ (right) indicates, that the average radius $\bar{R}(t)$ obeys the temporal scaling law $\bar{R}(t)^3 = \bar{R}(0)^3 + K(\phi)t$. The coarsening rate $m = K(\phi)$ is obtained by an affine linear fit, and the values are similar to the theoretical results of [20, 13].

and [13] (Fig. 2). (For a comparison note, that with our parameters $D\rho^*\tilde{\gamma} = 10$ in Eq. (3.35).) Numerical results of the evolution of the average island size in the mixed regime and the crossover to the attachment limited regime are depicted

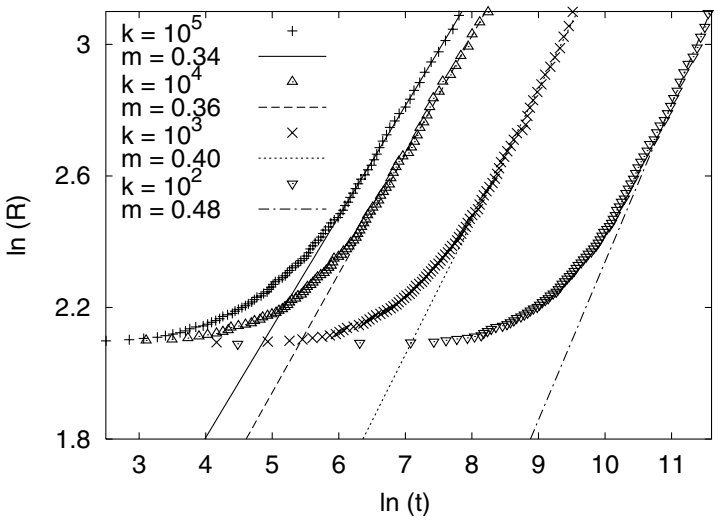

FIGURE 7. Scaling of average island radius $\bar{R}$: Crossover from diffusion to attachment limited ripening with coverage $\phi = 0.085$. The scaling exponents ($1/a = m$) for different values of the attachment rate k are obtained by an affine linear fit of the log-log plot (average radius versus time) of the numerical data in the late stage.

in Fig. 7. The log-log plot of the average radius versus time indicates a temporal power law for the average island radius $\bar{R}$ in the late stage, i.e.,

$$\bar{R} \sim t^{1/a}, \tag{4.2}$$

where (for fixed coverage ϕ) a is a monotone increasing function of the attachment rate k interpolating the attachment limited regime (k small, $a = 2$) and the diffusion limited regime ($k = \infty$, $a = 3$). This is a quite remarkable result, which is clearly valid only for finite systems and finite time, since for an infinite system, the asymptotic regime should always become diffusion limited due to the fact that $\bar{R} \to \infty$ for $t \to \infty$. Table 1 shows, that for the parameters used in the simulations, there is a crossover from the diffusion limited to the attachment limited regime.

4.4. Island size distribution function

In all simulations, the initial island size distribution was chosen to be the LSW distribution for the diffusion limited ripening as depicted in Fig. 2. As predicted by mean field theories for finite coverages in the diffusion limited regime (see, e.g., [20, 13]), the scaled distribution function broadens until it reaches an asymptotic time independent shape. Moreover, the asymptotic distribution becomes broader with increasing coverage. In Fig. 8 the scaled normalized distribution function of the numerical simulations is depicted for two different coverages. For the coverage

Attachment rate k	10^5	10^4	10^3	10^2
Average radius $\bar{R}$	22.0	22.1	22.2	23
$\alpha := k\bar{R}\ln(1/\phi^{1/2})/D$	27.1	2.72	0.274	0.0285

TABLE 1. Crossover from diffusion limited to attachment limited regime: According to Eqs. (3.12),(3.13), $\alpha \gg 1$ corresponds to the diffusion limited regime, whereas $\alpha \ll 1$ characterizes the attachment limited regime. The average radius $\bar{R}$ is taken at the end of the simulations (i.e., number of remaining islands $N = 50$), and $\phi = 0.085$.

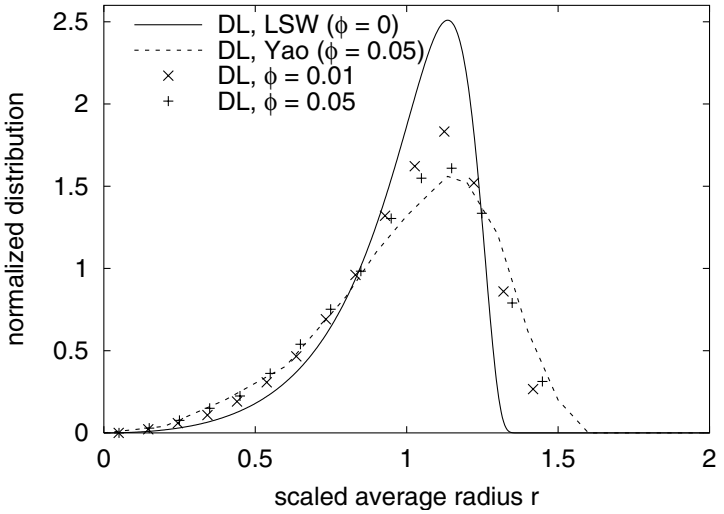

FIGURE 8. Asymptotic scaled normalized island size distribution function for diffusion limited ripening. The numerical data have been averaged over 5 different initial configurations and over the distributions from $N = 100$ to $N = 50$ (N being the number of remaining islands), to get a good statistic. We note, that in all cases, the distributions stop to broaden at least after $N = 200$.

$\phi = 0.05$ it shows pretty good agreement with the distribution predicted by [20]. Finally, we have investigated the influence of the attachment rate on the shape of the late stage distribution function (with fixed coverage ϕ). As shown in Fig. 9, the distribution function broadens with decreasing attachment rate, becoming very close to the LSW ($\phi = 0$) distribution for attachment limited ripening, if the attachment rate k becomes small enough. Concluding, there are two reasons, which cause a broadening of the late stage island size distribution (as compared to the

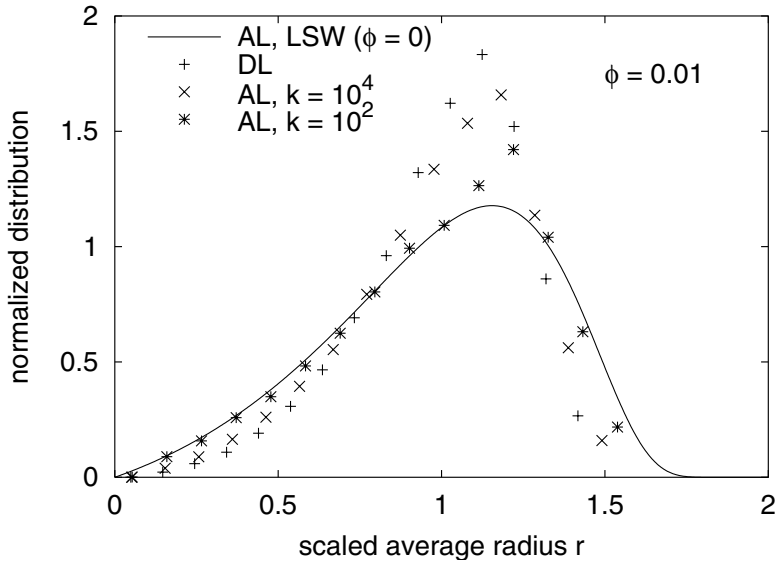

FIGURE 9. Scaled normalized island size distribution in the late stage: Crossover from diffusion limited to attachment limited ripening. It is clearly seen, that the distribution function broadens with decreasing attachment rate, and becomes very close to the LSW ($\phi = 0$) distribution for attachment limited ripening, if the attachment rate k becomes small enough.

diffusion limited LSW distribution): The distribution becomes broader with increasing coverage and with decreasing attachment rate (i.e., when crossing from the diffusion limited to the attachment limited regime).

5. Conclusions and outlook

Using numerical simulations, it is possible to investigate and compare two-dimensional Ostwald ripening for finite coverages in the diffusion limited, attachment limited and intermediate regime. The simulations indicate, that the coarsening kinetics of the average island radius is described by a $t^{1/a}$ power law, where $2 \leq a \leq 3$. Here a approaches 2, if the ripening is purely kinetics limited (low attachment rate at the island boundaries) and increases with increasing attachment rate – taking the value $a = 3$, if the ripening is purely diffusion limited (infinite attachment rate at the island boundaries). Moreover we have started to investigate, how the scaled island size distribution function depends on the kinetic regime. Some more detailed investigations have to be done to quantitatively

analyse the dependence of the distributions in the mixed and also the attachment limited regime on the coverage ϕ and also on the initial distribution.

It would be desirable to develop a mean field theory for finite coverages for the intermediate and the attachment limited regimes and to compare it with the numerical results.

References

[1] N. Akaiwa, D.I. Meiron, *Numerical simulation of two-dimensional late-stage coarsening for nucleation and growth.* Phys. Rev. E **51** no.6 (1995), 5408–5421

[2] H.A. Atwater, C.M. Yang *Island growth and coarsening in thin films - conservative and nonconservative systems.* J. Appl. Phys. **67** (1990), 6202–6213

[3] N.C. Bartelt, W. Theis, R.M. Tromp, *Ostwald ripening of two-dimensional islands on Si(001).* Phys. Rev. B **54**(16) (1996), 11741–11751

[4] E. Bänsch and F. Haußer and O. Lakkis and B. Li and A. Voigt, *Finite Element Method for Epitaxial Growth with Attachment-Detachment Kinetics.* J. Comput. Phys. **194** (2004), 409–434

[5] F. Haußer and A. Voigt, this volume

[6] E. Bänsch and F. Haußer and A. Voigt, *Finite Element Method for epitaxial growth with thermodynamic boundary conditions.* SIAM J. Sci. Comput. (2005), (to appear)

[7] T.M. Rogers and R.C. Desai, *Numerical study of late-stage coarsening for off-critical quenches in the Cahn-Hilliard equation of phase separation.* Phys. Rev. B **39** no.16 (1989), 11956–11964

[8] M. Hillert, *On the Theory of Normal and Abnormal Grain Growth.* Acta Metall. **13** (1965), 227–238

[9] J. Krug, this volume

[10] I.M. Lifshitz, V.V. Slyozov, *The kinetics of precipitation from supersaturated solid solutions.* J. Phys. Chem. Solids **19** (1961), 35–50

[11] J.A. Marqusee, J. Ross, *Kinetics of phase transitions: Theory of Ostwald ripening.* J. Chem. Phys. **79**(1) (1983), 373–378

[12] J.A. Marqusee, J. Ross, *Theory of Ostwald ripening: Competitive growth and its dependence on volume fraction.* J. Chem. Phys. **80**(1) (1984), 536–543

[13] J.A. Marqusee, J. Ross, *Dynamics of late stage phase separations in two dimensions.* J. Chem. Phys. **81**(2) (1984), 976–981

[14] B. Niethammer, F. Otto, *Domain Coarsening in Thin Films.* Comm. Pure and App. Math.**LIV** (2001), 361–384.

[15] B. Niethammer, R.L. Pego, *Non-self-similar behavior in the LSW theory of Ostwald Ripening.* J. Statist. Phys. **95** (1999), no. 5-6 867–902.

[16] M. Petersen, A. Zangwill, C. Ratsch, *Homoepitaxial Ostwald Ripening.* Surf. Sci. **536** (2003), 55–60

[17] L. Ratke, P.W. Voorhees, *Growth and Coarsening: Ripening in Material Processing.* Springer, 2002

[18] P.W. Voorhees, *The Theory of Ostald Ripening.* J. Statist. Phys. **38** (1985), no. 1-1 231–252.

[19] C. Wagner, *Theorie der Alterung von Niederschlägen durch Umlösen (Ostwald-Reifung).* Z. Elektrochemie **65** (1961), 581–591

[20] J.H. Yao, K.R. Elder, H. Guo, M. Grant, *Theory and simulation of Ostwald ripening.* Phys. Rev. B **47** no.21 (1993), 14110–14125

Frank Haußer and Axel Voigt
Crystal Growth group
research center caesar
Ludwig-Erhard-Allee 2
D-53175 Bonn, Germany
e-mail: hausser@caesar.de
e-mail: voigt@caesar.de

Part 3

Continuum Models

International Series of Numerical Mathematics, Vol. 149, 195–208

Continuum Models for Surface Growth

Martin Rost

Abstract. As an introductory lecture to the workshop an overview is given over continuum models for homoepitaxial surface growth using partial differential equations (PDEs). Their *heuristic derivation* makes use of inherent symmetries in the physical process (mass conservation, crystal symmetry, ...) which determines their *structure*. Two examples of applications are given, one for large scale properties, one including crystal lattice discreteness. These are: (i) a simplified model for *mound coarsening* and (ii) for the transition from *layer-by-layer* to *rough growth*. Virtues and shortcomings of this approach is discussed in a concluding section.

Mathematics Subject Classification (2000). Primary 82B26; Secondary 35K35.

Keywords. Surface evolution; mound coarsening; roughening transition.

1. Introduction

Crystal growth by Molecular Beam Epitaxy (MBE) involves processes on quite different physical scales, from atomic to micrometer scales. To capture the large scale features it may be appropriate to represent the surface as a continuous height field $h(\mathbf{x}, t)$ above a set of so called base points $\mathbf{x}$ where $h : (\mathbf{x}, t) \in \mathbb{R}^2 \times \mathbb{R} \to \mathbb{R}$. The surface dynamics is then modeled by a parabolic PDE for $h(\mathbf{x}, t)$, which often is a starting point for interesting mathematical problems, and in some cases for rigorous results [1, 2], which were an important part of this workshop.

Their mathematical tractability somehow contrasts with the lack of rigor in their derivations, as we shall see below. It would be nice to "prove" a certain PDE to be the appropriate large scale model for some underlying more elementary model, typically a stochastic model of the solid-on-solid type. This would connect the result for large scales with the microscopic model which is much closer to physical reality.

Nevertheless, often this chain can be closed in a heuristic sense, and this lecture presents some examples. It is organised as follows: First, the heuristic procedure of deriving a continuum model is motivated and its structure is explained.

Then, two examples of applications are presented, covering in some sense extreme cases of applicability of continuum models; (i) coarsening of mound patterns in homoepitaxy and (ii) damping of width oscillations in the transition from layer-by-layer to rough growth. Last, the general applicability of continuum models to MBE growth is discussed, in particular those features of discreteness of the underlying process which can only be covered incompletely by a continuum model. Open questions in the derivation which have not been addressed so far, but appear to be solvable, are mentioned here.

The main purpose of this introductory lecture is to recollect the physical motivation of the class of models which deal with the largest spatial and temporal scales involved in MBE growth, and to give some intuition to other more mathematical approaches.

2. Derivation and structure

2.1. General background

Continuum models for surface growth are comparable to the hydrodynamic limit of microscopic models of fluid dynamics. Behind the continuous macroscopic height field $h(\mathbf{x}, t)$ one has to imagine an ensemble of microscopic configurations. They may be locally in a steady state or, in growth modes where the crystal layer structure is relevant such as layer-by-layer or step flow growth, a sequence of states may repeat itself periodically. On time scales larger than the layer completion time also the latter case may be considered a quasi-steady state. Figure 1 illustrates this relationship. The local state is subject to changes on time scales, ideally longer than the relaxation times into those states, which leads to the dynamics of the height field.

The structure of the PDE governing the dynamics of $h(\mathbf{x}, t)$ reflects different elementary processes and their symmetries. In growth from molecular beam epitaxy there is

- a deposition flux $F_{\{h\}}(\mathbf{x}, t)$, i.e., the deposited volume per time and surface area,
- possibly an evaporation loss $E_{\{h\}}(\mathbf{x}, t)$, again volume per time and area,
- a surface current $\mathbf{J}_{\{h\}}(\mathbf{x}, t)$ on terraces and along steps, transported volume per time and length, i.e., cross section on the surface.

Multiplied with a volume density ρ these quantities become mass fluxes and currents. All three depend on the actual surface configuration h, e.g., on local slopes, their orientations and curvatures. Elastic interactions and terrace adatom detachment with subsequent redeposition couple the dynamics at a surface point *non-locally* to surface configurations at other places. There may also be an *explicit* space dependence beyond the influence of the height configuration, e.g., for a non-uniform deposition with pulsed flux.

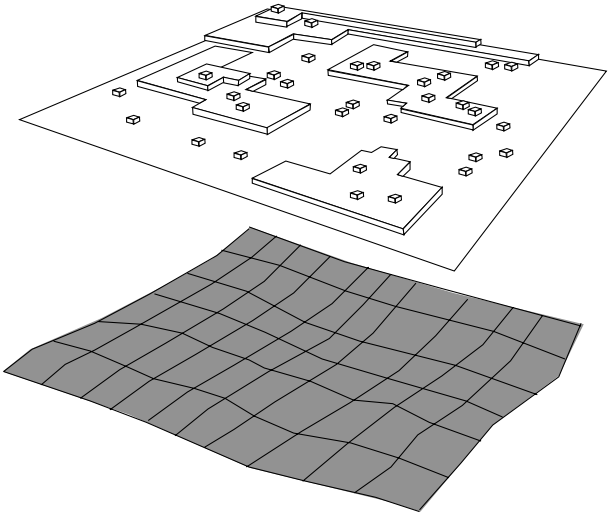

FIGURE 1. Sketch of the height field representation for surface configurations. Upper: one surface configuration out of an ensemble in local steady states. Lower: a smooth height field $h(\mathbf{x}, t)$ as a representation.

Deposition, evaporation, and surface current are combined into a *continuity equation*

$$\frac{\partial}{\partial t}\, h(\mathbf{x}, t) = F_{\{h\}}(\mathbf{x}, t) - \nabla \cdot \mathbf{J}_{\{h\}}(\mathbf{x}, t) - E_{\{h\}}(\mathbf{x}, t). \tag{2.1}$$

Note that small local slopes are assumed, such that in front of the surface current divergence nonlinear terms arising from the metric $\sqrt{1+(\nabla h)^2}$ typically are neglected.

A full derivation from local steady states in the sense postulated above is of course impossible in almost any case, apart from some one-dimensional examples related to growth models, as, e.g., [3], which is however not of MBE type. One therefore has to rely on heuristically justified (*reasonable*) assumptions for the dynamic quantities involved. The connection to the more detailed models on smaller scales is given by length scales which influence the surface morphology and become visible. Explained more precisely in the other introductory lectures of this conference [4, 5] they are

- a, the lattice spacing of the crystal.
- ℓ_{D}, the diffusion length, i.e., the "typical" distance of nucleation sites on a terrace, with a non-trivial dependence on the deposition rate F and adatom diffusivity D.
- $\ell_{\mathrm{ES}} = a\big[\exp \varepsilon_{\mathrm{ES}} - 1\big]$, the Ehrlich–Schwoebel length [6]. $\varepsilon_{\mathrm{ES}}$ is the magnitude of the Ehrlich–Schwoebel barrier in units of $k_{\mathrm{B}}T$. It is a measure for the reflectivity of the barrier at a downward step. Roughly speaking, an adatom

located right at a downward step is equally likely to hop downward as it is to get caught by the next upward step at distance $\ell_{\rm ES}$.
- $\ell_{\rm step}$, the average distance between two truly ascending step without counting islands etc. between them. So, a slope $|\mathbf{m}|$ of a vicinal surface is equivalent to $\ell_{\rm step} = a/|\mathbf{m}|$.

2.2. Surface current

Ehrlich–Schwoebel effect on terraces

As was realised quite early the most important ingredient of Eq. (2.1) is a non-equilibrium current on surface terraces induced by Ehrlich–Schwoebel (ES) barriers [7, 8, 9, 11].

For small average slopes $\mathbf{m} = \nabla h$ with $|\mathbf{m}| \ll a/\ell_{\rm D}$ or $\ell_{\rm D} \ll \ell_{\rm step}$, the ES barrier induces a net uphill current [25]

$$\mathbf{J}_{\rm EST} = \frac{F\ \ell_{\rm D}\ell_{\rm ES}}{2a(1+\ell_{\rm ES}/\ell_{\rm D})}\ \mathbf{m}. \tag{2.2}$$

Inserted into the surface current in Eq. (2.1) this results in a *destabilising* term for the height equation $\partial_t h = -c\,\nabla\cdot\nabla h + \cdots$.

Of course one would like to know the functional dependence of the surface current $\mathbf{J}_{\rm EST}$ beyond this approximation for small slopes. Following an argument of Siegert for $1+1$ dimensions [9] there must also be surface orientations with stabilising surface current: Think of $\mathbf{J}_{\rm EST}$ as a vector field on the tangent bundle of the unit sphere of possible surface orientations. By the ES instability all high symmetry orientations have $\mathbf{J}_{\rm EST}$ pointing outward around a zero. By continuity of $\mathbf{J}_{\rm EST}$ as a function of the orientation there must be zeroes with the current field pointing inward to the zero, i.e., orientations stabilised by the surface current.

These qualitatively fundamental properties, the existence of unstable and stable surface orientations, can be cast into a heuristically postulated function $\mathbf{J}_{\rm EST}(\mathbf{m})$. Figure 2 shows two such examples, one isotropic within the crystal terrace – a somewhat artificial but nevertheless theoretically interesting case, one isotropic, with four-fold ($\pi/2$) rotational symmetry.

Ehrlich–Schwoebel effect at steps

The Ehrlich–Schwoebel effect also has an influence on adatom diffusion along steps, allowing for attachment of atoms to kinks preferentially from one side, as is sketched in Fig. 3. It is one important mechanism causing a step meandering instability on growing vicinal surfaces [12, 13]. Politi and Krug derived the contribution $\mathbf{J}_{\rm ESS}$ of non-equilibrium current along steps to the total surface current for a surface with given average slope which is assumed to be constant on a sufficiently large region such that steps have a well defined average density and orientation with respect to the underlying crystal lattice [14].

Curvature relaxation

Clearly on small scales the destabilising ES effects encountered in this section so far are balanced. Too thin protrusions are forbidden by their cost in surface free

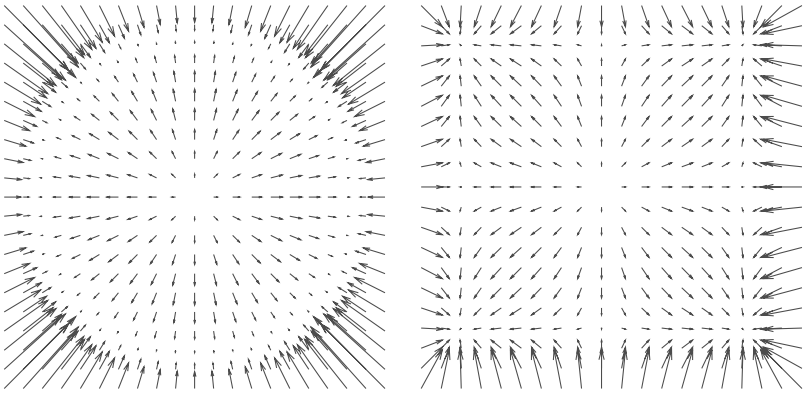

FIGURE 2. Examples of heuristic choices for nonequilibrium terrace Ehrlich–Schwoebel surface current $\mathbf{J}_{\mathrm{EST}}(\mathbf{m})$. Left: in-plane isotropy, $\mathbf{J}_{\mathrm{EST}}(\mathbf{m}) = (1 - |\mathbf{m}|^2)\ \mathbf{m}$, continuous set of stable slopes $\{\mathbf{m} \mid |\mathbf{m}| = 1\}$. Right: anisotropy, four-fold symmetry, $J_{\mathrm{EST},i}(\mathbf{m}) = (1 - m_i^2)\ m_i$ with $i = x, y$, discrete set of stable slopes at $(\pm 1, \pm 1)$.

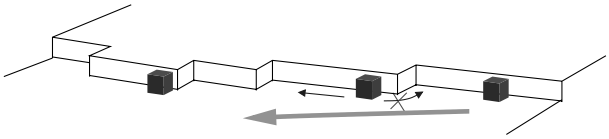

FIGURE 3. The ES effect at step kinks favors adatom incorporation from one side and induces a net current along the step.

energy. For thermal relaxation towards equilibrium the corresponding continuum dynamics are straightforward to derive. The surface free energy

$$\mathcal{F} = \int \gamma(\nabla h)\ \sqrt{1 + (\nabla h)^2}\ d^d x \tag{2.3}$$

weights each surface element by its orientation dependent contribution $\gamma(\nabla h)$. The gradient in chemical potential $\mu = \delta\mathcal{F}/\delta h$ drives the relaxational surface current which is also proportional to the (tensorial and orientation dependent) adatom mobility $\boldsymbol{\sigma}(\nabla h)$. A linear expansion around a surface of constant slope $h = \mathbf{m} \cdot \mathbf{x}$ small enough to again neglect geometric effects [10, 11] yields

$$\mathbf{J}_{\mathrm{CURV}} = \boldsymbol{\sigma} \cdot \nabla\ \nabla \cdot [\gamma\ \mathbf{1} + (\nabla_{\mathbf{m}} \nabla_{\mathbf{m}} \gamma)] \cdot \nabla h. \tag{2.4}$$

The expression in square brackets is generally called the surface *stiffness*

$$\tilde{\boldsymbol{\gamma}} = \gamma\ \mathbf{1} + \nabla_{\mathbf{m}} \nabla_{\mathbf{m}} \gamma \tag{2.5}$$

where $\nabla_{\mathbf{m}}$ denotes derivation with respect to the slope dependence of γ and $\mathbf{1}$ is the unity matrix.

Strictly speaking this derivation applies only to *equilibrium relaxation*. For a far from equilibrium process like MBE growth it does not make sense to define a surface free energy per area $\gamma(\nabla h)$, although the "true" contribution of the surface current due to relaxation by curvature most likely has a functional form of that type. Some attempts to identify these contributions have been made [15], but the correct derivation of the corresponding continuum form remains an open question.

2.3. Deposition, desorption and noise

For most applications it will be correct to assume a *deposition* intensity F constant in time and space. Interesting cases with *explicit* space and time dependence are (i) pulsed molecular beams, used to decrease the second layer island nucleation rate, and (ii) geometric inhomogeneities if the beam does not reach every part of the surface under the same angle. The most important mechanism for *implicit* deposition heterogeneity is steering, where the incident atoms are deflected by attractive interaction with surface features such as islands and mounds, an effect which is of course most prominent under grazing incidence [16, 17].

At sufficiently high temperatures *desorption* may become an important effect. Terrace adatoms then will be most susceptible to desorption at a rate $1/\tau$, during their diffusion time before they reach the stronger binding steps. To a first approximation the desorption rate depends on the average distance to the next reachable step and therefore on the surface slope: the higher the slope, the more steps are present and the lower the desorption loss. Within an ansatz à la Burton–Cabrera–Frank [18] one can relate the desorption length $x_\mathrm{s} = 2a\sqrt{D\tau}$, diffusion length ℓ_D, and slope $\nabla h = a/\ell$ [19, 11] to an expression for the desorption loss in volume per time and surface area

$$E_{\{h\}}(\mathbf{x},t) = F\ [(x_\mathrm{s}/\ell)\tanh(\ell/x_\mathrm{s}) - 1] \approx F\ \frac{(\ell_\mathrm{D}/x_\mathrm{s})^2/3}{1+(\nabla h)^2}. \tag{2.6}$$

There are three sources for *noise* in MBE growth [21]: (i) Deposition is a stochastic process of single events, so F has to be complemented by a "shot noise" term $\xi(\mathbf{x},t)$ with statistics

$$\langle \xi(\mathbf{x},t)\rangle = 0 \quad \text{and} \quad \langle \xi(\mathbf{x},t)\xi(\mathbf{x}',t')\rangle = a^3 F\ \delta(\mathbf{x}-\mathbf{x}')\ \delta(t-t'). \tag{2.7}$$

(ii) Adatom diffusion also consists of single events, and to a first approximation surface currents are blurred by a "diffusion noise" term $\boldsymbol{\eta}(\mathbf{x},t)$ with statistics

$$\langle \boldsymbol{\eta}(\mathbf{x},t)\rangle = 0 \quad \text{and} \quad \langle \boldsymbol{\eta}(\mathbf{x},t)\cdot\boldsymbol{\eta}(\mathbf{x}',t')\rangle = \ell_\mathrm{D} F\ \nabla^2\delta(\mathbf{x}-\mathbf{x}')\ \delta(t-t'). \tag{2.8}$$

(iii) Nucleations also occur at random but the precise form of this contribution remains an open question. There are nontrivial correlations in time, as new islands tend to nucleate close to centers of previously nucleated islands. The space dependence of the nucleation noise correlator $\langle \nu(\mathbf{x},t)\nu(\mathbf{x}',t')\rangle$ is expected to have the form $(\nabla^2)^2\delta(\mathbf{x}-\mathbf{x}')$ [22].

2.4. Structure and symmetry of continuum equations for MBE

Heuristic surface currents as in the example in Fig. 2 lead to a symmetry in the resulting dynamical equation which can be used for evaluation, but is too strong a restriction compared to the "real" dynamics and may lead to erroneous results.

If $\mathbf{J}_{\mathrm{EST}}$ uniquely depends on the slope $\mathbf{m}$ and not on derivative of its functions then a fourfold or sixfold crystal symmetry in the terrace layers imposes $\mathbf{J}_{\mathrm{EST}}(\mathbf{m}) = -\mathbf{J}_{\mathrm{EST}}(-\mathbf{m})$. (A threefold symmetry plays a special role [23]). The resulting term of surface dynamics is invariant under the transformation $h \to -h$ and so will be the surface configurations obtained from that. Breaking of this symmetry, e.g., by terms as $\nabla f\left((\nabla h)^2\right)$ in $\mathbf{J}$ or an evaporation term $e(\left((\nabla h)^2\right)$ do in fact change the characteristics of the dynamics substantially [19].

One can take advantage of this simple slope dependence if there is a scalar function $V(\mathbf{m})$ such that $\mathbf{J}_{\mathrm{EST}} = -\nabla_{\mathbf{m}} V(\mathbf{m})$. Stable zeroes of $\mathbf{J}_{\mathrm{EST}}$ then are minima of $V(\mathbf{m})$. If additionally the curvature relaxation is of a simple "scalar" form $\boldsymbol{\sigma} \cdot \tilde{\boldsymbol{\gamma}} = K\mathbf{1}$ there is a Lyapunov functional of the dynamics

$$\mathcal{F}\{\mathbf{m}\} = \int \left[\frac{K}{2}(\nabla \mathbf{m})^2 + V(\mathbf{m})\right] d^2x \tag{2.9}$$

and the surface dynamics Eq. (2.1) can be written for the field of slopes $\mathbf{m} = \nabla h$ as

$$\partial_t \mathbf{m} = \partial_t(\nabla h) = \nabla\, \nabla \cdot \frac{\delta \mathcal{F}}{\delta \mathbf{m}}. \tag{2.10}$$

If $\mathbf{m}$ is interpreted as a two-dimensional magnetic order parameter this form compares to conserved (model B) relaxational dynamics, with the only restriction that it remains a conservative field at all times, $\nabla \wedge \mathbf{m} = 0$. Facets in the surface are regions of constant slope, and appear as domains of constant "magnetisation", edges between them are domain walls. As compared to its magnetic analogon, here the parallel component of $\mathbf{m}$ remains constant across a domain wall, which in the case of discrete stable zeroes of the current function (right panel of Fig. 2) restricts the possible domain wall orientations and imposing constraints on the relaxational dynamics [24, 9, 23].

3. Examples of applications

Continuum equations are now applied in two examples of very basic choices in Eq. (2.1). In some sense they highlight two opposite regimes, (i) on very long length and time scales coarsening of mounds in homoepitaxy, and (ii) on short scales resolving the lattice structure in the transition from layer-by-layer to rough growth.

3.1. Coarsening

The simplest example of a surface dynamics equation is the analogon to the classical XY-model in the sense of Eq. (2.10)

$$\partial_t h = -(\nabla^2)^2 h - \nabla \cdot \left[\left(1 - (\nabla h)^2\right)\, \nabla h\right], \tag{3.1}$$

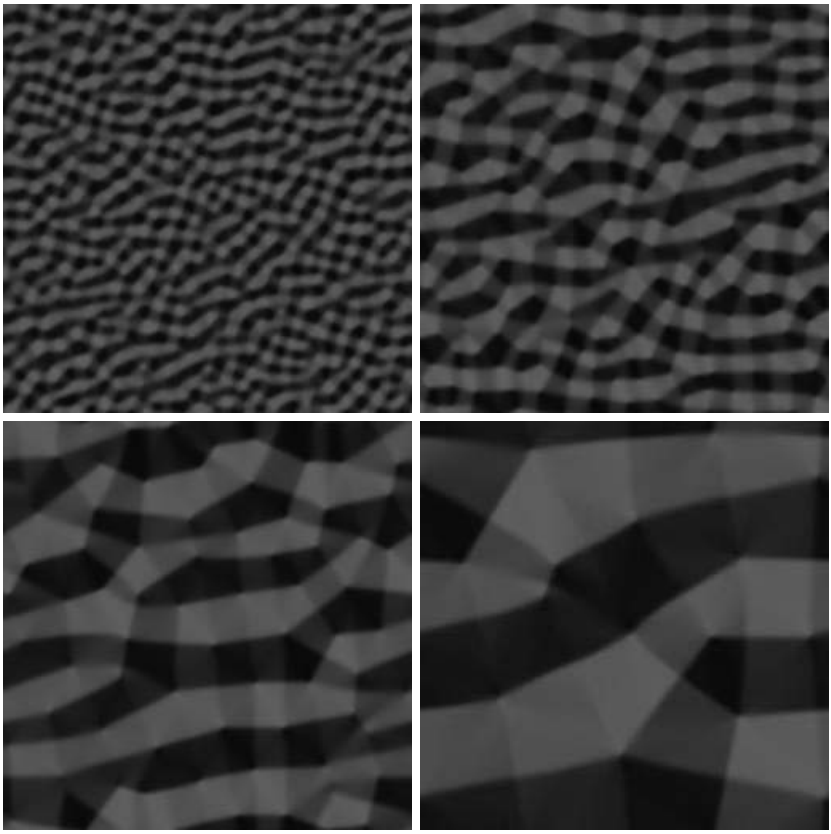

FIGURE 4. Coarsening of surface mounds, between subsequent panels time advances by a factor of 10. The local surface slope is represented by colors, facets appear as regions of uniform color. Spontaneous facet formation, although no anisotropy is imposed, $\mathbf{J}_{\mathrm{EST}}(\mathbf{m}) = (1 - |\mathbf{m}|^2)\,\mathbf{m}$ (c.f. left panel in Fig. 2).

i.e., with the current function depicted in the left panel of Fig. 2. An initially flat surface $h = const$ is linearly unstable to fluctuations of wave lengths $\lambda > 2\pi$ which therefore initially grow exponentially. Once slopes of $O(1)$ are reached the surface organise itself into a pattern of regular mounds and troughs which keep the symmetry $h \leftrightarrow -h$ of Eq. (3.1). The in-plane isotropy of (3.1) is locally broken by the need to arrange the mounds and troughs into a regular pattern and facets with sharp wedges form [25].

Subsequently the pattern of mounds and troughs coarsens keeping a single typical length scale and a statistically self similar pattern at every time. The average mound size is found to increase with time as $L \sim t^{1/3}$ [24, 23]. In a weak

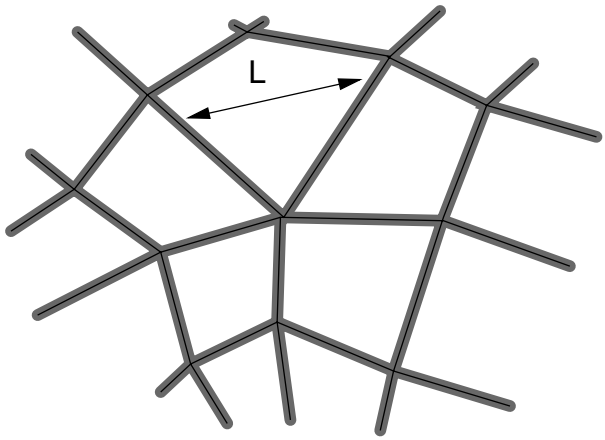

FIGURE 5. Sketch of facets and wedges, i.e., domains of constant slope and their separating boundaries, as obtained in the simulations shown in Fig. 4. The only macroscopic length scale is the domain size L.

sense this can be proved as an upper bound for an appropriate time average of the length scales L observed up to a give time t [2]. Here only a quick handwaving argument is given following [26]:

The spatial average of the interface width $W \equiv \langle h^2 \rangle$ (where $\langle h \rangle = 0$) increases due to Eq. (3.1) as

$$\frac{1}{2}\,\partial_t W^2 = \frac{1}{2}\,\partial_t \langle h^2 \rangle = -\langle (\Delta h)^2 \rangle + \langle (\nabla h)^2 \rangle - \langle |\nabla h|^4 \rangle. \tag{3.2}$$

By the sketch of Fig. 5 the contributions of these terms are estimated to be of order $1/L$: The facets are flat and the curvature is restricted to narrow strips of width $O(1)$ at the domain boundaries, which have a relative weight of $1/L$. Also, here the slopes are smaller than the stable value $|\nabla h| = 1$ attained at the facets. So all terms give a contribution of $O(1/L)$ and because of the stable slope $W \sim L$ the increase in width leads to the estimate

$$\partial_t L^2 \sim \partial_t W^2 \sim 1/L, \quad \text{integrated to} \quad L \sim t^{1/3}. \tag{3.3}$$

The same rough heuristic argument holds for anisotropic surface currents with discrete minima, i.e., a discrete set of preferential surface orientations, but the four-fold symmetry (right panel of Fig. 2) plays a special role because two kinds of edges occur, such that in general the assumption of a single length scale L in the system is wrong [23].

Clearly, Equation (3.1) is far from experimental realisations, and it is interesting by its challenge for mathematical, analytic and numerical methods.

Numerically, the coarsening exponent is found correctly only if one goes to very late times, when asymptotic mound sizes of at least 10 times the initial most

unstable wave length are reached [24]. Following [23], it may be interesting to verify the absence of any macroscopic length scales other than the mound size, e.g., to check possible orientational long range ordering of the mounds. This may require quite involved methods to avoid any artificial anisotropy from numerical lattices.

Mathematically, an improvement on the analysis of [2] is desirable but probably difficult to obtain. Physical intuition would call for a bound on the length scale $L(t)$ itself rather than its "history average" $\int_0^t L(s)ds$. It may be possible to obtain dynamical equations for the movements and merging of the singular points in the pattern of Fig. 4), for its maxima, minima, and saddle points. Such analysis has proven very helpful in 1+1 dimensions, e.g., [1, 27], and for anisotropic (2+1)-dimensional models, e.g., [23].

As the dynamics of these singular features play a crucial role, it is important to study their change in the presence of additional terms in Eq. (3.1). Based on analytic arguments assisted by simulations, noise is known to cause coarsening or to determine its properties [28]. Other additional nonlinear terms influence the morphology of the mound pattern, such as slope dependent evaporation [19], or other terms breaking up-down symmetry as $\nabla^2(\nabla h)^2$ [20]. A more difficult task may be the study of nonlinearities in prefactors to the smoothing term $-\Delta^2 h$ of Eq. (3.1).

3.2. Roughening

Layer by layer growth is technologically interesting because one can monitor the subsequent deposition of layers by oscillations in the surface width. It is nearly flat around integer fillings and the roughness takes maxima at half integer fillings. During growth the interface roughens and the width oscillations decay [29]. The Ehrlich–Schwoebel barrier and mounding instability is one prominent mechanism destroying layer-by-layer growth, and so can be any inhomogeneity in the deposition intensity $F_{\{h\}}(\mathbf{x}, t)$. Although weaker, even the fluctuations of shot noise have this effect, and it can be captured by a simple renormalisation group calculation.

The simplest way to implement layer lattice effects into an continuum surface equation like Eq. (2.1) is pursued by the conserved *sine-Gordon*-equation

$$\partial_t h(\mathbf{x}, t) = -K\Delta^2 h(\mathbf{x}, t) - V\Delta \sin \frac{2\pi h(\mathbf{x}, t)}{a_\perp} + F + \xi(\mathbf{x}, t). \tag{3.4}$$

Among other the surface current is driven to regions of incomplete fillings such that $h(\mathbf{x}, t)/a_\perp$ is favored to take integer values [30]. The notation distinguishes between the lattice constant normal ($a_\perp$) and parallel ($a_\parallel$) to the surface terraces which will be used in the following analysis.

In a momentum shell renormalisation one can average over the fluctuations caused by the short wavelength components of the noise, $\xi = \bar{\xi} + \delta\xi$, where $\bar{\xi}$ only contains modes of wavenumber smaller than some cutoff Λ and $\delta\xi$ the others. One now tries to approximate the dynamic equation for the averaged height field $\bar{h} = \langle h \rangle_{\delta\xi}$ by an equation like (3.4) with suitably adjusted parameters. After

rescaling, an effective *renormalised* equation is obtained. Three important physical interpretations can be obtained from the renormalised parameters of Eq. (3.4).

(i) by the interplay of the driving force F and the lattice potential the up-down symmetry ($h \leftrightarrow -h$) is broken and a term $-\lambda\Delta(\nabla h)^2$ is created.

(ii) The strength of the lattice potential V is damped out and decays exponentially with coverage $\theta = Ft$ like $\propto \exp\left(-a_\parallel^2/\ell_\mathrm{D}^2\sqrt{\theta}\right)$

(iii) In a sample of finite size Λ momentum shell renormalisation stops at minimal wavenumbers $|\mathbf{k}| = 2\pi/\Lambda$ and corresponding coverages $\theta = (\Lambda/\ell_\mathrm{D})^4$. The lattice potential therefore remains present in the renormalised large scale description if $\Lambda \ll \tilde{\ell} = \ell_\mathrm{D}^2/a_\parallel$, where $\tilde{\ell}$ is called *layer coherence* length [29, 30]. Expressed in more physical terms: shot noise fluctuations cannot accumulate to the point where width oscillations are completely blurred.

4. Discussion

In presenting the model derivations and examples of their application it becomes clear that continuum models are a good tool for questions where the inherent *simplifications* are justified. The insight gained from partial differential equations is different from results of more microscopic model. Last not least continuum equations can handle larger systems and longer times than Monte Carlo simulations or Molecular Dynamics.

In many cases the phenomena of particular technological interest cannot be captured by continuum equations of the type described in this lecture. Magic island shapes, surface reconstruction, certain aspects of step bunching, formation of quantum dots and wires are just a few examples.

Even if one is not interested in these inherently discrete phenomena themselves they nevertheless carry over to the behavior on larger scales and a naive straightforward derivation of large scale continuum models may be wrong. The implementation of noise for some questions, such as roughening, is one such example. Also, the effective "large scale" Ehrlich–Schwoebel barrier of a step is influenced by kinks along the step which may serve as channels for downward incorporation of a terrace adatom. Obtaining the correct effective barrier, dependent on orientation and curvature of the step certainly is a nontrivial task.

An important part of the surface current $\mathbf{J}$ flows along steps, as has become clear in the above derivation. In Ref. [14] the step current due to kink ES barriers is derived as a function of the surface orientation or slope. An open question is the role of step curvature and therefore of surface curvature on the step current.

Also on the surface itself, the regularising term as it is derived in Eq. (2.4), should be derived from true nonequilibrium arguments. To do so, one would have to incorporate island nucleations, the creation and annihilation of steps. One possible approach is to introduce fields for the densities of adatoms, advacancies, steps, kinks, and for their orientations. Locally they could be treated as mean

field densities with certain effective "reaction" rates, but in their spatial interaction, by diffusion and advective transport, one could obtain a conceptually more fundamental continuum model for surface growth.

5. Conclusion

In this lecture an overview of continuum models for MBE surface growth has been given which includes

- the conceptual foundation of continuum models as a limit of more detailed small scale approaches,
- heuristic derivations due to lack of rigorous or even exact ways to obtain them,
- the structure and the symmetry of the equations obtained in that way,
- two examples emphasizing two opposite time limits in the growth process with the application of two contrary methods,
- criticism of weak points in continuum modelling, open questions and some speculations about answers to them.

The main purpose was to highlight the physical background and give some intuition of possible approaches to it as a basis for mathematical treatments, both rigorous and numerical. It should be seen as a complement of the lectures [4] and [5] which give a similar introduction to lattice and Burton–Cabrera–Frank models respectively. Although continuum models seem to fail in some important physical aspects they nevertheless are a good tool and subject for mathematical approaches.

Acknowledgement

This work, as well as the participation at the workshop was supported by the Deutsche Forschungsgemeinschaft through the SFB "Singular Phenomena and Scaling in Mathematical Models" at the University of Bonn.

References

[1] R.V. Kohn and F. Otto, *Upper bounds on coarsening rates*, Comm. Math. Phys. **229** (2002) 375–395.

[2] R.V. Kohn, X.D. Yan, *Upper bound on the coarsening rate for an epitaxial growth model*, Comm. Pure Appl. Math. **56** (2003) 1549–1564.

[3] B. Derrida, E. Domany, and D. Mukamel, *An exact solution of the one dimensional asymmetric exclusion model with open boundaries*, J. Stat. Phys. **69** (1992) 667–687; G. Schütz and E. Domany, *Phase transitions in an exactly soluble one-dimensional asymmetric exclusion model*, J. Stat. Phys. **72** (1993) 277–296.

[4] M. Biehl, this volume.

[5] J. Krug, this volume.

[6] P. Politi and J. Villain, *Ehrlich-Schwoebel instability in molecular-beam epitaxy: A minimal model*, Phys. Rev. B **54** (1996) 5114–5129.

[7] G. Ehrlich and F.G. Hudda, *Atomic view of surface diffusion: Tungsten on Tungsten*, J. Chem. Phys. **44** (1966) 1036–1099.

[8] L. Schwoebel and E.J. Shipsey, *Step motion on crystal surfaces*, J. Appl. Phys. **37** (1966) 3682–3686.

[9] M. Siegert, *Ordering dynamics of surfaces in molecular beam epitaxy*, Physica A **239** (1997) 420–427.

[10] W.W. Mullins, *Flattening of a Nearly Plane Solid Surface Due to Capillarity*, J. Appl. Phys. **30** (1959) 77–83.

[11] J. Villain, *Continuum models of crystal growth form atomistic beams with and without desorption*, J. de Physique I **1** (1991) 19–42.

[12] O. Pierre-Louis, M.R. D'Orsogna, and T.L. Einstein, *Edge diffusion during growth: The kink Ehrlich-Schwoebel effect and resulting instabilities*, Phys. Rev. Lett. **82** (1999) 3661–3664.

[13] J. Kallunki, J. Krug, M. Kotrla, *Competing mechanisms for step meandering in unstable growth*, Phys. Rev. B **65** (2002) 205411.

[14] P. Politi and J. Krug, *Crystal symmetry, step-edge diffusion, and unstable growth*, Surface Science **446** (2000) 89–97.

[15] P. Politi and J. Villain, *Kinetic coefficients in a system far from equilibrium*, in *Surface Diffusion: atomistic and collective processes*, Ed. M.C. Tringides, Plenum Press, New York (1997) 177–189.

[16] S. van Dijken, L.C. Jorritsma, and B. Poelsema, *Steering-Enhanced Roughening during Metal Deposition at Grazing Incidence*, Phys. Rev. Lett. **82** (1999) 4038–4041.

[17] J. Yu, J.G. Amar, and A. Bogicevic, *First-principles calculations of steering forces in epitaxial growth*, Phys. Rev. B **69** (2004) 113406.

[18] W.K. Burton, N. Cabrera, F.C. Frank, *The growth of crystals and the equilibrium of their surfaces*, Phil. Trans. Roy. Soc. London A **243** (1951) 299–358.

[19] P. Šmilauer, M. Rost, and J. Krug, *Fast coarsening in unstable epitaxy with desorption*, Phys. Rev. E **59** (1999) R6263–R6266.

[20] M. Rost (2004), unpublished.

[21] D.E. Wolf, *Computer simulation of molecular-beam epitaxy*, in *Scale Invariance, Interfaces and Non-Equilibrium Dynamics*, Eds. A.J. McKane, M. Droz, J. Vannimenus, and D.E. Wolf, Plenum Press, New York (1995).

[22] E. Somfai, D.E. Wolf, and J. Kertész, *Correlated island nucleation in layer-by-layer growth*, J. de Physique I **6** (1996) 393–401.

[23] M. Siegert, *Coarsening dynamics of crystalline thin films*, Phys. Rev. Lett. **81** (1998) 5481–5484.

[24] D. Moldovan and L. Golubovic, *Interfacial coarsening dynamics in epitaxial growth with slope selection*, Phys. Rev. E **61** (2000) 6190–6214.

[25] P. Politi, G. Grenet, A. Marty, A. Ponchet, and J. Villain, *Instabilities in crystal growth by atomic or molecular beams*, Physics Reports **324** (2000) 271–404.

[26] M. Rost and J. Krug, *Coarsening of surface structures in unstable epitaxial growth*, Phys. Rev. E **55** (1997) 3952–3957.

[27] P. Politi, *Kink dynamics in a one-dimensional growing surface*, Phys. Rev. E **58** (1998) 281–294

[28] L.H. Tang, P. Šmilauer, and D.D. Vvedensky, *Noise-assisted mound coarsening in epitaxial growth*, Eur. J. PhysḂ **2** (1998) 409–412.

[29] H. Kallabis, L. Brendel, J. Krug, J., and D.E. Wolf, *Damping of oscillations in layer-by-layer growth*, Int. J. Mod. Phys. B **31** (1997) 3621–3634.

[30] M. Rost and J. Krug, *Damping of growth oscillations in molecular beam epitaxy: A renormalization group approach*, J. de Physique I **7** (1997) 1627–1638.

Martin Rost
Bereich Theoretische Biologie
Insitut für Zelluläre und Molekulare Botanik
Kirschallee 1, Universität Bonn
D-53115 Bonn, Germany
e-mail: martin.rost@uni-bonn.de

International Series of Numerical Mathematics, Vol. 149, 209–225

Configurational Continuum Modelling of Crystalline Surface Evolution

Navot Israeli and Daniel Kandel

Abstract. We propose a novel approach to continuum modelling of dynamics of crystal surfaces. Our model follows the evolution of an ensemble of step configurations, which are consistent with the macroscopic surface profile. Contrary to the usual approach where the continuum limit is achieved when typical surface features consist of many steps, our continuum limit is approached when the number of step configurations of the ensemble is very large. The model is capable of handling singular surface structures such as corners and facets and has a clear computational advantage over discrete models.

Mathematics Subject Classification (2000). Primary 80A22; Secondary 35R35.

Keywords. continuum modeling; multi scale modeling; step flow; surface evolution.

1. Introduction

The behavior of classical physical systems is typically described in terms of equations of motion for discrete microscopic objects (e.g., atoms). The dynamics of the microscopic objects is usually very erratic and complex. Nevertheless, in many cases a smooth behavior emerges when the system is observed on macroscopic length and time scales (e.g., in fluid flow through a pipe). A fundamental problem in physics is to understand the emergence of the smooth macroscopic behavior of a system starting from its microscopic description. A useful way to address this problem is to construct a continuum, coarse-grained model, which treats the dynamics of the macroscopic, smoothly varying, degrees of freedom rather than the microscopic ones. The derivation of continuum models from the microscopic dynamics is far from trivial. In most cases it is done in a phenomenological manner by introducing various uncontrolled approximations.

In this work we address the above problem in the context of the dynamics of crystal surfaces. The evolution of crystal surfaces below the roughening transition

proceeds by the motion of discrete atomic steps which are separated by high symmetry orientation terraces. One can model step motion by solving the diffusion problem of adatoms on the terraces with appropriate boundary conditions at step edges. This approach was introduced long ago by Burton, Cabrera and Frank [1], and was further developed by other authors [2]. The resulting models specify the normal velocity of each step in the system as a function of its position and shape and as a function of position and shapes of neighboring steps. These step flow models are capable of describing surface evolution on the mesoscopic scale with significant success [3, 4]. However, step flow models pose a serious challenge for numerical computations, and can be solved only for small systems.

Several attempts were made to construct continuum models for stepped surfaces [5, 6, 7, 8, 9, 10, 11, 12, 13, 14, 15, 16], in order to understand their large scale properties. The general idea behind these attempts is that step flow can be treated continuously in regions where every morphological surface feature is composed of many steps. If we label surface steps by the index n, the continuum limit in these models is obtained by taking n to be continuous. In what follows we will refer to these models as the *conventional* approach.

In the literature, there are two methods to derive conventional continuum models. One method is to write down the discrete step equations of motion and then transform them into a partial differential equation by taking the step index n to be continuous [7, 11, 12, 13, 14]. The second method is to start with a continuous surface free energy density and derive a surface dynamic equation that minimizes it [6, 8, 10, 15, 16]. These two methods are complementary provided that: 1. The free energy density of the second method is the continuum analog of the free energy of an array of discrete steps. 2. The two methods uses the same mass transport mechanism. Such continuum models are fairly successful in describing the evolution of smooth surfaces with very simple morphologies. However, they suffer from fundamental drawbacks, which do not allow generalizations to more complex and realistic situations.

The most severe drawback is that below the roughening temperature, crystal surfaces have singularities in the form of corners and macroscopic facets. The latter are a manifestation of the cusp singularity of the surface free energy at high symmetry crystal orientations. The assumption that every surface feature is composed of many steps clearly breaks down on macroscopic facets where there are no steps at all. Thus, existing continuum models fail conceptually near singular regions. Several authors have tried to overcome this problem by solving a continuum model only in the non-singular parts of the surface and then carefully match the boundary conditions at the singular points or lines [10, 13, 12, 14]. In most cases however it is not at all clear how these matching conditions can be derived. This difficulty is a fundamental drawback of conventional continuum models and not merely a technicality. As we argue below, boundary conditions at the singular points or lines cannot be derived in the context of conventional continuum models.

To see why this is true consider the situation near a facet edge. The step at the facet edge is special and obeys a unique equation of motion. In contrast to steps

in the sloping parts of the surface which all have two neighboring steps of the same sign, a facet step has only one neighbor of the same sign and potentially a second neighbor of an opposite sign. There might also be special physical conditions such as surface reconstruction that add to the uniqueness of a facet step. As we found in several cases [11, 12, 13, 14], the unique behavior of a facet step sensitively determines the amount of material emitted or absorbed at the facet and the rate at which steps cross the facet and annihilate. When going to the continuum limit these quantities serve as flux boundary conditions at the singularity. The problem is that conventional continuum models are derived from the equations of motion (or from the surface free energy density) that apply away from the facet and are therefore ignorant of the special behavior of facet steps. Thus, the boundary conditions at the facet edge must be derived from a careful analysis of the discrete dynamics of faces steps. However, in going to the continuum in the conventional way, one loses the information regarding the position of individual steps and the discrete analysis cannot be performed.

Another approach for dealing with surface singularities is to round the surface free energy cusp [15, 16], approximating true facets by relatively flat but analytic regions. This method avoids the need of specifying explicit boundary conditions at the singularity by assuming analyticity of the surface. The correct surface behavior is then expected to be captured in the limit of vanishing cusp rounding. This procedure completely ignores the key role of facet steps and implicitly assumes that the surface free energy derived for non singular orientations determines the dynamics on facets as well. This assumption is generally false due to the same reasons discussed above. An example for a case where cusp rounding leads to erroneous results can be found in Appendix A.

In this work we propose a conceptually new definition of the continuum limit, which we term Configurational Continuum [17]. Configurational Continuum allows construction of continuum models, which are free of all the limitations of conventional continuum models discussed above. It provides a rigorous way of deriving the continuum model directly from the discrete step equations of motion. Like other continuum models, Configurational Continuum has a clear computational advantage over the discrete step model due to the small number of discretization points it requires for the description of smooth surface regions in a numerical scheme.

2. Configurational continuum

In order to overcome the limitations of conventional continuum models we now propose a conceptually new definition of the continuum limit for stepped surfaces. Our key observation is that a continuous surface height profile can be represented by many similar, but not identical, step configurations. Figure 1 is a one-dimensional demonstration of this point. It shows a continuous height function, $h(x)$, of position x (thick solid line), and three valid microscopic representations of this profile

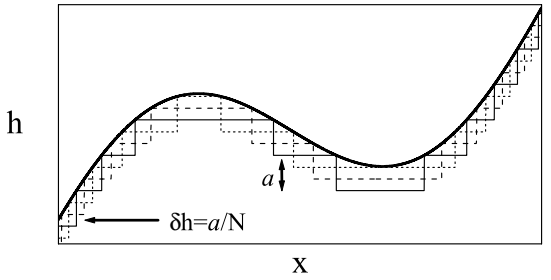

FIGURE 1. A schematic illustration of the ensemble of configurations whose upper envelope defines the continuum limit.

as step configurations. The main idea of this work is to define the height profile in the continuum limit as the upper envelope of the discrete height functions of an *ensemble* of many such step configurations.

To construct the configurations of the ensemble let a be the height of a single step and N the number of configurations in the ensemble. We construct the ensemble so that the height difference δh, between two adjacent configurations is a/N, as depicted in Fig. 1. The continuum limit is obtained when $N \to \infty$. The generalization to higher dimensions is straightforward.

The dynamics of the continuum model is as follows. Each step configuration of the ensemble evolves according to the microscopic dynamics. As a result, the envelope of discrete height functions changes with time, thus defining the evolution of the continuous height function $h(\vec{r})$ where $\vec{r}$ is a vector in the high symmetry xy plane. There is one technical complication which might arise if two steps from different configurations cross each other. Such an event would make $h(\vec{r})$ a multi valued function of position and requires a more general mathematical description of the surface. For simplicity we ignore this and assume that $h(\vec{r})$ remains single valued.

There is a crucial assumption hidden in this definition of the continuum model. We postulate that our construction leads to a mathematically well defined height function at all times. When does this assumptions hold? Consider two initially similar configurations of the ensemble. Our continuum limit is well defined provided these two configurations have similar microscopic dynamics and hence remain similar at later times. Note however that this assumption has to hold in the conventional continuum definition as well, and therefore does not put additional restrictions on our model. In fact, if two initially similar configurations evolve very differently, one must abandon the continuum limit and follow the specific microscopic configuration of interest, using discrete dynamics.

We now derive the evolution equation for the continuous height, $h(\vec{r}, t)$, at position $\vec{r}$ and time t. As a basis for the derivation we assume knowledge of the discrete equations of motion for the underlying step flow model. These equations of motion specify the normal velocity of a step that passes through $(\vec{r}, t)$ as a

function of the local step configuration. We denote this dependency by writing

$$\vec{v}\,(\vec{r},t) = \vec{v}\,(C_{\vec{r},t})\,, \tag{2.1}$$

where $C_{\vec{r},t}$ denotes the configuration of steps in the region that influences the step velocity at $(\vec{r},t)$. In most models of step flow this region of influence covers a small number of neighboring steps. Note that in the context of the discrete step model, $C_{\vec{r},t}$ is the actual configuration of steps in the system. When going to the continuum we will be interested in the ensemble of configurations $\{C_{\vec{r},t}\}$ which are consistent with $h(\vec{r},t)$.

The continuous height $h(\vec{r},t)$ changes with time due to the flow of steps through $\vec{r}$, and due to nucleation and annihilation of steps. At this stage we disregard nucleation processes and include them later. First, we consider positions which are not local extrema of the height profile. It is obvious from the construction of the Configurational Continuum, that for each point $\vec{r}$ there is exactly one configuration $C_{\vec{r},t}$ in the ensemble, which has a step that passes through $\vec{r}$ at time t. That step lies along the unique equal-height contour line, which passes through $\vec{r}$. As is demonstrated in Fig. 1, the exact positions of neighboring steps in the configuration $C_{\vec{r},t}$ can be calculated from the knowledge of $h(\vec{r},t)$, and the fact that in this configuration there is a step at $\vec{r}$. Hence, we can use the discrete step model Eq. (2.1) and calculate the normal velocity of the step $\vec{v}\,(C_{\vec{r},t})$. Note that at different positions, $\vec{v}\,(C_{\vec{r},t})$ is the normal velocity of steps which may belong to *different* configurations in the ensemble.

Next we define the directional gradient in the direction from which steps flow towards $\vec{r}$

$$\nabla h_{-\hat{v}}(\vec{r},t) \equiv -\hat{v}(\vec{r},t) \lim_{\epsilon\to 0_+} \frac{h\left(\vec{r}-\epsilon\cdot\hat{v}(\vec{r},t)\right) - h\left(\vec{r},t\right)}{\epsilon}\,, \tag{2.2}$$

where $\hat{v}(\vec{r},t) = \frac{\vec{v}\left(C_{\vec{r},t}\right)}{\left|\vec{v}\left(C_{\vec{r},t}\right)\right|}$. This is useful for the calculation of the current of steps arriving at $\vec{r}$:

$$J(\vec{r},t) = \frac{N}{a}\left|\nabla h_{-\hat{v}}(\vec{r},t)\cdot\vec{v}\,(C_{\vec{r},t})\right|\,, \tag{2.3}$$

where we have used the fact that the local step density is $|\nabla h_{-\hat{v}}(\vec{r},t)|\,N/a$. Note that J is the current of steps belonging to all configurations in the ensemble, and not to one particular configuration. Since each step (from any configuration), which passes through $\vec{r}$ changes the height of the ensemble envelope by a/N, the continuous height profile obeys the evolution equation

$$\frac{\partial h(\vec{r},t)}{\partial t} = -\nabla h_{-\hat{v}}(\vec{r},t)\cdot\vec{v}\,(C_{\vec{r},t})\,. \tag{2.4}$$

The above derivation of the evolution in the continuum is not valid at local extrema of the surface, because generally one cannot define a unique equal-height contour line which passes through such a point. To avoid the problem, we define $\partial h/\partial t$ at local extrema as the limit of the height time derivative as one approaches

these points. This limiting procedure is justified, since there are no microscopic realizations of the surface with steps exactly at the local extrema.

At this point we emphasize that the Configurational Continuum evolution is formally identical to the evolution of the discrete step model. This statement is almost trivial, since the definition of Eq. (2.4) follows the envelope of the ensemble of configurations, and each configuration evolves with step velocities calculated from the discrete step model. Thus Eq. (2.4) is exact. Moreover, the use of directional derivatives in the derivation of Eq. (2.4) makes it valid even at singular surface regions such as corners or facet edges. Similarly to other continuum models it is solved numerically by discretization of space, which is the only approximation involved in such solutions.

What is the relation between Configurational Continuum and conventional continuum models? In regions where $h(\vec{r},t)$ is analytic, the evolution equation (2.4) reduces to the continuity equation

$$\frac{\partial h(\vec{r},t)}{\partial t} = -\nabla h(\vec{r},t)\cdot\vec{v}\left(C_{\vec{r},t}\right) \ . \tag{2.5}$$

If $h(\vec{r},t)$ is sufficiently smooth, $\vec{v}\left(C_{\vec{r},t}\right)$ can be approximated as a local function of h and its spatial derivatives, as is commonly done in conventional continuum models. Making this approximation will therefore recover the conventional continuum approach. We can conclude that in analytic surface regions the conventional continuum approach approximates the Configurational Continuum model and that the approximation quality depends on the smoothness of the surface. However, near corners, facets or regions where the profile is not smooth, one cannot reconstruct the microscopic step configuration from the local value of h and its spatial derivatives. In these regions $\vec{v}\left(C_{\vec{r},t}\right)$ contains non local information and as a result Eq. (2.4) cannot even be written as a differential equation.

Is there any computational gain in using such a continuum model? After all, we replaced a discrete model, which follows the evolution of a single microscopic step configuration, by a model which follows a whole ensemble of step configurations. The key point is that we do not have to follow all the steps of all configurations. To calculate $\partial h(\vec{r},t)/\partial t$, it is enough to locally follow the single configuration which has a step that passes trough $\vec{r}$ at time t. In addition, the continuum evolution equation is solved on a grid, and the density of grid points can be very small in regions where the continuous height profile is smooth. The smoothness of the profile allows very accurate interpolation between these points. Only near singular points or lines we have to use a rather dense grid, and there is no computational gain in these regions. In practice, the total number of grid points used can be orders of magnitude smaller than the number of points one has to use in order to follow the evolution of a single microscopic step configuration.

So far we ignored the possibility of island or void nucleation. It is possible to include island or void nucleation in our model provided that we have a microscopic description for these events which determines the nucleation probability in a given step configuration. Within our continuum approach, the nucleation probability

at a point on the continuous surface is the ensemble average of the microscopic nucleation probabilities at this point. For demonstration proposes we consider a simple model where the probability for the nucleation of an island on a terrace grows as the square of the local concentration of diffusing adatoms. Information regarding the values of terrace adatom concentrations is already contained in the underlying step flow model Eq. (2.1), since it is used in the calculation of adatom fluxes into and out of steps.

3. Numerical solutions of the Configurational Continuum

We now apply our approach to a few simple cases. First, we consider a conic structure which consists of circular concentric steps. This crystalline cone was studied in Refs. [11, 12] where we wrote a one-dimensional step flow model for the step radii in the absence of growth flux. In the diffusion limited case where adatom diffusion across terraces is the rate limiting process, the equation of motion for the step radii r_n read:

$$\begin{aligned} \frac{dr_1}{dt} &= \frac{D_s C_\infty^{eq}\Omega}{k_B T r_1}\frac{\mu_1-\mu_2}{\ln(r_1/r_2)}\,, \\ \frac{dr_n}{dt} &= \frac{D_s C_\infty^{eq}\Omega}{k_B T r_n}\left(\frac{\mu_n-\mu_{n+1}}{\ln(r_n/r_{n+1})}-\frac{\mu_{n-1}-\mu_n}{\ln(r_{n-1}/r_n)}\right)\,, \quad n>1\,, \end{aligned} \tag{3.1}$$

with the step chemical potentials μ_n given by

$$\mu_n = \frac{\Omega\Gamma}{r_n} + \Omega G\left[\frac{2r_{n+1}}{r_{n+1}+r_n}\cdot\frac{1}{(r_{n+1}-r_n)^3}-\frac{2r_{n-1}}{r_n+r_{n-1}}\cdot\frac{1}{(r_n-r_{n-1})^3}\right]\,. \tag{3.2}$$

In the above expressions D_s is the adatom diffusion constant, Ω is the atomic area of the crystal and C_∞^{eq} is the equilibrium concentration in the vicinity of a straight isolated step. Γ is the step line tension, G is the step-step interaction strength, T is the temperature and k_B is the Boltzmann constant. Eq. (3.2) can be used for calculating the chemical potential of the top step, μ_1, by omitting the second interaction term.

Numerical integration of the above step model shows that the cone decays through the collapse of individual islands. During the decay a facet develops at the top of the cone with a radius that grows with time as $t^{1/4}$. Similar equations can be written in the presence of growth flux. With flux, the cone grows except at the peak which initially decays and then saturates. A facet forms at the peak after saturation.

The continuum model we solved in the context of this example is a fully two-dimensional model, which can, in principle, develop non radially symmetric morphologies. The microscopic dynamics we used were a two-dimensional generalization of the microscopic equations for step radii of the discrete one-dimensional

model given above. In particular the step chemical potential was generalized to

$$\mu\left(\vec{r}\right) = \Omega\Gamma\kappa\left(\vec{r}\right) + \Omega G\left(\frac{\exp\left[\frac{|\vec{r}_d-\vec{r}|\cdot\kappa(\vec{r}_d)}{2}\right]}{\left|\vec{r}_d-\vec{r}\right|^3} - \frac{\exp\left[-\frac{|\vec{r}_u-\vec{r}|\cdot\kappa(\vec{r}_u)}{2}\right]}{\left|\vec{r}_u-\vec{r}\right|^3}\right), \qquad (3.3)$$

where $\kappa\left(\vec{r}\right)$ is the local step curvature. $\vec{r}_d$ and $\vec{r}_u$ are the coordinates at which the lower and upper neighboring steps are closest to the step at $\vec{r}$. It is assumed that these neighbors have the same sign as the step at $\vec{r}$ and that steps of opposite signs do not interact (in which case the relevant interaction terms in Eq. (3.3) are omitted). This expression was derived assuming an l^{-2} repulsion between two segments of two different steps which are separated by a distance l. Under this assumption, Eq. (3.3) is exact to first order in the curvature of neighboring steps and qualitatively captures the interaction when they have large curvatures.

The equations describing adatom diffusion on terraces were solved assuming the steps at $\vec{r}$, $\vec{r}_d$ and $\vec{r}_u$ are circular and concentric and that the radius of the step at $\vec{r}$ is $1/\kappa(\vec{r})$. Any microscopic dynamics, such as a full solution of the diffusion equation on each terrace, or a more detailed calculation of the interactions between steps can easily be used in the framework of our model. For the sake of demonstrating the validity of Configurational Continuum the simple dynamics we chose are sufficient.

Figure 2 shows a comparison between a numerical solution of the discrete step model and a cross section from the two-dimensional solution of our continuum model in the absence of growth flux and when nucleation of new steps is not allowed. Clearly the continuum model captures the main features of the surface evolution. In particular the width and height of the top facet are in excellent agreement with the discrete model. Fig. 3 shows a similar comparison in the presence of growth flux. Again the agreement is quite impressive. In this case we allowed new islands to nucleate and our simulation indicates that nucleation events occur on the top facet once it becomes large enough. There is hardly any nucleation on the finite slope regions, because the steps there efficiently absorb the excess material. Figure 3(c) shows an island on the top facet, which nucleated and started growing.

We now turn to the more demanding example of bidirectional sinusoidal grating relaxation. Here the initial surface height profile of wave length L is given by

$$h_L(\vec{r}, t=0) = h_0 \sin\left(\frac{2\pi x}{L}\right)\sin\left(\frac{2\pi y}{L}\right).$$

The relaxation of this profile towards a flat surface was studied by Rettori and Villain [18], who gave an approximate solution to a step flow model, in the limit where the interaction between steps can be neglected with respect to the step line tension. We now apply our model to this problem assuming diffusion limited kinetics without deposition flux or island nucleation.

For weak interactions between steps, the surface height evolves according to $\partial h_L/\partial t \propto \nabla^2\kappa \sim L^{-3}$, where κ is the step curvature. We therefore expect the

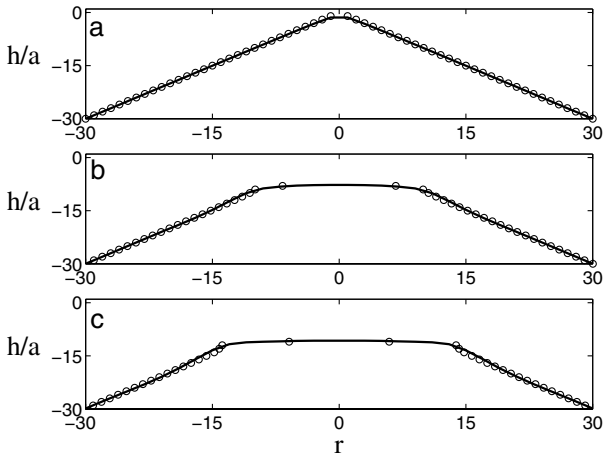

FIGURE 2. Decay of a crystalline cone. The solid line shows a cross section of the two-dimensional solution of Eq. (2.4). Circles show the surface evolution according to the one-dimensional step flow model Eq. (3.1). (a) is the initial morphology and (b) and (c) show the surface at later times.

following scaling law for $h_L(\vec{r}, t)$:

$$h_L(\vec{r}, t) = h_{L=1}(\vec{r}/L, t/L^3) \; . \tag{3.4}$$

Figure 4 shows the data collapse of cross sections of profiles resulting from our continuum model. The different symbols correspond to profiles of different wave lengths at time $t = t_0 L^3$ for some fixed t_0. The quality of the data collapse shows that the scaling scenario (3.4) holds very accurately. Note that large facets have developed at the surface extrema, and they are connected by very steep slopes. This shape does not agree with Rettori and Villain's heuristic argument [18], which predicts that facets appear also near $h = 0$ lines. Nevertheless, their prediction that after a short transient the amplitude of the height profile decays as t/L^3 is in agreement with both Eq. (3.4) and our numerical solutions.

Figure 5 shows results for a much stronger repulsive interactions between steps, where the scaling law (3.4) clearly does not hold. Fig. 5 (a) shows profiles of different wavelengths which have relaxed to half of the initial amplitude. Here profiles with a smaller wavelength have small facets and moderate slopes. This happens because repulsion between steps becomes increasingly important as the profile wavelength is reduced. At long wavelengths the weak step-step interaction limit of Fig. 4 is recovered. Fig. 5 (b) shows the different amplitudes as a function of scaled time t/L^3.

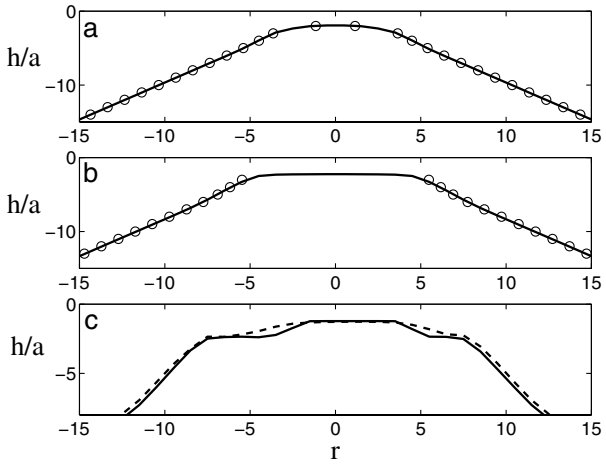

FIGURE 3. Evolution of a crystalline cone under growth conditions. The lines show cross sections of the two-dimensional solution of Eq. (2.4). Circles show the surface evolution according to the one-dimensional step flow model. The initial shape is the exact cone shown in Fig. 2 (a). (a) and (b) show the generation and evolution of a facet at the top at later times. (c) shows an island which nucleated (solid) and grew (dashed) on the top facet. Here no comparison is made with the step flow model.

4. Conclusions

We proposed a novel continuum model for the evolution of sub roughening crystal surfaces. Our model, which we term Configurational Continuum, is derived directly from the underlying dynamics of atomic steps. Unlike conventional continuum models, Configurational Continuum is fully consistent with the step dynamics and is capable of handling singular surface features such as facets and corners.

The key idea in our model is to view the continuous surface profile as the envelope of an ensemble of step configurations which are all consistent with the continuous profile. Knowing the ensemble envelope, it is always possible to reconstruct individual configurations and evolve them in time. This evolution of individual configurations determines the evolution of the ensemble envelope which within our model is interpreted as the evolution of the profile. The continuum limit in our model is naturally realized because the continuous profile induces a continuum of possible step configurations.

Like other continuum models, Configurational Continuum has a computational advantage over the underlying discrete step model. When solved on a computer, it is possible to use a sparse grid in regions where the profile is very smooth. However, near corners or facets our model requires a fine discretization grid. The fine grid is necessary in order to faithfully reconstruct the step configurations which

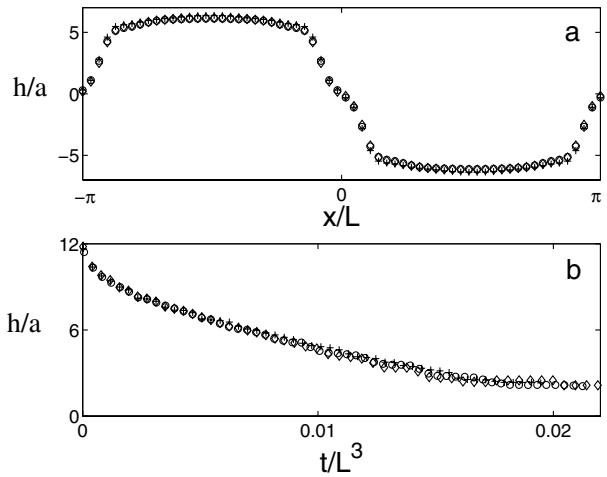

FIGURE 4. Data collapse in the evolution of bidirectional sinusoidal profiles with different wave lengths when the repulsive interaction between steps is very weak. Wave lengths shown are $L = 64$ (circles), $L = 128$ (squares) and $L = 256$ (triangles). a) Cross sections of the profiles with different wave lengths measured at time $t = t_0 L^3$. The cross sections are along the $y = -L/4$ line (peak to valley). b) Amplitude decay of the different wave lengths as a function of scaled time t/L^3.

are possible near a singular point. Our model thus has the important property of being capable of describing step flow on different scales in a consistent way. In smooth surface regions, Configurational Continuum provides a coarse grained numerical description of surface dynamics. However it is still capable of accounting for the unique behavior of steps near singular points or lines.

The problem of connecting between different scales in dynamical systems is not limited to the evolution of surfaces. This problem is widespread in physics, engineering and biology as well as in other fields. Our hope is that the ideas at the basis of Configurational Continuum can be applied in other multi-scale problems.

Appendix A. Failure of the cusp rounding method

In this appendix we give an example which shows how rounding of the surface free energy cusp can lead to erroneous solutions for surface evolution. As an example system we again choose the crystalline cone studied in Refs. [11, 12]. For simplicity we consider the diffusion limited case. This system is convenient since it exhibits scaling. In the scaling limit conventional continuum modelling of the cone becomes exact [11, 12] and we can concentrate on effects introduces by the cusp rounding method. We start by solving a model with a rounded free energy cusp and later

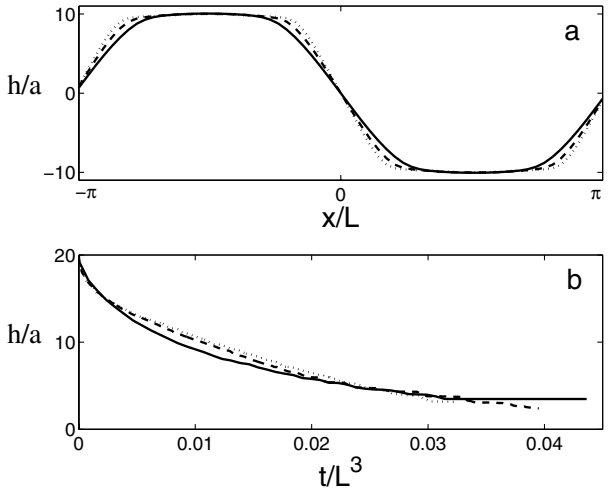

FIGURE 5. Bidirectional sinusoidal profiles in the case of stronger step-step interactions. Wave lengths shown are $L = 64$ (solid), $L = 128$ (dashed) and $L = 192$ (dotted). a) Cross sections of the profiles with different wave lengths which have relaxed to half of their initial amplitude. The cross sections are along the $y = -L/4$ line (peak to valley). b) Amplitude decay of the different wave lengths as a function of scaled time t/L^3.

compare the solution of this model with the relevant discrete step model and with the solution of the Configurational Continuum.

In the conventional continuum approach, the continuous free energy density of sub roughening surfaces has a cusp singularity at the high symmetry orientation. In a coordinate system where (x, y) is the high symmetry plane and $h(x, y)$ is the surface profile, the projected (on (x, y)) surface free energy density assumes the form [19]:

$$\mathcal{F}(x,y) = \mathcal{F}_0 + \Gamma |\nabla h(x,y)| + \frac{G}{3} |\nabla h(x,y)|^3 \ . \tag{A.1}$$

This form is the continuum analog of the free energy of an array of steps with line tension Γ and an inverse square repulsive step-step interaction of strength G.

The singular nature of the surface free energy complicates the modelling of surface evolution. Several authors have tried to overcome this problem by rounding the cusp with a small parameter α:

$$\mathcal{F}_\alpha(x,y) = \mathcal{F}_0 + \Gamma \left[(\nabla h(x,y))^2 + \alpha^2 \right]^{1/2} + \frac{G}{3} \left[(\nabla h(x,y))^2 + \alpha^2 \right]^{3/2} \ . \tag{A.2}$$

The hope behind this regularization scheme is that in the limit $\alpha \to 0$ the resulting model captures the correct surface dynamics.

Surface dynamics is derived from $\mathcal{F}_\alpha$ as follows. Taking the functional derivative of $\mathcal{F}_\alpha$ we obtain the surface chemical potential:

$$\mu_\alpha = \frac{\delta \mathcal{F}_\alpha}{\delta h} = -\Omega \left(\frac{\partial}{\partial x} \frac{\partial \mathcal{F}_\alpha}{\partial h_x} + \frac{\partial}{\partial y} \frac{\partial \mathcal{F}_\alpha}{\partial h_y} \right) , \tag{A.3}$$

where $h_x = \partial h/\partial x$ and $h_y = \partial h/\partial y$. For a radially symmetric profile $h(r,t)$ we find that

$$\mu_\alpha = -\frac{\Omega}{\sqrt{h_r^2 + \alpha^2}} \left[\left(\frac{h_r}{r} + h_{rr} \right) \left(\Gamma + G \left(h_r^2 + \alpha^2 \right) \right) + h_r^2 h_{rr} \left(G - \frac{\Gamma}{h_r^2 + \alpha^2} \right) \right] , \tag{A.4}$$

where $h_r = \partial h/\partial r$ and $h_{rr} = \partial^2 h/\partial r^2$.

In diffusion limited kinetics variations in the chemical potential give rise to currents which are proportional to the chemical potential gradient. For our radially symmetric profile we can consider only the radial component of this current

$$J = -\frac{D_s \tilde{C}^{eq}}{k_B T} \frac{\partial \mu_\alpha}{\partial r} . \tag{A.5}$$

The dynamic equation for the profile can now be written using the continuity equation

$$\frac{\partial h}{\partial t} = -\Omega \cdot \nabla J = \frac{\Omega D_s \tilde{C}^{eq}}{k_B T} \frac{1}{r} \frac{\partial}{\partial r} \left(r \frac{\partial \mu_\alpha}{\partial r} \right) . \tag{A.6}$$

The $\alpha \to 0$ limit of Eq. (A.6) automatically gives the correct equilibrium crystal shapes because Eq. (A.2) goes to Eq. (A.1) in this limit. We want to check whether this limit also gives the correct (consistent with step flow) dynamics.

We applied Eq. (A.6) to a crystalline cone $h(r, t = 0) \sim -r$. The similarity sign here indicates that the tip of the initial profile was smoothed in order to have an analytic surface. Analyticity at the origin was also used as a boundary condition for the surface evolution. Numerical solutions show that, at long times the profile slope obeys a scaling law

$$h_r(r,t) = -F(rt^{-1/4}) . \tag{A.7}$$

This behavior agrees with the scaling properties exhibited by a discrete step flow model of the same surface structure [11, 12]. In Fig. 6 we show the resulting scaled slopes (dots) for different values of the cusp rounding parameter α. These long time solutions are not sensitive to the initial smoothing of the cone. As α is reduced we observe the appearance of a very flat region around the origin. This flat region supposedly becomes a true facet in the $\alpha = 0$ limit.

For small values of α, solutions of the dynamic equation (A.6) approach scaling very slowly. For this reason it becomes increasingly difficult to probe the $\alpha = 0$ scaling state. In order to reach smaller values of α we continued in the following way. We assumed that the scaling ansatz (A.7) holds and used it to transform Eq. (A.6) into an ordinary differential equation for the scaling function

$F(\xi)$ in the scaling variable $\xi = rt^{-1/4}$. Replacing $h_r(r,t)$ in Eq. (A.6) by the scaling function $F(\xi)$ we obtain the following equation:

$$-\frac{1}{4}F' = \frac{\Omega D_s \tilde{C}^{eq}}{k_B T}\frac{d}{d\xi}\left[\frac{1}{\xi}\frac{d}{d\xi}\left(\xi\frac{d\eta_\alpha}{d\xi}\right)\right],$$
$$\eta_\alpha = -\frac{\Omega}{\sqrt{F^2+\alpha^2}}\left[\left(\frac{F}{\xi}+F'\right)\left(\Gamma + G\left(F^2+\alpha^2\right)\right) + F^2F'\left(G - \frac{\Gamma}{F^2+\alpha^2}\right)\right], \tag{A.8}$$

with $F' = dF/d\xi$.

Solutions of the above equation for the large values of α agree with the scaling states of the dynamic equation (A.6). The dashed lines in Fig. 6 show the resulting scaling functions for smaller values of α. Finally in order to determine the $\alpha = 0$ limit we estimated the scaled position of the facet edge from the $\alpha \neq 0$ solutions. This position selects [11, 12] a unique scaling solution for the $\alpha = 0$ case of Eq. (A.8). The resulting scaling function is shown by the solid line in Fig. 6. By our procedure this function is an approximation for the true scaling function of the system according to the cusp rounding method.

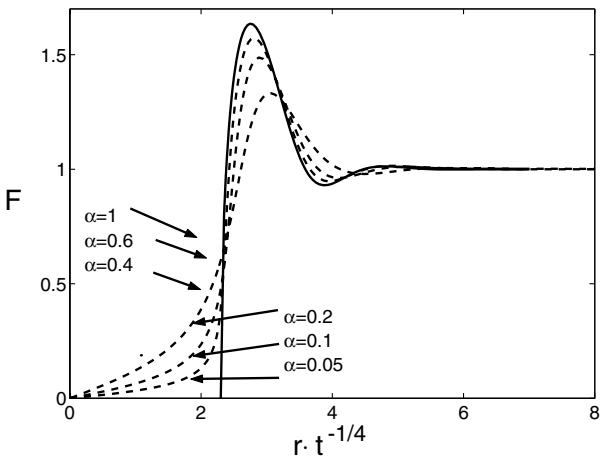

FIGURE 6. Scaling functions of the slope for different values of the cusp rounding parameter. Dots show scaling functions obtained from a direct solution of the dynamic equation (A.6). Dashed lines show solutions of the scaling equation (A.8). The solid line shows the estimated $\alpha = 0$ solution of Eq. (A.8).

The solid line in Fig. 6 should be compared with the behavior of a system of discrete steps. For this purpose we introduce the following step model:

$$\begin{aligned}
\frac{dr_1}{dt} &= \frac{D_s C_\infty^{eq}\Omega}{k_B T r_1}\,\frac{\mu_1-\mu_2}{\ln\left(r_1/r_2\right)}\,,\\
\frac{dr_n}{dt} &= \frac{D_s C_\infty^{eq}\Omega}{k_B T r_n}\left(\frac{\mu_n-\mu_{n+1}}{\ln\left(r_n/r_{n+1}\right)}-\frac{\mu_{n-1}-\mu_n}{\ln\left(r_{n-1}/r_n\right)}\right)\,,\quad n>1,\\
\mu_n &= \frac{\Omega\Gamma}{r_n}+\Omega G\left[\frac{2r_{n+1}}{r_{n+1}+r_n}\cdot\frac{1}{\left(r_{n+1}-r_n\right)^3}+\frac{r_{n+1}}{\left(r_{n+1}^2-r_n^2\right)^2}\right.\\
&\qquad\left.-\frac{2r_{n-1}}{r_n+r_{n-1}}\cdot\frac{1}{\left(r_n-r_{n-1}\right)^3}+\frac{r_{n-1}}{\left(r_n^2-r_{n-1}^2\right)^2}\right]\,. \qquad \text{(A.9)}
\end{aligned}$$

This is the same step model studied in Section 3 and in Refs. [11, 12] with modified step chemical potentials. The modification has a small effect on the model behavior and does not introduce any qualitative changes. In particular, this step model obeys the same scaling properties that were studied in Refs. [11, 12], i.e., the density of steps in this model scales according to $D(r,t) = F_{discrete}(rt^{-1/4})$. In addition, applying the scaling analysis of Refs. [11, 12] to this modified step model results in an ordinary differential equation for the scaling function $F_{discrete}$ which is identical to the $\alpha = 0$ limit of Eq. (A.8). This fact gives us a basis for comparison between the step model and the cusp rounding scheme. Identifying the step density of the discrete model with the slope of the continuum model we can finally compare the limiting solution from the cusp rounding method with the scaled density of steps. In Fig. 7 we show that these two functions do not coincide. The scaled position of the facet edge in the cusp rounding method is about 40% larger than the one in the discrete system. This means that the difference between the two facets in real space diverges at long times. The height at the origin according to the cusp rounding method will suffer from the same errors. By assuming analyticity of the profile throughout the limiting procedure of the cusp rounding method, we have imposed erroneous boundary conditions at the facet edge.

Figure 7 also shows a one-dimensional solution of the Configurational Continuum model for this cone system. The Configurational Continuum model predicts scaling of the slope as well. The discrepancy between the resulting scaling function and the discrete step system is much smaller and is consistent with what one would expect from discretization errors.

References

[1] W.K. Burton, N. Cabrera and F.C. Frank, *The growth of crystals and the equilibrium structure of their surfaces*, Trans. R. Soc. London Ser. A **243** (1951), 299–358.

[2] For general reviews see H.-C. Jeong and E.D. Williams, *Steps on surfaces: experiment and theory.* Surf. Sci. Rep. **34** (1999), 171–294; E.D. Williams, *Surface steps*

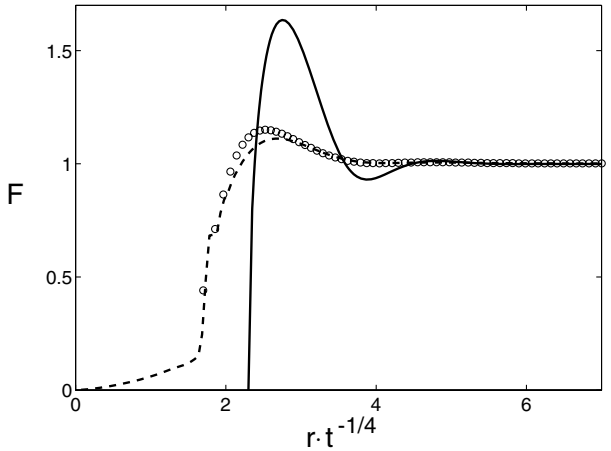

FIGURE 7. Comparison between the scaling function predicted by the cusp rounding procedure (solid), scaling function from a one-dimensional solution of the Configurational Continuum (dashed) and the scaled density of steps in the discrete model (circles).

and surface morphology – understanding macroscopic phenomena from atomic observations. Surf. Sci. **299** (1994), 502–524.

[3] E.S. Fu, M.D. Johnson, D.-J. Liu, J.D. Weeks, and E.D. Williams, *Size scaling in the decay of metastable structures.* Phys. Rev. Lett. **77** (1996), 1091–1094.

[4] S. Tanaka, N.C. Bartelt, C.C. Umbach, R.M. Tromp, and J.M. Blakely, *Step permeability and the relaxation of biperiodic gratings on Si(001).* Phys. Rev. Lett. **78** (1997), 3342–3345.

[5] W.W. Mullins, *Theory of thermal groovings.* J. Appl. Phys. **28** (1957), 333–339.

[6] M. Ozdemir and A. Zangwill, *Morphological equilibration of a corrugated crystalline surface.* Phys. Rev. B **42** (1990), 5013–5024.

[7] P. Nozières, *On the motion of steps on a vicinal surface.* J. Phys. I France **48** (1987), 1605–1608.

[8] F. Lançon and J. Villain, *Dynamics of a crystal-surface below its roughening transition.* Phys. Rev. Lett. **64** (1990), 293–296.

[9] M. Uwaha, J. Phys. Soc. Jpn. *Relaxation of crystal shapes caused by step motion.* **57** (1988), 1681–1686.

[10] J. Hager and H. Spohn, *Self-similar morphology and dynamics of periodic surface profiles below the roughening transition.* Surf. Sci. **324** (1995), 365–372.

[11] N. Israeli and D. Kandel, *Profile scaling in decay of nanostructure.* Phys. Rev. Lett. **80** (1998), 3300–3303.

[12] N. Israeli and D. Kandel, *Profile of a decaying crystalline cone.* Phys. Rev. B **60** (1999), 5946–5706.

[13] N. Israeli and D. Kandel, *Decay of one-dimensional surface modulations.* Phys. Rev. B **62** (2000), 13707–13717.

[14] N. Israeli, H.-C. Jeong, D. Kandel and J.D. Weeks, *Dynamics and scaling of one-dimensional surface structures.* Phys. Rev. B **61** (2000), 5698–5706.

[15] H.P. Bonzel, E. Preuss and B. Steffen, *The dynamical behavior of periodic surface profiles on metals under the influence of anisotropic surface-energy.* Appl. Phys. A **35** (1984), 1–8.

[16] H.P. Bonzel and E. Preuss, *Morphology of periodic surface-profiles below the roughening temperature – Aspects of continuum theory.* Surf. Sci. **336** (1995), 209–224.

[17] N. Israeli and D. Kandel, *Novel continuum modeling of crystal surface evolution.* Phys. Rev. Lett. **88**, 116103 (2002).

[18] A. Rettori and J. Villain, *Flattening of grooves on a crystal-surface – A method of investigation of surface roughness.* J. de Phys. **49** (1988), 257–267.

[19] M.M. Gruber and W.W. Mullins, *On the theory of anisotropy of crystalline surface tension.* J. Phys. Chem. Solids **28** (1966), 875–876.

Navot Israeli and Daniel Kandel
Department of Physics of Complex Systems
Weizmann Institute of Science
Rehovot, 76100, Israel
e-mail: navot.israeli@weizmann.ac.il
e-mail: daniel.kandel@weizmann.ac.il

International Series of Numerical Mathematics, Vol. 149, 227–237

On Level Set Formulations for Anisotropic Mean Curvature Flow and Surface Diffusion

Ulrich Clarenz, Frank Haußer, Martin Rumpf,
Axel Voigt and Ulrich Weikard

Abstract. Anisotropic mean curvature motion and in particular anisotropic surface diffusion play a crucial role in the evolution of material interfaces. This evolution interacts with conservations laws in the adjacent phases on both sides of the interface and are frequently expected to undergo topological chances. Thus, a level set formulation is an appropriate way to describe the propagation. Here we recall a general approach for the integration of geometric gradient flows over level set ensembles and apply it to derive a variational formulation for the level set representation of anisotropic mean curvature motion and anisotropic surface flow. The variational formulation leads to a semi-implicit discretization and enables the use of linear finite elements.

Mathematics Subject Classification (2000). Primary 35K55; Secondary 53C44.

Keywords. level set method; anisotropic mean curvature flow; anisotropic surface diffusion; semi-implicit time discretization.

1. Introduction

To capture the surface evolution in epitaxial growth on a large scale it is appropriate to assume the surface to be smooth and to describe its evolution by continuum equations. For a review of such approaches see [1]. Even if most of these models are heuristically introduced, most of them can be considered as small slope approximations of anisotropic geometric evolution laws, such as mean curvature flow or surface diffusion. These geometric nonlinear evolution laws can therefore be viewed as a prototype of a more general class of models to describe epitaxial growth. In this paper we present an approach to anisotropic second and fourth order geometric evolution laws in a level set formulation. For more details on the background and the derivation we refer to [2, 3]. A connection to the physical

problems in epitaxial growth and a comparison with the models described in [1] will be given elsewhere. Level set formulations for isotropic geometric evolution laws have already been discussed and used numerically in the literature. In particular, isotropic surface diffusion is considered within a level set context, i.e., in [4, 5, 6].

For a given initial surface $\mathcal{M}_0$, a geometric evolution law defines a family of surfaces $\mathcal{M}(t)$, $t \geq 0$ with $\mathcal{M}(0) = \mathcal{M}_0$. Now consider $\mathcal{M}(t)$ to be given implicitly as a specific level set of a corresponding function $\phi(t)$. Thus the evolution of $\mathcal{M}(t)$ can be described by an evolution of $\phi(t)$. Given a velocity field v the evolution of ϕ is described by the convection equation $\partial_t \phi + \|\nabla \phi\| v = 0$, which is called the level set equation. If the velocity v is determined through the geometric evolution law we can implicitly evolve the surface $\mathcal{M}$ by solving the level set equation, [7]. Let us emphasize that different from second order problems, such as mean curvature flow, no maximum principle is known for fourth order problems. Indeed two surfaces both undergoing an evolution by surface diffusion might intersect in finite time. Hence, a level set formulation in general will lead to singularities and we expect a blow up of the gradient of ϕ in finite time. If one is solely interested in the evolution of a single level set, one presumably can overcome this problem by a reinitialization with a signed distance function with respect to this evolving level set. We are here aiming to derive a suitable weak formulation for such evolution problem, which only makes use of first derivatives of unknown functions and test functions. In particular this will allow for a discretization based on a mixed formulation with piecewise affine finite elements, closely related to results by Rusu [8]. Hence we have to reformulate the problem in order to avoid curvature terms, i.e., derivatives of the normal. Here, we take advantage of a fairly general gradient flow perspective to geometric evolution problems. Indeed, given a gradient flow for parametric surfaces, we derive a level set formulation, which describes the simultaneous evolution of all level sets corresponding to this gradient flow. This approach is based on the co-area formula (cf. for example to the book of Ambrosio et al. [9]) and a proper identification of the temporal change of the level set function and the corresponding evolution speed of the level surfaces. Thereby, we are able to identify the natural dependent variables. This approach provides an insight into the geometry of evolution problems on the space of level set ensembles.

The paper is organized as follows: In Section 2 we present a level set formulation for a gradient flow with respect to the L^2 surface metric and recover the well-known level set formulation for isotropic mean curvature flow, as given in [10]. In Section 3 this setting is adapted to derive a level set formulation for anisotropic mean curvature flow and anisotropic surface diffusion. Based on these results a numerical scheme for anisotropic surface diffusion is described in Section 4, and in Section 5 some numerical results in two and three dimensions are presented.

2. Parametric gradient flow

Consider a closed, immersed, oriented, and smooth surface $x : \mathcal{M} \to \mathbb{R}^3$ with a two-dimensional parameter manifold $\mathcal{M}$. Given an energy density $f : \mathcal{M} \to \mathbb{R}$, the surface energy is denoted by

$$e[\mathcal{M}] := \int_{\mathcal{M}} f \, \mathrm{d}A.$$

We consider the gradient flow with respect to a specific surface metric $g(\mathcal{M})$

$$\partial_t x = -\mathrm{grad}_{g(\mathcal{M})} e[\mathcal{M}].$$

To derive a level set formulation of this equation, let us first introducing some useful geometric notation. Furthermore, we derive representations for geometric quantities on level sets $\mathcal{M}$ in terms of the corresponding level set function ϕ. Let $\phi : \Omega \to \mathbb{R}$ be some smooth function on a domain $\Omega \subset \mathbb{R}^{d+1}$. Suppose $\mathcal{M}_c := \{x \in \Omega \,|\, \phi(x) = c\}$ is a level set of ϕ for the level value c. In what follows we write $\mathcal{M} = \mathcal{M}_c$ if no confusion is possible and always assume that $\|\nabla\phi\| \neq 0$ on $\mathcal{M}$. Thus, $\mathcal{M}_c$ is a smooth hypersurface and the normal

$$n = \nabla\phi \Big/ \|\nabla\phi\|$$

on the tangent space $\mathcal{T}_x\mathcal{M}$ is defined for every x on $\mathcal{M}$. The projection onto $\mathcal{T}_x\mathcal{M}$ is given by

$$P := \mathbb{1} - n \otimes n \,,$$

where $\mathbb{1}$ denotes the identity on $\mathbb{R}^{d+1}$. In what follows we will make extensive use of the Einstein summation convention. Furthermore vectors $v \in \mathbb{R}^{d+1}$ and matrixes $A \in \mathbb{R}^{d+1,d+1}$ are written in index form $v = (v_i)_i$, $A = (A_{ij})_{ij}$. For a tangential vector field v on $\mathcal{M}$ and a scalar function u on $\mathbb{R}^{d+1}$ the tangential divergence and tangential gradient are defined as

$$\begin{aligned} \mathrm{div}_{\mathcal{M}} v &= \partial_i v_i - n_i n_j \partial_j v_j \\ \nabla_{\mathcal{M}} u &= (\partial_i u - n_i n_j \partial_j u)_i \,. \end{aligned}$$

Furthermore we use the notation $\partial_i u = u_{,i}$ and $\partial_i \partial_j u = u_{,ij}$. Furthermore ∂_n denotes the normal derivative and $h := \mathrm{div}\, n = n_{i,i}$ the mean curvature on $\mathcal{M}$. Finally, for the the shape operator S on $\mathcal{M}$ - which is defined as the restriction of Dn on the tangent space $\mathcal{T}_x\mathcal{M}$ - we obtain

$$S = Dn\, P = \frac{1}{\|\nabla\phi\|} P\, D^2\phi\, P \,. \tag{2.1}$$

2.1. The general procedure to derive a level set formulation

Let us assume that we simultaneously want to evolve all level sets $\mathcal{M}_c$ of a given level set function ϕ. We take into account the co-area formula [18, 9] and define the global energy

$$E[\phi] := \int_{\mathbb{R}} e[\mathcal{M}_c] \mathrm{d}c = \int_{\Omega} \|\nabla\phi\| \, f \, \mathrm{d}x.$$

Here, we set $e[\mathcal{M}_c] = 0$ if $\mathcal{M}_c = \emptyset$. We interpret a function ϕ or the corresponding set $\{\mathcal{M}_c\}_{c\in\mathbb{R}}$ as an element of the manifold $\mathcal{L}$ of level set ensembles. Here, we follow the exposition in [3, 11]. A tangent vector $s := \partial_t\phi$ on $\mathcal{L}$ can be identified with a motion velocity v of the corresponding level set $\mathcal{M}_c$ via the classical level set equation

$$s + \|\nabla\phi\|\, v = 0$$

(cf. the book of Osher and Paragios [12] for a detailed study). Thus, we are able to define the corresponding metric on $\mathcal{L}$. If the L^2 metric is used it follows

$$\begin{aligned} g_\phi(s_1, s_2) &:= \int_{\mathbb{R}} \int_{\mathcal{M}_c} v_1 \cdot v_2 \,\mathrm{d}A\,\mathrm{d}c \\ &= \int_\Omega \frac{s_1}{\|\nabla\phi\|} \frac{s_2}{\|\nabla\phi\|} \|\nabla\phi\| \,\mathrm{d}x = \int_\Omega s_1 s_2 \,\|\nabla\phi\|^{-1} \,\mathrm{d}x\,. \end{aligned}$$

Finally, we are able to rewrite the simultaneous gradient flow of all level sets in terms of the level set function ϕ as

$$\partial_t\phi \;=\; -\mathrm{grad}_{g_\phi} E[\phi]\,,$$

which is equivalent to

$$g_\phi(\partial_t\phi, \vartheta) = \int_\Omega \partial_t\phi\,\vartheta\,\|\nabla\phi\|^{-1} \,\mathrm{d}x = -\langle E'[\phi], \vartheta\rangle \tag{2.2}$$

for all functions $\vartheta \in C_0^\infty(\Omega)$.

As an example let us consider the area functional $e[\mathcal{M}] = \mathrm{area}(\mathcal{M})$ with $f = 1$. Hence, $E[\phi] = \int_\Omega \|\nabla\phi\|$ and we obtain the evolution equation

$$\int_\Omega \partial_t\phi\vartheta\,\|\nabla\phi\|^{-1} \,\mathrm{d}x = -\int_\Omega \frac{\nabla\phi}{\|\nabla\phi\|} \cdot \nabla\vartheta \,\mathrm{d}x\,.$$

Indeed, this is the weak formulation of mean curvature motion in level set form [10].

3. Anisotropic evolution laws

By considering the specific choice of the energy density $f = \gamma(n)$, with γ an anisotropy function, we obtain a generalization of the area functional in the above example.

3.1. Anisotropy function

The anisotropy function γ is a smooth function

$$\begin{aligned} \gamma \;:\; & S^2 \to \mathbb{R}^+ \\ & z \mapsto \gamma(z)\,, \end{aligned} \tag{3.1}$$

and we may assume, that γ is given as a one-homogeneous function on $\mathbb{R}^3$, i.e., for $\lambda > 0$ we have $\gamma(\lambda z) = \lambda\gamma(z)$. In addition, let there be a positive constant m such that for the second derivative we have

$$D^2(\gamma(z) - m|z|) \geq 0\,.$$

In this case, γ is called elliptic and the eigenvalues of $D^2\gamma(z)$ restricted to $z^\perp = \{x \in \mathbb{R}^3 | x \cdot z = 0\}$ are bounded from below by m.

By parameterizing γ over the unit sphere

$$\begin{aligned} \gamma_z &: S^2 \to \mathcal{W}_\gamma \\ &\quad z \mapsto \gamma_z(z)\,, \end{aligned} \tag{3.2}$$

the so-called Wulff-shapes $\mathcal{W}_\gamma$ are obtained. Solutions of the isoperimetric problem for e_γ are given by these Wulff-shapes [13]. For a proof of the isoperimetric property of the Wulff-shape and more references to the literature see [14].

Considering a surface $x : \mathcal{M} \to \mathbb{R}^3$, we can give a version of the second derivative of γ on its tangential space as follows

$$\begin{aligned} \mu_\gamma &: T_\xi\mathcal{M} \to T_\xi\mathcal{M} \\ &\quad v \mapsto Dx^{-1}\gamma_{zz}(n)Dx(v)\,. \end{aligned} \tag{3.3}$$

The endomorphism field μ_γ is well defined due to the fact that $D^2\gamma(z)\,z = 0$ for all $z \neq 0$. By ellipticity, μ_γ is positive definite. The classical area functional is obtained for the function $\gamma(z) = |z|$. In this case, μ_γ is the identity

3.2. Anisotropic mean curvature flow

Anisotropic mean curvature flow is the L^2-gradient flow of $e_\gamma[\mathcal{M}] := \int_\mathcal{M} \gamma \; dA$. The first variation of e_γ in direction ϑ may be represented in the L^2-metric by a generalized mean curvature vector

$$\langle e'_\gamma[x], \vartheta \rangle = \int_\mathcal{M} h_\gamma (n \cdot \vartheta)\, dA\,. \tag{3.4}$$

Here $h_\gamma = \mathrm{tr}(\mu_\gamma S)$ will be called the γ-mean curvature. In level set formulation this can also be expressed as follows (where S_{ij} are the components of the symmetric shape operator defined in Section 2)

$$h_\gamma = \gamma_{z_j z_i} S_{ij} \tag{3.5}$$

$$= \frac{1}{||\nabla\phi||}\gamma_{z_j z_i}(\delta_{ik} - n_i n_k)\partial_{kl}\phi(\delta_{lj} - n_l n_j) \tag{3.6}$$

$$= \frac{1}{||\nabla\phi||}\gamma_{z_j z_i}\partial_{ij}\phi = \mathrm{div}\,\gamma_z(n). \tag{3.7}$$

The corresponding level set functional is similar to the isotropic case

$$E_\gamma[\phi] = \int_\mathbb{R} e_\gamma[\mathcal{M}_c]\, dc = \int_\Omega \gamma(n)\|\nabla\phi\|\, dx \; = \int_\Omega \gamma(\nabla\phi)\, dx\,. \tag{3.8}$$

From this we easily obtain the representation of the anisotropic mean curvature flow in level set formulation

$$\langle E'_\gamma[\phi], \vartheta \rangle = \int_\Omega \gamma_z(\nabla\phi)\nabla\vartheta\, dx\,. \tag{3.9}$$

Note that at this point we need a suitable regularization of $\nabla\phi/|\nabla\phi|$ due to the fact that γ_z is zero-homogeneous. This regularization, denoted by n^ϵ, will be chosen as

$$n^\epsilon = \frac{\nabla\phi}{\sqrt{\epsilon^2 + \|\nabla\phi\|^2}} = \frac{\nabla\phi}{\|\nabla\phi\|_\epsilon}\,,$$

for $\epsilon > 0$, where obviously we use the definition $\|\nabla\phi\|_\epsilon = \sqrt{\epsilon^2 + \|\nabla\phi\|^2}$. For more details on regularization see [3]. If we consider a regularized version of the L^2-gradient flow in the level set case we obtain for any admissible test function ϑ

$$\int_\Omega \partial_t\phi\vartheta \frac{1}{\|\nabla\phi\|}\,dx = -\int_\Omega \gamma_z(n^\epsilon)\nabla\vartheta\,dx\,, \tag{3.10}$$

which is the weak formulation of anisotropic curvature motion in level set form.

3.3. Anisotropic surface diffusion

Anisotropic surface diffusion is the H^{-1}-gradient flow of e_γ. The corresponding H^{-1} metric is

$$g(s_1, s_2) = -\int_\Omega (\Delta_\mathcal{M})^{-1}\left[\frac{s_1}{\|\nabla\phi\|}\right]\frac{s_2}{|\nabla\phi|}\,\|\nabla\phi\|\,dx\,,$$

where $\mathcal{M}$ denotes the level set, the integration point x belongs to. The gradient flow w.r.t. the H^{-1} metric of e_γ in level set formulation is now given by

$$g(\partial_t\phi, \vartheta) = -\int_\Omega \gamma_z(\nabla\phi)\nabla\vartheta\,dx\,,$$

which is by the above representation of g

$$-\int_\Omega (\Delta_\mathcal{M})^{-1}\left[\frac{\vartheta}{\|\nabla\phi\|}\right]\partial_t\phi\,dx = -\int_\Omega \gamma_z(\nabla\phi)\nabla\vartheta\,dx\,.$$

Replacing ϑ by $\|\nabla\phi|\Delta_\mathcal{M}\vartheta$ we arrive at

$$\int_\Omega \partial_t\phi\,\vartheta\,dx = -\int_\Omega h_\gamma\,\Delta_\mathcal{M}\vartheta\,\|\nabla\phi\|\,dx\,.$$

From this representation of the H^{-1} gradient flow, one is lead to introduce the additional variable $y = h_\gamma$. Thus we just have to find a numerically suitable form of the expression $\int_\Omega y|\nabla\phi|\Delta_\mathcal{M}\,dx$. We observe

$$\begin{aligned}\int_\Omega y\|\nabla\phi\|\,\Delta_\mathcal{M}\vartheta\,dx &= \int_{\mathbb{R}}\int_{\mathcal{M}_c} y\,\Delta_{\mathcal{M}_c}\vartheta\,dA\,dc = -\int_{\mathbb{R}}\int_{\mathcal{M}_c}\nabla_{\mathcal{M}_c}y\,\nabla_{\mathcal{M}_c}\vartheta\,dA\,dc\\ &= -\int_\Omega P\nabla y\cdot P\nabla\vartheta\,\|\nabla\phi\|\,dx\end{aligned}$$

taking into account the properties $P^T = P$ and $P^2 = P$. Concluding, the weak formulation of anisotropic surface diffusion for level sets is given by

$$\begin{aligned}\int_\Omega \partial_t\phi\,\vartheta\,dx &= \int_\Omega P\nabla y\cdot\nabla\vartheta\,\|\nabla\phi\|\,dx\\ \int_\Omega y\,\psi\,dx &= -\int_\Omega \gamma_z(\nabla\phi)\nabla\psi\,dx\,.\end{aligned}$$

4. Numerical schemes

In this section we want to derive numerical schemes which can be used to discretize the anisotropic surface diffusion problem. We provide both, spatial and time discretization schemes.

4.1. Spatial discretization

Let us consider a uniform mesh $\mathcal{C}$ covering the whole image domain Ω and consider the corresponding interpolation on cells $C \in \mathcal{C}$ to obtain discrete intensity functions in the accompanying finite element space V^h. Here, the superscript h indicates the grid size. Suppose $\{\Phi_i\}_{i\in I}$ is the standard basis of hat shaped base functions corresponding to nodes of the mesh indexed over an index set I. To clarify the notation we will denote spatially discrete quantities with upper case letters to distinguish them from the corresponding continuous quantities in lower case letters. Hence, we obtain

$$V^h = \{\Phi \in C^0(\Omega) \,|\, \Phi|_C \in \mathcal{P}_1 \,\forall C \in \mathcal{C}\} \,,$$

where $\mathcal{P}_1$ denotes the space of $(d+1)$-linear functions. Suppose $\mathcal{I}_h$ is the Lagrangian interpolation onto V^h. Now, we formulate the semi-discrete and regularized finite element problem

Problem 4.1. Find a function $\Phi : \mathbb{R}_0^+ \to V^h$ with $\Phi(0) = \mathcal{I}_h\phi_0$ and a corresponding weighted mean curvature function $Y : \mathbb{R}^+ \to V^h$, such that

$$\begin{aligned} \int_\Omega \partial_t\Phi(t)\Theta \,\mathrm{d}x &= \int_\Omega P_\epsilon[\Phi(t)]\nabla Y(t)\cdot\nabla\Theta \,\|\nabla\Phi(t)\| \,\mathrm{d}x \\ \int_\Omega Y(t)\Psi \,\mathrm{d}x &= -\int_\Omega \gamma_z(N^\epsilon)\cdot\nabla\Psi \,\mathrm{d}x \end{aligned}$$

for all $t > 0$ and all test functions Θ, $\Psi \in V^h$.

Here, we use the notation

$$P_\epsilon[\Phi] = \left(1\!\!1 - \frac{\nabla\Phi}{\|\nabla\Phi\|_\epsilon} \otimes \frac{\nabla\Phi}{\|\nabla\Phi\|_\epsilon}\right) \,, \quad N^\epsilon = \frac{\nabla\Phi}{\|\nabla\Phi\|_\epsilon}$$

and consider Neumann boundary conditions on $\partial\Omega$.

4.2. Time discretization

For a given time step $\tau > 0$ we aim to compute discrete functions $\Phi^k(\cdot) \in V^h$, which approximate $\phi(k\tau, \cdot)$ on Ω. Thus, we replace the time derivative $\partial_t\phi$ by a backward difference quotient and evaluate all terms related to the metric on the previous time step. In particular in the $(k+1)$th time step the weight $\|\nabla\Phi\|$ and the projection P are taken from the kth time step. Explicit time discretizations are ruled out due to accompanying severe time step restrictions of the type $\tau \le C(\epsilon)h^4$, where h is the spatial grid size (cf. results presented in [15, 16]). We are left to decide, which terms in each time step to consider explicitly and which implicitly. Taking all linear terms implicitly, leads to

Problem 4.2. Find a sequence of level set functions $(\Phi^k)_{k=0,\dots} \subset V^h$ with $\Phi^0 = \mathcal{I}_h\phi_0$ and a corresponding sequence of weighted mean curvature functions $(Y^k)_{k=0,\dots} \subset V^h$ such that

$$\begin{aligned}\int_\Omega \frac{\Phi^{k+1}-\Phi^k}{\tau}\,\Theta\,\mathrm{d}x &= \int_\Omega P_\epsilon[\Phi^k]\nabla Y^{k+1}\cdot\nabla\Theta\,\|\nabla\Phi^k\|_\epsilon\,\mathrm{d}x\\ \int_\Omega Y^{k+1}\,\Psi\,\mathrm{d}x &= -\int_\Omega \gamma_z\left(\frac{\nabla\Phi^k}{\|\nabla\Phi^k\|_\epsilon}\right)\cdot\nabla\Psi\,\mathrm{d}x\end{aligned}$$

for all test functions Θ, $\Psi \in V^h$.

However, this algorithm leads to a completely explicit time-discretization. Therefore, we use the advice of Deckelnick and Dziuk [17] and add an implicit term to the second equation as follows.

Problem 4.3. Find a sequence of level set functions $(\Phi^k)_{k=0,\dots} \subset V^h$ with $\Phi^0 = \mathcal{I}_h\phi_0$ and a corresponding sequence of weighted mean curvature functions $(Y^k)_{k=0,\dots} \subset V^h$ such that

$$\begin{aligned}\int_\Omega \frac{\Phi^{k+1}-\Phi^k}{\tau}\,\Theta\,\mathrm{d}x &= \int_\Omega P_\epsilon[\Phi^k]\nabla Y^{k+1}\cdot\nabla\Theta\,\|\nabla\Phi^k\|_\epsilon\,\mathrm{d}x\\ \int_\Omega Y^{k+1}\,\Psi\,\mathrm{d}x &= -\int_\Omega \gamma_z\left(\frac{\nabla\Phi^k}{\|\nabla\Phi^k\|_\epsilon}\right)\cdot\nabla\Psi\,\mathrm{d}x\\ &\quad -\lambda\int_\Omega \frac{\gamma\left(\frac{\nabla\Phi^k}{\|\nabla\Phi^k\|_\epsilon}\right)}{\|\nabla\Phi^k\|_\epsilon}\nabla(\Phi^{k+1}-\Phi^k)\nabla\Psi\;\mathrm{d}x\end{aligned}$$

for all test functions Θ, $\Psi \in V^h$ and some parameter λ.

As a motivation for this additional term lets consider the isotropic case. Here $\gamma = |z|$ and $\gamma_z = id$. Thus the second equation in Problem 4.3 becomes

$$\int_\Omega Y^{k+1}\,\Psi\,\mathrm{d}x = -\int_\Omega \frac{\nabla\Phi^k}{\|\nabla\Phi^k\|_\epsilon}\cdot\nabla\Psi\,\mathrm{d}x - \lambda\int_\Omega \frac{\nabla(\Phi^{k+1}-\Phi^k)}{\|\nabla\Phi^k\|_\epsilon}\nabla\Psi\;\mathrm{d}x$$

which leads for $\lambda = 1$ to the implicit formulation. Compare [17] for more details and an optimal choice of the parameter λ.

5. Implementation and numerical results

In this section we show some preliminary results of our implementation. All calculations were performed on a regular, uniform triangulation, where we used standard Courant finite elements (i.e., globally continuous and piecewise affine). We employed a Schur complement approach and used left and right diagonal preconditioning for the resulting linear system. In Figures 1 and 2 we show results for the isotropic case in 2d and 3d respectively.

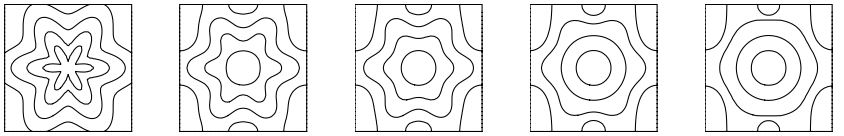

FIGURE 1. Isotropic surface diffusion in 2d. Level sets -0.5, 0.0, 0.5, 1.0 (from inner to outer curve).
From left to right $t = 0.0, 0.01, 0.02, 0.05, 0.1$. Computational domain: 4×4 square; triangulation: 2.100 grid points; time step: 10^{-4}; $\lambda = 1.0$.

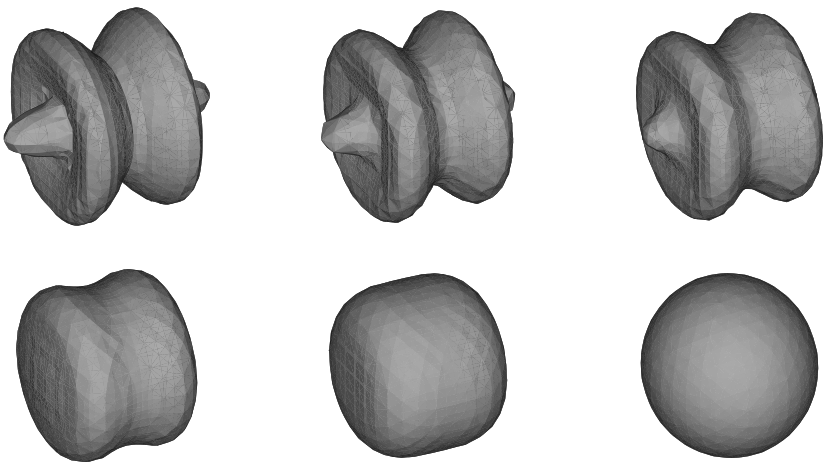

FIGURE 2. Isotropic surface diffusion in 3d. Level set 0 at $t = 0.0$, 0.001, 0.002, 0.005, 0.01, 0.05 (from top left to bottom right). Computational domain: $4 \times 4 \times 4$ cube; triangulation: 36.000 grid points; time step: 10^{-5}; $\lambda = 1.0$.

Neumann boundary conditions have been imposed and one sees that the bizarrely shaped initial data become ever more ball shaped as the evolution proceeds, approximating the steady state solution of isotropic surface diffusion.

In Figures 3 and 4 we present numerical results for anisotropic surface diffusion with anisotropy function

$$\gamma(x) = \sum_{k=1}^{d} \left(\epsilon|x|^2 + |x_k|^2\right)^{\frac{1}{2}}, \quad \epsilon = 0.01; \quad d = 2, 3. \tag{5.1}$$

Here the limit configuration is clearly determined by the rectangular symmetry of the anisotropy.

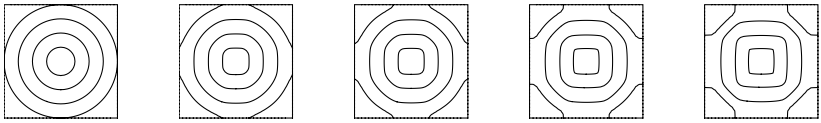

FIGURE 3. Anisotropic surface diffusion in 2d. Levesets -0.5, 0.0, 0.5, 1.0 (from inner to outer curve). From top left to bottom right $t = 0.0, 0.001, 0.002, 0.005, 0.01$. Computational domain: 4×4 square; triangulation: 2.100 grid points; time step: 10^{-4}, $\lambda = 10.0$.

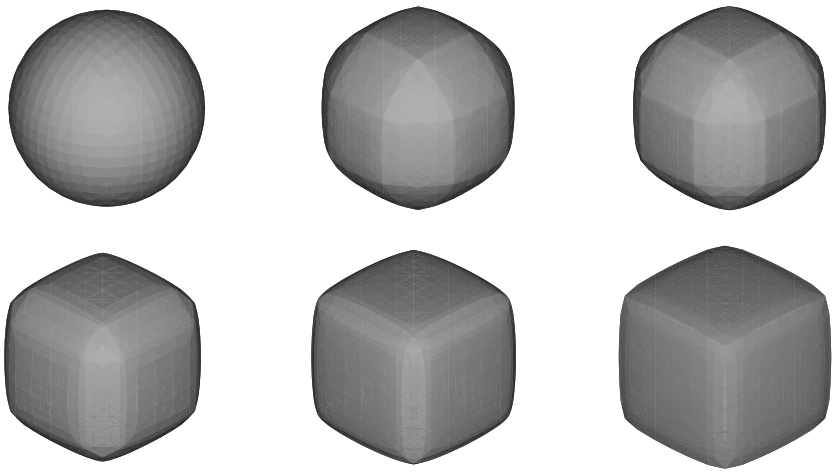

FIGURE 4. Anisotropic surface diffusion in 3d. Levelset 0 at $t = 0.0, 0.001, 0.002, 0.005, 0.01, 0.02$ (from top left to bottom right). Computational domain: $4 \times 4 \times 4$ cube; triangulation: 36.000 grid points; time step: 10^{-5}, $\lambda = 20.0$.

References

[1] M. Rost, (this volume).

[2] U. Clarenz, *The Wulff-shape minimizes an anisotropic Willmore functional.* DFG-Forschergruppe Freiburg, Preprint 15 (2003).

[3] M. Droske, M. Rumpf, *A level set formulation for Willmore flow.* Interfaces and Free Boundaries **6** (2004), 361–378.

[4] D.L. Chopp, J.A. Sethian, *Motion by intrinsic Laplacian of curvature.* Interfaces Free Bound. **1** (1999), 107–123.

[5] M. Khenner, A. Averbuch, M. Israeli, M. Nathan, *Numerical solution of grain boundary grooving by level set method.* J. of Comput. Phys. **170** (2001), 764–784.

[6] P. Smereka, *Semi-Implicit Level Set Methods for Curvature and Surface Diffusion Motion* J. of Sci. Comput. **19** (2003), 439–456.

[7] S. Osher, J.A. Sethian, *Fronts propagating with curvature dependent speed: Algorithms based on Hamilton-Jacobi formulations.* J. of Comput. Phys. **79** (1988), 12–784.

[8] R. Rusu, *An algorithm for the elastic flow of surfaces.* Mathematische Fakultät Freiburg, Preprint 35 (2001).

[9] L. Ambrosio, N. Fusco, D. Pallara, *Functions of bounded variation and free discontinuity problems.* Oxford University Press, 2000.

[10] L.C. Evans, J. Spruck, *Motion of Level Sets by Mean Curvature I.* J. Diff. Geom. **33** (1991), 635–681.

[11] U. Clarenz, G. Dziuk, M. Droske, M. Rumpf, *Level set formulation for anisotropic geometric evolutions problems* manuscript, in preparation

[12] S. Osher, N. Paragios, *Geometric Level Set Methods in Imaging, Vision and Graphics.* Springer, 2003.

[13] G. Wulff, *Zur Frage der Geschwindigkeit des Wachsthums und der Auflösung der Kristallflächen.* Zeitschrift der Kristallographie **34** (1901), 449–530.

[14] I. Fonseca, S. Müller, *A uniqueness proof for the Wulff theorem.* Proc. Roy. Soc. Edinb. A **119** (1991), 125–136.

[15] S. Yoshizawa, A.G. Belyaev, *Fair Triangle Mesh Generation with Discrete Elastica.* in Geometric Modeling and Processing, RIKEN, Saitama, 2001, 119–123

[16] T.F. Chan, S.H. Kang, J. Shen, *Euler's Elastica and curvature-based inpainting.* SIAM Appl. Math. **63** (2002), 564–592.

[17] K. Deckelnick, G. Dziuk, *A fully discrete numerical scheme for weighted mean curvature flow.* Numer. Math. **91** (2002), 423–452.

[18] L.C. Evans, R.F. Gariepy, *Measure Theory and Fine Properties of Functions.* CRC Press, 1992.

Ulrich Clarenz, Martin Rumpf and Ulrich Weikard
Numerical Analysis and Scientific Computing
Universität Duisburg-Essen,
Lotharstr. 65
D-47048 Duisburg, Germany
e-mail: clarenz@math.uni-duisburg.de
e-mail: rumpf@math.uni-duisburg.de
e-mail: weikard@math.uni-duisburg.de

Frank Haußer and Axel Voigt
Crystal Growth group
research center caesar
Ludwig-Erhard-Allee 2
D-53175 Bonn, Germany
e-mail: hausser@caesar.de
e-mail: voigt@caesar.de